



HAL
open science

Experimental characterization of heat transfer in nanostructured silicon-based materials

Mouhannad Massoud

► **To cite this version:**

Mouhannad Massoud. Experimental characterization of heat transfer in nanostructured silicon-based materials. Materials. Université de Lyon, 2016. English. NNT : 2016LYSEI063 . tel-01688545

HAL Id: tel-01688545

<https://theses.hal.science/tel-01688545>

Submitted on 19 Jan 2018

HAL is a multi-disciplinary open access archive for the deposit and dissemination of scientific research documents, whether they are published or not. The documents may come from teaching and research institutions in France or abroad, or from public or private research centers.

L'archive ouverte pluridisciplinaire **HAL**, est destinée au dépôt et à la diffusion de documents scientifiques de niveau recherche, publiés ou non, émanant des établissements d'enseignement et de recherche français ou étrangers, des laboratoires publics ou privés.



NNT : 2016LYSEI063

THESE de DOCTORAT DE L'UNIVERSITE DE LYON
opérée au sein de
L'INSA de Lyon

Ecole Doctorale ED34
Matériaux de Lyon

Spécialité de doctorat : Matériaux
Discipline : Caractérisation des matériaux

Soutenue publiquement le 20/06/2016, par :

Antonin Mouhannad MASSOUD

**Experimental characterization of heat
transfer in nanostructured silicon-based
materials**

Devant le jury composé de :

ALZINA	Francesc	Directeur de recherche (ICN2)	Président
BEZENCENET	Odile	Ingénieur-docteur (Thales)	Examinatrice
BLUET	Jean-Marie	Professeur (INSA)	Directeur de thèse
CHAPUIS	Pierre-Olivier	Chargé de recherche (INSA)	Co-directeur de thèse
LERONDEL	Gilles	Professeur (UTT)	Rapporteur
ROBILLARD	Jean-François	Maître de conférences (IEMN)	Examineur
VOLZ	Sebastian	Directeur de recherche (ECP)	Rapporteur

Département FEDORA – INSA Lyon – Ecoles Doctorales – Quinquennal 2016-2020

SIGLE	ECOLE DOCTORALE	NOM ET COORDONNEES DU RESPONSABLE
CHIMIE	CHIMIE DE LYON http://www.edchimie-lyon.fr Sec : Renée EL MELHEM Bat Blaise Pascal 3 ^e étage 04 72 43 80 46 INSA : R. GOURDON secretariat@edchimie-lyon.fr	M. Stéphane DANIELE Institut de Recherches sur la Catalyse et l'Environnement de Lyon IRCELYON-UMR 5256 Équipe CDFA 2 avenue Albert Einstein 69626 Villeurbanne cedex directeur@edchimie-lyon.fr
E.E.A.	ELECTRONIQUE, ELECTROTECHNIQUE, AUTOMATIQUE http://edeea.ec-lyon.fr Sec : M.C. HAVGOUDOUKIAN Ecole-doctorale.eea@ec-lyon.fr	M. Gérard SCORLETTI Ecole Centrale de Lyon 36 avenue Guy de Collongue 69134 ECULLY Tél : 04.72.18 60.97 Fax : 04 78 43 37 17 Gerard.scorletti@ec-lyon.fr
E2M2	EVOLUTION, ECOSYSTEME, MICROBIOLOGIE, MODELISATION http://e2m2.universite-lyon.fr Sec : Bat Atrium – UCB Lyon 1 04.72.44.83.62 INSA : S. REVERCHON secretariat.e2m2@univ-lyon.fr	Mme Gudrun BORNETTE CNRS UMR 5023 LEHNA Université Claude Bernard Lyon 1 Bât Forel 43 bd du 11 novembre 1918 69622 VILLEURBANNE Cédex Tél : 06.07.53.89.13 e2m2@univ-lyon1.fr
EDISS	INTERDISCIPLINAIRE SCIENCES-SANTE http://www.ediss-lyon.fr Sec : Bat Atrium – UCB Lyon 1 04 72 44 83 62 INSA : Safia.ait-chalal@univ-lyon1.fr	Mme Emmanuelle CANET-SOULAS INSERM U1060, CarMeN lab, Univ. Lyon 1 Bâtiment IMBL 11 avenue Jean Capelle INSA de Lyon 696621 Villeurbanne Tél : 04.72.11.90.13 Emmanuelle.canet@univ-lyon1.fr
INFOMATHS	INFORMATIQUE ET MATHEMATIQUES http://infomaths.univ-lyon1.fr Sec : Renée EL MELHEM Bat Blaise Pascal 3 ^e étage infomaths@univ-lyon1.fr	Mme Sylvie CALABRETTO LIRIS – INSA de Lyon Bat Blaise Pascal 7 avenue Jean Capelle 69622 VILLEURBANNE Cedex Tél : 04.72. 43. 80. 46 Fax 04 72 43 16 87 Sylvie.calabretto@insa-lyon.fr
Matériaux	MATERIAUX DE LYON http://ed34.universite-lyon.fr Sec : M. LABOUNE PM : 71.70 –Fax : 87.12 Bat. Direction 1 ^{er} étage Ed.materiaux@insa-lyon.fr	M. Jean-Yves BUFFIERE INSA de Lyon MATEIS Bâtiment Saint Exupéry 7 avenue Jean Capelle 69621 VILLEURBANNE Cedex Tél : 04.72.43 71.70 Fax 04 72 43 85 28 Ed.materiaux@insa-lyon.fr
MEGA	MECANIQUE, ENERGETIQUE, GENIE CIVIL, ACOUSTIQUE http://mega.universite-lyon.fr Sec : M. LABOUNE PM : 71.70 –Fax : 87.12 Bat. Direction 1 ^{er} étage mega@insa-lyon.fr	M. Philippe BOISSE INSA de Lyon Laboratoire LAMCOS Bâtiment Jacquard 25 bis avenue Jean Capelle 69621 VILLEURBANNE Cedex Tél : 04.72 .43.71.70 Fax : 04 72 43 72 37 Philippe.boisse@insa-lyon.fr
ScSo	ScSo* http://recherche.univ-lyon2.fr/scso/ Sec : Viviane POLSINELLI Brigitte DUBOIS INSA : J.Y. TOUSSAINT viviane.polsinelli@univ-lyon2.fr	Mme Isabelle VON BUELTZINGLOEWEN Université Lyon 2 86 rue Pasteur 69365 LYON Cedex 07 Tél : 04.78.77.23.86 Fax : 04.37.28.04.48

*ScSo : Histoire, Géographie, Aménagement, Urbanisme, Archéologie, Science politique, Sociologie, Anthropologie

A ma mère et à mon père.
A ma sœur et à mon frère.

Acknowledgements – Remerciements

Directeur et co-directeur

Je souhaite remercier Jean-Marie Bluet (directeur de thèse) et Pierre-Olivier Chapuis (co-directeur de thèse) pour m'avoir fait confiance et laissé des libertés d'initiative tout au long de ces trois ans et demi de travail en commun. Vous m'avez toujours assuré la possibilité de travailler dans les meilleures conditions. Nos rapports ont évolué au cours de mon doctorat et je peux dire aujourd'hui que j'ai eu beaucoup de chance de vous avoir comme directeur et co-directeur de thèse. Au cours de ces dernières années, vous vous êtes impliqués dans l'orientation de mes travaux et je vous en suis infiniment reconnaissant. Vous avez eu un réel impact positif sur mon parcours professionnel et personnel. Je suis heureux que vous fassiez ainsi partie aujourd'hui des personnes qui ont marqué ma vie.

Membre de jury

Je tiens à remercier chaleureusement tous les membres de jury d'avoir accepté l'invitation. Merci beaucoup M. Volz et M. Lerondel d'avoir accepté de juger mes travaux et d'avoir dégagé du temps pour vous y consacrer. J'ai été touché que vous ayez répondu si rapidement, et avec enthousiasme, à ma demande.

Directeurs des laboratoires

J'aimerais remercier Mme. Chevalier, directrice du laboratoire INL et M. Bonjour, directeur du laboratoire CETHIL, pour m'avoir accueilli au sein de leurs laboratoires.

Equipes

Je tiens à remercier tous les membres de l'équipe Spectroscopie et Nanomatériaux de l'INL. Merci à Bruno (Masenelli), Vladimir et Nicolas pour toutes les discussions scientifiques, courtes, mais très intéressantes. Merci à Georges de s'être toujours intéressé à mes travaux et de m'avoir toujours encouragé. Je tiens également à remercier tous les membres de l'équipe MiNT du CETHIL. Merci beaucoup pour vos suggestions et pour toutes les discussions scientifiques et non scientifiques que j'ai eues durant mes années de doctorat. Un grand merci pour Séverine et Stéphane pour toutes les informations que vous m'avez offertes concernant la microscopie à sonde locale. Cette partie ne peut pas être finie avant de remercier Rodolphe et Olivier (Merchier il faut bien le préciser, parce qu'il n'y pas mal de Olivier dans l'équipe MiNT!) d'avoir toujours envoyé les mails de rappel pour les réunions d'équipe et de s'intéresser aux travaux des autres. Merci Rodolphe pour les discussions concernant l'espace et la vie !

Personnel

Un grand merci pour Virginie, Annie et Cindy (INL), et pour Florence et Sophie (CETHIL) pour leurs aides si précieuses pour faciliter les démarches administratives ! Merci pour Philippe et Robert (qui est déjà parti à la retraite) de m'avoir aidé quand j'avais besoin des outils pour réaliser les manips. Je tiens à remercier la plateforme technologique NanoLyon, surtout Jean-Louis Leclercq, Khaled et Joëlle d'avoir toujours été là quand j'avais besoin de leur aide. Merci aux informaticiens et surtout Loïc qui a été toujours présent quand il y avait un souci.

Aides diverses

Je tiens à remercier Abdelkader Souifi pour ses encouragements et pour m'avoir fait confiance pour continuer le chemin jusqu'au bout !

Cette étude a nécessité des irradiations. J'en profite donc pour remercier chaleureusement Bruno Canut pour les irradiations des échantillons de silicium. Je tiens à remercier David Trodec pour la préparation des lames minces pour la microscopie électronique à transmission, Lucain Roiban pour regarder la structure de ces échantillons. Je tiens à remercier Romain Bachelet pour son aide pour caractériser les multicouches de silicium poreux avec la réflectivité des rayons X.

Collaboration

Une partie de cette thèse a été réalisée en collaboration avec le laboratoire IEMN à Lille. Je tiens à remercier Jean-François Robillard pour cette agréable et fructueuse collaboration. Un grand merci pour Valeria Lacatena et Mciej Haras (anciens doctorants, ils ont déjà eu leurs diplômes) pour la fabrication des membranes phononiques. J'aurais aimé trouver des défauts sur les échantillons pour faciliter leur caractérisation en microscopie électronique à balayage, mais non pas de chance, les échantillons étaient trop propres ! Quel joli travail !

Collègues

Si un laboratoire tourne c'est grâce à ces doctorants. Merci pour tous les doctorants du CETHIL et les doctorants de l'INL avec qui j'ai eu des discussions diverses et intéressantes. Je tiens surtout à remercier Jia et Anton avec qui j'ai partagé le bureau au rez-de-chaussée à l'INL et Sandra et Chi Kien avec qui j'ai partagé le bureau au CETHIL.

Amis

J'adresse toute ma gratitude à tous mes ami(e)s et à toutes les personnes qui m'ont aidé dans la réalisation de ce travail. Je commence par remercier Dominique qui m'a toujours encouragé et qui m'a donné beaucoup de confiance en moi (vas-y fonce you are the best !), et grâce à lui j'ai appris beaucoup de nouvelles expressions françaises que je ne connaissais pas avant. Merci beaucoup de m'avoir toujours remonté le moral, et de m'avoir consacré beaucoup de temps. Ahhh ces voyages inoubliables et ces moments de rire et de folie. Tu devais être dans la partie 'Famille' mais bon ici on peut écrire plus de choses marrantes. Cher ami Ghassan (Gass), merci pour toutes ces balades en ville (cheesecake ou café ?) et pour ton aide quand j'avais des problèmes en informatique ! Mais tu dois passer plus de temps sur ta Playstation pour que tu puisses me battre en Mortel Kombat. Mais bon tu n'es pas loin, un jour tu y arriveras ! Je tiens à remercier tous mes amis grenoblois, Roland, Sandra, Hind et Jihad. On a passé une très bonne année ensemble, dure c'est sûr, mais avec la bonne humeur, les pains au

chocolat, les pizzas et les bons plats libanais ... on a tous réussi nos études et on est passé à l'étape suivante, ce qu'on appelle le plus haut niveau d'étude ! Merci à Mahmoud pour cette agréable année de Master 2, tu dois t'entraîner plus aux jeux de foot sur la Playstation, afin que tu puisses me battre. Je tiens à remercier Benatu pour toutes ces promenades en voiture à Sherbrooke et pour tous ces bons moments qu'on a pu passer ensemble (ça te dit d'aller faire du shopping ? je suis prêt dans 5 minutes, je t'attends). Merci beaucoup pour ton aide en salle blanche ! Amer sans toi je n'aurais pas pu avoir un logement à Sherbrooke, un merci ne suffit pas mais bon ... C'était un grand plaisir de partager les déjeuners avec toi (désolé on dit diners au Québec) ! Floriane et Arnaud, c'était un grand plaisir de faire votre connaissance à Sherbrooke et j'espère vous revoir en France (Orléans ce n'est pas loin !). Merci pour tous ces moments sympas et surtout pour le délicieux repas que Floriane a préparé, du poulet, du sirop d'érable ... il ne faut pas tout dire, chuttt c'est un secret ! Arnaud connaissait les jeux de vidéo par cœur et ben c'était impossible de le battre, avec Benatu et Floriane on a essayé, mais bon, on n'a jamais réussi ! Richard, l'amitié c'est sacré, et de t'avoir eu comme ami depuis l'enfance est un grand bonheur, tu arrives à me faire rire même dans des situations compliquées. Merci beaucoup d'avoir toujours été là pour me faire sourire. Franck, ça ne fait pas longtemps qu'on se connaît, mais tu es quelqu'un de formidable qu'on apprécie tout de suite. Merci pour toi et je te souhaite tout le bonheur du monde parce que tu le mérites ! Si un rire m'avait donné l'envie de rire, c'est surtout celui de Wassim. Ravis d'avoir fait ta connaissance et merci pour toutes les agréables poses café ... Abdul Salam, cher ami 'orange'. Merci beaucoup pour tous ces agréables moments qu'on a passés ensemble que ce soit à l'INL ou à l'extérieur. Tu as un long chemin à faire, mais tu l'as commencé avec beaucoup de succès. Tout le meilleur pour la suite ! Je tiens à remercier mes vrais amis d'enfance, Jad, Hanna, Jean et Wahib. La vie nous a séparés mais l'Amitié gagne toujours. Merci beaucoup pour tous vos encouragements et pour tous les rires et les inoubliables beaux souvenirs qui restent gravés dans ma mémoire ! Je ne peux pas finir avant de dire merci à Louay qui m'a aidé dans les démarches administratives avant d'arriver en France.

Ma famille

Enfin, les mots les plus simples étant les plus forts, j'adresse toute mon affection à ma famille. Je me limite à ma mère, mon père, ma sœur et mon frère. Sinon on n'en finit pas ! Maman, Zeina, je te remercie du fond de mon cœur d'avoir toujours été là pour m'aider. De m'avoir toujours épaulé et encouragé (je suis connecté sur Skype je ne te vois pas connecté, je t'attends vas-y). Papa, Fawaz, merci infiniment pour ton soutien et pour la confiance que tu as mise en moi le jour de mon départ pour cette fabuleuse aventure. Ranine, ma magnifique petite sœur, je te remercie pour tes encouragements et pour tous les bons moments qu'on a partagés ensemble. Mon grand frère, Moutaz, et sa femme, Mireille, merci beaucoup pour vos encouragements, vous êtes un couple formidable. On ne dit pas des choses pareilles ici mais bon je n'ai pu m'empêcher de les dire. Je vous aime.

Abstract

This PhD thesis deals with the experimental characterization of heat transfer at the nanoscale in materials compatible with microelectronic processes. Two characterization techniques are applied to two different systems, irradiated mesoporous silicon and suspended silicon membranes. The first characterization technique is micro-Raman thermometry. The laser power heats up the exposed sample. The determination of the thermal conductivity requires the modeling of the heat source using finite element simulations. The modeling of the heat source relies on different parameters that should be carefully determined.

The second characterization technique is Scanning Thermal Microscopy (SThM), an Atomic Force Microscopy (AFM)-based technique. Operated in its active mode, the AFM probe is replaced by a resistive Wollaston probe that is heated by Joule heating. Used in AFM contact mode, this technique allows a local thermal excitation of the studied material. The determination of the thermal conductivity requires the analysis of the thermal response of the probe using calibration samples and modeling when dealing with complicated geometries. The effect of the tip position on heat transfer between the tip and the sample is studied. A new method decoupling the heat transfer between the tip and the sample, at the contact and through air, is proposed for determining the thermal conductivity of complicated geometries.

The results obtained from the two techniques on irradiated mesoporous silicon samples using heavy ions in the electronic regime are in good agreement. They show a degradation of the thermal conductivity of mesoporous silicon due to the increase in the amorphous phase while increasing the ion fluence.

The results obtained on suspended silicon membrane strips show a decrease in the thermal conductivity of more than 50 % in comparison to bulk silicon. When perforated into a phononic structure of sub-100 nm period, the membrane thermal conductivity is about one order of magnitude lower than the bulk.

A chapter introducing a promising silicon-based material for the evidence of phonon coherence concludes the manuscript.

Keywords: Nanothermometry, Scanning Thermal Microscopy, micro-Raman thermometry, thermal conductivity, phonons, heat conduction, mesoporous silicon, heavy ions irradiation, electronic regime, amorphous silicon, suspended membranes, phononic membranes, superlattice, phonon coherence

Résumé

Ce mémoire de thèse aborde la caractérisation expérimentale du transfert thermique à l'échelle nanométrique dans des matériaux compatibles avec les procédés de la micro-électronique. Pour cela deux techniques de caractérisation sont appliquées chacune à deux différents systèmes, le silicium mésoporeux irradié et les membranes de silicium suspendues.

La première technique de caractérisation est la thermométrie micro-Raman. La puissance du laser chauffe l'échantillon exposé. La détermination de la conductivité thermique nécessite la modélisation de la source de chaleur par la méthode des éléments finis. Dans les cas considérés la modélisation de la source de chaleur repose sur différents paramètres qui doivent être soigneusement déterminés.

La seconde technique de caractérisation est la microscopie à sonde locale (d'acronyme anglais SThM), basée sur le principe de la microscopie à force atomique (d'acronyme anglais AFM). Utilisée en mode actif, la sonde AFM est remplacée par une sonde résistive de type Wollaston qui est chauffée par effet Joule. Utilisée en mode AFM contact, cette technique permet une excitation thermique locale du matériau étudié. La détermination de la conductivité thermique nécessite l'analyse de la réponse thermique de la sonde au moyen d'échantillons d'étalonnage et également via la modélisation dans le cas des géométries complexes. L'effet de la position de la pointe sur le transfert de chaleur entre la pointe et l'échantillon est étudié. Une nouvelle méthode de découplage entre le transfert de chaleur entre la pointe et l'échantillon, respectivement à travers l'air et au contact, est proposée pour la détermination de la conductivité thermique des géométries complexes.

Les résultats obtenus avec les deux techniques pour les échantillons de silicium mésoporeux irradiés à l'aide d'ions lourds dans le régime électronique sont en bon accord. Ils montrent la dégradation de la conductivité thermique du silicium mésoporeux suite à une augmentation dans la phase d'amorphe lorsque la dose d'irradiation croît.

Les résultats obtenus sur les membranes de silicium suspendues montrent une réduction de la conductivité thermique de plus de 50 % par rapport au silicium massif. Lorsque la membrane est perforée périodiquement afin de réaliser une structure phononique de période inférieure à 100 nm, cette réduction est approximativement d'un ordre de grandeur.

Un chapitre introduisant un matériau prometteur à base de silicium pour observer des effets de cohérence phononique conclut le manuscrit.

Mots-clés: Nanothermométrie; microscopie à sonde locale; thermométrie micro-Raman; conductivité thermique; phonons; transfert conductif; silicium mésoporeux; irradiation ions lourds; régime électronique; silicium amorphe, membranes suspendues, membrane phononique; super-réseaux; cohérence phononique

Table of Contents

Acknowledgements – Remerciements	7
Abstract	11
Résumé.....	13
Table of Contents.....	15
List of Figures	19
List of Tables.....	25
General introduction.....	27
Chapter 1. Phonon transport in bulk and nanostructured materials	29
1.1 Introduction	29
1.2 Phonons	29
1.3 Phonon dispersion.....	29
1.3.1 Monoatomic crystals.....	30
1.3.2 Diatomic crystals	31
1.3.3 Superlattice crystals	34
1.4 Phonon population.....	36
1.5 Macro and micro heat conduction	37
1.5.1 Mean free path	38
1.5.2 Scattering mechanisms.....	38
1.5.2.1 Main scattering mechanisms	38
1.5.2.2 Boundary scattering in a film	39
1.5.3 Boltzmann Transport Equation	41
1.5.4 Fourier’s law	41
1.6 Heat conduction in amorphous materials	43
1.7 Thermal transport studies in suspended nanostructured materials	44
1.7.1 Wires and beams	44
1.7.1.1 Low temperature regime	44

1.7.1.2 Transition from room temperature to low temperatures	46
1.7.2 Two-dimensional periodic arrays	47
1.7.2.1 Membranes	47
1.7.2.2 Phononic structures	48
1.8 Coherent phonon heat conduction in superlattices	52
1.9 Summary.....	55
Bibliography.....	57

Chapter 2. Two characterization techniques for thermal conductivity determination.....59

2.1 Micro-Raman thermometry	59
2.1.1 Experimental temperature measurements	60
2.1.2 Determination of the thermal conductivity	62
2.1.3 Temperature determination using FEM simulations.....	65
2.1.4 Measurement of the laser spot	66
2.1.5 Determination of the absorbance	68
2.2 Scanning thermal microscopy (SThM).....	69
2.2.1 Experimental setup.....	69
2.2.1.1 Operational modes.....	70
2.2.2 The Wollaston probe: geometry and characteristics	72
2.2.3 Numerical study of heat transfer between a Wollaston tip and a sample	72
2.2.3.1 Heat loss coefficient and air box side determination	73
2.2.3.2 Tip-sample air heat transfer.....	74
2.2.3.2.1 Tip-sample distance.....	74
2.2.3.2.2 Straight tip configuration	75
2.2.3.2.3 Tilted tip configuration.....	78
2.2.4 Calibration method using SThM.....	81
2.2.4.1 Measurements on bulk samples.....	81
2.2.4.2 Samples with complex geometries	82
2.2.4.2.1 Out-of-contact method for thermal conductivity determination	82
2.2.4.2.2 Splitting the air and contact heat transfers	83
2.3 Brief comparison between the two characterization techniques	84
2.4 Summary.....	84
Bibliography.....	86

Chapter 3. Thermal conductivity of porous silicon irradiated by swift heavy ions	89
3.1 Context and goal of the study	89
3.1.1 Swift heavy ions irradiation	90
3.2 Samples manufacturing and structural characterization	92
3.2.1 Preparation of porous silicon samples	92
3.2.2 Samples irradiation by ^{129}Xe	95
3.2.3 Determination of porosity by microreflectivity	97
3.2.4 Scanning electron microscopy analysis	98
3.2.5 Determination of the amorphous fraction	99
3.3 Impact of irradiation on porous silicon thermal conductivity	104
3.3.1 Micro-Raman thermometry	104
3.3.2 Scanning thermal microscopy	105
3.3.3 Comparison of the results	107
3.4 Summary and perspectives	109
Bibliography.....	111
Chapter 4. Thermal conductivity of suspended silicon phononic membranes	115
4.1 Sample preparation	115
4.2 SThM on suspended membranes	117
4.2.1 Impact of the scan direction	117
4.2.2 Plain and phononic membranes	119
4.2.3 Sensitivity of the technique.....	120
4.2.4 Membrane thermal conductivity from SThM	122
4.3 Micro-Raman thermometry measurement method.....	124
4.3.1 FEM simulations and analytical calculations	125
4.3.2 Determination of the membrane heat loss coefficient	129
4.3.3 Temperature measurements	130
4.3.4 Calculation of the absorbance	131
4.3.4.1 Study of the membrane thickness.....	132
4.3.4.2 Hole size study	133
4.3.5 Membrane thermal conductivity from micro-Raman thermometry.....	135
4.4 Comparison of the results	137
4.5 Summary and perspectives	141
Bibliography.....	143

Chapter 5. Towards phonon coherence in porous silicon superlattices.....	145
5.1 Introduction	145
5.2 Formation of porous silicon superlattices.....	146
5.2.1 Calibration of the anodization cell.....	146
5.2.1.1 Micrometric porous silicon mono- and bilayers	146
5.2.1.2 Nanometric porous silicon monolayer	148
5.2.1.3 Porous silicon superlattice: nanometric periods.....	149
5.3 Towards thermal characterization of porous silicon superlattices.....	152
5.4 Summary and perspectives	153
Bibliography.....	154
General conclusions.....	155
Appendix. Comparison between volume heat generation and pointlike heat source	157

List of Figures

Figure 1.1 Monoatomic one-dimensional chain of atoms.....	30
Figure 1.2 Dispersion curve for monoatomic one-dimensional crystal.	31
Figure 1.3 Diatomic one-dimensional chain of atoms.	32
Figure 1.4 (a) Optical and acoustic phonon branches of the dispersion relation for a diatomic linear lattice. (b) Group velocity.	33
Figure 1.5 Phonon dispersion for silicon. [2].....	34
Figure 1.6 Sketch of a superlattice structure made of two different materials <i>A</i> and <i>B</i>	34
Figure 1.7 Structure of a superlattice consisting of two fcc lattices with atoms of different masses.....	35
Figure 1.8 Phonon dispersion relation in the growth direction of (5x5)-Si/Ge superlattice	35
Figure 1.9 Comparison between the phonon dispersion relations of 1D monoatomic structure and superlattice structures.	36
Figure 1.10 Phonon dominant wavelength as a function of temperature in Si	37
Figure 1.11 Comparison between the heat conduction regimes.....	37
Figure 1.12 Schematic representation of different collisions processes between phonons.	38
Figure 1.13 Phonons scattering mechanisms that reduce the thermal conductivity of a medium of thickness d_0	39
Figure 1.14 Mean free path of phonons in silicon nanowires as a function of temperature for $\Lambda_{Cas} = 160$ nm and $\xi_0 = 4.4$ nm.	40
Figure 1.15 Silicon thermal conductivity versus temperature.....	43
Figure 1.16 Diffusons, locons and propagons in amorphous Si.....	44
Figure 1.17 Monocrystalline GaAs suspended device for mesoscopic thermal conductance measurements.....	45
Figure 1.18 (a) Thermal conductance measurements vs temperature of the four suspended GaAs beams. (b) Mean free path deduction from the experimental work	45
Figure 1.19 Thermal conductance of straight and curved nanowires normalized to eight quanta of thermal conductance	46
Figure 1.20 Thermal conductivity of different diameter Si nanowires	46
Figure 1.21 Thermal conductivity of rough silicon nanowires (red squares) and silicon nanowires with low roughness (black squares) as a function of temperature.....	47
Figure 1.22 Thermal conductivity measurements. Membranes with 27 nm thickness and with 9 nm thickness.....	47
Figure 1.23 (a) Nanomesh structure showing a periodicity of 34 nm. (b) Thermal conductivity of different suspended structures.....	48
Figure 1.24 Thermal conductivity vs temperature of Si ribbons with different pitches	49
Figure 1.25 (a) SEM image of the PnCs. (b) Integrated DOS as a function of frequency for bulk and PnCs with $d/a=0.6$	49

Figure 1.26 (a) Band structure of full membrane. (b) Band structure of phononic membrane $a = 970$ nm. (c) Band structure of phononic membrane $a = 2425$ nm. (d) Resulting DOS. (e) Resulting average phonon group velocity	50
Figure 1.27 Measured emitted phonon power versus temperature	51
Figure 1.28 (a) Thermal conductivity measurements of, monocrystalline and polycrystalline Si PnCs. (b) Thermal conductivity measurements of Si PnCs of different porosities at room temperature and at 4 K.	51
Figure 1.29 Thermal conductivity of ordered and disordered phononic crystals. (a) Measurements at room temperature (RT). (b) Measurements at 3.7 K.....	52
Figure 1.30 Thermal conductivity in one dimension as a function of the SL period in nanometers	53
Figure 1.31 (a) Cross sectional transmission electron microscope image of 3 periods of the SL. (b) SL thermal conductivity versus the number of periods. (c) SL thermal conductivity for different temperatures	54
Figure 1.32 Thermal conductivity for different interface densities at room temperature. (a) STO/CTO SLs. (b) STO/BTO SLs	54
Figure 1.33 Thermal conductivity of $^{28}\text{Si}/^{30}\text{Si}$ SLs with perfect interfaces, $^{28}\text{Si}/^{30}\text{Si}$ SLs with intermixed interfaces, natural silicon and $^{28}\text{Si}_{0.5}/^{30}\text{Si}_{0.5}$ alloy.	55
Figure 2.1 Raman shift dependence on temperature	61
Figure 2.2 Schematic of the Renishaw Raman microscope with a 532 nm YAG laser beam with an objective x50 and NA of 0.5	61
Figure 2.3 Determination of the temperature increase based on Stokes peak positions. (a) Stokes Raman shift versus laser power. (b) Deduced temperature rise versus laser power based on the room-temperature peak position.....	62
Figure 2.4 Temperature rise versus absorbed laser power.	63
Figure 2.5 (a) 3D view of the real configuration. (b) 2D axisymmetric schematic of the modeling geometry including the boundary conditions.....	63
Figure 2.6 (a) Temperature profile on the surface. (b) Isothermal contours	64
Figure 2.7 Temperature difference.....	65
Figure 2.8 Temperature rise versus laser beam radius.....	66
Figure 2.9 Principle of knife edge technique.	66
Figure 2.10 Typical curves obtained during knife edge measurements. (a) Normalized power intensity versus beam position obtained for $\lambda = 532$ nm with an objective 50x/0.5 NA. (b) Normalized power intensity versus beam position obtained for $\lambda = 473$ nm with an objective 100x/0.95 NA	67
Figure 2.11 Principle of the integrating sphere. (a) The sample is placed into the sphere and the laser is directed on the sphere wall far from the sample. (b) The laser is directed onto the sample.....	68
Figure 2.12 Integrating sphere spectra for experiments obtained on porous silicon sample with 56 % porosity.	68
Figure 2.13 Principle of the technique.	69
Figure 2.14 Schematic of a Wheatstone bridge.....	70
Figure 2.15 Wheatstone bridge calibration: variable resistance of the bridge as a function of the bridge power input.....	71

Figure 2.16 (a) Scanning electron microscope image of the Wollaston probe. (b) Schematic of the Wollaston probe	72
Figure 2.17 Determination of the heat loss coefficient and the air box side dimension	73
Figure 2.18 Two methods accounting for the tip-sample heat transfer modeling both ballistic and diffusive heat conduction (a) The tip-sample contact involves a boundary contact conductance. (b) The tip is set at a distance d above the sample.....	74
Figure 2.19 Modeled geometries: ‘Full probe’ and ‘Only Pt90/Rh10 part’.....	75
Figure 2.20 Mesh characteristics for: the ‘Full probe’ and the ‘Only Pt90/Rh10 part’	76
Figure 2.21 Results of simulations executed on a polyimide sample. (a) 2D temperature distribution for the ‘Full probe’. (b) 2D temperature distribution for ‘Only Pt90/Rh10 part’. (c) Temperature profiles matching along the Pt90/Rh10. (d) Conductive heat flux matching along the Pt90/Rh10.	77
Figure 2.22 Straight tip (a) 2D temperature distribution on a polyimide sample surface. (b) Temperature profiles on the sample surface along a direction perpendicular (purple curve) and parallel (black curve) to the ‘tip plane’. (c) 2D heat flux density in the z direction on a polyimide sample surface. (d) Heat flux profiles on the sample surface along a direction perpendicular (purple curve) and parallel (black curve) to the ‘tip plane’.....	78
Figure 2.23 Scanning electron microscopy image of the tilted Wollaston probe, angle of tilt 20° with respect to the sample surface.....	78
Figure 2.24 Mesh characteristics for the tilted tip configuration	79
Figure 2.25 Results of simulations performed on a polyimide sample. (a) 2D temperature distribution. (b) Temperature profiles along the Pt90/Rh10 for a straight and a tilted tip. (c) Conductive heat flux profiles along the Pt90/Rh10 for a straight and a tilted tip.....	80
Figure 2.26 Tilted tip of 20° (a) 2D temperature distribution on a polyimide sample surface. (b) Temperature profiles on the sample surface along a direction perpendicular and parallel to the ‘tip plane’. (c) 2D heat flux density in the z direction on a polyimide sample surface.....	81
Figure 2.27 Calibration process using the tilted tip. (a) Unbalanced Wheatstone bridge voltage versus calibration samples thermal conductivities. (b) Mean tip temperature after going into contact with calibration samples, obtained based on (a).....	81
Figure 2.28 Calibration method. (a) Tip withdrawal on calibration samples. (b) Simulated tip temperature variation as a function of the tip-sample distance on a polyimide sample. Straight and 20° tilted tip.	82
Figure 2.29 $\Delta\theta_{contact}$ for different experiments and simulations performed on standards	83
Figure 3.1 Si effective thermal conductivity.....	89
Figure 3.2 Schematic showing the structural destruction of PSi sample due to its irradiation with slow light ions ($^4\text{He}^+$) in the nuclear regime.	91
Figure 3.3 Schematic showing the irradiation of a PSi sample with swift heavy ions (^{129}Xe) in the electronic regime with a structural conservation.....	91
Figure 3.4 Schematic of a cross-section view of anodization cell.	92
Figure 3.5 Cross-section SEM image of mesoporous silicon showing its sponge-like structure. .	93
Figure 3.6 Cross section SEM image showing the $10\ \mu\text{m}$ thick PSi layer.....	94
Figure 3.7 Stopping power vs ion energy for ^{129}Xe in bulk silicon calculated using SRIM.....	96
Figure 3.8 (a) Schematic based on a cross section SEM image showing incident light interferences at the interfaces between air/PSi/bulk Si. (b) Interferences fringes on a $10\ \mu\text{m}$ thick non-irradiated 56 % PSi layer.	97

Figure 3.9 Interferences fringes on a 10 μm thick PSi with 56 % porosity irradiated with ^{129}Xe at 91 MeV at $3 \times 10^{13} \text{ cm}^{-2}$	98
Figure 3.10 Cross-section SEM images of the 56 % PSi samples irradiated at two different energies and at different fluences.....	99
Figure 3.11 Micro-Raman spectra for different fluences for 91 MeV and 29 MeV ^{129}Xe irradiations of 56 % PSi	100
Figure 3.12 Complete Raman spectra of: (a) Crystalline bulk silicon (b) Non-irradiated porous silicon 56 % porosity showing its crystalline phase, (c) Irradiated PSi (56 % porosity) with ^{129}Xe at energy 91 MeV and at fluence $3 \times 10^{13} \text{ cm}^{-2}$. (d) Amorphous fraction determination used in this study.....	102
Figure 3.13 Amorphous phase versus fluence as obtained from micro Raman spectra of the irradiated PSi (56 % porosity) with ^{129}Xe at two different energies: 90 MeV and 29 MeV.....	103
Figure 3.14 Thermal conductivity determination using micro Raman thermometry. (a) Stokes Raman shift as a function of the absorbed laser intensity before and after irradiation. (b) Corresponding temperature rise (ΔT) as a function of the absorbed laser intensity.	104
Figure 3.15 Effective thermal conductivity as a function of the irradiation fluence for the PSi of 56 % porosity obtained by Raman thermometry	105
Figure 3.16 $\Delta P/P$ calibration curve as a function of samples thermal conductivities	106
Figure 3.17 Effective thermal conductivity as a function of the irradiation fluence for the PSi of 56 % porosity obtained by SThM. The results show the decrease in PSi effective thermal conductivity, starting from the NIPSi to the irradiated ones at the lowest and the highest energies.....	106
Figure 3.18 Effective thermal conductivity as a function of the irradiation fluence of the PSi of 56 % porosity obtained by SThM and micro-Raman thermometry.....	107
Figure 3.19 Effective thermal conductivity as a function of the amorphous phase based on Raman and SThM measurements.....	109
Figure 4.1 (a) Top-view SEM image of the suspended membrane with a Pt heater and two Pt sensors. (b) Cross-section schematic of the same suspended membrane.....	116
Figure 4.2 (a) Cross-sectional schematic of the suspended membrane. (b) Top SEM image of the same suspended membrane showing the ‘underetched’ parts. (c) Zoom from (b) showing the PhNC membrane with a pitch of 60 nm.	117
Figure 4.3 (a) Optical image showing the starting point of the scan. (b) Tip perpendicular to the suspended membrane. (c) Tip parallel to the suspended membrane.....	117
Figure 4.4 (a) Voltage profiles obtained from a perpendicular scan on a plain membrane and on its corresponding phononic membrane	118
Figure 4.5 Voltage variation obtained from a parallel scan on a plain membrane, its phononic membrane and with the cavity only	119
Figure 4.6 (a) Voltage profiles for four plain suspended membranes of the same cross sectional area but with different lengths. (b) Corresponding average tip temperature profiles. ..	120
Figure 4.7 (a) Voltage profiles for four suspended membranes of the same dimensions, Plain, P60, P80 and P100. (b) Corresponding average tip temperature profiles.....	120
Figure 4.8 Results of simulations done on a 59.4 nm thick, 10 μm large and 200 μm long suspended membrane with $\lambda_{\text{membrane}} = 10 \text{ W.m}^{-1}.\text{K}^{-1}$ (a) Modelled geometry showing the	

maximum tip temperature rise. (b) Temperature rise distribution on the surface of the membrane from (a) and in the air around.....	121
Figure 4.9 Study of the sensitivity of the SThM technique on bulk and on suspended membranes using FEM simulations: tip temperature rise in these two cases.	121
Figure 4.10 (a) 2D axisymmetric schematic of the geometry for modeling heat transfer below the contact, including the boundary conditions. (b) $\lambda_{membrane}$ as a function of the contact radius for four different plain membranes.....	123
Figure 4.11 Effective thermal conductivities of 200 μm long, 10 μm large and 59.4 nm thick suspended membranes.....	124
Figure 4.12 (a) Schematic showing the configuration of the studied geometry. (b) The principle of the ‘power variation’ method. (c) The principle of the ‘temperature profile’ method.....	125
Figure 4.13 Schematic of the suspended membrane.....	125
Figure 4.14 Temperature rise along the half of the membrane from (a) the analytical model and (b) the FEM simulations.....	127
Figure 4.15 (a) Temperature rise showing the difference in maximum temperature level and in shape of the peaks. The heat source is applied in the middle of the membrane. (b) Profiles resulting from the maximum temperature rise at each position of the power source. (c) Maximum temperature rise as a function of the membrane thermal conductivity from analytical (green curve) and FEM simulations (blue curve).....	128
Figure 4.16 Configuration of the modelled geometry.....	129
Figure 4.17 Determination of the heat loss coefficient using the ‘temperature profile’ method.	130
Figure 4.18 (a) Temperature rise as function of the laser power from the ‘power variation’ method. (b) Temperature rise as a function of the laser position on the membrane. (c) Schematic showing the position of the laser at two different points of the membrane with their 2D temperature distribution profiles.	131
Figure 4.19 Schematic of a two-dimensional periodic structure simulated using RCWA.	132
Figure 4.20 Absorbance as a function of the plain membrane thickness.....	132
Figure 4.21 (a) Statistical study of the hole size distribution obtained on the membrane with P60. The white shells are considered as Si. (b) 2D plot showing the absorbance for different hole radii and membrane thicknesses, as calculated with the RCWA method. (c) Absorbance calculated for the membrane with P60.	133
Figure 4.22 (a) Absorbance calculated for the membrane with P80. (b) Absorbance calculated for the membrane with P100.	134
Figure 4.23 Thermal conductivity determination using micro Raman thermometry. The white shells are considered as Si for the absorbance calculations (a) Temperature rise as a function of the absorbed laser power. (b) Thermal conductivity values obtained from the ‘power variation’ and the ‘temperature profile’ methods.....	136
Figure 4.24 Thermal conductivity determination using micro Raman thermometry. The white shells are considered as transparent for the absorbance calculations (a) Temperature rise as a function of the absorbed laser power. (b) Thermal conductivity values obtained from the ‘power variation’ and the ‘temperature profile’ methods.	137
Figure 4.25 (a) Theoretical thermal conductivity reduction as a function of membrane thickness. (b) Experimental thermal conductivity reduction $\lambda_{membrane}/\lambda_{bulk Si}$ of the suspended membranes.....	138
Figure 4.26 Normalized thermal conductivities of PhNC samples vs porosity.....	139

Figure 4.27 Thermal conductivities of the PhNC samples as a function of Surface/Volume ratio.....	140
Figure 4.28 Schematic of a PhNC membrane showing its dimensions	140
Figure 5.1 (a) Superlattice with interfaces made of two different materials. (b) Superlattice without interfaces made of porous silicon.....	145
Figure 5.2 Calibration curve for the formation of porous silicon at -40 °C with an electrolyte that consists of 48 wt% HF and pure ethanol in a volume ratio of 1:1 [10]	147
Figure 5.3 Reflectivity spectra for a PSi bilayer at -35 °C (a) Simulated profile with the expected thicknesses. (b) Fit of the experimental curve. The electrolyte consists of 48 wt% HF and pure ethanol in a volume ratio of 1:1.....	148
Figure 5.4 X-ray reflectivity profile of mono porous silicon layer of 30 nm thickness. $P = 24\%$ (a) Simulated profile (red curve) with low interface roughness 0.2 nm. (b) Simulated profile with interface roughness 8.9 nm.....	149
Figure 5.5 Reflectivity spectrum from a PSi-SL with 135 nm periodicity.	150
Figure 5.6 PSi-SL. (a) 600 nm thick PSi-SL with 10 periods of 58 nm each on bulk silicon with a 10 nm Pt layer on top. (b) Zoom showing the porous structures. (c) Zoom showing the atomic resolution with the FFT as inset..	151
Figure 5.7 (a) SEM image of PSi-SL with a period of 2.42 μm ($d_1 = 1.21 \mu\text{m}$ and $d_2 = 1.21 \mu\text{m}$) [8]. (b) TEM image, at high magnification, of a PSi-SL.....	151
Figure 5.8 Manufacturing process of Au transducers using laser lithography.....	152
Figure 5.9 SEM image showing the principle of the 3ω measurements.....	153
Figure A.1 Normalized maximum temperature rise at each position on the membrane.....	157

List of Tables

Table 2.1 Comparison between two characterization techniques: micro-Raman thermometry and SThM.....	84
Table 3.1 Summary of the experimental characteristics of the irradiation.....	95
Table 3.2 Main features of ^{129}Xe irradiation in Si, for S_e and S_n calculation, and in PSi at 56 % porosity, for Rp calculations.....	96
Table 3.3 Results of the fits: B is the maximum value of amorphous fraction, Ad is the cross-section of electronic interactions.....	103
Table 4.1 Summary of all tip temperature rise from FEM and from experiments.....	122
Table 4.2 The white shells are considered as Si. (a) Absorbance and porosity for the membrane with P60. (b) Absorbance and porosity calculations for the membrane with P80. (c) Absorbance and porosity calculations for the membrane with P100.....	135
Table 4.3 Same as Table 4.2 with the white shells considered as transparent.....	135
Table 5.1 Summary of the anodization parameters.....	147

General introduction

Mesoscopic physics has been a thriving area of research for thirty years now, thanks to advances in technology for manufacturing nanoscale objects. Heat transport in nanoscale systems has become an increasingly important subject. Physics describing heat transfer at the macroscale fail at the nanoscale. For this reason, a better understanding of the basic principles governing the transport of phonons at very small scales, whether at room or at low temperatures, is required.

This fundamental field of physics opens the way to many applications. With the downsizing of components in microelectronics, heat dissipation problems at the nanoscale are now technological barriers. Decreasing the thermal conductivity has become increasingly important in recent years, not only for the design of insulating materials in the field of construction but also for high-performance materials in various fields such as electronics and thermoelectricity. While travelling within a medium, phonons can be considered as particle-like incoherent or wave-like coherent. These two aspects affect the thermal conductivity in a different way.

Electronic industries are interested in materials that are compatible with complementary-metal-oxide semiconductor (CMOS) process and have at the same time low (high) thermal (electronic) conductivity. This definition allows us to understand the reasons for the low interest shown by the microelectronics industry for thermoelectric components in the classical BiTe technology.

This thesis is in the framework of the understanding and the control of thermal properties of low dimensional materials and in particular of nanomaterials compatible with the microelectronics industry. To this aim, three different configurations of Si-based materials are investigated: irradiated porous silicon, suspended silicon phononic membranes and porous silicon superlattices. Samples' thermal properties are characterized using two different techniques, micro-Raman thermometry and scanning thermal microscopy (SThM).

The first chapter of this manuscript is devoted to a review of the main concepts of physics of heat conduction. These notions are essential to the understanding of heat transport, first in bulk materials and second in nanomaterials. This chapter introduces the phonons giving us a simplified picture of collisional processes undergone by these phonons and generating what is commonly known as heat. The scattering mechanisms in bulk and nanomaterials at room and cryogenic temperatures are detailed. The derivation of the macroscopic law describing the propagation of heat known as Fourier's law is obtained from the Boltzmann Transport Equation. This chapter introduces also the fundamental concepts of heat transport in amorphous materials, two-dimensional periodic arrays and superlattice materials. Finally a review of the present state of the art on thermal transport studies in structured nanomaterials is presented. The observation of coherence in heat-conduction in these structures is discussed.

The second chapter tackles the thermal characterization techniques. It first details micro-Raman thermometry. It shows how to determine the thermal conductivity based on experimental and simulated temperatures using finite element method. The effect of the

different parameters used in the model on the obtained thermal conductivity is highlighted. In a second part, the scanning thermal microscopy (SThM) technique is described. A numerical study of heat transfer between the Wollaston probe and the sample is presented. Based on modelling and experimental investigations, the heat coefficient of the tip and the distance at which it should be put above the sample are determined. This chapter presents two different tip configurations and highlights the effect of each configuration on heat transfer between the tip and the sample. A new measurement method of the thermal conductivity using SThM is detailed.

The third chapter is devoted to the study of heat conduction in porous silicon irradiated by swift heavy ions. It highlights the interaction mechanisms between heavy ions and matter. Then the manufacturing process of irradiated porous silicon samples is detailed. The structural properties of the samples are then presented. Finally, the results on thermal conductivity obtained from micro-Raman thermometry and SThM are discussed and compared.

The fourth chapter is devoted to the study of heat conduction in suspended phononic membranes. The techniques used for the determination of the thermal conductivity are detailed. This chapter opens the way to a new methodology for the determination of the thermal conductivity using SThM when dealing with complicated geometries. It shows also the results obtained from two different micro-Raman thermometry techniques. The results for the three techniques are discussed and compared to previous studies in the end of this chapter. The last chapter of the manuscript presents the concept of superlattice formed of thin layers of porous silicon towards eventual demonstration of coherent phonon heat conduction in this structure. It shows the possibility of obtaining layers of the order of the pores size (~ 10 nm) with simple manufacturing techniques.

The manuscript ends with a summary of the main conclusions.

Chapter 1. Phonon transport in bulk and nanostructured materials

1.1 Introduction

The energy transport process known as heat transfer is a consequence of temperature differences. Heat transfer phenomena are commonly faced in everyday life and play a crucial role in many industrial applications. Depending on the nature of the medium, various types of heat carriers are possible. These carriers transmit heat from one point to another. Electrons, phonons and photons are the most important heat carriers. During a radiation mechanism, heat is carried by photons, while in conductors and semiconductors or dielectrics, heat is carried by electrons and phonons. In this chapter, we underline concepts related to the propagation of heat in solids. As silicon is the material of choice in this work, we do not highlight the heat transfer due to electrons or photons in order to focus our attention on the lattice vibrational aspects.

1.2 Phonons

In crystalline materials, atoms are structured in a periodical array known as lattice. Lattice vibrations contribute to heat transfer and so to the thermal conductivity of the studied material. At zero temperature, the minimum potential of interactions between atoms, where the repulsive and attractive forces balance each other, defines the equilibrium position. Once atoms start to vibrate, their displacement is constrained by their neighboring atoms and the potential of interactions plays an important role in the total energy of the system. An atom vibration can create the propagation of a lattice wave in the whole system. The place where the amplitude of this propagative wave is maximum corresponds to the hottest side of the solid.

According to the principle of quantum physics, each lattice vibration has a discrete energy and is a multiple of $\frac{h}{2\pi}\omega$, where h is the Planck constant and ω is the frequency. Phonon is defined as the quanta of lattice vibration. Phonons can be considered as particles as long as their mean free path is smaller than the crystal size. They are considered as bosons and follow the Bose-Einstein distribution. They are divided into optical and acoustic phonons. The latter ones dominate the heat transport due to their large mean free path and due to their large group velocity in comparison to that of the former ones.

1.3 Phonon dispersion

Phonon dispersion curves are required to know how phonons affect the thermal conductivity of the studied media. They are divided into acoustic branches of low frequencies and optical branches of higher frequencies. In order to plot the phonon dispersion curves, a better understanding of the interatomic forces is needed. To do so, a mass-spring system is

considered as a simplified picture of the interatomic interaction in crystalline solids. If the positions between the atoms were fixed, it would be impossible to determine the thermal conductivity, the specific heat and the melting point of the solid. Therefore, the elastic vibration model of balls and springs should be considered. The spring is a conceptual representative of the attractive and repulsive forces [1]. We will consider first a monoatomic chain and secondly a diatomic one. Finally the case of superlattice crystals is considered.

1.3.1 Monoatomic crystals

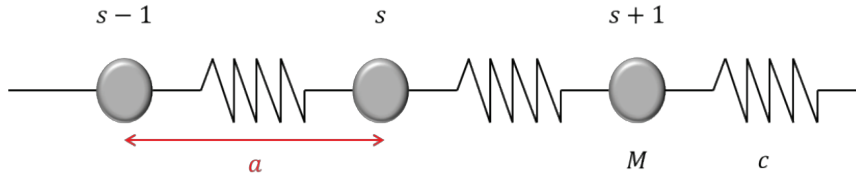


Figure 1.1 Monoatomic one-dimensional chain of atoms.

Monoatomic crystals have one atom per basis in the primitive cell. As atoms vibrate, they are displaced from their equilibrium positions. In this case, we consider a one-dimensional (1D) model where only longitudinal modes exist, and atoms can only vibrate in the direction of the heat flow. Two assumptions are made in the frame of this simple model:

It is assumed that the elastic response of the crystal is a linear function of forces. Thus, Hook's law can be used. According to this assumption, a harmonic vibration between atoms is considered.

It is assumed that all the forces applied on a given atom can only come from its nearest neighbors.

Figure 1.1 is an illustration of a 1D chain of N atoms of the same mass M , separated by a distance a of spring constant c , where u is considered as the small displacement of an atom regarding its equilibrium position. Therefore, the equation of motion is determined by:

$$M \frac{\partial^2 u_s}{\partial t^2} = c(u_{s+1} + u_{s-1} - 2u_s), \quad (1.1)$$

where t is the time and s is the atom number assigned. The above equation is a special form of the differential wave equation

$$M \frac{d^2 u_s}{dt^2} = ca^2 \frac{d^2 u_s}{dx^2}, \quad (1.2)$$

where x is the atom position. The solution of equation 1.2 can be written as:

$$u_s = u e^{[-(i\omega t - kas)]}, \quad (1.3)$$

where k is the wavevector. Displacements at s_{\pm} are given by:

$$u_{s\pm} = u e^{[-(i\omega t - ka(s\pm 1))]} \quad (1.4)$$

Substituting equations 1.3 and 1.4 into equation 1.1 and after some manipulations, the frequency of vibrations in the monoatomic chain is:

$$\omega = 2\sqrt{\frac{c}{M}} \left| \sin\left(\frac{ka}{2}\right) \right|. \quad (1.5)$$

This equation is depicted in Figure 1.2. Only wavevectors inside the first Brillouin zone are represented. Close to the origin atoms oscillate in phase and give birth to acoustic modes of the dispersion relation. This zone is bounded by k values lying between $-\frac{\pi}{a}$ and $\frac{\pi}{a}$ where standing waves can be found; at these positions atoms oscillate in opposite directions and their average movements are cancelled out. Phonon group velocity in a solid is the given by:

$$\frac{\partial \omega}{\partial k} = a\sqrt{\frac{c}{M}} \cos\left(\frac{ka}{2}\right). \quad (1.6)$$

This allows determining the energy of the elastic waves of frequency ω and is the starting point for thermal properties determination of a given solid: $E = \frac{h}{2\pi} \omega$.

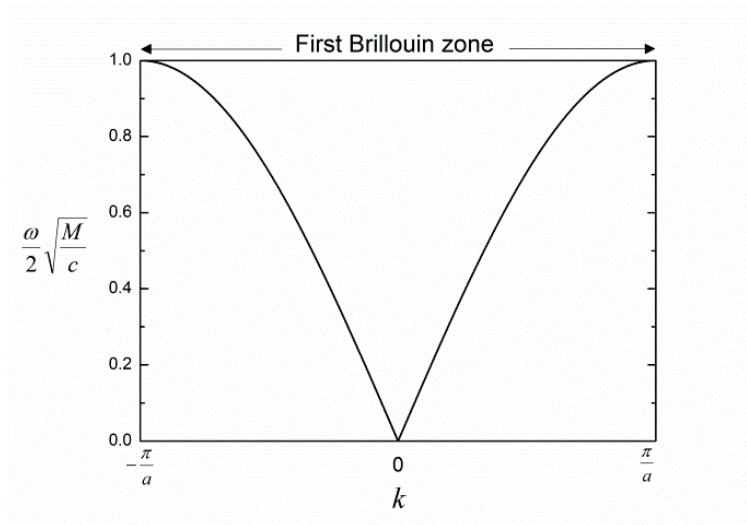


Figure 1.2 Dispersion curve for monoatomic one-dimensional crystal.

1.3.2 Diatomic crystals

Diatomic crystals have two atoms per basis in the primitive cell. The same procedure as monoatomic crystals for $\omega(k)$ determination can be followed. However, the interatomic forces and the mass of the nearest neighbor atoms can be different (see Figure 1.3).

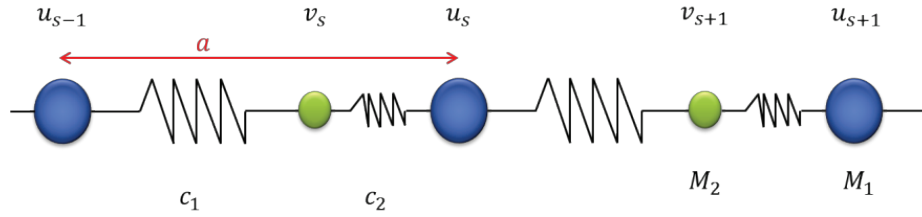


Figure 1.3 Diatomic one-dimensional chain of atoms.

Equations of motions of atoms are written as follow:

$$M_1 \frac{d^2 u_s}{dt^2} = -c_1(v_s - u_s) + c_2(u_s - v_{s-1}), \quad (1.7)$$

$$M_2 \frac{d^2 v_s}{dt^2} = -c_2(u_{s+1} - v_s) + c_1(v_s - u_s), \quad (1.8)$$

where M_1 and M_2 are the masses of each atom with u and v their small displacements. c_1 and c_2 are the spring constants between the atoms. Using equation 1.3 and after some manipulations, we obtained the two following equations:

$$(c_1 + c_2 - M_1 \omega^2)u - (c_1 + c_2 e^{iak})v = 0, \quad (1.9)$$

$$(c_1 + c_2 - M_2 \omega^2)v - (c_1 + c_2 e^{iak})u = 0. \quad (1.10)$$

The homogeneous linear equations have a solution only if the determinant of the coefficient of u and v is equal to zero:

$$2c_1 c_2 - (M_1 + M_2)(c_1 + c_2)\omega^2 + M_1 M_2 \omega^4 - 2c_1 c_2 \cos(ak) = 0. \quad (1.11)$$

Considering that $c_1 = c_2 = c$, we can write the solutions of equation 1.11 as following:

$$\omega_{\pm}^2 = \frac{c(M_1 + M_2)}{M_1 M_2} \pm c \left[\left(\frac{M_1 + M_2}{M_1 M_2} \right)^2 - \frac{4 \sin^2(ka/2)}{M_1 M_2} \right]^{1/2}. \quad (1.12)$$

The phonon dispersion curve splits into two branches (see Figure 1.4 (a)). The upper branch contains atoms oscillating in opposite direction (out of phase) with ω_+ and k . If all atoms move together there is creation of an electric dipole moment within the cell. Hence, this mode can be excited by photons. For this reason the upper branch is called optical branch. The lower branch contains atoms oscillating in phase with ω_- and k at long wavelengths, similar to sound waves. Thus the lower branch is called acoustic branch. Near the Brillouin zone center, $ka \ll 1$:

$$\begin{cases} \omega_+^2 = \frac{2k(M_1 + M_2)}{M_1 M_2}, \\ \omega_-^2 = \frac{1}{2} \frac{ck^2}{(M_1 + M_2)}. \end{cases} \quad (1.13)$$

$$\begin{cases} \omega_+^2 = \frac{1}{2} \frac{ck^2}{(M_1 + M_2)}. \\ \omega_-^2 = \frac{2k}{M_1}. \end{cases} \quad (1.14)$$

Near the Brillouin zone edge, $k = \pm \frac{\pi}{a}$:

$$\begin{cases} \omega_+^2 = \frac{2k}{M_2}, \\ \omega_-^2 = \frac{2k}{M_1}. \end{cases} \quad (1.15)$$

$$\begin{cases} \omega_+^2 = \frac{2k}{M_2}, \\ \omega_-^2 = \frac{2k}{M_1}. \end{cases} \quad (1.16)$$

The frequency gap seen in Figure 1.4 (a) at the boundaries $k_{max} = \pm \pi/a$ of the Brillouin zone is a characteristic feature of elastic waves in polyatomic lattices, where wavelike solutions do not exist.

Figure 1.4 (b) shows the results of the group velocities for the two branches. The group velocity of the optical branch is significantly lower than the acoustic one. Very often, the contribution of the optical phonons to heat conduction is neglected when compared with the acoustic phonons.

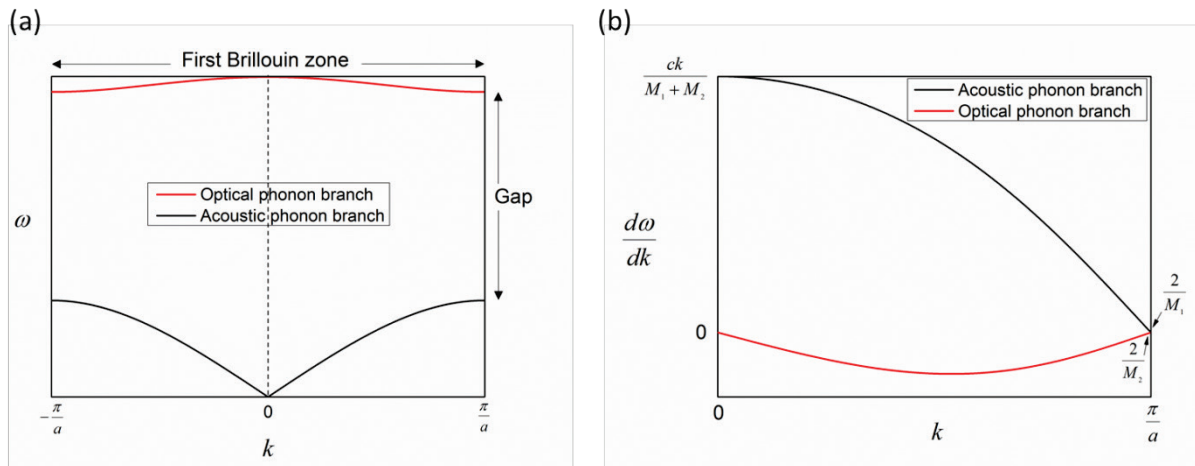


Figure 1.4 (a) Optical and acoustic phonon branches of the dispersion relation for a diatomic linear lattice for $M_1 > M_2$. **(b)** Group velocity of one-dimensional diatomic lattice chain for $M_1 > M_2$.

Figure 1.5 provides the phonon dispersion relation for silicon [100] which has a three-dimensional diatomic lattice and is the material of interest in this manuscript. This dispersion is of great importance for thermal transport in nanostructures.

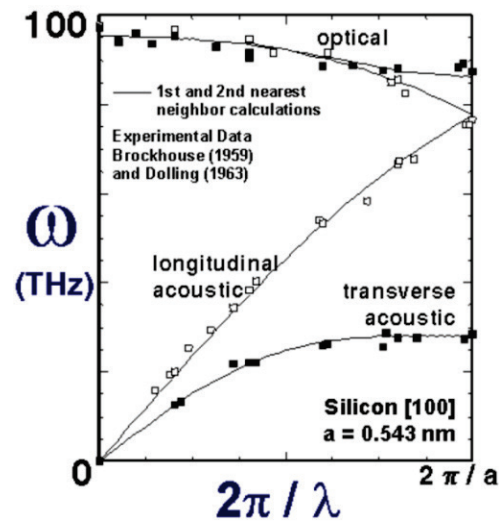


Figure 1.5 Phonon dispersion for silicon. [2]

1.3.3 Superlattice crystals

A superlattice is a periodic structure made of alternating repetition of two or more different materials as shown in Figure 1.6. Superlattices have applications in semiconductor lasers and have potential application in thermoelectric devices. The former need high thermal conductivity materials, while the latter requires low thermal conductivity materials.

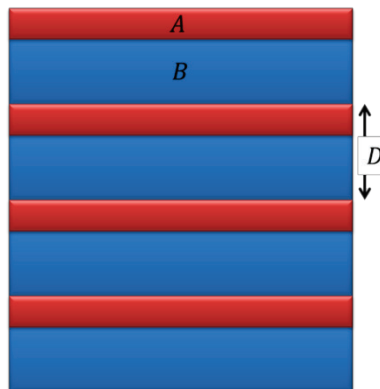


Figure 1.6 Sketch of a superlattice structure made of two different materials A and B . D is the period.

To plot the phonon dispersion relation of a superlattice, we follow Tamura et al. [3] who considered a 1D periodic superlattice formed by A and B materials, where the unit period is assumed to be made up of two face centered cubic (fcc) lattices, with atoms parallel to the x - y plane (see Figure 1.7). Atoms in lattice A (B) of mass M_A (M_B) are connected to their 12 nearest neighbors by springs of the same stiffness c for A - A , B - B and A - B pairs. The spacing between the nearest neighbors is taken to be $\sqrt{2}a$, where a is the unit cell length. The thickness of each layer is $d_A = n_A a$ and $d_B = n_B a$, where n represents the number of monolayers and $D = d_A + d_B$ is the period thickness.

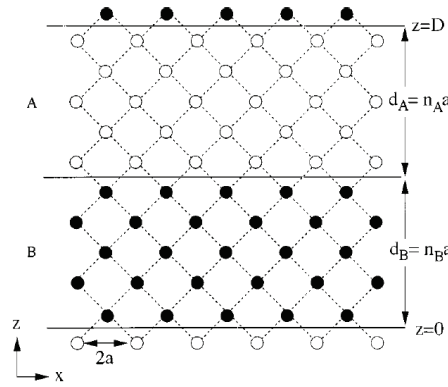


Figure 1.7 Structure of a superlattice consisting of two fcc lattices with atoms of different masses. [3]

The equation of motion of the superlattice assumed to be periodic in the z direction is given by [3]:

$$M_n \frac{\partial^2 u_{lmn}^x}{\partial t^2} = \frac{c}{2} (u_{l+1,m+1,n}^x + u_{l+1,m,n+1}^x + u_{l+1,m-1,n}^x + u_{l+1,m,n-1}^x + u_{l-1,m+1,n}^x + u_{l-1,m,n+1}^x + u_{l-1,m-1,n}^x + u_{l-1,m,n-1}^x - 8u_{lmn}^x + u_{l+1,m+1,n}^y - u_{l+1,m-1,n}^y + u_{l-1,m-1,n}^y - u_{l-1,m+1,n}^y + u_{l+1,m,n+1}^z - u_{l+1,m,n-1}^z + u_{l-1,m,n-1}^z - u_{l-1,m,n+1}^z), \quad (1.17)$$

where $u_{lmn}^{(N)} = u_n(z)e^{[ik_{\parallel}x_{lm} + k_z Nd - \omega t]}$ is the Bloch function, u_{lmn} is the displacement from the equilibrium position $r_{lmn} = (x_{lm}, z) = (la, ma, na)$ and $k_{\parallel} = k_x, k_y$ (wavevectors parallel to the layer interfaces) is common to lattices A and B, and k_z is the Bloch wavenumber in the periodic direction. $M_n = M_A$ or $M_n = M_B$, depending on the site n . The equation of motion for $\frac{\partial^2 u_{lmn}^y}{\partial t^2}$ and $\frac{\partial^2 u_{lmn}^z}{\partial t^2}$ can be obtained by permutation of the subscripts and superscripts of equation 1.17. Figure 1.8 shows the dispersion relation of phonons of a Si_n/Ge_n superlattice provided by [3]. The calculations were made using the fcc model. In the case of $n = 5$, the arrows in Figure 1.8 show that at the highest frequencies (frequencies at which phonons carry heat) for Si and Ge, a flattening of the branches is observed resulting from zone folding effects.

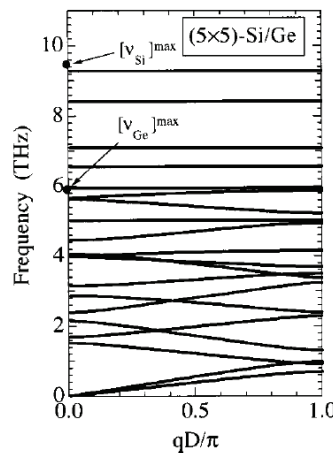


Figure 1.8 Phonon dispersion relation in the growth direction of (5x5)-Si/Ge superlattice. [3]

The first Brillouin zone edge in bulk materials is given by $\frac{2\pi}{a}$ while in the case of superlattices it is given by $\frac{2\pi}{D}$ (see Figure 1.9). This means that the zone is folded into smaller regions, which is a typical feature of superlattices called mini-bands. The zone-folding effect induces a flattening of the bands.

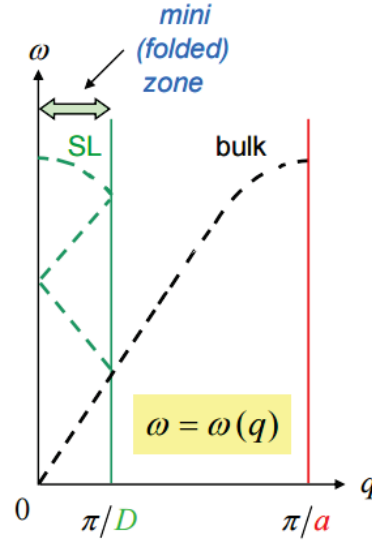


Figure 1.9 Comparison between the phonon dispersion relations of 1D monoatomic structure (bulk) and superlattice (SL) structures. [4]

1.4 Phonon population

The Bose-Einstein distribution function shows a dependence on temperature (T) of modes of wavevector K , polarization s and frequency $\omega_s(K)$:

$$n_s(K) = \frac{1}{e^{\left(\frac{h\omega_s(K)}{2\pi K_B T}\right)} - 1}, \quad (1.18)$$

where K_B is the Boltzmann constant. According to Wien's displacement law for phonons, the phonon wavelength depends inversely on temperature. Thus, the wavelength of the dominant phonons decreases significantly when temperature increases. The relation defining the dominant phonon wavelength is given by [5][6]:

$$\lambda_{\text{dom}} = \frac{h v_s}{4.25 K_B T} = \frac{v_s}{90 \cdot 10^6 T}, \quad (1.19)$$

where $v_s = 6400 \text{ ms}^{-1}$ is the sound velocity for silicon (Si) based materials [7]. This characteristic length describes the average width of phonons wave packets in the system. Using equation 1.19 we plotted Figure 1.10. It depicts that in Si, at room temperature (300 K), the dominant phonon wavelength would be about 0.2 nm in the frame of a Debye model,

while at 4 K it is about 24 nm. It is known that the populated wavelengths span over a decade around this dominant wavelength for bosons.

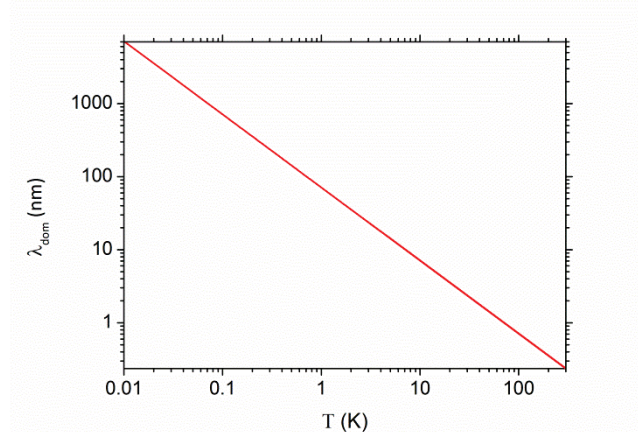


Figure 1.10 Phonon dominant wavelength as a function of temperature in Si.

1.5 Macro and micro heat conduction

In heat conduction two regimes can be defined: macroscale and microscale scales heat conduction. Characteristic time and length are used in order to distinguish between the two regimes. At the macroscale, heat conduction is studied by taking advantage of local thermal equilibrium. At this scale thermal conductivity is independent of size, whereas at the microscale it will be shown that one has to consider it as size dependent. The Knudsen number is given by $Kn = \Lambda/L$, where Λ is the mean free path of the heat carrier (here phonons) and L is the studied system dimension. It is a dimensionless number which is widely used in the study of heat conduction. When $L \gg \Lambda$ ($Kn < 0.05$), heat transport occurs in the macroscopic regime and is considered as purely diffusive. When $L \ll \Lambda$, heat conduction occurs in the microscopic regime and two cases may take place: partially ballistic (ballistic-diffusive) when $0.05 < Kn < 10$ and purely ballistic when $Kn > 10$. Figure 1.11 shows the limits of each regime when considering a film of known boundaries temperatures T_h (hot side) and T_c (cold side).

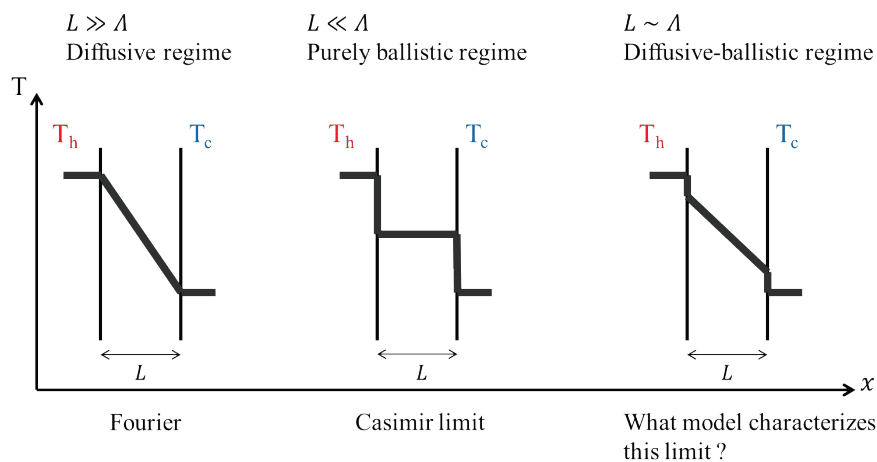


Figure 1.11 Comparison between the heat conduction regimes.

Fourier's law can be applied for studying heat conduction, in the diffusive regime. This law is no more valid and breaks down when considering the ballistic regimes. Size effect study on thermal conductivity has started by an experimental work done by Haas and Biermasz and followed by a theoretical study done by Casimir [8]. Casimir found that in the purely ballistic regime no temperature gradient can be established, and according to Fourier's law, it was impossible to prescribe a thermal conductivity. In the ballistic regime, the temperature at the boundaries governs the heat transport, and not the temperature gradient within the film. We can then talk about thermal conductance. In this case, particle scattering at the boundaries is responsible for the thermal state of the system, and Casimir used the photon radiation heat transfer model as an analogy. Similar conclusions are presented by Ziman [9] by solving the Boltzmann Transport Equation (BTE).

1.5.1 Mean free path

Fourier's law breaks down when the length of the studied system becomes comparable to the mean free path (MFP). For a better understanding of heat conduction at the microscale, it is important to describe what the mean free path (Λ) is. It is the average travelled distance covered by a moving particle (i.e. phonon in this work) between two subsequent collisions. This length is affected by the carrier direction and energy. At microscale Λ can be of the order of the system dimension or bigger. This means that particles have less chance to collide and local thermal equilibrium is not valid unless it is at the boundaries.

1.5.2 Scattering mechanisms

1.5.2.1 Main scattering mechanisms

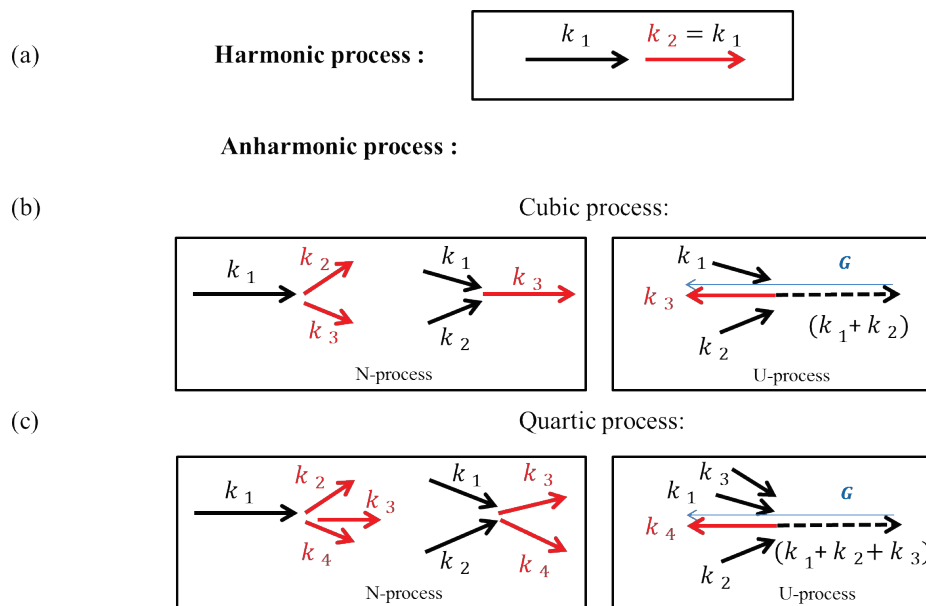


Figure 1.12 Schematic representation of different collisions processes between phonons. **(a)** harmonic process. **(b)** and **(c)**: anharmonic processes.

In the harmonic approximation, phonons would never be scattered (see Figure 1.12 (a)), so no changes in the phonon momentum and energy are allowed due to impossible redistribution of energy within the system. Therefore, harmonic phonons do not contribute to the reduction of the thermal conductivity of the system and if we consider the approximation of a perfect and infinite crystal, the thermal conductivity in this case tends to an infinite value. Thus, the thermal equilibrium within a system cannot be established without processes allowing the redistribution of the energy of the different modes. For this reason, two different processes are present, the intrinsic processes resulting from anharmonic interactions between phonons and the extrinsic processes resulting from the scattering by defects in the material (dislocations and impurities) or with interfaces. Figure 1.13 shows the different extrinsic scattering mechanisms depicting the different types of heat resistances that heat flow faces in a given material. For the intrinsic scattering mechanisms, two types of phonon-phonon collisions have to be considered: they are called normal process (N-process) and Umklapp process (U-process). They are illustrated in Figure 1.12. Cubic and quadratic processes involve, respectively, three and four carriers. The higher the temperature, the greater the influence of high orders. By considering the case of cubic process in Figure 1.12 (b), an incident phonon can split into two other phonons of lower energies. In the diffusion case, two incident phonons can give birth to a phonon of higher energy. When the wavevector of the new obtained phonon does not fit into the Brillouin zone, the latter is brought back to the Brillouin zone by addition of a vector from the reciprocal space G [9]. The processes that provide the vector G are the ones responsible for thermal flux degradation by creating a flux in the opposite direction. They are called Umklapp processes.

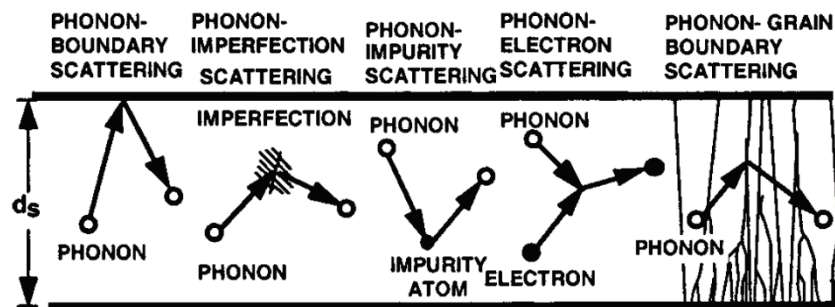


Figure 1.13 Phonons scattering mechanisms that reduce the thermal conductivity of a medium of thickness d_s . [10]

1.5.2.2 Boundary scattering in a film

The effective mean free path due to boundary scattering depends on temperature (see Figure 1.14). It can be expressed using the following expression [11]

$$\Lambda_{ph} = \frac{1 + p(\lambda_{ph}, T)}{1 - p(\lambda_{ph}, T)} \Lambda_{Cas}, \quad (1.20)$$

where Λ_{Cas} is the Casimir mean free path defined as an average over all directions in the pure ballistic regime. In the case of a rectangular cross-section ($e \times w$), it can be written as [11]

$$\Lambda_{Cas} = 1.12\sqrt{ew}. \quad (1.21)$$

$p(\lambda_{ph}, T)$ is a parameter that describes the probability of a phonon of wavelength λ_{ph} at the temperature T to be specularly reflected. When $p = 0$, an incident phonon on the surface will be scattered in all directions (this is the limit of the Casimir model of perfectly rough surfaces). Rather, in the case of perfectly smooth surfaces, every single phonon will be specularly reflected when hitting the surface with $p = 1$. This parameter can be calculated using [9][11]

$$p(\lambda_{ph}, T) = \int_0^\infty P(\xi) e^{-\pi \frac{16\pi^2 \xi^2}{\lambda^2}} d\xi \cong \int_0^{\lambda_{dom}/4\pi} P(\xi) d\xi, \quad (1.22)$$

where $P(\xi)$ is the probability distribution of the roughness amplitude and ξ is the variance of the roughness amplitude. This probability can be expressed as following [9][11]

$$P(\xi) = \frac{1}{\xi_0} e^{-\xi/\xi_0}, \quad (1.23)$$

where ξ_0 is the mean value of the roughness. By comparing Figures 1.10 and 1.14, we observe that at very low cryogenic temperatures (< 1 K), only phonons with high wavelengths and mean free paths are present, while most of the other modes are frozen. In this case, only phonon-boundary scattering is responsible for not allowing the propagation of phonons [10][12][13]. When temperature increases (~ 6 K), dominant phonon wavelength decreases and becomes comparable to the size of the defects present in the crystal, while the phonon mean free path remains not negligible. Phonons scattering due to defects is dominant. At high temperatures (> 100 K), Umklapp processes are dominant.

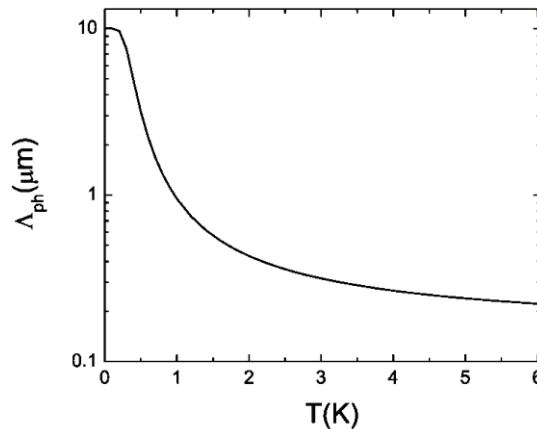


Figure 1.14 Mean free path of phonons in silicon nanowires as a function of temperature for $\Lambda_{Cas} = 160$ nm and $\xi_0 = 4.4$ nm. [11]

1.5.3 Boltzmann Transport Equation

The phonon-particle transport theory is derived from the Boltzmann Transport Equation (BTE). The BTE can be applied for phonons and electrons transport modelling and can require experimental results to determine the fitting parameters for the models. It gives particle distribution in space having a momentum (\vec{v}) at any time (t). It is used to study the deviation from equilibrium state when a temperature difference is applied. The nonequilibrium thermodynamic phonon distribution function $f(\vec{r}, \vec{v}, t)$ gives the density of carriers in the phase space at any given time. Suppose a particle at spatial location \vec{r} moving with a group velocity \vec{v} at a time t . At $t + dt$, when particles are colliding, the particle can reach a position $\vec{r} + d\vec{r} = \vec{r} + \vec{v}dt$ with a velocity $\vec{v} + d\vec{v} = \vec{v} + \vec{a}dt$ (\vec{a} is the acceleration of the particle). Therefore, the general form of the BTE is given by [14]:

$$\frac{f(\vec{r} + d\vec{r}, \vec{v} + d\vec{v}, t + dt) - f(\vec{r}, \vec{v}, t)}{dt} = \frac{\partial f}{\partial t} + \vec{v} \cdot \frac{\partial f}{\partial \vec{r}} + \vec{a} \cdot \frac{\partial f}{\partial \vec{v}} = \left(\frac{\partial f}{\partial t} \right)_{scatt}, \quad (1.24)$$

where $\frac{\partial f}{\partial t}$ is the rate of particles in time, $\vec{v} \cdot \frac{\partial f}{\partial \vec{r}}$ describes the convective transport of the distribution function due to the group velocity of the carriers, $\vec{a} \cdot \frac{\partial f}{\partial \vec{v}}$ is the convective flux due to acceleration in velocity space: since phonon cannot be excited by external forces this term vanishes. $\left(\frac{\partial f}{\partial t} \right)_{scatt}$ is the scattering term due to collisions, which brings the system back to the equilibrium state. Since the BTE is a nonlinear integro-differential equation, it cannot be exactly solved. As a result, the relaxation time approximation is used. In this case, it is assumed that the phonons relax linearly to the equilibrium state. Thus

$$\left(\frac{\partial f}{\partial t} \right)_{scatt} = \frac{f_0 - f}{\tau}, \quad (1.25)$$

where f_0 is the thermodynamic distribution function at equilibrium, i.e. the Bose-Einstein distribution for bosons (such as phonons), and τ is the relaxation time (the mean time between two collisions). We note that in the ballistic heat conduction regime ($K_n \gg 1$), phonons are only scattered at the boundaries of the studied system and the local equilibrium assumption is only valid at the boundaries [15].

This BTE theory breaks down when the sizes studied are comparable to the phonon wavelength.

1.5.4 Fourier's law

Boltzmann transport equation is used to derive Fourier's law of heat conduction when the characteristic length of the media is much greater than the mean free path of the heat carriers. For a one-dimensional steady-state case under the relaxation time approximation, equation 1.25 describes the particle diffusion and can be written as following:

$$v_x \frac{\partial f}{\partial x} = \frac{f_0 - f}{\tau}. \quad (1.26)$$

Under local thermal equilibrium conditions, we have

$$\frac{\partial f}{\partial x} = \frac{\partial f_0}{\partial x} = \frac{df_0}{dT} \frac{dT}{dx}. \quad (1.27)$$

Substituting equation 1.27 in equation 1.26 leads to:

$$v_x \frac{df_0}{dT} \frac{dT}{dx} = \frac{f_0 - f}{\tau}. \quad (1.28)$$

Multiplying equation 1.28 by $v_x \hbar \omega D(\omega)$, where $D(\omega)$ is the density of state of particles, and integrating it over all frequencies gives

$$\int_0^{\omega_D} v_x^2 \hbar \omega \frac{df_0}{dT} \frac{dT}{dx} D(\omega) d\omega = \int_0^{\omega_D} v_x \hbar \omega D(\omega) \frac{f_0 - f}{\tau} d\omega, \quad (1.29)$$

where ω_D is the Debye frequency, i.e. the maximum vibration frequency of atoms in the crystal. The first term on the right side is zero (v_x is an odd function and f_0 is an even function of v_x), which means that the particle flux vanishes at the equilibrium state. Thus the flux of particles can be obtained by rearranging equation 1.29:

$$q(x) = -\frac{dT}{dx} \int_0^{\omega_D} v_x^2 \tau \frac{df_0}{dT} \hbar \omega D(\omega) d\omega, \quad (1.30)$$

The Fourier's law has been obtained:

$$q(x) = -\lambda \frac{dT}{dx}. \quad (1.31)$$

Equation 1.30 gives us the expression of the thermal conductivity

$$\lambda = \int_0^{\omega_D} v_x^2 \tau \frac{df_0}{dT} \hbar \omega D(\omega) d\omega. \quad (1.32)$$

We remind that $C = \int_0^{\omega_D} \frac{df_0}{dT} \hbar \omega D(\omega) d\omega$ is the lattice specific heat, i.e. the derivative of the internal energy with respect to temperature. In the following the phonon velocity is considered to be the same in all directions ($v_x^2 = \frac{1}{3} v^2$) and $\tau v = \Lambda$. Therefore, equation 1.30 can be written as

$$q(x) = -\frac{1}{3} C v \Lambda \frac{dT}{dx}. \quad (1.33)$$

Based on the kinetic theory, the thermal conductivity is related to the heat capacity via the relation:

$$\lambda = \frac{1}{3} C v \Lambda. \quad (1.34)$$

Equation 1.32 shows that the theoretical calculation of the thermal conductivity depends on many parameters. If the distribution function is that of Bose-Einstein model, the main limitations come from the knowledge of the dispersion relation, the group velocity and especially the relaxation time of phonons.

Figure 1.15 depicts the variation in the thermal conductivity of Si as a function of temperature. This Figure shows the dominant scattering mechanisms, discussed in Section 1.5.2.1, for different temperature ranges.

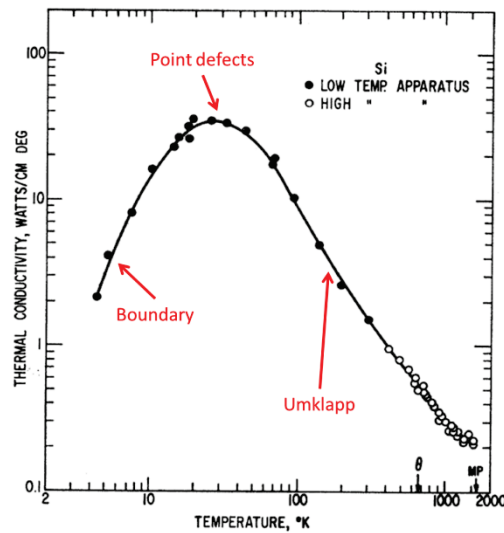


Figure 1.15 Silicon thermal conductivity versus temperature [16]. The dominant mechanisms in heat conduction were added to the original image.

1.6 Heat conduction in amorphous materials

In contrast to crystalline materials, amorphous materials do not have a long-range periodic order of atoms. They can have structural order on different length scales but remain amorphous as a whole. In an amorphous material, the distinction between optical and acoustic modes remains blurred; they can have both characters and can contribute with unequal weights.

In crystals all vibrational modes are extended and propagate throughout the system, while in amorphous materials this is no longer true. Allen et al. [17] classified vibrational modes in amorphous silicon into propagons (plane wave like), diffusons and locons (localized modes). Figure 1.16 shows the different vibrational modes regimes as a function of frequency. Propagating modes are present at low frequencies and travel ballistically with a wavevector over a distance defined as the mean free path before scattering from disorder. In [17], they

represent 4% of the total existing modes. At very high frequencies, localized modes are present and consist 3% of the total existing modes. In the L region, the mean free path becomes comparable to phonons wavelength. The modes are called ‘localized states’ because atoms have vibrations which are different from those of the perfect crystal. Diffusons fill 93% of the spectrum. They do not have a wavevector and lose their memory rapidly. The decrease in disordered solids thermal conductivity is ascribed [18] to a random walk of energy rather than to propagating phonons.

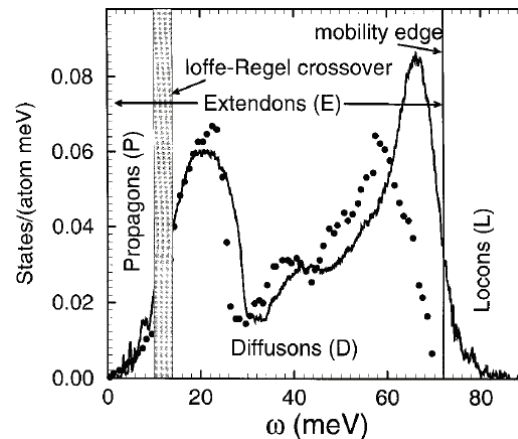


Figure 1.16 Diffusons, locons and propagons in amorphous Si. [17]

Moon et al. [19] determined the thermal conductivity of amorphous silicon (a-Si) thin films. Their results at room temperature showed that for 53 and 97 nm thick a-Si layers, the thermal conductivity remains unchanged and is about $1.5 \text{ W.m}^{-1}\text{.K}^{-1}$, which is more than 2 orders of magnitude lower than the thermal conductivity of bulk crystalline silicon. The independence of thermal conductivity on the amorphous film thickness was also shown by Nath and Chopra [20] on amorphous Ge thin films.

1.7 Thermal transport studies in suspended nanostructured materials

1.7.1 Wires and beams

1.7.1.1 Low temperature regime

The Caltech group led by Prof. Roukes [21][22][23] was one of the pioneers in the measurement of thermal properties using suspended semiconductor nanostructures. The first thermal conductance measurement was done for single-crystal GaAs based nanostructures (see Figure 1.17). The use of suspended structures significantly increases the experimental difficulties but offers a clear and well defined path for heat to flow. This type of structures also enhances thermal insulation by increasing phonon scattering on the boundaries.

The first step in the measurement is the calibration of the resistance of the doped semiconductor lines, which play the role of transducers (heater and thermometer), depending on the temperature. This is achieved by a 4-point measurement by injecting an alternating

current (ac) of about few nanoamperes in the transducers in order to avoid overheating the sample.

The thermal properties (see Figure 1.18) of the four suspended beams are obtained by applying a direct current of the order of microamperes carefully controlled in two of the lines to produce Joule heating. The heat dissipated by the suspended membrane through the four beams is sensed due to the change in the thermometer thermal resistance. The excellent coupling between the central region and the conductive lines allows considering that the electron temperature of the conductive lines is equal to the temperature of phonons of the GaAs.

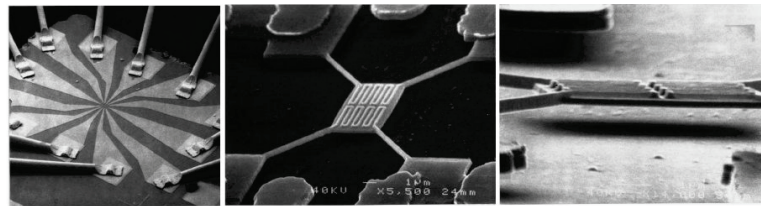


Figure 1.17 Monocrystalline GaAs suspended device for mesoscopic thermal conductance measurements. (Left) Overview of the device with an area of 1 mm^2 with 12 gold finger pads connecting the device to the central region. (Center) Focus on the central region showing the GaAs membrane suspended by four bridges of GaAs of $5.5 \text{ }\mu\text{m}$ long (transverse section $200 \text{ nm} \times 300 \text{ nm}$). The transducer is composed of a pair of n+ GaAs conductor serpentine, epitaxially grown on the GaAs substrate. (Right) Side view of the device of 300 nm thickness suspended at $1 \text{ }\mu\text{m}$ above the substrate. [21]

Figure 1.18 (a) shows the thermal conductance trend versus temperature for the four suspended beams. Figure 1.18 (b) shows the decrease in the phonon mean free path when increasing the temperature.

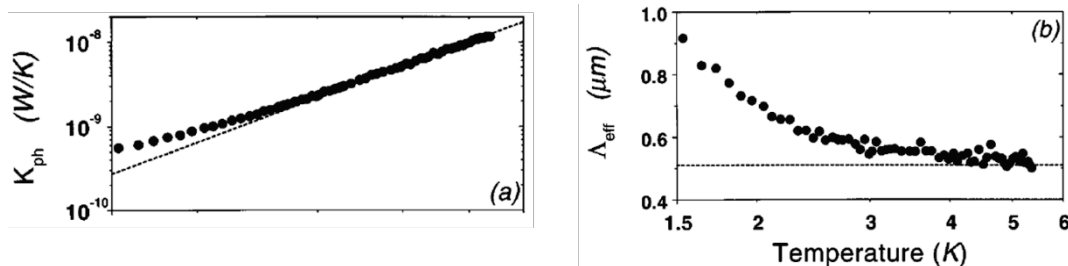


Figure 1.18 (a) Thermal conductance measurements vs temperature of the 4 suspended GaAs beams. The dashed line is the Debye model prediction for $\Lambda = 0.51 \text{ }\mu\text{m}$ **(b)** Mean free path deduction from the experimental work. [21]

Heron [11] showed the effect of the geometry at the nanoscale on the phonon transport by manufacturing straight and curved silicon nanowires. The thermal conductance of the wires normalized to eight quanta of thermal conductance, from 3ω measurements, in the temperature range from 0.4 K to 4.8 K is shown in Figure 1.19. Compared to straight silicon

nanowires, a larger decrease in the thermal conductance was observed for the curved nanowires. Indeed, curved nanowires at the nanoscale block phonons more than straight ones.

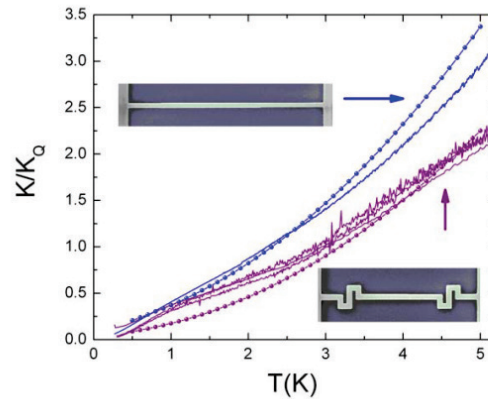


Figure 1.19 Thermal conductance of straight and curved nanowires normalized to eight quanta of thermal conductance. [11]

1.7.1.2 Transition from room temperature to low temperatures

In 2003, the team of Arun Majumdar of Berkeley (California) published their work on thermal conductivity measurements of silicon nanowires [24]. They presented thermal conductivity measurements of single crystalline silicon nanowires of 22, 37, 56 and 115 nm in diameter. They used electrical means to measure samples thermal conductivities. They observed that the thermal conductivity in this kind of structures is lower than the bulk value. They also showed that the thinner the nanowire the lower its thermal conductivity, due to phonon-boundary scattering (see Figure 1.20).

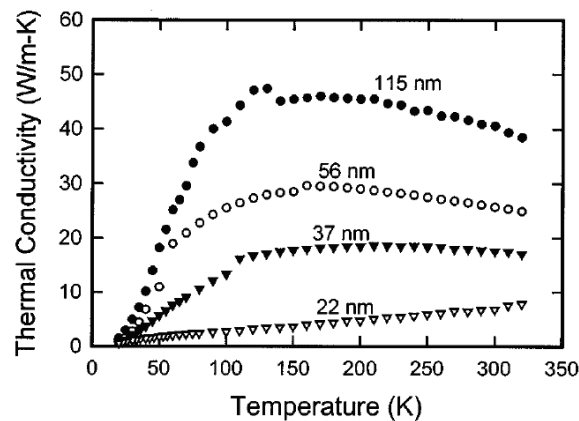


Figure 1.20 Thermal conductivity of different diameter Si nanowires. [24]

Since then, no experiments have confirmed this decrease and the impact if the wall roughness.

Later, Hochbaum et al. [25] studied the thermal conductivity of rough silicon nanowires (SNWs). They showed that a larger decrease in thermal conductivity can be obtained in the

case of rough SNWs when compared to SNWs of the same diameter and with lower roughness (see Figure 1.21).

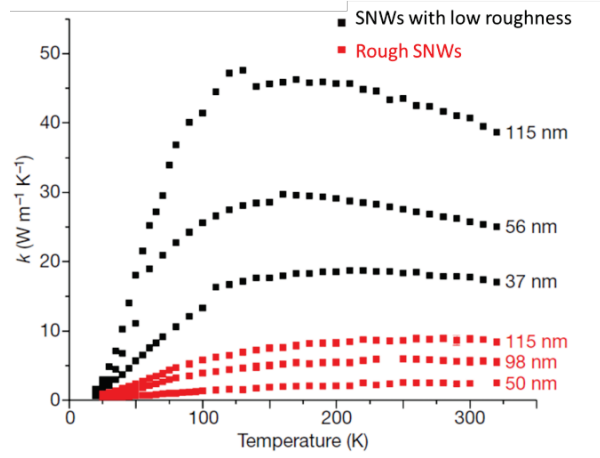


Figure 1.21 Thermal conductivity of rough silicon nanowires (red squares) and silicon nanowires with low roughness (black squares) as a function of temperature. [25]

1.7.2 Two-dimensional periodic arrays

1.7.2.1 Membranes

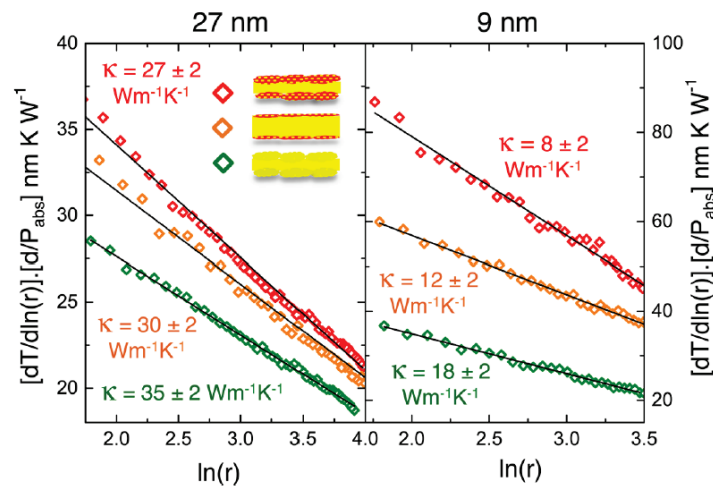


Figure 1.22 Thermal conductivity measurements. On the left, membranes with 27 nm thickness. On the right, membranes with 9 nm thickness. Green, orange and red diamonds represent, respectively, membranes without, with native oxide, and with 6 h oxidation. [28]

Following previous study by Goodson in particular [26] and Chavez-Angel et al. [27], Neogi et al. [28] studied the relation between structure and heat transport at the nanoscale by engineering down to sub-20 nm thick free-standing crystalline silicon membranes. They measured the thermal conductivity of 9 nm and 27 nm thick silicon membranes, without oxide (green diamonds), with native oxide (orange diamonds) and with additional grown rough

oxide (red diamonds) (see Figure 1.22). Measurements were done at room temperature using an optical technique: two-laser Raman thermometry [28]. They showed that the thinner the membrane, the lower the in-plane thermal conductivity. They also demonstrated the effect of oxide on thermal conductivity, which remains to be theoretically understood. This reduction is ascribed to the shortening of the phonon mean free path after being scattered by the rough surface.

1.7.2.2 Phononic structures

In 2010, Yu et al. [29] showed that Si suspended nanomesh (NM) structures (thickness of 22 nm) (see Figure 1.23 (a)) have lower thermal conductivity than Si thin films (TF) (thickness of 25 nm), Si electron beam mesh (EBM) (thickness of 22 nm) and an array of Si nanowires (NWA) (thickness of 20 nm) (see Figure 1.23 (b)) of corresponding Surface to Volume ratio. They used electrical means to measure samples thermal conductivities. They suggested that periodic holes induce Bragg reflections, so they suggested that the drop in thermal conductivity in their structures to the decrease in the phonon group velocity as a direct consequence of the flattening of phonons branch modes.

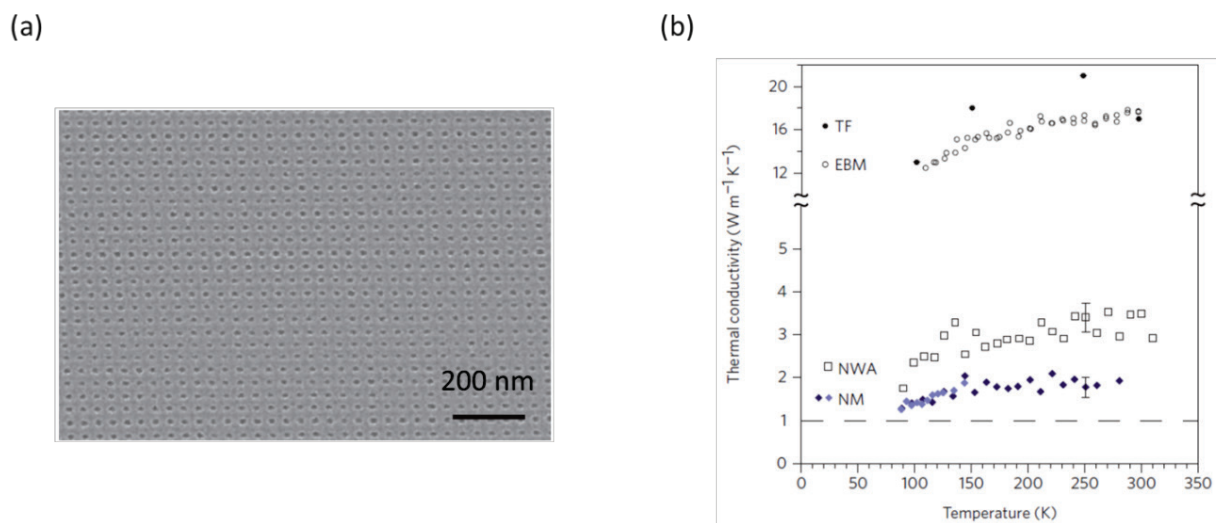


Figure 1.23 (a) Nanomesh structure showing a periodicity of 34 nm. **(b)** Thermal conductivity of different suspended structures. [29]

Tang et al. [30] showed the pitch (period) size effect on thermal conductivity for 100 nm thick silicon ribbons (see Figure 1.24). They used electrical means to measure samples thermal conductivities. They kept the same porosity (35 %) while varying the average pitch and neck sizes. They showed that the smallest the pitch the smallest the thermal conductivity. Moreover, the obtained thermal conductivity of the ribbon of pitch 55 nm approaches the value of silicon dioxide. They suggested that for pitch 55 nm phonons can experience more backscattering from the nanohole sidewalls.

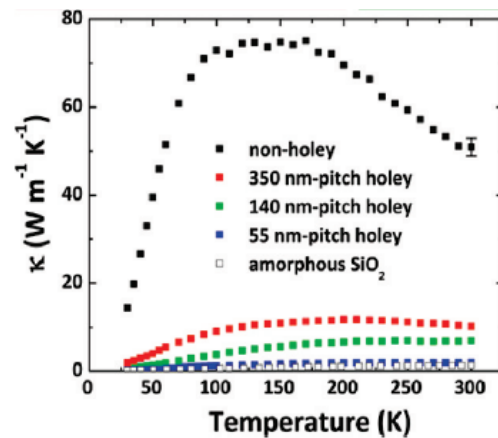


Figure 1.24 Thermal conductivity vs temperature of Si ribbons with different pitches. [30]

Hopkins et al. [31] studied the effect of phononic crystals (PnCs) on Si thermal conductivity using time domain thermorefectance. PnCs are made of periodic arrays of scattering inclusions in a homogeneous material (see Figure 1.25 (a)). The obtained room temperature thermal conductivities for 500 nm thick Si PnCs are over an order of magnitude lower than the value obtained for bulk Si. Moreover, they observed that these values are very close to each other for the different porosities and the neck and diameter sizes. In bulk Si, phonon scattering is dominated by the Umklapp processes, with a relatively small contribution from impurity scattering. They also accounted for the diffusive phonon scattering at the pore boundaries. In addition they accounted for the contribution of the removal of material to the thermal conductivity reduction by multiplying the experimentally obtained thermal conductivity values by $(1 + \frac{2P}{3})/(1 - P)$, where P is the porosity. By combining all these contributions together, an order of magnitude of difference was obtained between the predicted thermal conductivities by the Callaway-Holland-type model [32] and the experimental ones. To understand the origin of this difference, they calculated the phonon density of states of the PnCs from its dispersion (see Figure 1.25 (b)). Following these authors, a downshift in the mode density (see Figure 1.25 (b)) leads to a reduction in thermal conductivity. This result was ascribed to phonon coherent effect in the PnCs.

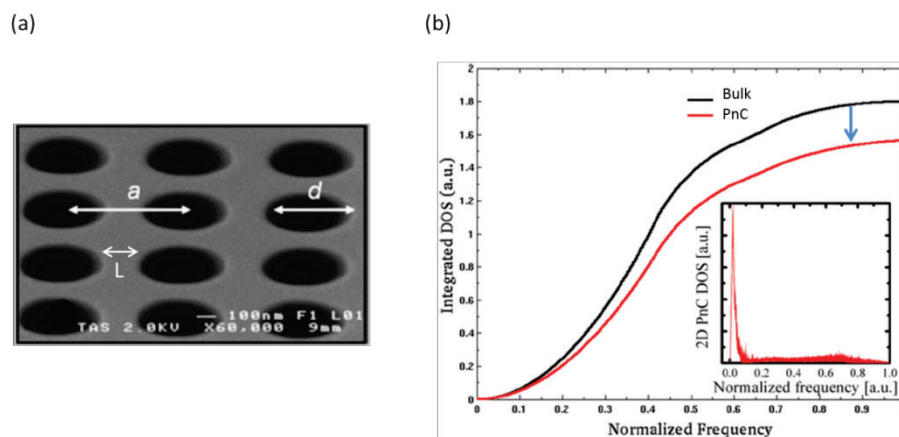


Figure 1.25 (a) SEM image of the PnCs. **(b)** Integrated DOS as a function of frequency for bulk and PnCs with $d/a=0.6$. [31]

We note that all the measurements were performed at temperatures where the dominant phonon wavelength is much smaller than the characteristic size, and coherent effect is certainly questionable.

In contrast Maasilta et al. [33] studied perforated silicon nitride (SiN) membranes (thickness of 485 nm with a filling factor of 0.7) thermal conductivities by electrical means at very low temperature. To look at coherent phonon heat transport, they worked at temperatures below 1 K where the dominant phonon wavelength is increased by more than 2 orders of magnitude compared to room temperature. This led to a negligible bulk scattering and a change in the phonon band structure. This change is caused by the periodic hole structure and leads to a suppression of the phonon transport due to coherence effects. They plotted the SiN phonon band structure of full membrane (see Figure 1.26 (a)), of a membrane with a lattice constant $a = 970$ nm (see Figure 1.26 (b)) and lattice constant $a = 2425$ nm (see Figure 1.26 (c)) up to 20 GHz. This is the frequency range that contains all of the populated phonons at $T = 0.1$ K. Compared to the full membrane, the calculated band structure of the phononic membrane $a = 970$ nm contains a band gap at frequency 3.3 GHz while the band structure of the phononic membrane with $a = 2425$ nm has a flatter branch modes. Figures 1.26 (d) and (e) depict, respectively, the DOS and the average group velocity. They showed more important suppression of heat conduction in a $a = 2425$ nm due to the flatness of the band structure. This implies that the band gap alone has a minor effect on thermal transport.

Figure 1.27 shows that the temperature dependence and the magnitude of thermal conductance (G) are both modified. These imply that the reduction of thermal conductance is not a simple geometrical effect of bulk or boundary scattering. Note that $G = P/\Delta T$, where P is the emitted power and $\Delta T = T_{measured} - T_{bath}$: no thermal conductivity can be calculated.

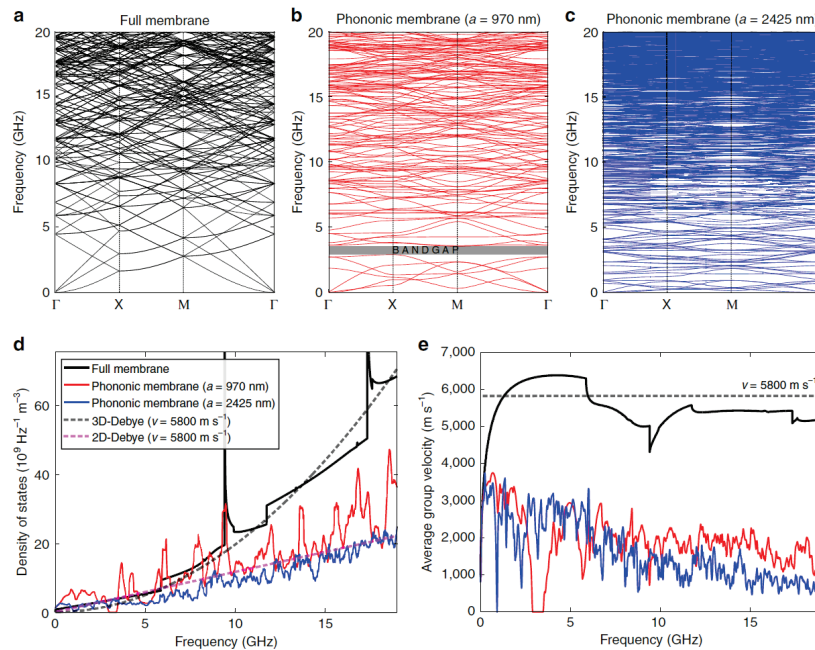


Figure 1.26 (a) Band structure of full membrane. (b) Band structure of phononic membrane $a = 970$ nm. (c) Band structure of phononic membrane $a = 2425$ nm. (d) Resulting DOS. (e) Resulting average phonon group velocity. [33]

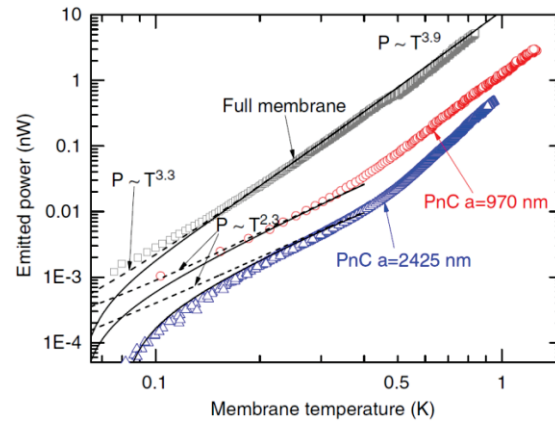


Figure 1.27 Measured emitted phonon power versus temperature. [33]

Very recently, Nomura et al. [34][35] investigated heat transport in silicon-based suspended phononic membranes using time domain thermorefectance. Their first study was carried at room temperature on monocrystalline (145 nm thick) and polycrystalline (thickness of 143 nm) PnCs with a variety of hole radius, with a fixed period $a = 300$ nm [35]. They showed that patterned polycrystalline membranes have lower thermal conductivity than monocrystalline ones (see Figure 1.28 (a)). In addition to the reduction in the thermal conductivity due to the surface scattering, grain boundary scattering further reduces the phonon MFP.

The same perforated membranes were studied at 4 K [34]. Figure 1.28 (b) shows the strong difference between the thermal conductivity reductions at 4 K compared to that at room temperature for the same PnCs. The large impact of PnCs at lower temperature comes from the presence of specularly and the change in the phonon MFP distribution.

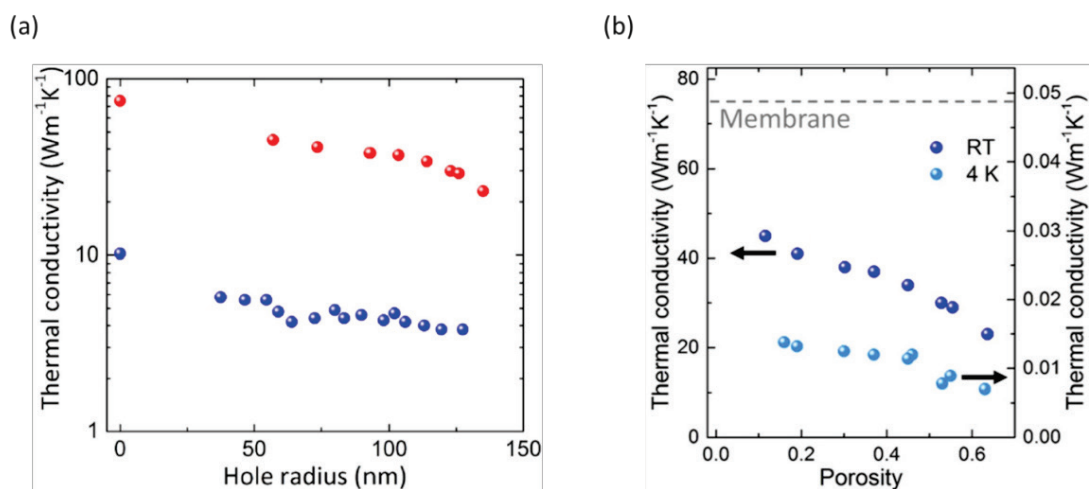


Figure 1.28 (a) Thermal conductivity measurements of, monocrystalline (red circles) and polycrystalline (blue circles) Si PnCs [35]. (b) Thermal conductivity measurements of Si PnCs of different porosities at room temperature (blue circles, left axis) and at 4 K (light blue circles, right axis) [34].

Last year, Maire et al. [36], from the same group, measured the thermal conductivity of ordered and disordered phononic suspended silicon membranes with hole diameters $d = 135$ nm (red circles) and $d = 170$ nm (blue squares) (see Figure 1.29). Their results, at room temperature (RT), showed no variation in the thermal conductivity for the two configurations (see Figure 1.29 (a)). Rather, measurements at 3.7 K showed an increase in the thermal conductivity of the crystals while increasing the disorder (see Figure 1.29 (b)). Indeed, at room temperature, incoherent thermal transport is independent of disorder, while at 3.7 K coherent behaviors affect the transport.

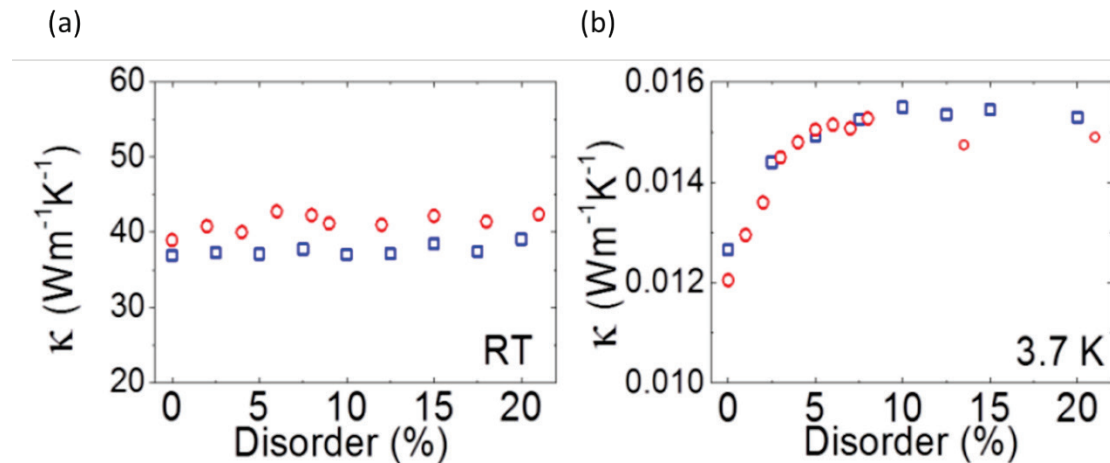


Figure 1.29 Thermal conductivity of ordered and disordered phononic crystals. **(a)** Measurements at room temperature (RT). **(b)** Measurements at 3.7 K. [36]

1.8 Coherent phonon heat conduction in superlattices

Owing to the short coherence length of phonons, previous demonstrations related to the presence of wave-like phonon scattering at room temperature remain debatable. Accessing coherent phonons requires that the characteristic dimension of studied system must be of the order or smaller than the dominant phonon wavelength at a given temperature. Unfortunately, it remains difficult to engineer 2D periodic arrays with characteristic lengths smaller than the room temperature dominant wavelength due to manufacturing process capability and specification limits. However, the possibility of obtaining very thin layers, down to the atomic scale, made superlattices ideal model systems for the understanding of the wave-particle crossover.

Simkin et al. [37] predicted, in superlattices, a minimum in thermal conductivity as a function of interface density (see Figure 1.30), and ascribed this minimum to a crossover from particle-like to wave-like transport of phonons. Their calculations were done by including wave interferences in the superlattice and by accounting for the MFPs of the phonons. For layers larger than the mean free path, they treated phonons as particles. In this case, the thermal conductivity increases as the period increases. However, for layers thinner than the MFP, they applied the wave theory. In this case, the thermal conductivity increases as the period decreases in the SL, due to band folding effect. By combining both theories, they concluded

that the thickness of the layers for a minimum thermal conductivity depends on the average MFP, and so it is temperature dependent.

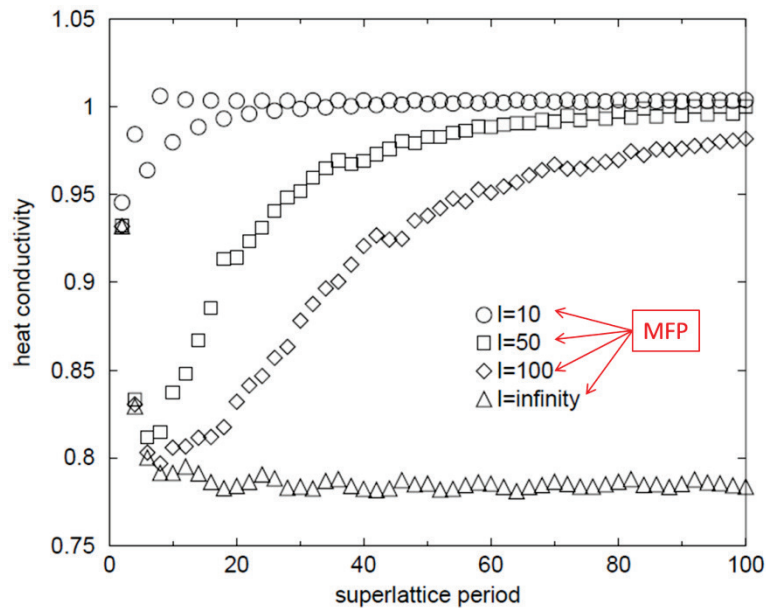


Figure 1.30 Thermal conductivity in one dimension as a function of the SL period in nanometers. [37]

Capinski et al. [38] obtained a decrease in GaAs/AlAs superlattices thermal conductivity, of different number of periods, at temperatures between 100 and 375 K, as an indication of non-coherent effect in heat transport. The first experimental confirmation of coherent heat conduction in GaAs/AlAs superlattices was revealed by the group of Prof. Chen at MIT [39]. GaAs/AlAs SLs (12 nm/12 nm) were prepared using molecular beam epitaxy (MBE), starting with a GaAs wafer (see Figure 1.31 (a)). Samples thermal properties were characterized using time domain thermoreflectance at temperatures between 30 and 300 K. They decided to keep the same periodicity and to change the number of periods of the SL. If the interfaces behave like thermal resistors because of the Kapitza resistances [40], phonons are scattered diffusely and thus lose their phase information. In this case the effective thermal conductivity of the SLs should be independent of the number of grown layers. However, if phonons travel through the SL without feeling the interfaces and have a MFP larger than the SL size, phonons transport is considered as coherent. In this case, these phonons are eigenmodes of the SL and therefore modify the phonon dispersion curve. Figures 1.31 (b) and (c) show the linear relation between the SL thermal conductivity and the total thickness from 30 to 150 K. This result is consistent with a coherent phonon heat conduction picture. At temperatures greater than 150 K, anharmonic processes become more and more important leading to a breaking of the linearity of the relation between the SL' thermal conductivity and its number of periods. However, thermal conductivity is still increasing while increasing the number of periods; this means that coherent phonons still conduct a considerable fraction of heat even at 300 K. We note that no minimum in thermal conductivity as a function of interface density was shown in this study.

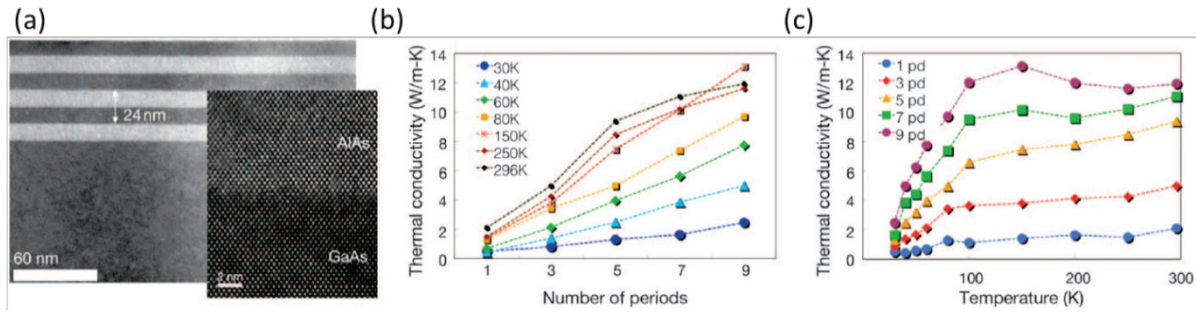


Figure 1.31 (a) Cross sectional transmission electron microscope image of 3 periods of the SL. (b) SL thermal conductivity versus the number of periods. (c) SL thermal conductivity for different temperatures. [39]

Ravichandran et al. [41] studied heat transport in perovskite SLs of SrTiO₃/CaTiO₃ (STO/CTO) and SrTiO₃/BaTiO₃ (STO/BTO) with atomically sharp interfaces. STO/CTO SLs were grown by MBE means on three different substrates in order to prove that the choice of the substrate does not influence the obtained results. Figures 1.32 (a) and (b) show a minimum in 200 nm thick STO/CTO and STO/BTO SLs, respectively when varying the interface density. For both SLs, the curve is split into two regimes: thermal conductivity decreases (incoherent phonons) or increases (coherent phonons). These measurements were performed at room temperature, using time domain thermorefectance. The authors used a modified form of the Simkin-Mahan (SM) model to account for the disorder and volume fraction corrections, to highlight the trend of thermal conductivity as a function of interface density for the studied materials.

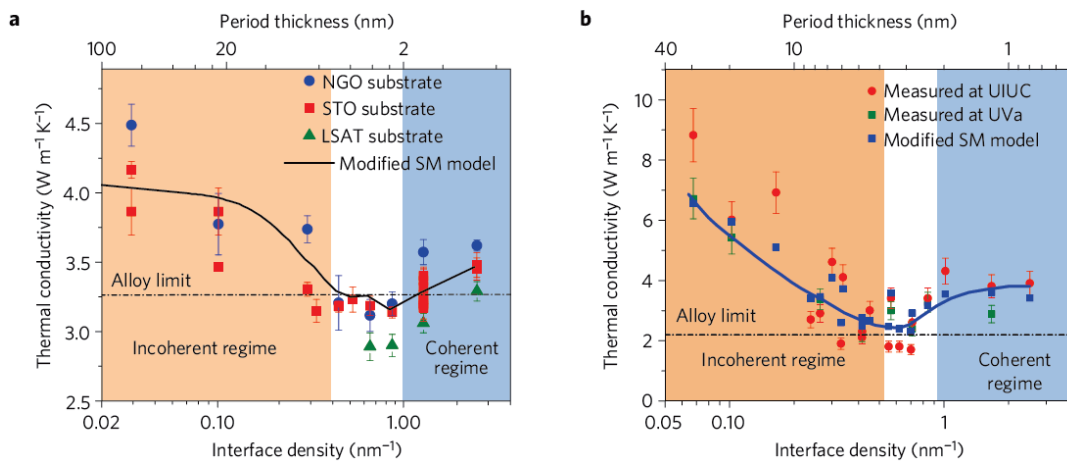


Figure 1.32 Thermal conductivity for different interface densities at room temperature. (a) STO/CTO SLs. (b) STO/BTO SLs. The black trend line represents the modified SM model. The blue line is used as a guide to eye. [41]

Frieling et al. [42] used non-equilibrium molecular dynamics (NEMD) to study the impact of SL period and interfacial intermixing on the thermal conductivity of isotopic silicon

superlattices ($^{28}\text{Si}/^{30}\text{Si}$). Simulations were done at an average temperature of 500 K considering a 400 nm thick SL. For atomic sharp interfaces (perfect interfaces), they observed a minimum in thermal conductivity for a period of 3 nm. This indicates the presence of a coherent regime. Contrarily, for intermixing interfaces, this minimum vanishes due to incoherent thermal transport of phonons. The randomly distributed isotopic defects break down the phase of phonon wavepackets. They also showed that an even larger reduction in Si thermal conductivity can be achieved with $^{28}\text{Si}_{0.5}/^{30}\text{Si}_{0.5}$ alloys (see Figure 1.33).

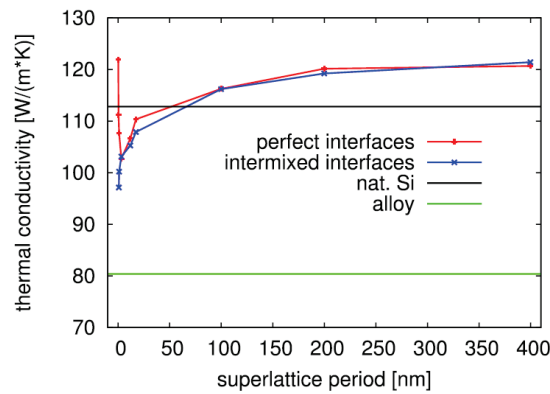


Figure 1.33 Thermal conductivity of $^{28}\text{Si}/^{30}\text{Si}$ SLs with perfect interfaces (red +), $^{28}\text{Si}/^{30}\text{Si}$ SLs with intermixed interfaces (blue crosses), natural silicon (black line) and $^{28}\text{Si}_{0.5}/^{30}\text{Si}_{0.5}$ alloy (green line). The red and blue lines are used to guide the eye. [42]

Latour et al. [43] showed also, theoretically, the transition from a coherent to an incoherent regime for Si/hSi superlattices with perfect interfaces at 500 K. The minimum of thermal conductivity was obtained for a period of 4 nm. This result is in good agreement with that obtained in [42].

1.9 Summary

The goal of this chapter was to remind the essential concepts of physics of solids associated with conductive heat transport phenomena by vibrations of the atoms. We first introduced phonons as the quanta of energy of lattice vibrations. We then set out the hypothesis of harmonic model taking into account only the interactions between an atom and its nearest neighbors. This model was applied for monoatomic, diatomic and superlattice crystals. It allowed us to introduce the concept of dispersion curves and the available modes in a crystal. Then, we described some phenomena related to particle heat transport. We used the Knudsen number to show that for very small medium dimension phonons particle transport is ballistic, while it is diffusive when the MFP is much lower than the dimension of the studied medium. In Section 1.6, we briefly analyzed the thermal properties of amorphous materials. We saw that very thin amorphous silicon layers can have thermal conductivities that are about two orders of magnitude lower than that of bulk silicon. Is it possible to obtain such a large decrease for thermal conductivity by processing thick micrometric crystalline silicon layers? The answer of this question will be given in Chapter 3.

In Sections 1.7.2, we analyzed the thermal properties of suspended membranes and especially the phonon coherence effects in 2D phononic structures. We reported recent experimental and theoretical results obtained by different scientific groups. Some of them reported on additional reduction in thermal conductivity, at room temperature, ascribed surprisingly to phonon coherence effects even when the characteristic dimension of their studied system is much larger than the dominant phonon wavelength. We note that the reduction in thermal conductivity at room temperature down to low levels is in itself already an original result. We will investigate the thermal conductivity reduction in 2D phononic structure in Chapter 4.

In Section 1.8, we reviewed current understanding of thermal properties of superlattices. For these 1D phononic structure, coherence effect due to the periodicity is clearly evidenced. However, from one hand, reduced scattering at the interfaces requires very high quality epitaxial materials (MBE epitaxy) and from the other hand the proposed materials are not CMOS-compatible. Towards this end, we propose a process using only silicon that would minimize interface scattering in the last chapter.

Bibliography

- [1] D. M. Howard and J. A. S. Angus, *Acoustics and psychoacoustics*, vol. 53, no. 9. 2013.
- [2] C. V. Anderson, "Thermal heat transport characterization for macroscale, microscale, and nanoscale heat conduction. Thesis," 2008.
- [3] S. Tamura, Y. Tanaka, and H. J. Maris, "Phonon group velocity and thermal conduction in superlattices," *Phys. Rev. B*, vol. 60, 1999.
- [4] S. Tamura, "Thermal Conductivity in Superlattices. <http://leaf-me.eng.hokudai.ac.jp/JSTP/pdf/tamura.pdf>," 2006. .
- [5] H. J. McSkimin and P. Andreatch, "Elastic moduli of silicon vs hydrostatic pressure at 25.0°C and -195.8°C," *J. Appl. Phys.*, vol. 35, no. 7, pp. 2161–2165, 1964.
- [6] T. Klitsner and R. Pohl, "Phonon scattering at silicon crystal surfaces.," *Phys. Rev. B. Condens. Matter*, vol. 36, no. 12, pp. 6551–6565, 1987.
- [7] G. Chen, "Phonon heat conduction in nanostructures," *Int. J. Therm. Sci.*, vol. 39, no. 4, pp. 471–480, 2000.
- [8] G. Chen and C. L. Tien, "Thermal conductivities of quantum well structures," *J. Thermophys. Heat Transf.*, vol. 7, no. 2, pp. 311–318, 1993.
- [9] J. M. Ziman, *Electrons and phonons: The Theory of Transport Phenomena in Solids*. Oxford: Clarendon Press, 1960.
- [10] M. Asheghi, K. Kurabayashi, R. Kasnavi, and K. E. Goodson, "Thermal conduction in doped single-crystal silicon films," *J. Appl. Phys.*, vol. 91, no. 8, pp. 5079–5088, 2002.
- [11] J.-S. Heron, "Transport des phonons à l'échelle du nanomètre. Thesis," 2009.
- [12] J. E. Turney, A. J. H. McGaughey, and C. H. Amon, "In-plane phonon transport in thin films," *J. Appl. Phys.*, vol. 107, no. 2, 2010.
- [13] D. P. Sellan, J. E. Turney, A. J. H. McGaughey, and C. H. Amon, "Cross-plane phonon transport in thin films," *J. Appl. Phys.*, vol. 108, no. 11, 2010.
- [14] W. G. Vincenti and C. H. Kruger, *Introduction to Physical Gas Dynamics*. Malabar, Florida: Krieger Publishing Company, 1965.
- [15] A. Majumdar, "Microscale Heat Conduction in Dielectric Thin Films," *J. Heat Transfer*, vol. 115, no. 1, p. 7, 1993.
- [16] C. J. Glassbrenner and G. A. Slack, "Thermal conductivity of silicon and germanium from 3 K to the melting point," *Phys. Rev.*, vol. 134, no. 4A, 1964.
- [17] P. B. Allen, J. L. Feldman, J. Fabian, and F. Wooten, "Diffusons, locons and propagons: character of atomic vibrations in amorphous Si," *Philos. Mag. B*, vol. 79, pp. 1715–1731, 1999.
- [18] C. J. Morath, H. J. Maris, J. J. Cuomo, D. L. Pappas, A. Grill, V. V. Patel, J. P. Doyle, and K. L. Saenger, "Picosecond optical studies of amorphous diamond and diamondlike carbon: Thermal conductivity and longitudinal sound velocity," *J. Appl. Phys.*, vol. 76, no. 5, pp. 2636–2640, 1994.
- [19] S. Moon, M. Hatano, M. Lee, and C. P. Grigoropoulos, "Thermal conductivity of amorphous silicon thin films," *Int. J. Heat Mass Transf.*, vol. 45, no. 12, pp. 2439–2447, 2002.
- [20] P. Nath and K. L. Chopra, "Thermal conductivity of amorphous and crystalline Ge and GeTe films," *Phys. Rev. B*, vol. 10, no. 8, pp. 3412–3418, 1974.
- [21] T. S. Tighe, J. M. Worlock, and M. L. Roukes, "Direct thermal conductance measurements on suspended monocrystalline nanostructures," *Appl. Phys. Lett.*, vol. 70, no. 20, pp. 2687–2689, 1997.
- [22] M. L. Roukes, K. Schwab, E. A. Henriksen, and J. M. Worlock, "Measurement of the quantum of thermal conductance," *Nature*, vol. 404, no. 6781, pp. 974–977, 2000.
- [23] W. Fon, K. C. Schwab, J. M. Worlock, and M. L. Roukes, "Phonon scattering mechanisms in suspended nanostructures from 4 to 40 K," *Phys. Rev. B*, vol. 66, p. 045302, 2002.
- [24] D. Li, Y. Wu, P. Kim, L. Shi, P. Yang, and A. Majumdar, "Thermal conductivity of individual silicon nanowires," *Appl. Phys. Lett.*, vol. 83, no. 14, pp. 2934–2936, 2003.
- [25] A. I. Hochbaum, R. Chen, R. D. Delgado, W. Liang, E. C. Garnett, M. Najarian, A. Majumdar, and P. Yang, "Enhanced thermoelectric performance of rough silicon nanowires," *Nature*, vol. 451, no. 7175, pp. 163–167, 2008.
- [26] Y. S. Ju and K. E. Goodson, "Phonon scattering in silicon films with thickness of order 100 nm," *Appl. Phys. Lett.*, vol. 74, no. 20, p. 3005, 1999.
- [27] E. Chavez-Angel, J. S. Reparaz, J. Gomis-Bresco, M. R. Wagner, J. Cuffe, B. Graczykowski, A. Shchepetov, H. Jiang, M. Prunnila, J. Ahopelto, F. Alzina, and C. M. Sotomayor Torres, "Reduction of the thermal conductivity in free-standing silicon nano-membranes investigated by non-invasive Raman thermometry," *APL Mater.*, vol. 2, no. 1, 2014.

- [28] S. Neogi, J. S. Reparaz, L. F. C. Pereira, B. Graczykowski, M. R. Wagner, M. Sledzinska, A. Shchepetov, M. Prunnila, J. Ahopelto, C. M. Sotomayor-Torres, and D. Donadio, "Tuning Thermal Transport in Ultrathin Silicon Membranes by Surface Nanoscale Engineering," *ACS Nano*, vol. 9, no. 4, pp. 3820–3828, 2015.
- [29] J.-K. Yu, S. Mitrovic, D. Tham, J. Varghese, and J. R. Heath, "Reduction of thermal conductivity in phononic nanomesh structures," *Nat. Nanotechnol.*, vol. 5, no. 10, pp. 718–21, 2010.
- [30] J. Tang, H. T. Wang, D. H. Lee, M. Fardy, Z. Huo, T. P. Russell, and P. Yang, "Holey silicon as an efficient thermoelectric material," *Nano Lett.*, vol. 10, no. 10, pp. 4279–4283, 2010.
- [31] P. E. Hopkins, C. M. Reinke, M. F. Su, R. H. Olsson, E. A. Shaner, Z. C. Leseman, J. R. Serrano, L. M. Phinney, and I. El-Kady, "Reduction in the thermal conductivity of single crystalline silicon by phononic crystal patterning," *Nano Lett.*, vol. 11, no. 1, pp. 107–112, 2011.
- [32] J. Callaway, "Model for lattice Thermal Conductivity at Low Temperatures," *Phys. Rev.*, vol. 113, no. 4, pp. 1046–1051, 1959.
- [33] N. Zen, T. a Puurtinen, T. J. Isotalo, S. Chaudhuri, and I. J. Maasilta, "Engineering thermal conductance using a two-dimensional phononic crystal," *Nat. Commun.*, vol. 5, p. 3435, 2014.
- [34] M. Nomura, J. Nakagawa, Y. Kage, J. Maire, D. Moser, and O. Paul, "Thermal phonon transport in silicon nanowires and two-dimensional phononic crystal nanostructures," *Appl. Phys. Lett.*, vol. 106, no. 14, 2015.
- [35] M. Nomura, Y. Kage, J. Nakagawa, T. Hori, J. Maire, J. Shiomi, R. Anufriev, D. Moser, and O. Paul, "Impeded thermal transport in Si multiscale hierarchical architectures with phononic crystal nanostructures," *Phys. Rev. B - Condens. Matter Mater. Phys.*, vol. 91, no. 20, pp. 1–6, 2015.
- [36] J. Maire, R. Anufriev, H. Han, S. Volz, and M. Nomura, "Thermal conductivity tuning by thermocrystals," *ArXiv*, pp. 1–8, 2015.
- [37] M. Simkin and G. Mahan, "Minimum thermal conductivity of superlattices," *Phys. Rev. Lett.*, vol. 84, no. 5, pp. 927–30, 2000.
- [38] W. Capinski, H. Maris, T. Ruf, M. Cardona, K. Ploog, and D. Katzer, "Thermal-conductivity measurements of GaAs/AlAs superlattices using a picosecond optical pump-and-probe technique," *Phys. Rev. B*, vol. 59, no. 12, pp. 8105–8113, 1999.
- [39] M. N. Luckyanova, J. Garg, K. Esfarjani, A. Jandl, M. T. Bultsara, A. J. Schmidt, A. J. Minnich, S. Chen, M. S. Dresselhaus, Z. Ren, E. A. Fitzgerald, and G. Chen, "Coherent Phonon Heat Conduction in Superlattices," *Science (80-.)*, vol. 338, no. 6109, pp. 936–939, 2012.
- [40] A. Giri, P. E. Hopkins, J. G. Wessel, and J. C. Duda, "Kapitza resistance and the thermal conductivity of amorphous superlattices," *J. Appl. Phys.*, vol. 118, no. 16, 2015.
- [41] J. Ravichandran, A. K. Yadav, R. Cheaito, P. B. Rossen, A. Soukiassian, S. J. Suresha, J. C. Duda, B. M. Foley, C.-H. Lee, Y. Zhu, A. W. Lichtenberger, J. E. Moore, D. A. Muller, D. G. Schlom, P. E. Hopkins, A. Majumdar, R. Ramesh, and M. A. Zurbuchen, "Crossover from incoherent to coherent phonon scattering in epitaxial oxide superlattices," *Nat. Mater.*, vol. 13, no. 1, p. 168, 2013.
- [42] R. Frieling, M. Radek, S. Eon, H. Bracht, and D. E. Wolf, "Phonon coherence in isotopic silicon superlattices," *Appl. Phys. Lett.*, vol. 105, no. 13, pp. 2012–2015, 2014.
- [43] B. Latour, S. Volz, and Y. Chalopin, "Microscopic description of thermal-phonon coherence: From coherent transport to diffuse interface scattering in superlattices," *Phys. Rev. B - Condens. Matter Mater. Phys.*, vol. 90, no. 1, pp. 1–9, 2014.

Chapter 2. Two characterization techniques for thermal conductivity determination

After having presented the theory of heat transfer in bulk and nanostructured materials in Chapter 1, we are going now to be interested in experimental approaches for thermal conductivity measurements.

The thermal conductivity remains a difficult parameter to obtain, as it requires the knowledge of three different physical quantities: a power, a length scale and a temperature difference as indicated by its unit ($\text{W}\cdot\text{m}^{-1}\cdot\text{K}^{-1}$). Different characterization techniques can be used in order to study materials thermal properties and especially to access thermal conductance and thermal conductivity information. Each of the following techniques has its own excitation source that generates a given heat flux, which could be electrical as in the direct method [1], the 3ω method [2][3], scanning thermal microscopy [4][5] or optical as in the flash method [6][7], AC-calorimetry [8], photo-thermal reflectance [9][10][11][12] or micro-Raman thermometry [13][14].

In this chapter we report on two different thermal characterization techniques used to study our samples: micro-Raman thermometry and scanning thermal microscopy. These techniques are applied for determining thermal conductivity in complex geometries.

2.1 Micro-Raman thermometry

Raman spectroscopy is an optical and non-destructive technique invented by C.V. Raman [15], whom pursued the idea of inelastic light scattering and explained that "... the character of the scattered radiations enables us to obtain an insight into the ultimate structure of the scattering substance.". His argument was convenient to support the quantum theory of light (after his discovery, Raman was awarded the Nobel Prize in physics in 1930). Raman spectroscopy is based on interactions of a monochromatic lighting source (laser) of a given frequency ω_i with lattice vibrations (phonons). After these interactions, the reemitted light is then analyzed in a spectrometer. The sample response to the laser exposure can contain either the same incident frequency ω_i due to Rayleigh scattering (backscattered signal) or a different frequency ω_k due to Raman scattering.

In the spectrometer, Rayleigh scattering is eliminated, allowing only the presence of Raman scattering. The obtained spectra consist of Stokes peaks (due to creation of phonons) and anti-Stokes (due to absorption of phonons); both are equally displaced from the Rayleigh line. Stokes peaks are more intense than the anti-Stokes ones, given by the Bose-Einstein distribution law for phonons. At the very most, the intensities of Raman lines are 10^{-5} of the intensity of the source. As a consequence, Stokes shift is usually measured in most of Raman spectrometer.

Raman spectroscopy can be used for structural characterization (grain size, stress ...), as the observed spectra depend on these parameters in a very sensitive way. It can also be used for determining the thermal conductivity by measuring the surface temperature of the heated zone. This technique is called micro-Raman thermometry. Practically, temperature is measured in

one of three manners: by evaluating the peak position shifts, by quantifying the broadening of the linewidth, or by looking at the intensity ratio of the anti-Stokes signal to the Stokes signal. This choice is complicated and the three techniques differ in the readiness which may lead to inaccurate temperature measurement. We decided to monitor the Stokes line position due to its practical ease of use. Any changes in the Raman spectra would be directly related to changes in the vibrational state of the target. These changes are reflected in the peak position, which has a red shift when increasing the temperature due to thermal expansion.

In our study, two different micro-Raman probes of wavelengths $\lambda = 532$ nm and $\lambda = 473$ nm were used in order to determine the thermal conductivities of two different kinds of materials: Irradiated porous silicon (see Chapter 3) and suspended phononic silicon membranes (see Chapter 4). In this chapter we provide examples on thermal conductivity determination of irradiated porous silicon samples. Two different methods can be used: one is called ‘power variation’ (used in Chapter 3) and the other one is called ‘temperature profile’ (used in Chapter 4).

2.1.1 Experimental temperature measurements

Theoretical and experimental studies were published in the literature showing a linear dependence of the Raman shift on temperature for monocrystalline silicon [16][17][18][18][19]. The linear relation is achieved in a given range of temperature. The temperature dependence on the Raman shift is given by [20][21]:

$$\Delta T = \frac{\Delta\omega}{\alpha}, \quad (2.1)$$

where ΔT is the temperature growth, $\Delta\omega = \omega - \omega_0$, where ω is the position to which the Stokes peak shifts, ω_0 is the Raman peak position at room temperature and α is the linear coefficient between first-order Raman shift and temperature. Populaire et al. [22] found that porous silicon (PSi) and bulk silicon have the same α coefficient. The value $-0.022 \text{ cm}^{-1} \cdot \text{K}^{-1}$ given in the literature for, both, bulk Si and Si nanowires was chosen in our study [23][24]. When the temperature increases and becomes too high, this linear relation breaks down due to a change in the thermal expansion coefficient [25][26] (see Figure 2.1). We therefore chose to work in a temperature range between 300 K (room temperature) and 420 K.

Referring to equation 2.1, a shift of the Raman line should occur for determining the temperature. Therefore, the energy released to the system should vary inducing a temperature rise. This energy is coming from the absorbed power of the laser beam illuminating the exposed material. Neutral density filters were used in order to change the laser power received by the target. Figure 2.2 shows a schematic of the Renishaw Raman microscope (used in Chapter 3) with a YAG laser beam (wavelength $\lambda = 532$ nm) going through the neutral density filters, and focused on the sample by an objective x50 with a numerical aperture (NA) of 0.5.

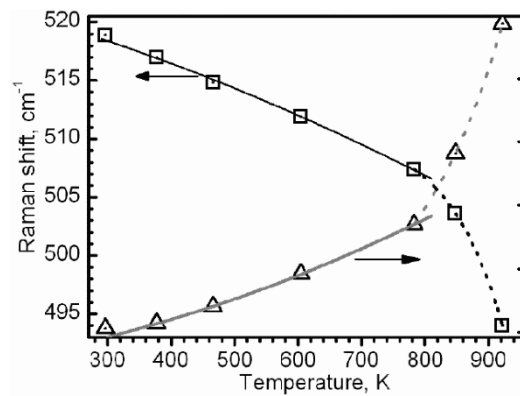


Figure 2.1 Raman shift dependence on temperature. [26]

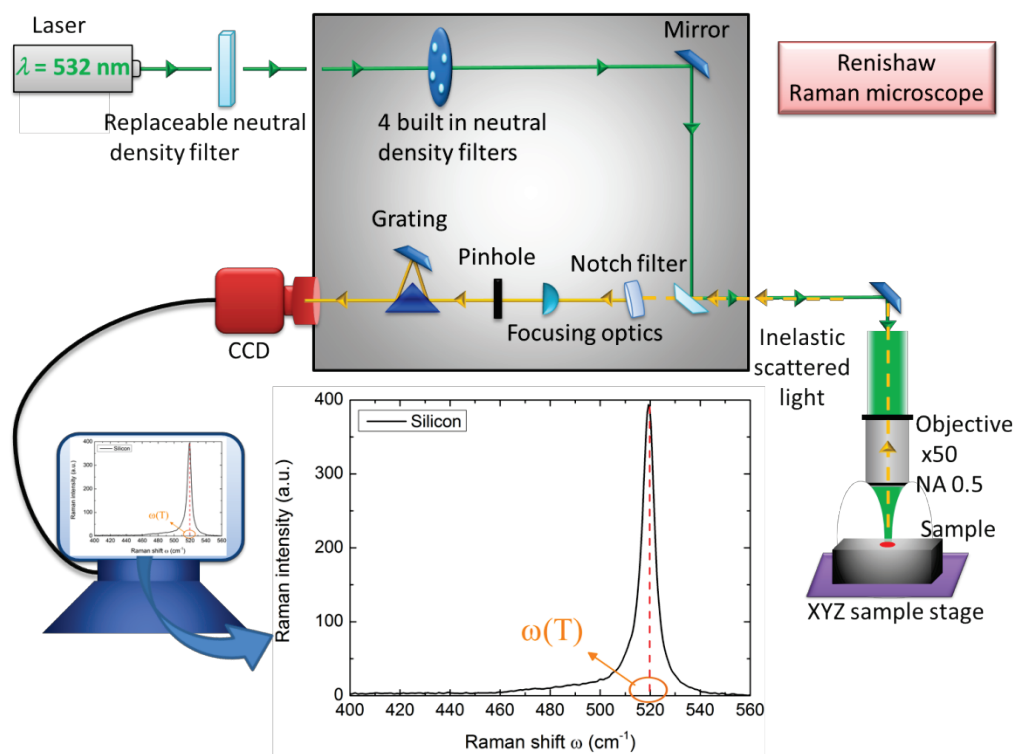


Figure 2.2 Schematic of the Renishaw Raman microscope with a 532 nm YAG laser beam with an objective x50 and NA of 0.5. Image not to scale.

In Figure 2.3 we show an example of temperature measurements on a porous silicon sample (56 % porosity) using the ‘power variation’ method. The green laser ($\lambda = 532$ nm) is focused on the sample. Two accumulations for each spectrum were considered and the power received by the sample (P_0) was measured using a photometer. The laser is focused for 5 minutes on the sample surface before starting any spectral acquisition in order to stabilize the sample temperature and reach the static regime. The absorbed laser power is different from the received one and depends on the absorption coefficient of the studied material. Each analyzed Raman spectrum is then fitted with a Lorentzian curve in order to determine precisely the peak position.

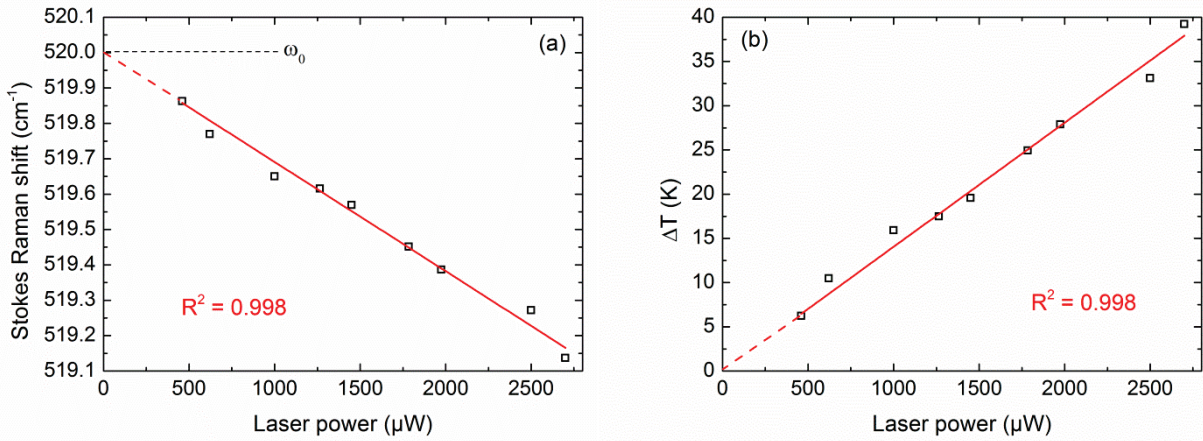


Figure 2.3 Determination of the temperature increase based on Stokes peak positions. **(a)** Stokes Raman shift versus laser power. The zero-intercept of the fit (red dashed line) is taken to be the room temperature peak position ($\omega_0 = 520 \text{ cm}^{-1}$). **(b)** Deduced temperature rise versus laser power based on the room-temperature peak position.

2.1.2 Determination of the thermal conductivity

In this section, we detail how to use the temperature rise for determining the thermal conductivity values from the Raman measurements and from finite element method (FEM) simulations.

For a given laser power density, heat dissipation occurring in a target depends on its capacity of dissipating heat, in other words, on its thermal conductivity. Therefore, the more conductive the material, the lower the temperature in the heated zone. Perichon et al. [27] obtained the thermal conductivity of PSi layers from a linear dependence between the absorbed laser power in the system and the temperature rise on its surface. Their analytical model is based on the one used by Nonnenmacher et al. [28] taken from [29]. In their model, the thickness of the probed material is semi-infinite compared to the laser spot diameter. They considered that the isotherms within the layer are hemispherical. This model is no more valid in our case when the laser penetration depth is $1.2 \mu\text{m}$ and the porous layer is $10 \mu\text{m}$ thick (for Renishaw Raman spectrometer study). For this reason, we have implemented a method for thermal conductivity determination based on FEM simulations using COMSOL as software. FEM simulations allow considering the Gaussian profile of the laser spot and its penetration depth. By substituting the laser power used in Figure 2.3 (b) by the absorbed laser power in the studied material (porous silicon with 56 % porosity here), the obtained slope (see Figure 2.4) is directly proportional to the system thermal resistance and can be written as [21]:

$$R_{system} = \frac{\Delta T}{\Delta P_{absorbed}}, \quad (2.2)$$

where $P_{absorbed} = A \cdot P_0$, where A is the absorbance. $A = 0.9$ for PSi of 56 % porosity (see Section 2.1.5).

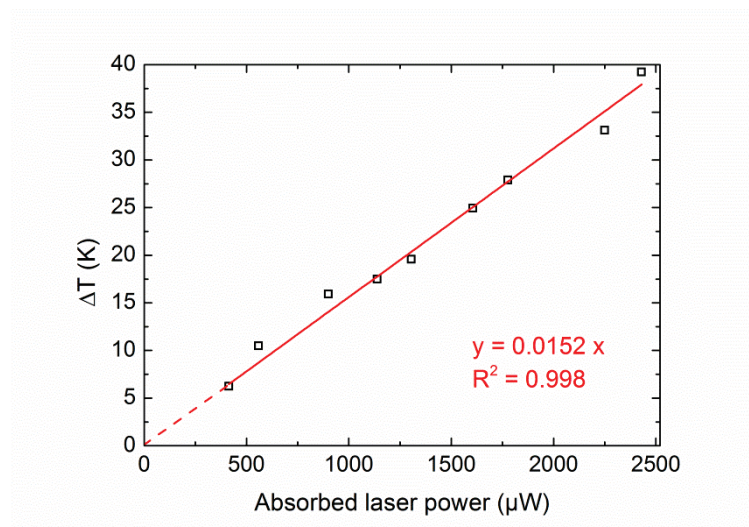


Figure 2.4 Temperature rise versus absorbed laser power.

FEM simulation:

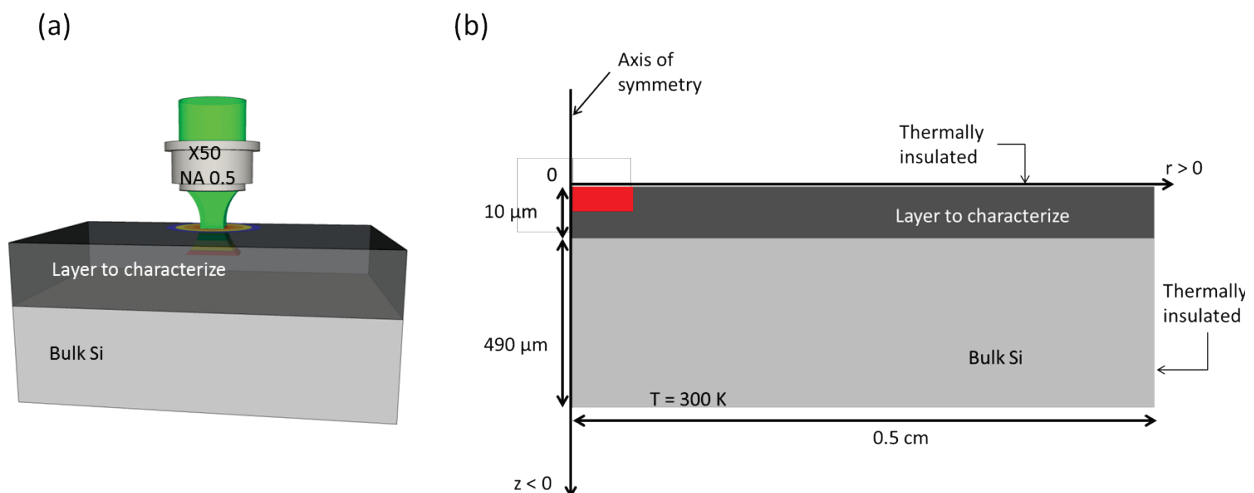


Figure 2.5 (a) 3D view of the real configuration (image not to scale). (b) 2D axisymmetric schematic of the modeling geometry including the boundary conditions. The red rectangle was added for mesh enhancement purposes.

In this chapter we highlight the model used for P*Si* thermal conductivity determination, while the model used for suspended membranes thermal conductivity determination is detailed in Chapter 4. The goal is to represent the real geometry in order to find which thermal conductivity in the simulation allows obtaining the same slope as the one found experimentally.

Figure 2.5 (a) represents a 3D schematic of the real geometry illuminated with the YAG laser ($\lambda = 532$ nm) with an objective x50. Two different materials, of respective thermal conductivities $\lambda_{\text{layer to characterize}}$ and $\lambda_{\text{bulk silicon}} = 148 \text{ W}\cdot\text{m}^{-1}\cdot\text{K}^{-1}$ at room temperature [30] and a

heat source due to the laser beam are shown. 2D axisymmetric steady state thermal analysis was used in FEM simulations to solve the conductive heat transfer equation. The model consists of a bilayer as shown in Figure 2.5 (b). The coordinates for the plane 2D axisymmetric calculation are (r, z) . The heat equation in the diffusive regime for stationary cases, considering material properties as constants, is given by:

$$\lambda \nabla^2 T + Q = 0, \quad (2.3)$$

where λ , ∇^2 and Q are, respectively, the material thermal conductivity, the Laplace operator and the heat input. System dimensions and boundary conditions are displayed in Figure 2.5 (b). We have verified that the presence of heat losses to the environment does not affect the results in our study. For this reason, except the bottom surface, all boundaries are set to be thermally insulated.

The laser used in the Raman experiments was modeled as a Gaussian beam. The body heat load within the layer to characterize is given by the following expression:

$$P(r, z) = \frac{2A \cdot P_0}{\pi \sigma^2} \alpha_a e^{\left(\frac{-2r^2}{\sigma^2}\right)} e^{(-|z| \cdot \alpha_a)}, \quad (2.4)$$

where σ is the laser beam radius at $1/e^2$ of the total power intensity, α_a is the absorption coefficient and was found in literature [31] for PSi of porosity 56 % to be equal to 8300 cm^{-1} . In equation 2.4, the first exponential stands for the Gaussian radial distribution of the power and the second exponential stands for the in depth absorption. Note that equation 2.4 is not the only way to express the intensity of a Gaussian laser beam. Some authors prefer to define the beam radius at a position where the amplitude drops to $1/e$ [32]. This choice does not affect the simulated maximum temperature.

Mesh geometry:

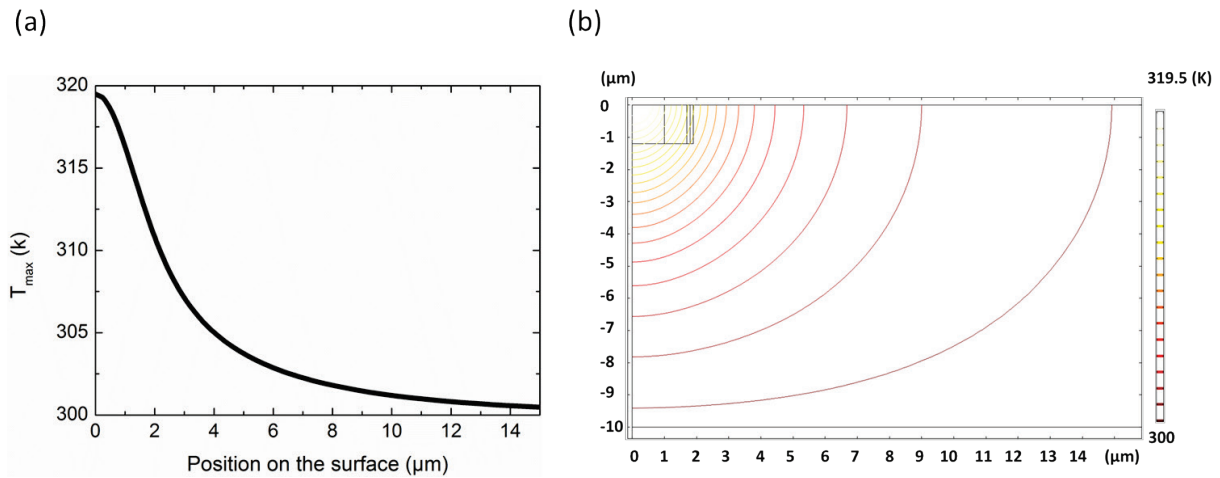


Figure 2.6 (a) Temperature profile on the surface. **(b)** Isothermal contours. The four used rectangles for mesh enhancement are displayed. $\lambda = 5 \text{ W} \cdot \text{m}^{-1} \cdot \text{K}^{-1}$, $\sigma = 1.9 \text{ }\mu\text{m}$, $A = 0.9$, $P_0 = 1 \text{ mW}$, $\alpha_a = 8300 \text{ cm}^{-1}$.

The choice of a 2D axisymmetric model was used for symmetry reasons that simplify the geometry. The less elements the faster the simulation and the quicker the results validation. To perform these simulations, a computer of 8 GB RAM was used. The reliability of results coming from FEM simulations relies on the choice of the mesh made for the modeled geometries. Quadrilateral elements were used to build the mesh. The number of mesh elements was increased until constant result convergence was obtained, independently of the mesh density. The simulations were performed using a power of 1 mW, an absorbance of 0.9, a beam radius of 1.9 μm and an absorption coefficient of 8300 cm^{-1} . Figure 2.6 (a) shows a Gaussian profile as expected on the surface and a maximum temperature of 319.5 K. We show in details in the following parts how the temperature determination can drastically affect the obtained thermal conductivity values. Figure 2.6 (b) shows the isothermal contours. For this simulation the total number of elements was 7410 with the smallest one of 88.1 nm and the time duration is 1s.

2.1.3 Temperature determination using FEM simulations

Thermal conductivity deduction is based on simulated temperatures using FEM simulations. Like previous studies (semi-infinite elements and analytical models), we considered the maximum temperature at the surface of the sample, in the center of the heated zone, as the temperature that should be taken into account for thermal conductivities determination. In Raman experiments, the laser beam (photons) interacts with the target (phonons) inducing a heating up of the latter. Photons coming from various depths do not have equal probability of being collected and we assumed that only photons coming from the surface are collected during the experiments. This assumption could be subject to further investigations.

In Figure 2.7 the red curve depicts $T_{\text{max}}(0) - T_{\text{max}}(r)$, while the black curve shows $T_{\text{max}}(0) - T_{\text{max}}(z)$, both as a function of position/ σ . The two curves do not match which makes evident that the isothermal contours are not hemispherical. Thus, the consideration of hemispherical isotherms is no more valid in the case of the modelling of the real geometry.

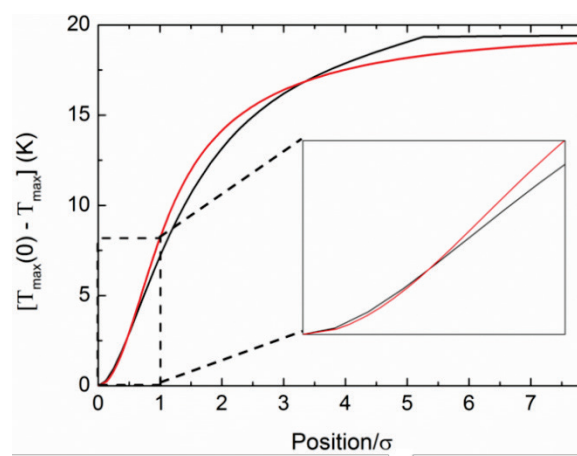


Figure 2.7 Temperature difference. The red curve represents the variation on the surface along r , while the black one represents the variation in T in depth along z . $\lambda = 5 \text{ W}\cdot\text{m}^{-1}\cdot\text{K}^{-1}$, $\sigma = 1.9 \mu\text{m}$, $A = 0.9$, $P_0 = 1 \text{ mW}$, $\alpha_a = 8300 \text{ cm}^{-1}$.

2.1.4 Measurement of the laser spot

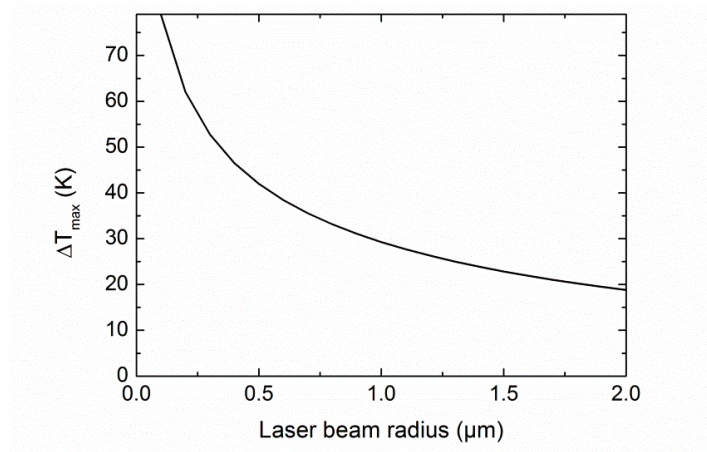


Figure 2.8 Temperature rise versus laser beam radius. $\lambda = 5 \text{ W.m}^{-1}\text{.K}^{-1}$, $A = 0.9$, $P_0 = 1 \text{ mW}$, $\alpha_a = 8300 \text{ cm}^{-1}$.

For many laser applications the beam quality is crucial as it defines the smallest area in the focal point. We studied the effect of the laser beam radius on the maximum surface temperature rise (see Figure 2.8). Based on Rayleigh criterion, and considering the diffraction limited case of a beam and all parts of the system are perfect, the laser beam diameter is given by

$$2\sigma = 1.22 \frac{\lambda}{NA}. \quad (2.5)$$

We find a theoretical laser beam radius $\sigma = 0.65 \text{ μm}$. The corresponding maximum temperature rise based on Figure 2.8 for this value of σ is 37 K. Using a Gaussian laser distribution, the spot diameter is not anymore governed by the above formula and its determination should be realized experimentally.

A basic, fast and accurate laser beam diameter measurement is the knife-edge technique [33] [34]. This kind of measurement can be performed using a power meter (for laser power detection) and a sharp cut cleaned silicon wafer (as a knife). A schematic of the setup is shown in Figure 2.9.

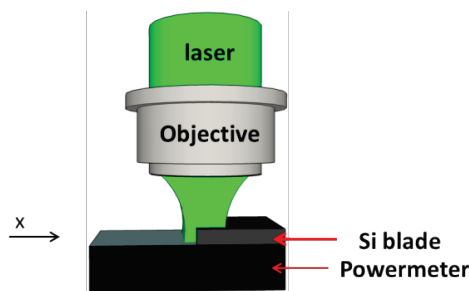


Figure 2.9 Principle of knife edge technique.

The measurement principle is as following: the laser beam is focused on the blade close to its edge (starting point of the experiment, for $x = 0$ and $P_0 = 0$ W), then the knife edge moves perpendicular to the beam propagation direction and the total power received by the photodiode is measured until the beam is totally incident on the photodiode (ending point of the experiment where $P_0 = P_{max}$). The obtained profile of the laser beam is plotted in Figure 2.10. It is very important to determine the maximum and the minimum values on the wings of the curve. The data can be fitted using the following function:

$$f(x) = \frac{1}{2} \left(1 + \operatorname{erf} \left(\frac{\sqrt{2} (x - B)}{\sigma} \right) \right), \quad (2.6)$$

where erf is the error function, B is the position at which the normalized power intensity corresponds to $\frac{1}{2}$ and the sign + is chosen for knife translation in the negative direction in our case.

The experimental beam radius value is $\sigma = 1.9 \mu\text{m}$ (see Figure 2.10 (a)), which is more than 2.9 times larger than the theoretically expected one. Based on Figure 2.8, the corresponding maximum temperature rise is 19.5 K. The relative decrease in ΔT maxima, comparing the two beam radiuses, is about 47 %. For the theoretical case and by using the same parameters, we find $\lambda = 9.5 \text{ W}\cdot\text{m}^{-1}\cdot\text{K}^{-1}$. This value is 1.9 times bigger than the real case. So, the choice of the laser beam radius can drastically affect the thermal conductivity determination, as its determination is based on the maximum temperature rise. The beam radius obtained based on Figure 2.10 (b) is used in Chapter 4 for the thermal characterization of the suspended membranes.

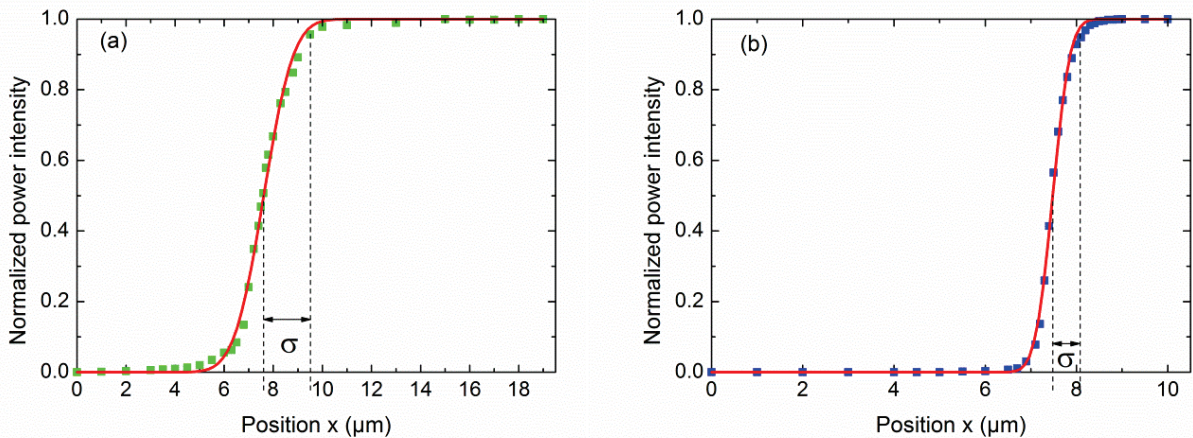


Figure 2.10 Typical curves obtained during knife edge measurements. **(a)** Normalized power intensity versus beam position obtained for $\lambda = 532$ nm with an objective 50x/0.5 NA. **(b)** Normalized power intensity versus beam position obtained for $\lambda = 473$ nm with an objective 100x/0.95 NA. Red curves fits are used for beam radius determination.

2.1.5 Determination of the absorbance

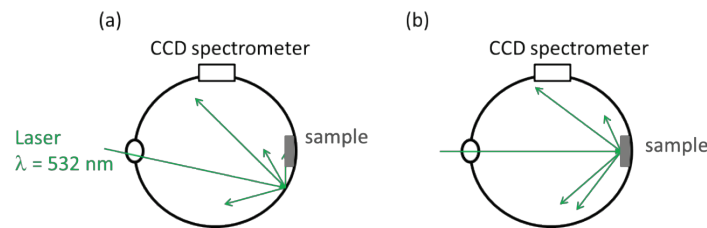


Figure 2.11 Principle of the integrating sphere. **(a)** The sample is placed into the sphere and the laser is directed on the sphere wall far from the sample. **(b)** The laser is directed onto the sample.

Integrating sphere was used for the calculation of the absorbance. The integrating sphere is a simple device for quantitative optical properties determination [35][36]. Figure 2.11 shows the experimental setup of an integrating sphere explaining the measurement procedure. The first step of the experiment is illustrated in Figure 2.11 (a), where the sample is placed inside the sphere and the laser is directed onto the sphere walls. The second step of the experiment is illustrated in Figure 2.11 (b), where the laser beam is directed onto the sample surface, which should be oriented such that the reflected laser signal from its surface is directed onto the sphere wall and not back through the entrance hole. The sample, in this case, is the porous silicon one with porosity of 56 %. The obtained spectra for the two experiments are shown in Figure 2.12. The absorbance is given by:

$$A = 1 - \frac{L_c}{L_b}, \quad (2.7)$$

where L_c and L_b are, respectively, the areas under the red and the black curves in Figure 2.12. For our PSi sample, we find that $A = 0.9$.

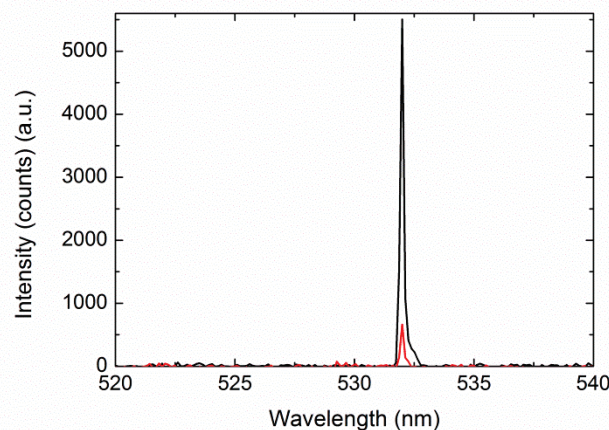


Figure 2.12 Integrating sphere spectra for experiments **(a)** (black curve) and **(b)** (red curve) obtained on porous silicon sample with 56 % porosity.

After detailing the micro-Raman thermometry technique used for the determination of the thermal conductivity in this manuscript and providing all the experimental parameters, we describe in the following section the SThM technique.

2.2 Scanning thermal microscopy (SThM)

The second thermal probing technique used in this manuscript is scanning thermal microscopy (SThM). This is a contact and nondestructive technique that allows measuring thermal properties at the nanoscale. These measurements can include temperature, thermal properties (thermal conductivity, heat capacity ...) and thermodynamics/calorimetric analysis (latent heat, enthalpy ...). However, SThM data analysis remains a challenge and requires a good understanding of the heat transfer mechanism between the probe and the studied sample. Result interpretation requires, in many cases, a modeling of the probe-sample system.

We first present the SThM setup used in this thesis with a description of the operational modes. We then describe in details the probe used for measurements, highlighting the probe position effect on the probe-sample heat transfer system. We then introduce a new calibration technique for the thermal characterization of complex geometries.

2.2.1 Experimental setup

What really distinguishes SThM from other forms of thermal analysis is its high spatial resolution, which can go down to sub-100 nm scale (micrometric for micro-Raman thermometry). The most common SThM setup is used in an atomic force microscopy (AFM) configuration. In AFM-based SThM, a sharp tip is mounted on a cantilever beam and attached to a piezoelectric actuator. This piezoelectric actuator can be moved up and down very sensitively using a control voltage unit. However, SThM does not probe the mechanical interactions between the tip and the sample, but rather the thermal interactions. Figure 2.13 is a schematic showing the principle of the SThM technique.

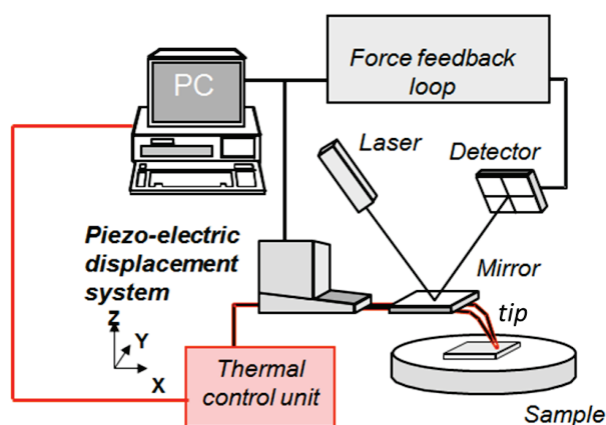


Figure 2.13 Principle of the technique.

2.2.1.1 Operational modes

In a resistive probe, the probe temperature can be determined by measuring its electrical resistance. The linear relationship between the electrical resistance of the probe and its temperature is given by:

$$R_p(T) = R_p(T_0)[1 + \alpha_{\rho e}(T - T_0)], \quad (2.8)$$

where $\alpha_{\rho e}$ is the temperature coefficient and $R_p(T_0)$ is the tip resistance at reference temperature T_0 , which is considered to be constant in our study. Knowing the injected current I one can write:

$$V(T) = R_p(T_0) I [1 + \alpha_{\rho e}(T - T_0)]. \quad (2.9)$$

The tip is one of the elements included in the Wheatstone bridge (see Figure 2.14).

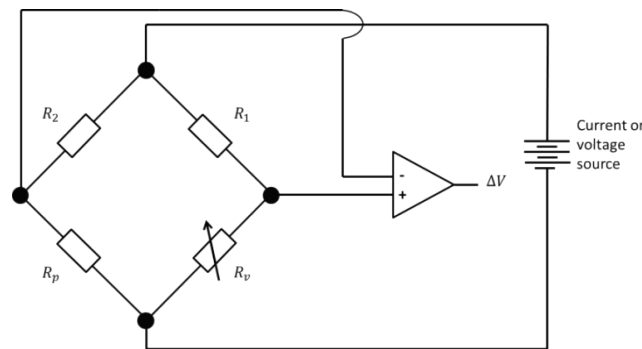


Figure 2.14 Schematic of a Wheatstone bridge.

Two operational modes are available in this case:

- Passive mode: This mode is used to study local heating of an active sample surface [37][38]. A very small current is injected in the probe in order to avoid any additional heating. The probe resistance is then measured.
- Active mode: This mode is performed to access studied sample thermal conductivity. The probe is considered as a heater and a sensor at the same time. Alternative current (AC) or direct current (DC) can be used in this case. Joule heating of the tip allows to increase the temperature of the tip (see Figure 2.15).

The variable resistance, which is related to $R_p(T)$, is plotted as a function of the Wheatstone bridge voltage in Figure 2.15. It shows a very good quadratic behavior due the Joule heating effect while the tip is far away from the sample.

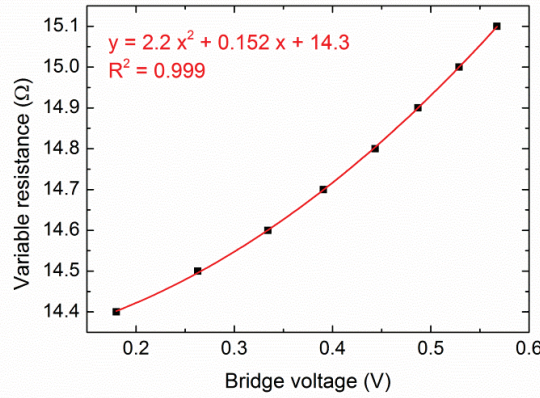


Figure 2.15 Wheatstone bridge calibration: variable resistance of the bridge as a function of the bridge power input (a very good quadratic behavior (red fitting curve) between the variable resistance and the bridge voltage).

In this study, the active mode with a DC current was used, which is the most widely used method [39][40][41][42][43]. A heated tip is brought into contact with the sample which is at room temperature. The heat flows from the tip to the sample causing a decrease in the tip temperature and so a change in the tip electrical resistance (R_p). This decrease in temperature is directly related to the studied sample thermal conductivity and induces a change in the output voltage (V_{out}) of the Wheatstone bridge. When the tip is far from the sample and a DC current flows inside, the tip temperature is given by $T_0 + \theta_{oc}$, with T_0 the room temperature and θ_{oc} the increase in the tip temperature when it is out of contact. When the tip goes into contact with the sample its temperature regarding the room temperature becomes

$$\theta_{tip\ exp} = \theta_{oc} - |\theta_{ic}|, \quad (2.10)$$

where $|\theta_{ic}|$ is the absolute value of the tip temperature decrease when it is in contact with the sample. Two different techniques can be used for the determination of sample thermal conductivity:

- ‘Purely experimental’ method: This method is mainly performed when having thick samples that can be considered as bulk ones. In this case, calibration samples are enough to determine the materials thermal conductivity. Usually, the relative dissipated probe power can be written as:

$$\frac{\Delta P}{P} = \frac{V_{ic}^2 - V_{oc}^2}{V_{ic}^2}, \quad (2.11)$$

where V_{ic} and V_{oc} are, respectively, the voltages needed to balance the Wheatstone bridge, in contact and out of contact. By plotting the relative dissipated probe power versus the calibration samples thermal conductivities, our porous silicon samples and the irradiated ones thermal conductivities were obtained. This is at the heart of Chapter 3.

- ‘Experimental and FEM simulations’ method: This method is required for samples of geometries different from the calibration ones. In our case the Wheatstone bridge was kept unbalanced. The decrease in the tip temperature when the probe goes into contact with the sample can be written as:

$$\theta_{ic} = \frac{\Delta V}{\alpha_{pe} R_p (T_0) I'} \quad (2.12)$$

where ΔV is the unbalanced Wheatstone bridge voltage value. In this method, in addition to the use of calibration samples, once θ_{ic} is known, FEM simulations have to be performed in order to determine samples thermal conductivities. This method is detailed in this chapter and is used in Chapter 4 for the determination of the thermal conductivity of suspended silicon membranes.

2.2.2 The Wollaston probe: geometry and characteristics

The Wollaston wire is an assembly of two coaxial cylinders. The central part is made of an alloy of platinum and rhodium, Pt90/Rh10, with a diameter of about 5 μm and a radius of curvature of about 15 μm (see Figure 2.16 (b)). This alloy wire is coated with silver to form the Wollaston probe with a diameter of about 75 μm . During the manufacturing process, the Wollaston wire is, at first, bent and, secondly, etched to reveal the Pt90/Rh10 part. This manufacturing step leaves a platinum rhodium area of 200 μm long in the open air [44]. The glue shown in Figure 2.16 (a) is used for mechanical stability reasons.

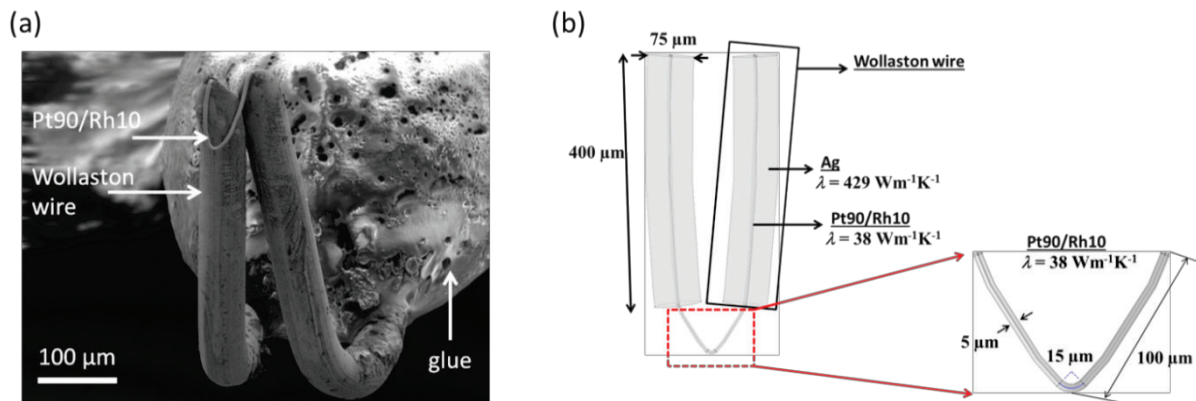


Figure 2.16 (a) Scanning electron microscope (SEM) image of the Wollaston probe. (b) Schematic of the Wollaston probe with its dimensions.

2.2.3 Numerical study of heat transfer between a Wollaston tip and a sample

When probed geometries become complex and differ from bulk substrates, the estimation of the heat transferred from the probe to the sample requires, in this case, a better understanding

of the tip-sample system. This necessitates a modeling of the entire studied system. The temperature cannot be deduced directly from the in-contact measurements (on calibration samples) as the flux lines may differ when dealing with complex geometries. This is especially the case for suspended membranes in our case (see Chapter 4).

2.2.3.1 Heat loss coefficient and air box side determination

Performing SThM experiments under ambient conditions leads to heat losses from the tip to the surrounding environment. The heat losses to the air are due to convection at macroscales and due to conduction [45] at low dimensions (micro-scale) in confined environment as the buoyancy forces decrease rendering the heat transfer coefficient due to convection small [46]. For both cases, the heat flux lost through the environment can be represented as an air box encountering the tip. In the out-of-contact case, the geometry around the Wollaston wire is open and heat convection may be possible for the losses. We note that thermal radiation losses are also present and are included in the wall losses coefficient h . Here we will evaluate the losses as if only heat conduction is responsible for all of them.

In order to determine the heat loss coefficient (h) we model the Wollaston wire and the Pt90/Rh10 part only (more details can be found in the following parts of this chapter). Using FEM simulations and by varying h we aim at obtaining the same experimental probe mean temperature $\theta_{oc} = 54.84$ K, when the tip is far away from the sample. The blue curve in Figure 2.17 leads to $h = 2506$ W.m⁻².K⁻¹. This value is in good agreement with the values obtained by Chapuis ($h = 3000$ W.m⁻².K⁻¹) [41] and Thiery et al. ($h = 2300$ W.m⁻².K⁻¹) [47] for a Wollaston probe. We, then put the tip in the middle of a square box of air ($\lambda = 0.025$ W.m⁻².K⁻¹) and vary the air box side dimension. The red curve in Figure 2.17 shows that the experimental mean probe temperature was obtained for an air box 1900 μ m large. By doing this we consider that h is the same even when the tip goes close to the sample surface and we make the hypothesis that h is temperature independent.

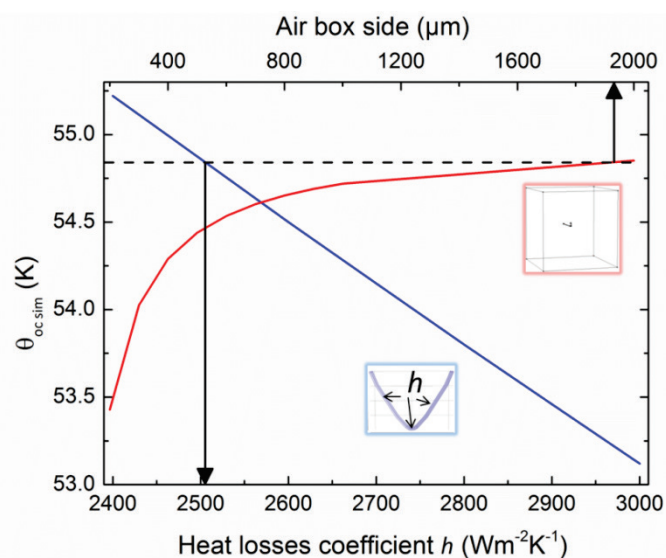


Figure 2.17 Determination of the heat loss coefficient (blue curve) and the air box side dimension (red curve). The black dashed line indicates the level where $\theta_{oc\ sim} = 54.84$ K.

2.2.3.2 Tip-sample air heat transfer

2.2.3.2.1 Tip-sample distance

Using FEM simulations, it is not possible to simulate ballistic heat transport through air when the tip is in contact with the sample (see Figure 2.18 (a)): it only solves the diffusion heat equation. For a given size, the ballistic flux is lower than the estimation based on the diffusive regime. Two methods are possible to account for this limit in a heuristic way. We adopted the one where the tip should be put at a distance d above the sample in order to account for the limit between the diffusive and the ballistic regime, and not into contact (see Figure 2.18 (b)). Under this distance an overestimation of the heat flux can take place. In the so-called slip regime, where $1 < d/\Lambda_a < 100$ (Λ_a is the mean free path of air), significant temperature discontinuity may develop at the air-solid boundaries because intermolecular collisions become less frequent and molecules arriving at the solid surface are unable to come into equilibrium with the surface [48]. In this regime the air conduction coefficient is given in 1D by

$$h_a = \frac{\frac{\lambda_a}{d}}{1 + \frac{2f\Lambda_a}{d}}, \quad (2.13)$$

where λ_a and Λ_a are, respectively, the thermal conductivity and the mean free path of air. $f = \frac{2(2-A_c)\gamma}{A_c(\gamma+1)Pr} = 2$, where A_c is a thermal accommodation coefficient and is equal to 0.9 [48], $\gamma = 1.401$ [49] is the ratio of air heat capacities, and $Pr = 0.713$ [49] is the Prandtl number. In our case the heat flux lines between the tip and the sample are considered to be parallel, which is possible due to the fact that the tip filament radius is much larger than Λ_a . In a 1D approximation the characteristic distance for the change of regime is obtained for $\lambda_a = d h_a$, with $d = 2f\Lambda_a = 4\Lambda_a$. Under ambient condition and at sea level the mean free path of air molecules is equal to 60 nm [48]. Thus the tip is put at 240 nm above the sample in the following sections.

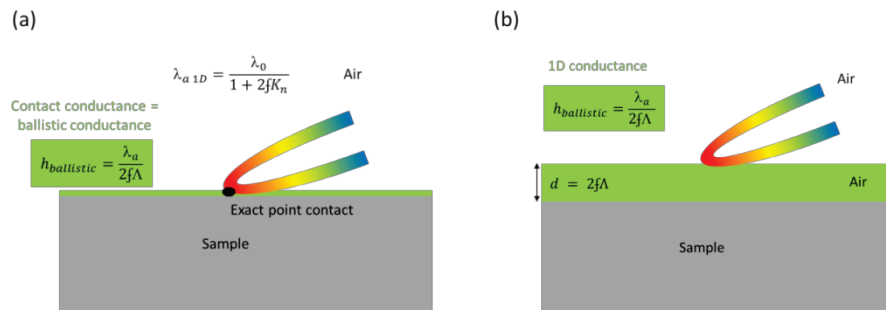


Figure 2.18 Two methods accounting for the tip-sample heat transfer modeling both ballistic and diffusive heat conduction **(a)** The tip-sample contact involves a boundary contact conductance. **(b)** The tip is set at a distance d above the sample. Case **(a)** requires precise local meshing, while case **(b)** requires much less elements while staying accurate.

2.2.3.2.2 Straight tip configuration

The most common case while carrying out SThM experiments is to have a straight tip probing the surface of a sample, which means having an angle of 90° between the tip and the sample. To prove the hypothesis that only accounting for the Pt90/Rh10 part is sufficient to model the Wollaston probe, FEM simulations were executed using a 3D model in the heat transfer module of COMSO. The two geometries ‘Full probe’ and ‘Only Pt90/Rh10 part’ are represented in Figure 2.19. The air surrounding the probe is illustrated by a solid square box of a side $1900 \mu\text{m}$ with a given $\lambda = 0.025 \text{ W}\cdot\text{m}^{-1}\cdot\text{K}^{-1}$. The second solid box depicts the studied sample with $1900 \mu\text{m}$ in large, $1900 \mu\text{m}$ in width and $500 \mu\text{m}$ in thickness, with a given thermal conductivity λ_s . The probes are put at a distance 240 nm above the sample surface. The ends of the silver parts in the first case and the ends of the Pt90/Rh10 in the second case are maintained at 300 K . We reproduced for both cases the exact real geometries with the previous mentioned dimensions. The air and sample boxes boundaries conditions are set at 300 K (room temperature).

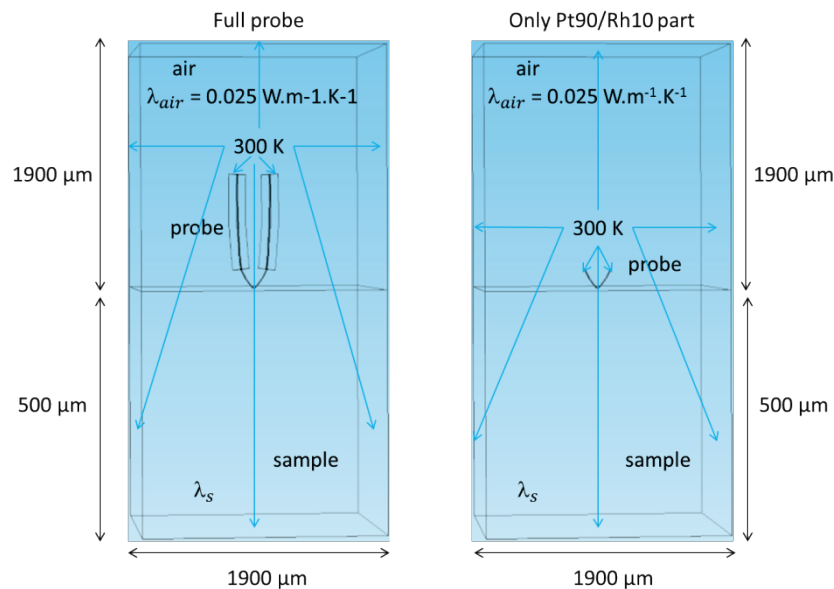


Figure 2.19 Modeled geometries: ‘Full probe’ (on the left) and ‘Only Pt90/Rh10 part’ (on the right).

To perform these simulations, a computer of 32 GB RAM was used. The reliability of the results coming from FEM simulations relies on the choice of the chosen mesh for the modelled geometries. In COMSOL, 3D geometries can be meshed using 4 different types of elements (tetrahedral, bricks, prisms and pyramids). But the user can only refine its drawn geometry when using tetrahedral elements. In our case, the distance between the tip-sample is the place where the heat transfer takes place the most. For this reason a special attention should be given to this zone when meshing the geometry. Figure 2.20 shows the tetrahedral mesh characteristics and the simulation durations for each geometry. Simulations with the ‘Only Pt90/Rh10 part’ model were 2 minutes faster than the ‘Full probe’ model which lasted 17 minutes.

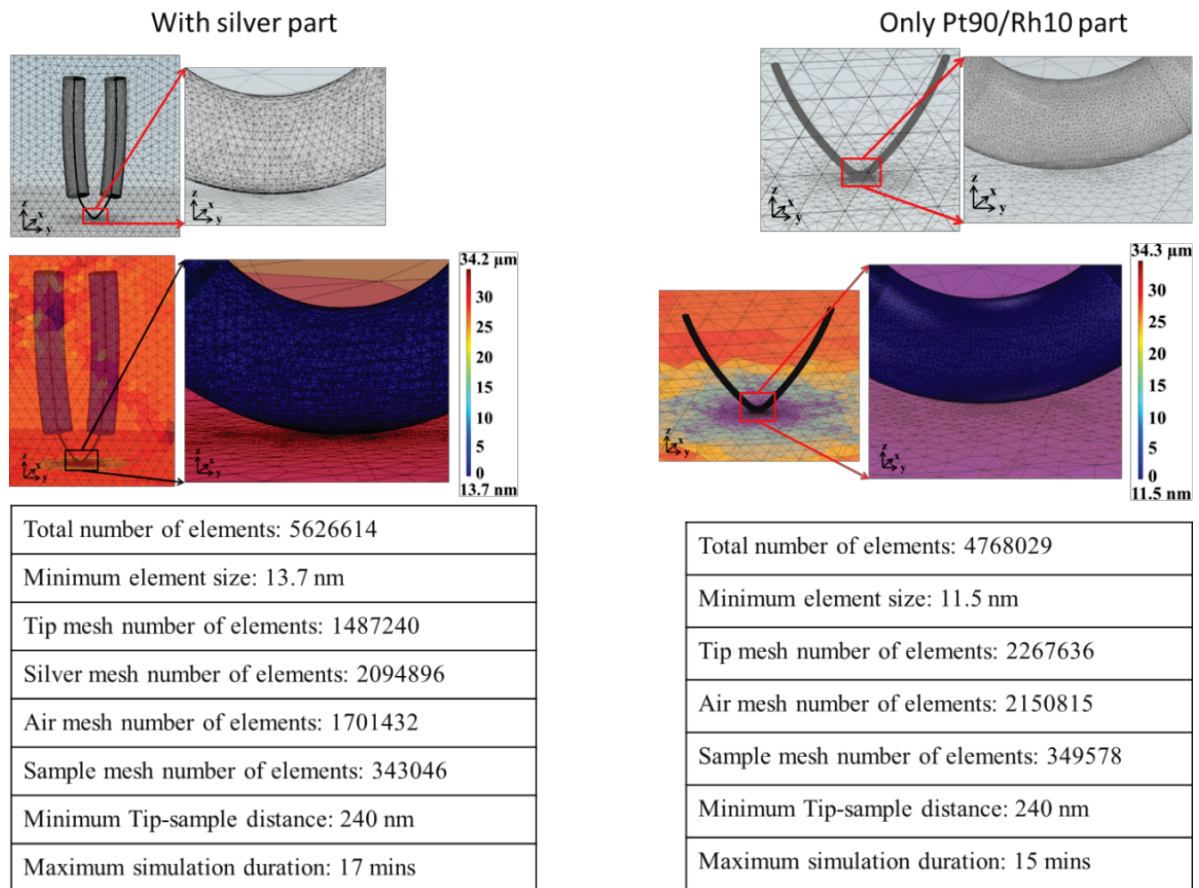


Figure 2.20 Mesh characteristics for: the ‘Full probe’ (on the left) and the ‘Only Pt90/Rh10 part’, (on the right). The colors indicate the mesh elements size distribution.

The results of these simulations shown in Figure 2.21 are based on a sample thermal conductivity $\lambda_s = 0.17 \text{ W.m}^{-1}.\text{K}^{-1}$ (polyimide), low value chosen arbitrarily. The maximum and average increase in the temperature of the tip obtained from simulations are called, respectively, $\theta_{sim\ max}$ and $\theta_{sim\ average}$. Figure 2.21 (a) and (b) show that, in the presence or absence of silver parts, the maximum temperature of the Pt90/Rh10 remains the same, localized at the tip apex in both cases. Figure 2.21 (c) shows the 100 % match between the temperature profile along the Pt90/Rh10 part for both cases and Figure 2.21 (d) shows the perfect match between the conductive heat flux along the Pt90/Rh10 for both geometries. This is in agreement with previous analysis modeling [40]. The central bump in this Figure comes from flux transfer from the tip to the sample through the tip apex.

As in SThM experiments the mean probe temperature is the measured signal, we calculated the mean temperature of the Pt90/Rh10 for both cases and found to be equal to 49.92 K. This value is 85.5 times bigger than the mean temperature of the silver. This confirms the hypothesis of considering only the Pt90/Rh10 part during simulations. The rest of this chapter is based on this model.

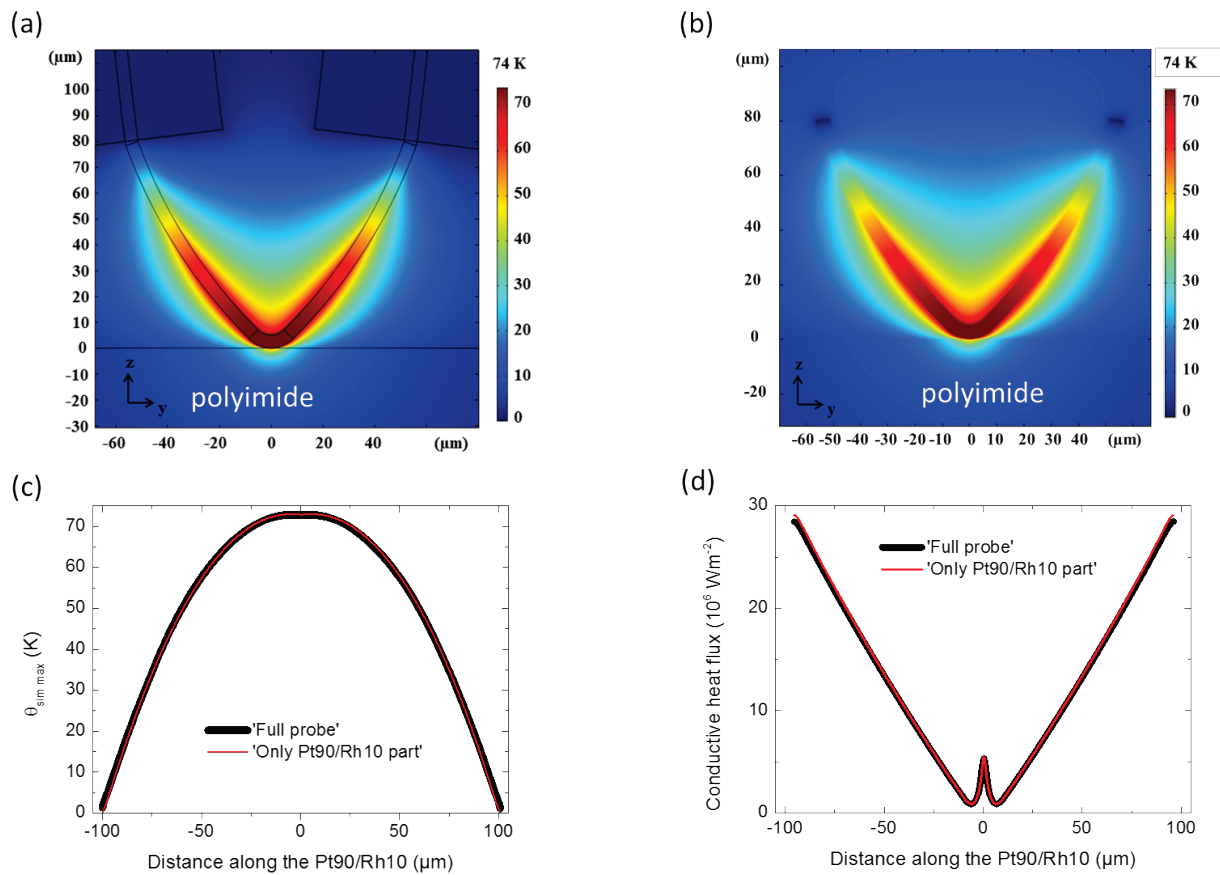


Figure 2.21 Results of simulations executed on a polyimide sample. **(a)** 2D temperature distribution for the ‘Full probe’. **(b)** 2D temperature distribution for ‘Only Pt90/Rh10 part’. **(c)** Temperature profiles matching along the Pt90/Rh10. **(d)** Conductive heat flux matching along the Pt90/Rh10.

Figures 2.22 (a) and (c) show, respectively, 2D temperature and heat flux density distributions on a polyimide sample surface. These distributions have a shape of spiric of Perseus (distorted ellipsis) [40]. Figure 2.22 (b) is a plot of the temperature profiles along a direction perpendicular and parallel to the ‘tip plane’. Figure 2.22 (d) shows a better resolution along the direction perpendicular to the ‘tip plane’, we find $\sim 8.2 \mu\text{m}$ when accounting for 90 % of the heat flux. This means that when having a straight tip, sample probing has to be performed using a perpendicular scan. The largest absolute flux density value calculated for a tip-sample distance of 240 nm is on the order of $3 \times 10^6 \text{ W}\cdot\text{m}^{-2}$.

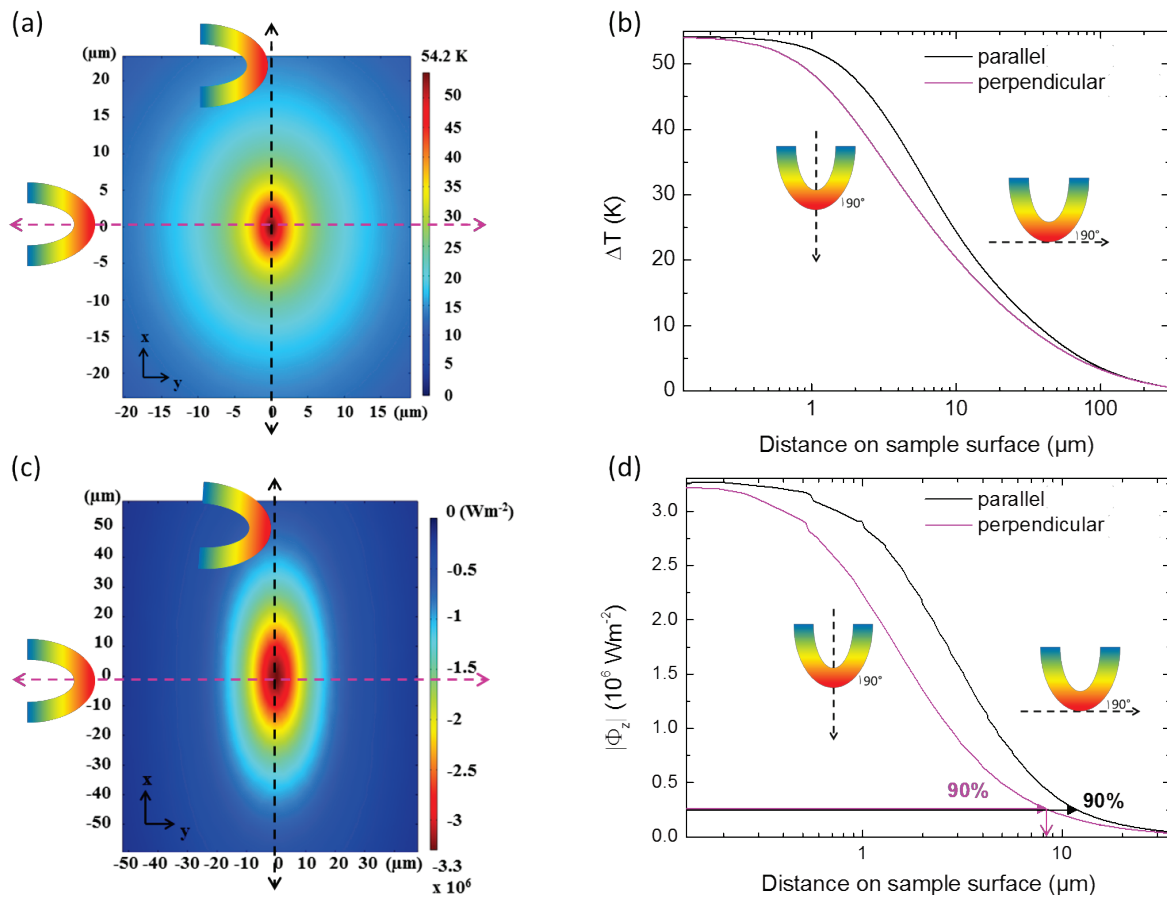


Figure 2.22 Straight tip (a) 2D temperature distribution on a polyimide sample surface. (b) Temperature profiles on the sample surface along a direction perpendicular (purple curve) and parallel (black curve) to the ‘tip plane’. (c) 2D heat flux density in the z direction on a polyimide sample surface. (d) Heat flux profiles on the sample surface along a direction perpendicular (purple curve) and parallel (black curve) to the ‘tip plane’.

2.2.3.2.3 Tilted tip configuration

In our study, the used tip was not a straight configuration; it was bent with an angle of 20° between the tip and the sample (70° from the normal to the sample). We will see later (Section 2.2.4) that this has been confirmed by the thermal data. Figure 2.23 shows a SEM image of the real geometry of the tip.

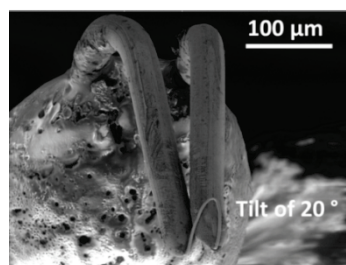


Figure 2.23 Scanning electron microscopy image of the tilted Wollaston probe, angle of tilt 20° with respect to the sample surface.

Consequently in order to respect the real case, we model the system with this angle of 20° . The tip is always set at 240 nm far from the sample. The same mesh method was used for this model and all the characteristics are showed in Figure 2.24. In this geometry the smallest mesh element is smaller than that of the straight geometry. We observe that when the tip is bent it becomes harder to build the mesh: tip and sample surfaces are more parallel, requiring more elements while the 5×10^6 elements are already at the limit of capability of our computer.

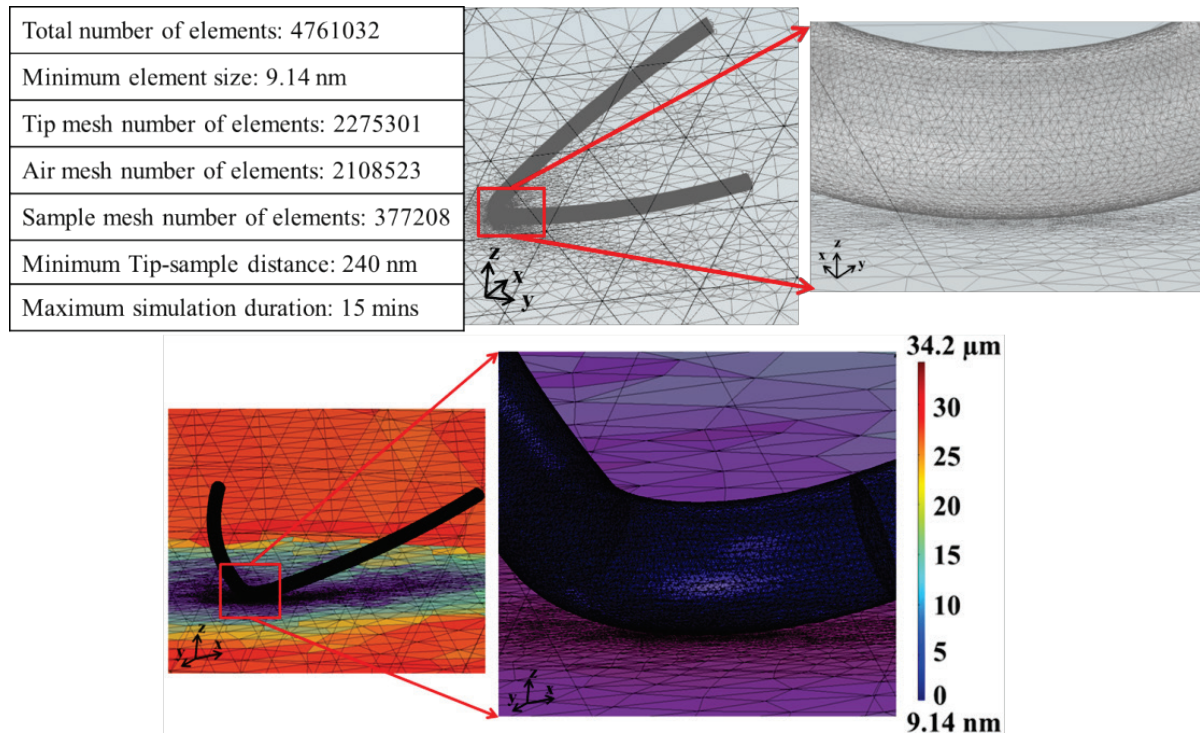


Figure 2.24 Mesh characteristics for the tilted tip configuration. The colors indicate the mesh elements size distribution.

Figure 2.25 (a) shows the temperature distribution for the tilted tip geometry, still for a polyimide sample. The plot in Figure 2.25 (b) shows the difference between the temperature profiles along the Pt90/Rh10 in a straight configuration (red curve) and a tilted one (blue curve). The maximum temperature of the tip apex is lower for the tilted configuration as the tip exchanges more heat with the sample in this configuration, and so a higher decrease in its temperature is obtained. By looking close to $x = 0$, we find that the red curve has a valley, while the blue one has not. This effect is better visible in Figure 2.25 (c) where the heat flux is plotted (the derivative of the temperature profile). In this Figure no bump is seen for $x = 0$ for the case of the tilted tip: the profile is closer to a plateau. For such case the classical analytical models that consider that the tip-sample exchanges are in the middle of the filament cannot be accurate.

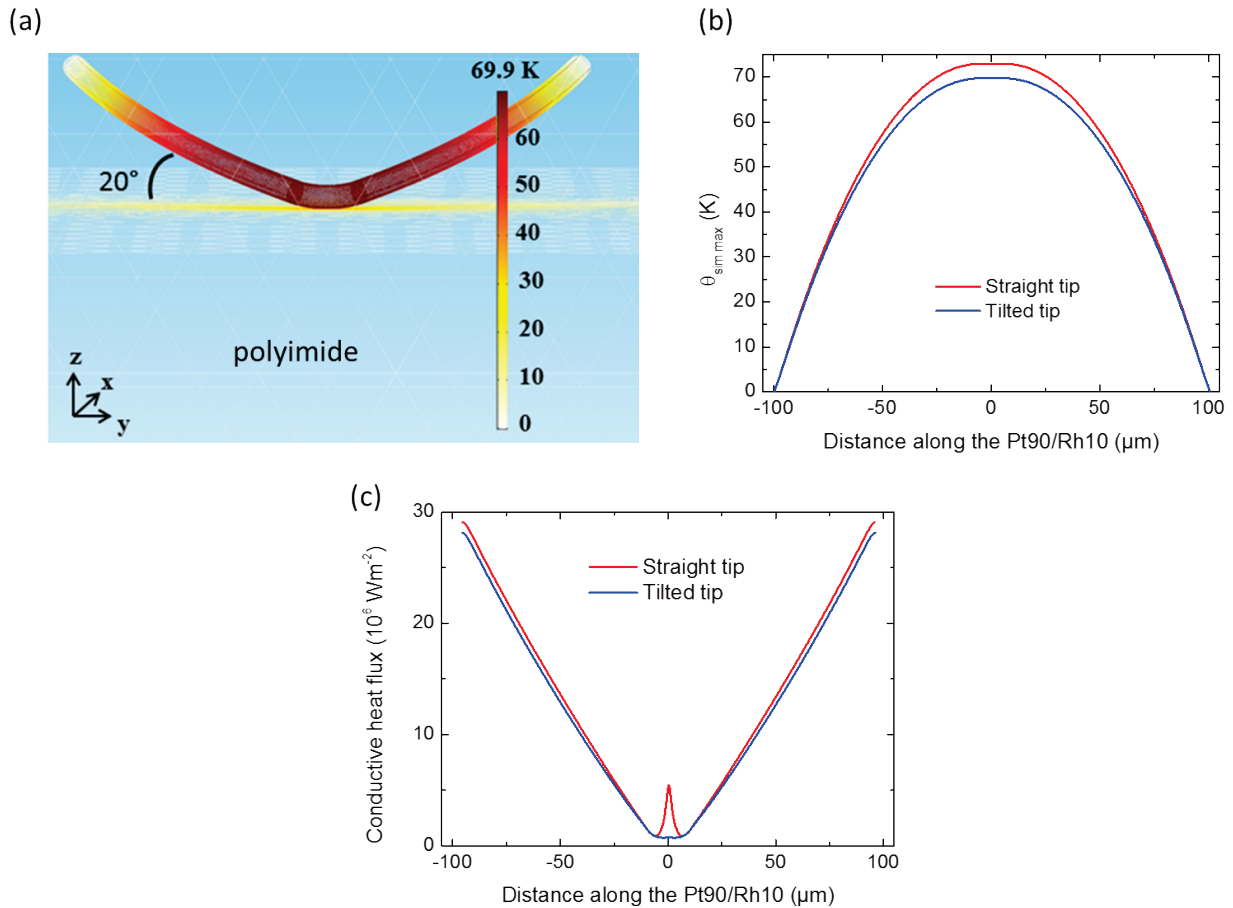


Figure 2.25 Results of simulations performed on a polyimide sample. **(a)** 2D temperature distribution. **(b)** Temperature profiles along the Pt90/Rh10 for a straight (red curve) and a tilted (blue curve) tip. **(c)** Conductive heat flux profiles along the Pt90/Rh10 for a straight (red curve) and a tilted (blue curve) tip.

We now investigate heat flux distributions. Figure 2.26 (a) shows a 2D D-shaped temperature distribution, while Figure 2.26 (c) shows a 2D bow-shaped heat flux density distributions, both calculated for a polyimide sample surface. Figure 2.26 (b) is a plot of the temperature profile along the direction perpendicular to the ‘tip plane’ and along the parallel direction, showing the asymmetry of the thermal exchange. Figure 2.26 (d) shows an asymmetric flux profile in a direction perpendicular to the ‘tip plane’. This asymmetry is depicted in Figures 2.26 (b) and (d) by the vertical dotted lines. These indicate that having a bent tip, it is better to use a parallel scan when studying the heat transfer between the tip and the samples, especially when the latter have geometries different than bulk ones. The largest absolute flux density value is on the order of $3.4 \times 10^6 \text{ W.m}^{-2}$, bigger than that obtained for a straight tip ($3.3 \times 10^6 \text{ W.m}^{-2}$). This means, more flux is exchanged with the sample leading to a better sensitivity to the sample thermal properties.

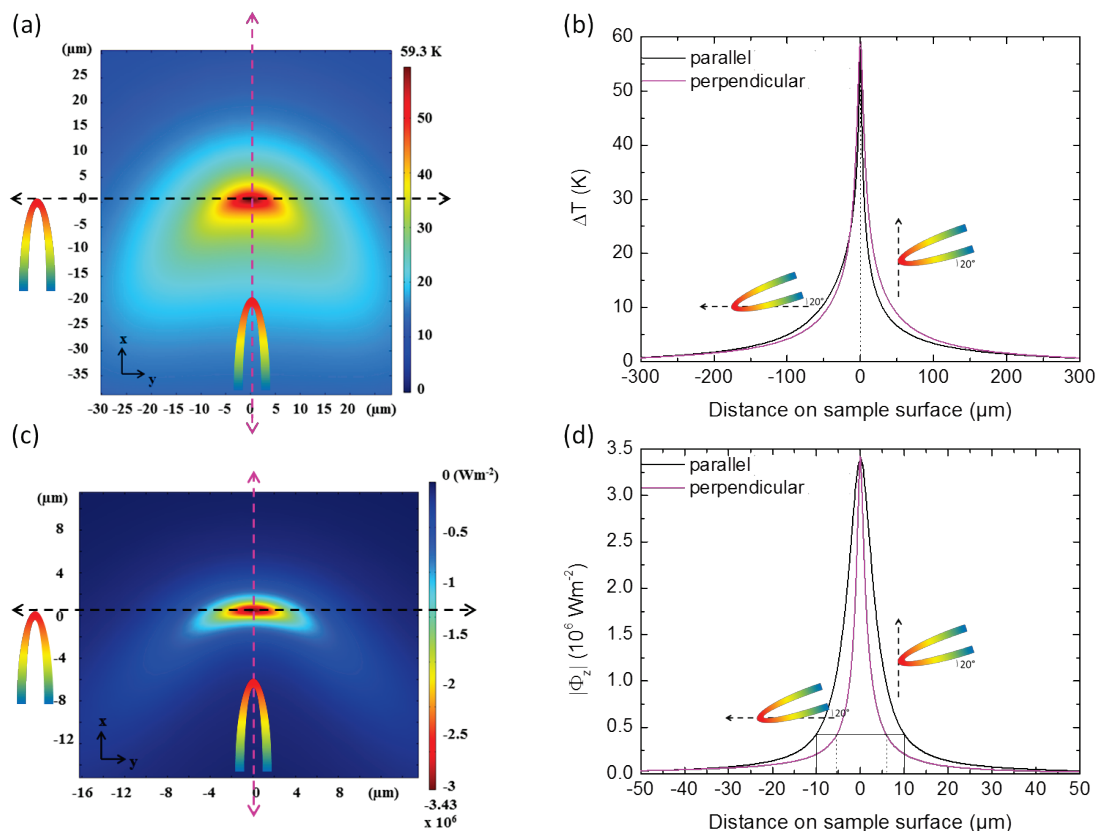


Figure 2.26 Tilted tip of 20° (a) 2D temperature distribution on a polyimide sample surface. (b) Temperature profiles on the sample surface along a direction perpendicular (purple curve) and parallel (black curve) to the 'tip plane'. (c) 2D heat flux density in the z direction on a polyimide sample surface. (d) See (b).

2.2.4 Calibration method using SThM

2.2.4.1 Measurements on bulk samples

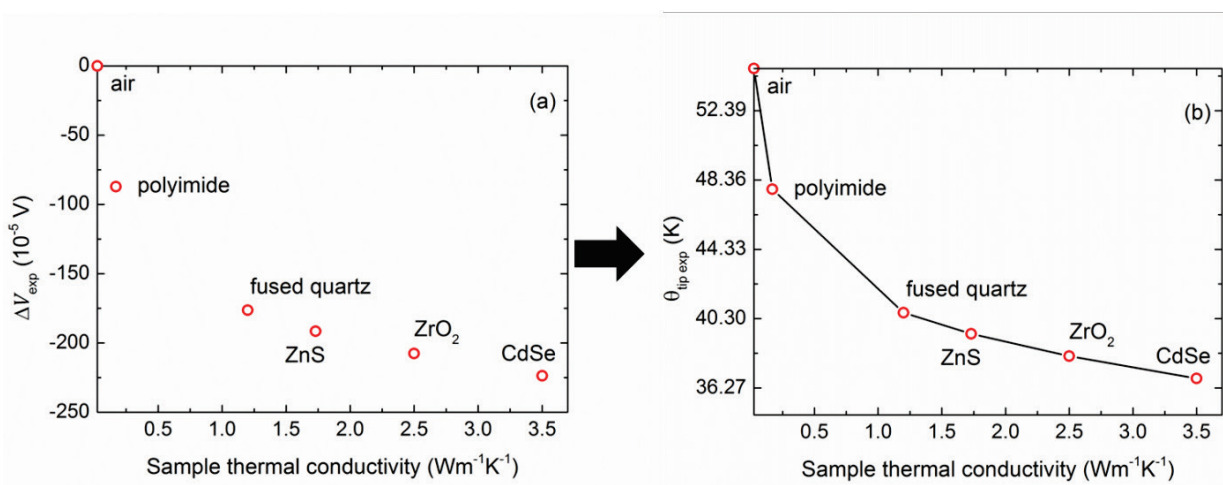


Figure 2.27 Calibration process using the tilted tip. (a) Unbalanced Wheatstone bridge voltage versus calibration samples thermal conductivities. (b) Mean tip temperature after going into contact with calibration samples, obtained based on (a). The black line is drawn to guide the eye. The air datum was added to the graph as a reference.

We then used five different calibration samples of well-known thermal conductivities. Experiments were performed under ambient conditions with the tilted tip. Figure 2.27 (a) shows the result of the calibration carried out using standards. The air datum was added to the curve as a reference when the tip is far away from the sample and the Wheatstone bridge is balanced ($\Delta V = 0$). Figure 2.27 (b) is deduced from equations 2.10 and 2.12, and shows the difference in the mean tip temperature when it is far from contact (at 1 mm) and at the contact (for a given AFM force). Such figure can be used to determine the thermal conductivity of bulk flat samples.

2.2.4.2 Samples with complex geometries

When the geometry becomes complex, understanding the heat transfer at the contact point between the tip and the sample becomes more difficult and requires a delicate tip modeling. In this case, calibration samples alone are not anymore sufficient for thermal conductivity determination. For this reason, two methodologies have been proposed for thermal conductivity determination of complex geometries.

2.2.4.2.1 Out-of-contact method for thermal conductivity determination

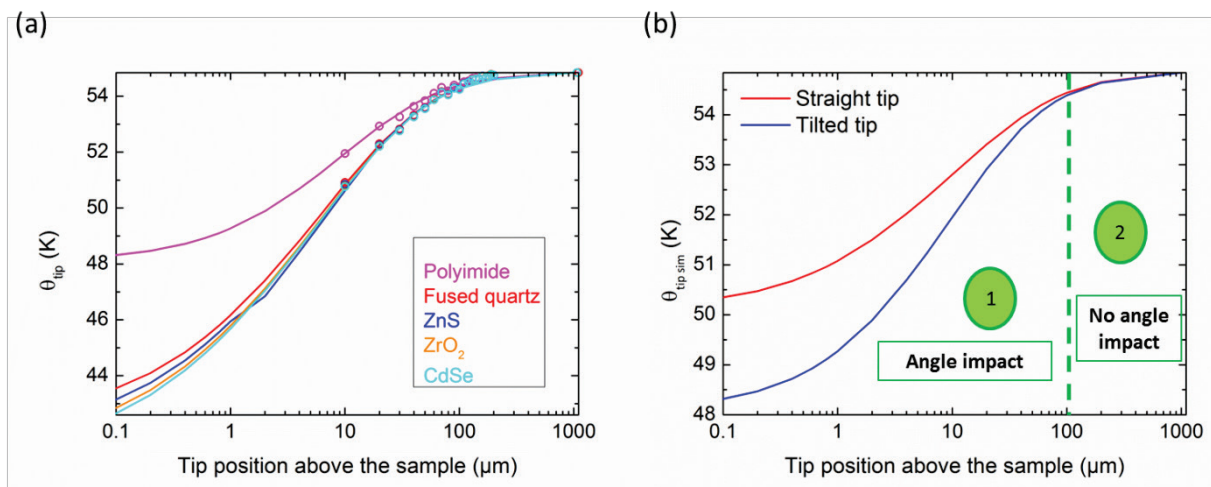


Figure 2.28 Calibration method. **(a)** Tip withdrawal on calibration samples. **(b)** Simulated tip temperature variation as a function of the tip-sample distance on a polyimide sample. Straight (red curve) and 20° tilted (blue curve) tip.

We first detail the ‘tip withdrawal’ method. The tip is set far away from the sample where no heat transfer between the tip and the sample is possible. The Wheatstone bridge is balanced ($\Delta V = 0$). The tip is then brought into contact with the sample, this causes a change in the Wheatstone bridge voltage and so in the tip temperature. The user lifts up the tip constantly aiming at bringing it back to its initial position. For each step ΔV is measured and is converted to $\theta_{tip, exp}$ using equations 2.10 and 2.12. Our SThM actuator allows using 10 μm steps. The results of the Wollaston probe withdrawal are converted into $\theta_{tip, exp}$ on the five calibration

samples and are represented by the open circles in Figure 2.28 (a). We then executed FEM simulations. The results are represented by the solid lines in Figure 2.28 (a). The very good match between the simulations and the experimental data for a distance $\geq 10 \mu\text{m}$ above the sample indicates the validity of this methodology. Unfortunately, with our actuator it was not possible to look at the places where the sensitivity of the technique is at its best. So we believe that this non-contact technique can be used in the future for samples of low thermal conductivities ($\lambda < 3.5 \text{ W}\cdot\text{m}^{-1}\cdot\text{K}^{-1}$). As FEM allows only simulating heat conduction, this result also demonstrates that heat convection does not affect our measurements. The tip-sample heat transfer is only due to heat conduction.

The impact of the tilt on the out-of-contact measurement technique developed here can be evaluated by FEM simulations. They were performed using the straight tip (0° from normal direction) and tilted tip (70° from normal direction) configurations. Figure 2.28 (b) presents the plots of the tip withdrawal on a polyimide sample. Region (1) is where the angle has an important influence on the suggested calibration technique. In region (2) the tip is far enough from the sample and so the tip-sample heat transfer is less subjected to the angle. This figure also shows that our simulations can reproduce the tilt of our tip.

2.2.4.2.2 Splitting the air and contact heat transfers

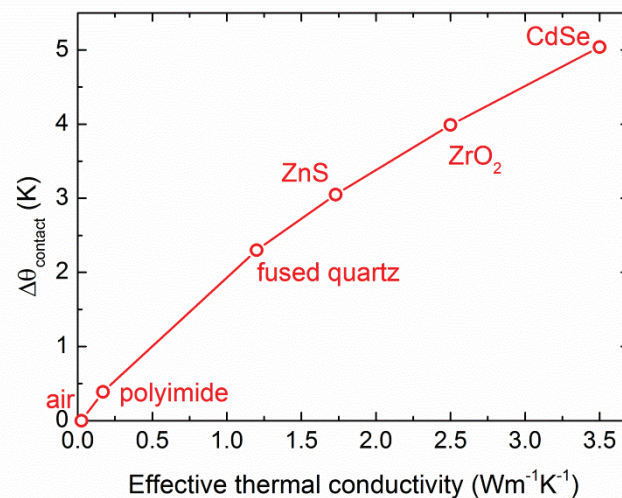


Figure 2.29 $\Delta\theta_{\text{contact}}$ for different experiments and simulations performed on standards. The air datum was added to the graph as reference.

We called the second method ‘Experimental and FEM simulations’. Figure 2.29 shows the difference in the tip temperature at the contact between simulations $\theta_{\text{tip sim}}$ (tip at 240 nm) and experiments $\theta_{\text{tip exp}}$. The differences in temperature resulting from the contact ($\Delta\theta_{\text{contact}} = \theta_{\text{tip sim}} - \theta_{\text{tip exp}}$) with the five standards are plotted in Figure 2.29. This curve is of great importance for the analysis of the data obtained in Chapter 4. Indeed, it splits the contribution of the air, which spreads over microns $\Delta\theta_{\text{air}} = \theta_{\text{oc}} - \theta_{\text{tip sim}}$, from the one due to the contact $\Delta\theta_{\text{contact}}$. As a result, it can allow dealing with complex geometries.

2.3 Brief comparison between the two characterization techniques

The two characterization techniques used in this thesis, micro Raman thermometry and SThM were detailed, respectively, in Sections 2.1 and 2.2. Table 2.1 is a summary of the characteristics of each technique highlighting its best and its limitations. In our study, these two techniques are adapted for probing PSi, irradiated PSi and suspended silicon membranes samples thermal conductivities.

Temperature measurement technique	μ -Raman thermometry	SThM
Specifications		
Type	Non contact ; non destructive	Contact non destructive
Principle	Inelastic light scattering	Electrical resistance
Spatial resolution	Micrometric	May be nanometric at contact, $\sim 8.2 \mu\text{m}$ with air
Limitation	Spot size, laser absorbing and Raman active samples	Bulk samples of thermal conductivities between 0.025 and $20 \text{ W}\cdot\text{m}^{-1}\cdot\text{K}^{-1}$

Table 2.1 Comparison between two characterization techniques: micro-Raman thermometry and SThM.

2.4 Summary

In this chapter, we showed two different thermal characterization techniques: micro-Raman thermometry and scanning thermal microscopy.

In the case of micro-Raman thermometry, we used FEM simulations for thermal conductivity determination. For the same experimental conditions and by applying the model used by Perichon et al. [27] we obtain a thermal conductivity which is 1.72 larger than the real one. We measured experimentally the laser beam radius and found it to be equal to $1.9 \mu\text{m}$ for $\lambda = 532 \text{ nm}$ using an objective x50 with NA 0.5. We showed the effect of the laser spot size on the temperature determination and so on thermal conductivity. Finally, we measured the absorbance for PSi sample with 56 % porosity and found it to be equal to 0.9.

For SThM technique, we modeled the tip configuration by accounting for its real geometry. We found the heat loss coefficient of the Wollaston tip to be equal to $2506 \text{ W}\cdot\text{m}^{-2}\cdot\text{K}^{-1}$. This value is in good agreement with the values obtained previously for the same type of probe. We then studied the effect of the tip position on the heat transfer between a Wollaston tip and a sample. We considered the usual case with a straight tip and our case with a tip with a large tilt angle of 70° from normal direction. We also proposed a technique based on a non-contact method for the determination of the thermal conductivity of materials of low thermal conductivities. In addition, we showed that heat convection does not affect the SThM measurements and that the tip-sample heat transfer is only due to heat conduction. Finally we

found that it is possible to split the contributions to the temperature decrease due to the air and to the contact. These two techniques will be applied in Chapter 3 and Chapter 4.

We ended the chapter by analyzing briefly the main differences between the two characterization techniques. When looking at the limitation of the two techniques, we note that SThM is limited to low thermal conductivity bulk materials like dielectrics for instance (ZrO_2 , quartz), while Raman thermometry, when the laser spot is used as a heater, necessitates absorbing samples in the visible like semiconductors. Consequently, materials where both techniques can be used as complementary tools and compared are rare. We will see in Chapters 3 and 4 that this is the case of nanostructured Si, given its thermal conductivity is strongly reduced below the bulk value ($148 \text{ W}\cdot\text{m}^{-1}\cdot\text{K}^{-1}$).

Bibliography

- [1] T. M. Tritt, M. G. Kanatzidis, H. B. Lyon, and G. D. Mahan, *Thermoelectric materials-new directions and approaches*, vol. 478. 1997.
- [2] D. G. Cahill, "Thermal conductivity measurement from 30 to 750 K: The 3ω method". *Rev. Sci. Instrum.*, vol. 61, no. 2, pp. 802–808, 1990.
- [3] D. G. Cahill and R. O. Pohl, "Thermal conductivity of amorphous solids above the plateau". *Phys. Rev. B*, vol. 35, no. 8, pp. 4067–4073, 1987.
- [4] D. G. Cahill, K. E. Goodson, and A. Majumdar, "Thermometry and Thermal Transport in Micro/Nanoscale Solid-State Devices and Structures". *J. Heat Transfer*, vol. 124, no. 2, p. 223, 2002.
- [5] A. Majumdar, "Scanning Thermal Microscopy". *Europhys. News*, vol. 28, no. 1, pp. 29–29, 1997.
- [6] P. G. Bison, S. Marinetti, A. Mazzoldi, E. Grinzato, and C. Bressan, "Cross-comparison of thermal diffusivity measurements by thermal methods". *Infrared Phys. Technol.*, vol. 43, no. 3–5, pp. 127–132, 2002.
- [7] W. J. Parker, R. J. Jenkins, C. P. Butler, and G. L. Abbott, "Flash method of determining thermal diffusivity, heat capacity, and thermal conductivity". *J. Appl. Phys.*, vol. 32, no. 9, pp. 1679–1684, 1961.
- [8] D. M. Rowe, *Handbook of thermoelectrics*. CRC press, 1995.
- [9] Z. L. Wu, M. Reichling, X. Q. Hu, K. Balasubramanian, and K. H. Guenther, "Absorption and thermal conductivity of oxide thin films measured by photothermal displacement and reflectance methods". *Appl. Opt.*, vol. 32, no. 28, pp. 5660–5665, 1993.
- [10] Z. L. Wu, M. Reichling, H. Groenbeck, Z. X. Fan, D. Schaefer, and E. Matthias, "Photothermal measurement of thermal conductivity of optical coatings". *Proceedings of SPIE-The International Society for Optical Engineering*, vol. 1624, pp. 331–361, 1991.
- [11] J. A. Malen, K. Baheti, T. Tong, Y. Zhao, J. A. Hudgings, and A. Majumdar, "Optical Measurement of Thermal Conductivity Using Fiber Aligned Frequency Domain Thermoreflectance". *J. Heat Transfer*, vol. 133, no. 8, p. 081601, 2011.
- [12] Z. Hua, "Hybrid Photothermal Technique for Microscale Thermal Conductivity Measurement. Thesis". 2013.
- [13] C. B. Saltonstall, J. Serrano, P. M. Norris, P. E. Hopkins, and T. E. Beechem, "Single element Raman thermometry". *Rev. Sci. Instrum.*, vol. 84, no. 6, 2013.
- [14] N. Lundt, S. T. Kelly, T. Rödel, B. Remez, A. M. Schwartzberg, A. Ceballos, C. Baldasseroni, P. A. F. Anastasi, M. Cox, F. Hellman, S. R. Leone, and M. K. Gilles, "High spatial resolution Raman thermometry analysis of TiO₂ microparticles". *Rev. Sci. Instrum.*, vol. 84, no. 10, 2013.
- [15] C. V. Raman, "A new radiation". *Proc. Indian Acad. Sci. - Sect. A*, vol. 37, no. 3, pp. 333–341, 1928.
- [16] G. Viera, S. Huet, and L. Boufendi, "Crystal size and temperature measurements in nanostructured silicon using Raman spectroscopy". *J. Appl. Phys.*, vol. 90, no. 8, pp. 4175–4183, 2001.
- [17] M. Yamada, K. Nambu, Y. Itoh, and K. Yamamoto, "Raman microprobe study on temperature distribution during cw laser heating of silicon on sapphire". *J. Appl. Phys.*, vol. 59, no. 4, pp. 1350–1354, 1986.
- [18] T. Hart, R. Aggarwal, and B. Lax, "Temperature Dependence of Raman Scattering in Silicon". *Phys. Rev. B*, vol. 1, no. 2, pp. 638–642, 1970.
- [19] M. Balkanski, R. Wallis, and E. Haro, "Anharmonic effects in light scattering due to optical phonons in silicon". *Phys. Rev. B*, vol. 28, no. 4, pp. 1928–1934, 1983.
- [20] S. Ghosh, D. L. Nika, E. P. Pokatilov, and A. A. Balandin, "Heat conduction in graphene: Experimental study and theoretical interpretation". *New J. Phys.*, vol. 11, 2009.
- [21] S. Ghosh, I. Calizo, D. Teweldebrhan, E. P. Pokatilov, D. L. Nika, A. A. Balandin, W. Bao, F. Miao, and C. N. Lau, "Extremely high thermal conductivity of graphene: Prospects for thermal management applications in nanoelectronic circuits". *Appl. Phys. Lett.*, vol. 92, no. 15, pp. 15–17, 2008.
- [22] C. Populaire, "Propriétés physiques du silicium poreux : traitements et applications aux microsystèmes". *PhD thesis*, 2005.
- [23] G. Doerk, C. Carraro, and R. Maboudian, "Temperature dependence of Raman spectra for individual silicon nanowires". *Phys. Rev. B*, vol. 80, no. 7, pp. 1–4, 2009.
- [24] K. F. Murphy, B. Piccione, M. B. Zanjani, J. R. Lukes, and D. S. Gianola, "Strain- and defect-mediated thermal conductivity in silicon nanowires". *Nano Lett.*, vol. 14, no. 7, pp. 3785–3792, 2014.
- [25] S. Kouteva-Arguirova, T. Arguirov, D. Wolframm, and J. Reif, "Influence of local heating on micro-Raman spectroscopy of silicon". *J. Appl. Phys.*, vol. 94, no. 8, pp. 4946–4949, 2003.
- [26] A. Nikolenko, "Laser heating effect on Raman spectra of Si nanocrystals embedded into SiO_x matrix". *Semicond. Physics, Quantum Electron. Optoelectron.*, vol. 16, no. 1, pp. 86–90, 2013.

- [27] S. Périchon, V. Lysenko, B. Remaki, D. Barbier, and B. Champagnon, "Measurement of porous silicon thermal conductivity by micro-Raman scattering". *J. Appl. Phys.*, vol. 86, no. 8, p. 4700, 1999.
- [28] M. Nonnenmacher and H. K. Wickramasinghe, "Scanning probe microscopy of thermal conductivity and subsurface properties". *Appl. Phys. Lett.*, vol. 61, no. 2, pp. 168–170, 1992.
- [29] W. P. Mason and R. N. Thurston, *Physical acoustics, principles and methods*. 1988.
- [30] Y. S. Touloukian, R. K. Kirby, R. E. Taylor, and P. D. Desai, *Volume 1 : Thermal conductivity - Metallic elements and alloys*. 1975.
- [31] P. J. Newby, B. Canut, J.-M. Bluet, S. Gomès, M. Isaiev, R. Burbelo, K. Termentzidis, P. Chantrenne, L. G. Fréchette, and V. Lysenko, "Amorphization and reduction of thermal conductivity in porous silicon by irradiation with swift heavy ions". *J. Appl. Phys.*, vol. 114, no. 1, p. 014903, 2013.
- [32] M. A. C. de Araújo, R. Silva, E. de Lima, D. P. Pereira, and P. C. de Oliveira, "Measurement of Gaussian laser beam radius using the knife-edge technique: improvement on data analysis". *Applied optics*, vol. 48, no. 2, pp. 393–396, 2009.
- [33] J. M. Khosrofiyan and B. A. Garetz, "Measurement of a Gaussian laser beam diameter through the direct inversion of knife-edge data". *Appl. Opt.*, vol. 22, no. 21, p. 3406, 1983.
- [34] J. a Arnaud, W. M. Hubbard, G. D. Mandeville, B. de la Clavière, E. A. Franke, and J. M. Franke, "Technique for Fast Measurement of Gaussian Laser Beam Parameters". *Appl. Opt.*, vol. 10, no. 12, p. 2775, 1971.
- [35] J. A. Jacquez and H. F. Kuppenheim, "Theory of the Integrating Sphere". *J. Opt. Soc. Am.*, vol. 45, no. 6, pp. 460–470, 1955.
- [36] J. C. de Mello, H. F. Wittmann, and R. H. Friend, "An Improved Experimental Determination of External Photoluminescence Quantum Efficiency". *Adv. Mater.*, vol. 9, no. 3, p. 230, 1997.
- [37] B. Gotsmann, M. A. Lantz, A. Knoll, and U. Dürig, *Nanoscale Thermal and Mechanical Interactions Studies using Heatable Probes*, vol. 6. 2009.
- [38] G. B. M. Fiege, A. Altes, R. Heiderhoff, and L. J. Balk, "Quantitative thermal conductivity measurements with nanometre resolution". *J. Phys. D. Appl. Phys.*, vol. 32, no. 5, pp. L13–L17, 1999.
- [39] S. Gomès, "La microscopie thermique à sonde locale". *PhD thesis*.
- [40] S. Lefevre, "Modélisation et élaboration des métrologies de microscopie thermique à sonde locale résistive". *PhD thesis* 1994.
- [41] P-O. Chapuis, "Contribution à l'étude des transferts thermiques à l'échelle nanométrique : interaction pointe-surface". *PhD thesis*, 2007.
- [42] L. David, "Développement de la microscopie thermique à sonde locale pour la détermination de la conductivité thermique de films minces Application aux céramiques pour le nucléaire". *PhD thesis*, 2006.
- [43] A. Assy, "Development of two techniques for thermal characterization of materials: Scanning Thermal Microscopy (SThM) and 2ω method". *PhD thesis*, 2015.
- [44] Dinwiddie, *Thermal conductivity contrast imaging with a scanning thermal microscope*. New York, 1995.
- [45] Z.-Y. Guo and Z.-X. Li, "Size effect on single-phase channel flow and heat transfer at microscale". *Int. J. Heat Fluid Flow*, vol. 24, no. 3, pp. 284–298, 2003.
- [46] X. J. Hu, A. Jain, and K. E. Goodson, "Investigation of the natural convection boundary condition in microfabricated structures". *Int. J. Therm. Sci.*, vol. 47, no. 7, pp. 820–824, 2008.
- [47] L. Thiery, E. Gavignet, and B. Cretin, "Two omega method for active thermocouple microscopy". *Rev. Sci. Instrum.*, vol. 80, no. 3, pp. 1–8, 2009.
- [48] L. Shi and A. Majumdar, "Thermal transport mechanisms at nanoscale point contacts". *J. Heat Transf. Asme*, vol. 124, no. 2, pp. 329–337, 2002.
- [49] "The engineering toolbox. <http://www.engineeringtoolbox.com>".

Chapter 3. Thermal conductivity of porous silicon irradiated by swift heavy ions

3.1 Context and goal of the study

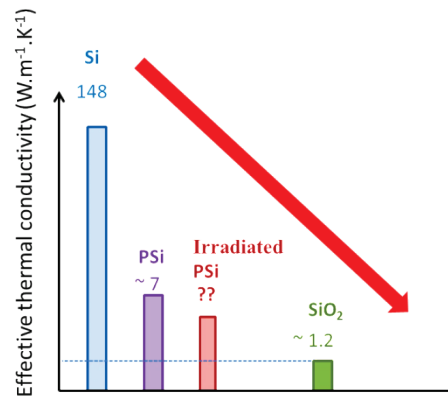


Figure 3.1 Si effective thermal conductivity.

Many phenomena can be related to an irradiation process in semiconductors while bombarding them with charged particles. Irradiation effects resulting from particle-material interactions can induce sample damaging. Sample irradiation affects considerably the microstructure and leads to a change in the morphology and in the physical properties of the studied material. This can lead to structural stiffening or embrittlement, and to a decrease in the thermal conductivity. A good understanding of these phenomena is crucial for a good conception of novel materials, in particular for stable operation for MEMS (Micro-Electro-Mechanical Systems) applications.

Porous silicon (PSi) was the candidate for this study. Thick PSi layer with high porosity can have a low thermal conductivity, two orders of magnitude lower than that of bulk silicon [1][2][3]. The thermal conductivity has been shown to decrease cubically with the porosity [4]. The relation between the PSi hardness and its porosity (P) was shown by [5] to be $(1-P)^{2/3}$ (valid for porosities up to 75 %) and it diminishes rapidly for higher porosities [6]. A trade-off between the materials' thermal conductivity and strength can then be found for MEMS applications.

It has been shown that a greater decrease in PSi thermal conductivity can be obtained by amorphising its crystalline phase [7][8]. Through irradiation how does Si thermal conductivity evolve (see Figure 3.1)? Irradiation induces at least two different types of effects that influence porous silicon thermal conductivity. They two can be classified as:

- Electronic interactions
- Nuclear interactions

Swift heavy ions are considered in this study. Our goal is to observe the evolution of PSi thermal conductivity using micro-Raman thermometry and scanning thermal microscopy after amorphising the crystalline phase and keeping the structure intact (no sample breaking or densification). To do so, our PSi (56 % porosity) samples were irradiated with swift heavy ions (^{129}Xe) at two different energies and five different fluences (eleven samples to be studied in total).

In this chapter, we present first the general goal of the study. Then we give a description of charged particle-matter interactions inducing structural damage. The manufacturing process of the studied samples will be discussed, followed by the sample structural characterization. Finally, thermal conductivity evolution resulting from sample damaging will be discussed in details.

3.1.1 Swift heavy ions irradiation

During material irradiation with charged particles, the latter release gradually their energy to the medium they go through, according to different processes. Among these processes, we mention particles that interact:

- elastically with the nuclei in the target. This regime is called "nuclear collisions";
- inelastically with the electrons in the target. This regime is called "electronic interactions".

At the beginning of the slow-down process of heavy projectiles in a solid, charged particles are slowed down mainly by the electronic stopping, due to inelastic interaction with the electrons of the target. Before getting to the end of their path, nuclear stopping, due to elastic interaction with the nuclei of the target, becomes more and more probable, finally dominating the slow-down process. The loss of energy E per unit path length is called the stopping power and is given by:

$$S(E) = -\frac{dE}{dx}. \quad (3.1)$$

The $-$ sign makes S positive. The total loss in energy per unit length due to the contribution of both electronic and nuclear stopping powers can be written as:

$$\left(\frac{dE}{dx}\right)_{total} = \left(\frac{dE}{dx}\right)_{electronic} + \left(\frac{dE}{dx}\right)_{nuclear}. \quad (3.2)$$

The slow-down process of charged particles depends mainly on the thickness of the target and on the projectile mass and energy. So it is important to know at which distance the stopping power becomes zero, i.e. when the ion implantation takes place. This distance is known as the "projected range" R_p .

Damage due to nuclear collisions

This process takes place especially when using projectiles of energies lower than 10 KeV per nucleon. During nuclear collisions, energy transfer from projectiles to nuclei of the targeted atoms is direct. This means that the atoms of the irradiated medium collect significant energies; they will be ejected from their initial lattice position, creating atom displacements (see Figure 3.2). This results in a cascade of collisions between atoms and incident particles. Knowing the repulsive potential between atoms, it is possible to calculate the nuclear stopping power.

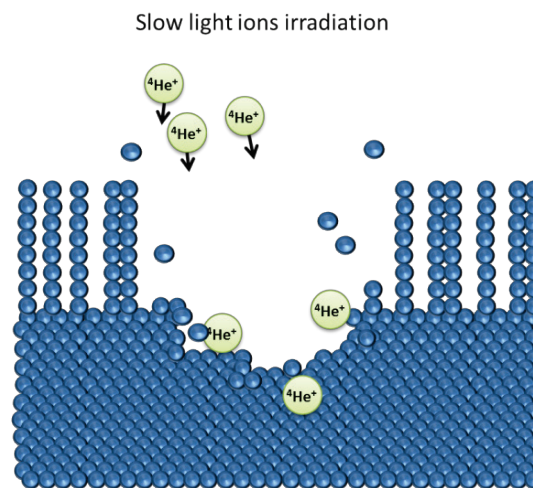


Figure 3.2 Schematic showing the structural destruction of PSi sample due to its irradiation with slow light ions ($^4\text{He}^+$) in the nuclear regime.

Damage due to electronic interactions

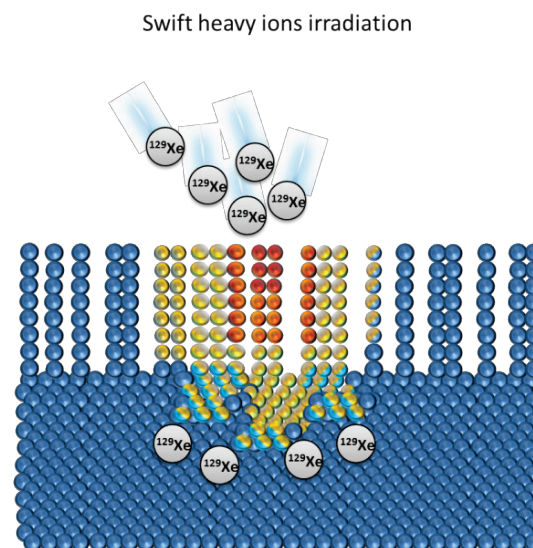


Figure 3.3 Schematic showing the irradiation of a PSi sample with swift heavy ions (^{129}Xe) in the electronic regime with a structural conservation.

This process takes place especially when using projectiles of energies higher than 10 KeV per nucleon; it is the case of the ions used in our study. If the heavy ions have sufficient energy, they can penetrate the target on a straight line. After interacting with the electrons of the target, they release their energy as heat, to then induce latent heat along their path [9][10]. This is explained by the *thermal spike model* proposed by Dessauer in 1923 [11]. It was adapted later in 1992 for heavy ions by Toulemonde [12]. For intense electronic excitations and a strong electron-phonon coupling, a cylindrical zone is created along the ions path (see Figure 3.3). 100 ps later, this region is going to cool back down and gets back to room temperature with a phase that differs from the initial one. The damaged path (amorphous) of the path is called ion tracks [13].

3.2 Samples manufacturing and structural characterization

Here we provide a description of the manufacturing process for obtaining irradiated porous silicon (IPSi) followed by a detailed study on samples' structural characterization.

3.2.1 Preparation of porous silicon samples

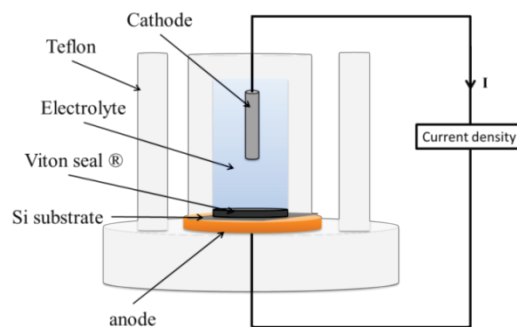


Figure 3.4 Schematic of a cross-section view of anodization cell.

Porous silicon is obtained by electrochemical means. The silicon dissolution process in hydrofluoric acid remains subject to discussion. The mostly known model that is used to describe the mechanism of p-type silicon dissolution is given by Lehmann and Gösele and represented by the following chemical reaction [14]:



A doped silicon substrate (holes), hydrofluoric acid and a current density are required for the obtaining of porous silicon.

Silicon porosification is done into an anodization cell made of Teflon (inert to HF). A schematic representation of the used cell is presented in Figure 3.4. The well-polished back side of the Si substrate assures a good ohmic contact with the copper plate and is used as anode. This contact controls the current flux lines and so the homogeneity of the porous layer. The cathode is made of platinum and immersed into the electrolyte. The Si substrate is placed

between a Viton seal ® and a copper plate, defining the area to be porisified. Mesoporous Si has a sponge-like structure (see Figure 3.5) [15][16].

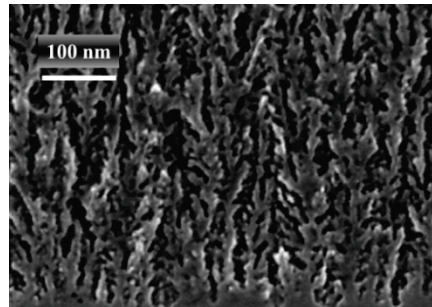


Figure 3.5 Cross-section SEM image of mesoporous silicon showing its sponge-like structure.

Pure silicon is hydrophobic, so when etched with pure hydrofluoric acid, non-uniform porous layers can be formed. Usually the electrolyte is a mix of hydrofluoric acid and ethanol, to improve surface wettability and ensure uniform porous layers. In addition to that, ethanol helps in hydrogen desorption [17][18]. Other surfactants can also be used to enhance surface wettability [19], for instance acetic acid and Mirasol but ethanol remains the most common used solution.

When preparing thick porous layers, the deeper we scratch into the silicon substrate the poorer the F^- concentration. This affects the porous layers uniformity in depth. To avoid this kind of problems, a pulsed current can be used, allowing the regeneration of the electrolyte and so obtaining uniform layers [20][21][22].

Sample doping (resistivity) [23], current density (electropolishing effects at very high current densities) [24] and lattice orientation (porous layer morphology) [25] can play a crucial role in the determination of the pore diameters and the structure of silicon crystalline parts.

Porous silicon manufacturing process details

Porous silicon layers were formed by electrochemical etching of 500 μm thick $\langle 100 \rangle$ monocrystalline boron-doped p^+ silicon wafers. Boron doping level is about 10^{19} cm^{-3} , which corresponds to a resistivity of $0.01 - 0.02 \Omega \cdot \text{cm}^{-1}$ (this parameter was fixed and is not subject to a particular investigation). The electrolyte consists of 48 wt% HF and pure ethanol in a volume ratio of 1:1. The choice of a p^+ type wafer was based on the goal of obtaining mesoporous silicon, with crystallites diameter average size lower than 20 nm. In our case, the average crystallite diameter was found to be 11 nm, based on the full width at half maximum (FWHM) of the Stokes Raman peak of the non-irradiated PSi sample [26]. More information on crystallite size measurements can be found in [27][28]. This kind of porous silicon is known to have, in general, a low thermal conductivity with good mechanical properties, making it a good candidate for our study.

HF concentration was maintained constant during the etching process by using a pulsed current. Switching the current was achieved through a pulsed current generator. A current density (J) of $150 \text{ mA} \cdot \text{cm}^{-2}$ during one second followed by zero current density during ten seconds was used after optimization. Optimal rest time (zero current density) was found to be

10 times the etching time [20]. The total etching time is seven hundred and ninety two seconds for the obtaining of a 10 μm thick PSi layer. The latter has a mesoporous structure (see Figure 3.6) and a porosity of 56 % as shown in the following. The layer thickness and porosity were obtained based on SEM images and microreflectivity, respectively.

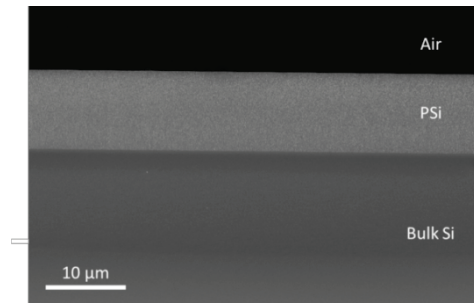


Figure 3.6 Cross section SEM image showing the 10 μm thick PSi layer.

Protocol for porous silicon preparation

One double-side polished 8 inch silicon wafer was used for this study. The sample preparation is now detailed.

Cleaning before anodization:

- Acetone solution for 5 mins.
- Ethanol solution for 5 mins in an ultrasonic cleaner.
- BOE (Buffered Oxide Etch) solution for 2 mins for native oxide elimination.
- Deionized water for 5 mins.
- Nitrogen gas dryer.

The silicon wafer is placed on the copper plate. The current is applied as mentioned before giving rise to a porous silicon layer area $S = \pi r^2$ with $r = 5$ cm.

Rinsing after anodization:

- Ethanol solution for 5 mins.
- N_2 gas dryer with precaution use.
- Sample cut using tweezers and a diamond cut pen.

Ten cut small porous silicon samples (surface of 1 cm^2), taken from the center of the obtained porous area, were selected for the next manufacturing steps. We chose the center of the obtained porous area because of the variation of the silicon resistivity going from its center to its edges. This variation can cause non-homogeneity in depth porosity due to non-homogeneous current flux lines.

3.2.2 Samples irradiation by ^{129}Xe

Here, a brief description of the experimental setup is given. We then discuss the necessary parameters to define an irradiation experiment, i.e. temperature, fluence and energy of the projectile.

GANIL cyclotron (heavy ions)

Classical cyclotrons are circular accelerators, where particles placed in a magnetic field follow a spiral trajectory and are accelerated by means of an electric field of energy that can be adjusted between few MeV up to few hundreds MeV. Sample irradiation was carried out by Dr. Bruno Canut at GANIL (Grand Accélérateur National d'Ions Lourds) cyclotron, in Caen (France). This accelerator allows obtaining different ion masses and energies ranging from carbon (lightest mass) to uranium (heaviest mass). In order to irradiate homogeneously a given surface, the ion beam was focused and scanned horizontally and vertically, by means of quadripole.

Our ten samples were fixed on a sample carrier using silver paste. One half of each PSi was protected from irradiation and the other half was irradiated by a single species ^{129}Xe ion (heavy ions) beam at two different energies (29 and 91 MeV) and at five different ion fluences (10^{12} , 3×10^{12} , 6×10^{12} , 10^{13} and $3 \times 10^{13} \text{ cm}^{-2}$) (see Table 3.1). Irradiation time varies between one hour (for the lowest fluence) and nine hours (for the highest fluence). It is reminded that the fluence is defined as the number of incident ions per unit area received by the exposed material.

^{129}Xe	Energy	
	$E_1 = 91 \text{ MeV}$	$E_2 = 29 \text{ MeV}$
Fluence (cm^{-2})		
10^{12}	A	F
3×10^{12}	B	G
6×10^{12}	C	H
10^{13}	D	I
3×10^{13}	E	J

Table 3.1 Summary of the experimental characteristics of the irradiation.

Damaged porous layer thickness

As seen in Section 3.1.2, the loss of energy results in a slowing down of the projectile; consequently the path of the projectile is finite (R_p). It stops after losing its whole kinetic energy due to interactions with the target. The understanding of this energy loss is crucial for a better understanding of the slow-down process and the target damage characteristics.

SRIM (Stopping and Range of Ions in Matter) software [29], based on a Monte-Carlo method, was used to calculate the electronic and nuclear interactions in porous silicon for ^{129}Xe at the two different energies. Calculations are based on ion mass and energy (E_1 and E_2) and target mass density. As the target is considered as amorphous, channeling effects were neglected in

these calculations. SRIM allows us to plot the electronic stopping power (S_e) and the nuclear stopping power (S_n) for ^{129}Xe interacting with bulk Si (see Figure 3.7). This plot shows the predominance of each regime depending on the ion energy. In this case, the mass density of our PSi samples should be taken identical as that of bulk silicon, because S_e and S_n represent the energy locally released, thus the energy exchanged with the crystallites (silicon).

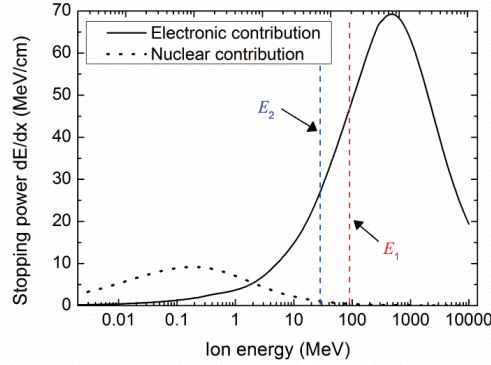


Figure 3.7 Stopping power vs ion energy for ^{129}Xe in bulk silicon calculated using SRIM. Electronic interactions are dominant for the two used energies.

For R_p calculations, the mass density of bulk silicon was replaced by the effective mass density of our 56 % PSi:

$$\rho_{PSi} = (1 - P)\rho_{Si}, \quad (3.4)$$

where ρ is the density and P is the porosity. In this case, the distance range for an ion travelling through the material depends on its surrounding, and so on holes and silicon together. Table 3.2 summarizes the S_e , S_n and R_p data for the two irradiation energies. It shows the dominance of the electronic regime over the nuclear one. Electronic stopping power is about 121 (28) times larger than the nuclear stopping power for the energy 91 MeV (29 MeV). Nuclear interactions become important around the maximum target depth just before ion implantation (ion at rest after losing its whole energy). As already mentioned, the porous layer is 10 μm thick, smaller than the calculated R_p . So we consider a dominance of the slow-down processes over the elastic ones in the whole PSi layer. The atomic displacements via collisional effects can be considered as negligible in our study of the PSi layer.

Summarizing, we showed that the electronic interaction regime is dominant for the irradiations performed at both energies E_1 and E_2 , where amorphisation of the porous structure may occur without any cascade effects that could result from nuclear interactions.

Energy	$E_1 = 91 \text{ MeV}$	$E_2 = 29 \text{ MeV}$
R_p (μm)	30.8	15.7
S_e (keV/nm)	10.9	6.5
S_n (keV/nm)	0.09	0.23

Table 3.2 Main features of ^{129}Xe irradiation in Si, for S_e and S_n calculation, and in PSi at 56 % porosity, for R_p calculations.

3.2.3 Determination of porosity by microreflectivity

The porosity of the obtained porous layer should be determined. To do so, we used the microreflectivity technique. The incident light (fiber optic source) gives rise to constructive or destructive interferences between the reflected beam on the air/PSi interface and the one at the PSi/bulk Si interface. These interferences can be observed as long as the layer thickness (e) is larger than the reflected wavelength (see Figure 3.8 (a)).

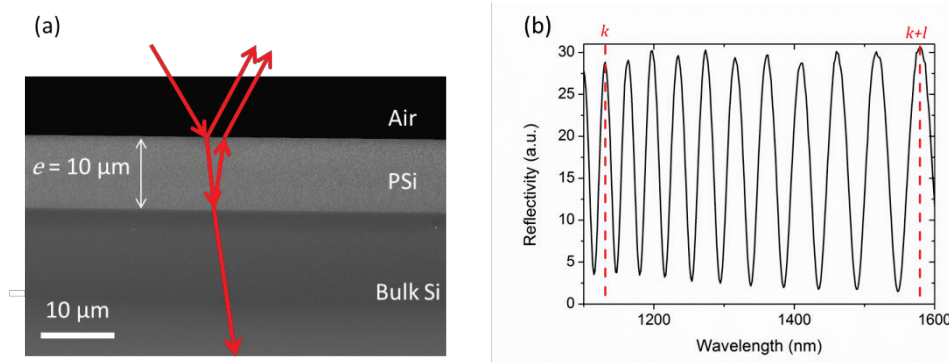


Figure 3.8 (a) Schematic based on a cross section SEM image showing incident light interferences at the interfaces between air/PSi/bulk Si. **(b)** Interferences fringes on a 10 μm thick non-irradiated 56 % PSi layer.

The refractive index of PSi n_{PSi} is calculated as follows:

$$n_{PSi} = \frac{((k + l) - k)}{2e} \left(\frac{1}{\lambda_k} - \frac{1}{\lambda_{k+l}} \right)^{-1} \quad (3.5)$$

The optical path of the two reflected beams in the porous layer is given by $2d = 2ne$ (e is obtained by means of cross section SEM images). If we have maximum reflectivity for a given wavelength λ_k , we can write $k\lambda_k = 2d$, where k is an integer. It is recommended to choose at least 10 fringes in a small range of wavelengths (keeping n constant). 11 fringes between the two maxima k and $k + l$ were chosen in our case (Figure 3.8 (b)). We find $n_{PSi} = 1.97$.

The average porosity can then be estimated using the model of the effective medium given by Bruggeman or Looyenga – Landau – Lifshitz (LLL) [30][31]:

$$P = \frac{n_{PSi}^{2/3} - n_{Bulk Si}^{2/3}}{n_{air} - n_{Bulk Si}^{2/3}}, \quad (3.6)$$

where n_{air} and $n_{Bulk Si}$ are respectively the air and the monocrystalline silicon refractive indices. The LLL model was adapted to be more suitable for high porosities, while for low porosities, as it is the case here, both models converge in a similar way. The deduced porosity is $P = 56\%$.

The same analysis was performed after irradiation in order to examine any change in the PSi initial porosity. Figure 3.9 shows the interferences on sample E. The deduced porosity was the same as the initial one: $P = 56\%$.

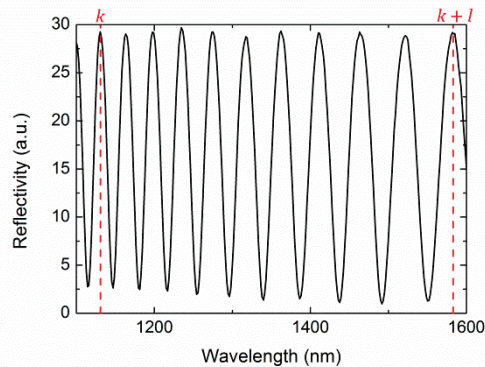


Figure 3.9 Interferences fringes on a 10 μm thick PSi with 56 % porosity irradiated with ^{129}Xe at 91 MeV at $3 \times 10^{13} \text{ cm}^{-2}$.

The very good agreement between the obtained porosity results confirms that sample irradiation does not induce any change in the sample porosity. We note that this technique provides an average sample porosity. Inaccuracies can be introduced by the experimental setup, the reading of the maxima of the fringe positions and by the assumption that the refractive index is constant over the chosen wavelength range. The uncertainty in our case is less than 1 %.

3.2.4 Scanning electron microscopy analysis

We now present a structural analysis of the porous layer in order to evaluate electronic interaction effects on this material. The electronic stopping affects the atoms when the deposited ion energy surpasses a threshold energy E_{th} . While the interaction mechanisms remain not well understood in crystalline silicon (cSi), Zinkle and Kinoshita found theoretically $E_{\text{th cSi}} = 35 \text{ eV}$ [32]. cSi structure is well known to be intact after electronic interactions resulting from irradiation with swift heavy ions [33][34]. Up to the present day, the only way to amorphise cSi in the electronic regime was achieved experimentally using a cluster of C_{60} [35]. Previous studies about porous silicon amorphisation in the nuclear regime realized with $^4\text{He}^+$ resulted in a structural destruction, caused by the porous layer densification rendering it less or non-porous [36].

We used SEM to study the irradiation effect, as it allows us to look at the structure down to the nanometric scale. Figure 3.10 shows the eleven investigated samples, starting from the non-irradiated 56 % PSi and ending with the ones irradiated at the highest fluence, at E_1 (E) and E_2 (J). All the images were taken at the same magnification while focusing the electron beam in the middle of the sample. Three different images were taken for each sample: close to the surface, in the middle and at the bottom of the porous layer. No destruction of the structure was observed for the ten studied irradiated samples. This confirms the avoidance of

sample cracks and that the structural change is due to electronic interactions. We can also observe the change in the silicon crystallite ramifications. For a given energy, the latter are turning into beads with increasing irradiation fluence. For samples E and J (irradiated at the highest fluence), the small dendrites disappear while keeping the sponge-like structure of a porous layer.

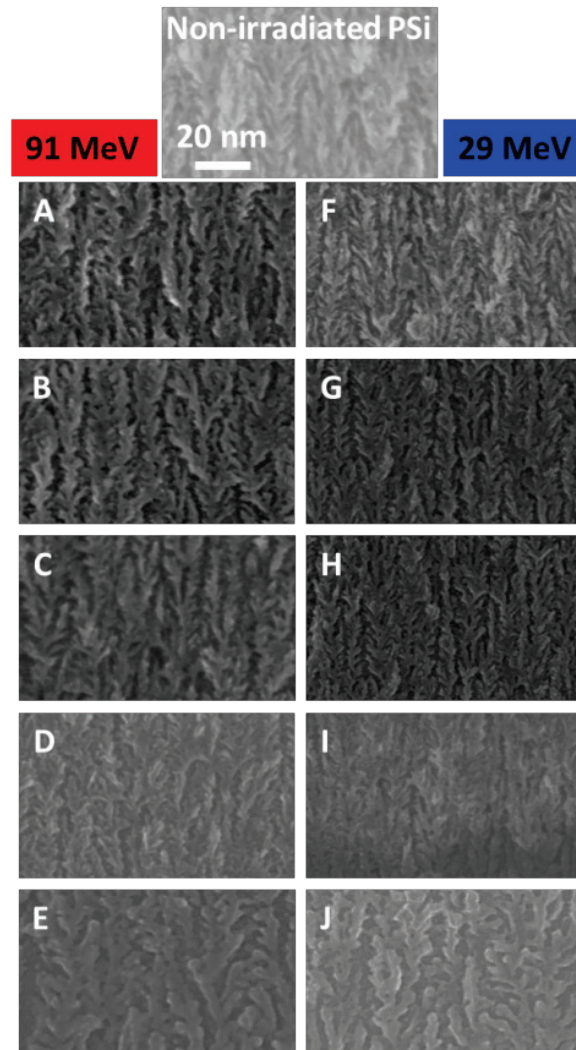


Figure 3.10 Cross-section SEM images of the 56 % PSi samples irradiated at two different energies and at different fluences.

3.2.5 Determination of the amorphous fraction

Here we show the presence of an amorphous fraction created by the swift heavy ions irradiation process in PSi.

The amorphous fractions of our irradiated samples were determined using Raman microscopy. The Raman investigations were carried out at Université Lyon 1 using the Renishaw described in Chapter 2. The spectra were collected through the 50x objective with a numerical aperture $NA = 0.5$. The depth resolution is about $1.2 \mu\text{m}$ using a green laser with a wavelength of 532 nm. The Raman signals were then recorded from the irradiated porous

layer far from the bulk silicon. Single spectra were recorded with an exposure time varying between 60 s (for the lowest energy and fluence) and 250 s (for the highest energy and fluence) with 2 accumulations. Special attention was paid while performing this kind of experiments to avoid systematic errors:

- calibration of the setup should be performed using a silicon wafer while being sure that the crystalline peak is around 520 cm^{-1} ;
- laser power calibration is needed to avoid overheating of the studied samples ($\sim 10 \text{ }\mu\text{W}$).

An example of change of the Raman spectrum shape as a function of the ion fluence is shown for ^{129}Xe ion irradiation in Figure 3.11 [37]. Only the spectra of the non-irradiated PSi sample and samples (A, F), (C, H) and (E, J) are plotted. The spectrum of the non-irradiated porous silicon (NIPSi) exhibits a crystalline peak around 520 cm^{-1} . When irradiated, a second broad peak appears around 480 cm^{-1} . This broad peak becomes more and more important in intensity when increasing the ion fluence and becomes comparable to the crystalline one for the highest irradiation energy and fluence. This peak arises from the amorphous silicon phase [38]. For the same ion fluence, the amorphous fraction is larger for the sample irradiated at the highest energy E_1 . This qualitative study validates the assumption that PSi samples could be amorphized in the electronic regime.

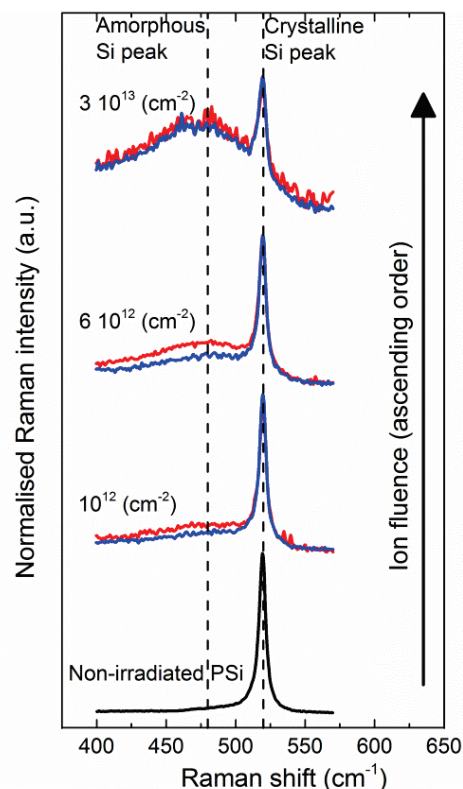


Figure 3.11 Micro-Raman spectra for different fluences for 91 MeV (red) and 29 MeV (blue) ^{129}Xe irradiations of 56 % PSi. Each spectrum is normalized to the intensity of its highest peak. Spectra are shifted vertically for figure clearness.

This qualitative study is an evidence of the predominance of the electronic regime interactions, which creates latent tracks (amorphising the crystallites) along the ions path when traveling through the target while keeping the porous structure. We will now perform a quantitative study to determine the amorphous fraction from the Raman spectra. The amorphous fraction can be determined quantitatively in amorphous/crystalline mixed phase samples using Raman spectroscopy. This can be done by separating the two contributions associated to the Stokes peak of the Raman spectrum, respectively in the crystalline and the amorphous phase.

Figure 3.12 (a) shows the Raman spectrum of crystalline bulk Si. The spectrum in Figure 3.12 (b) is obtained for a non-irradiated PSi (56 % porosity) sample and has a broader shape with a slight peak shift towards the lowest energies (not important in our case). These changes in shape were attributed to phonon confinement in the very small Si crystallites of the PSi samples [27][39]. Once the separation is done, the contribution from the fraction of amorphous ζ_a can be calculated by [40]

$$\zeta_a = \frac{I_a}{I_a + I_c/\eta}, \quad (3.7)$$

where I_c , I_a and $\eta = \Sigma_c/\Sigma_a$ [41] are, respectively, the integrated intensity of the crystalline phase, the integrated intensity of the amorphous phase and the ratio of the integrated Raman cross-section for crystalline silicon (Σ_c) to amorphous silicon (Σ_a). The term η is introduced due to a contrast in the emitted intensity level from a crystalline and an amorphous phase. Based on literature, different values of η can be found. It varies between 0.4 and 0.85 in [42], found to be equal to 0.88 in [43], 0.8 in [44], 1.7-1.8 in [45] and 1 in [7]. While the value of η is still debated in the literature, following Newby et al. [7], we chose it to be equal to 1.

The crystalline (amorphous) contribution is obtained by integrating the crystalline (amorphous) peak over the chosen range of Raman shift. Previous studies proposed to fit the crystalline phase peak with four Gaussian [46] or three Gaussian [42] to account for the broadening of the crystalline peak and with a single Gaussian curve for the amorphous phase. Their fits were performed on corrected baseline Raman spectra between 420 and 570 cm^{-1} to obtain the amorphous phase. Fit results are displayed in Figure 3.12 (c). A nice fit of the amorphous phase (sample E) is obtained. This fit technique consists of considering that the same part under the crystalline and the amorphous curves (intersection) can be attributed, at the same time, to a crystalline and to an amorphous phase. This causes an overestimation of the crystalline phase, especially at low ion fluences. The results of these fits are plotted in Figure 3.13 (red and blue circles). We proposed fitting the amorphous peak with a Gaussian and then to subtract its contribution from the whole spectrum to obtain the crystalline one (Figure 3.12 (d)). The remaining white part, under the dashed line (from the amorphous fraction fit), is added to the amorphous contribution after each spectrum analysis (Figure 3.12 (d) shows the evidence that this white part is a part of the amorphous phase). The Raman spectra of the bulk silicon, the non-IPSi (NIPSi) and the IPSi samples, were taken at the same low laser power to avoid overheating of the sample resulting in a Raman shift that can induce errors in the amorphous fraction determination. In our new fit procedure, we may underestimate the crystalline phase based on the choice of our base line. The results of our fits are plotted in Figure 3.13 (red and blue squares). It shows that for the same irradiation energy,

the amorphous fraction increases when increasing the ion fluence and levels off at the highest fluence. For the same fluence φ , the amorphous fraction is larger for the highest energy, when increasing the electronic stopping power. However, at the highest fluence, the difference in the amorphous fractions between both series is reduced and saturation is observed.

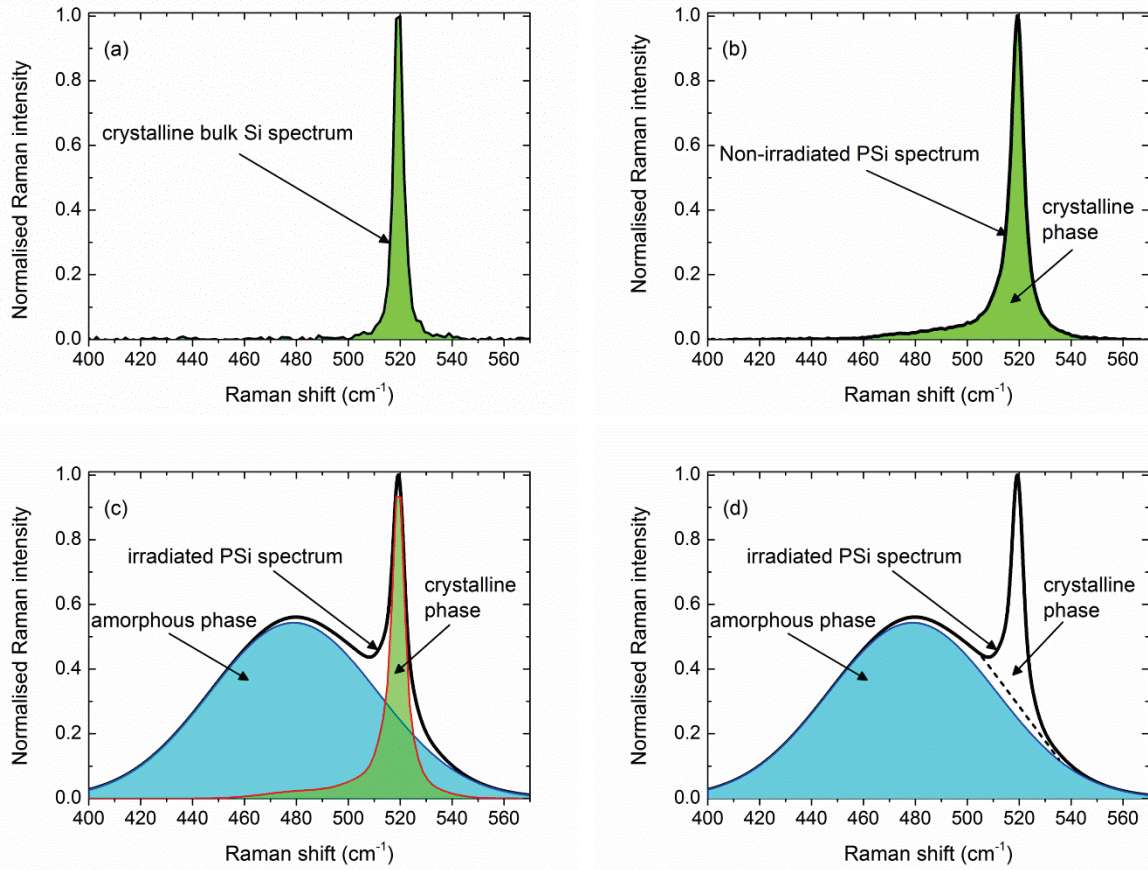


Figure 3.12 Complete Raman spectra (black line) of: **(a)** Crystalline bulk silicon **(b)** Non-irradiated porous silicon 56 % porosity showing its crystalline phase (green area), **(c)** Irradiated PSi (56 % porosity) with ^{129}Xe at energy 91 MeV and at fluence $3 \times 10^{13} \text{ cm}^{-2}$. The blue profile is a Gaussian fit of the amorphous fraction and the red profile is the result of a four Gaussian fit of the crystalline phase. The cyan and green areas represent respectively the amorphous and crystalline contributions. **(d)** Amorphous fraction determination used in this study. The dashed line is the baseline limit of the crystalline phase.

The resulting average amorphous fraction F_a resulting from the two fitting techniques can be fitted properly with classical Poisson's relation [47]:

$$F_a = B[1 - e^{-A_d \varphi}], \quad (3.8)$$

where B is the maximum amorphisation at a given energy, $A_d = \pi R_e^2$ is the amorphisation cross-section and R_e is an effective track radius. The obtained values of B and A_d from the fits together with the simulated cross-section for disordering the target in the nuclear regime (A_n) using the software SRIM [48] are listed in Table 3.3.

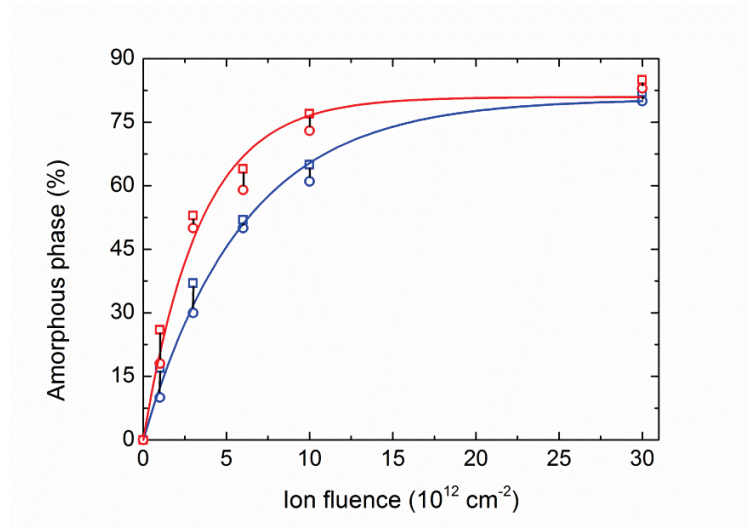


Figure 3.13 Amorphous phase versus fluence as obtained from micro Raman spectra of the irradiated PSi (56 % porosity) with ^{129}Xe at two different energies: 90 MeV (red squares and circles) and 29 MeV (blue squares and circles). Circles (squares) represent the results from Figure 3.12 (c) (Figure 3.12 (d)). The red and blue lines represent the fits respecting the middle of the black lines using the Poisson law. The point (0, 0) was added to the curves referring to the non-irradiated PSi sample.

Energy (MeV)	B (%)	A_d (nm^2)	A_n (nm^2)
29	80.5	17	0.032
90	80.9	30	0.012

Table 3.3 Results of the fits: B is the maximum value of amorphous fraction, A_d is the cross-section of electronic interactions. The simulated cross-sections via nuclear processes are given in the last column.

The values of A_d exceed by more than two (for the lowest irradiation energy) and three (for the highest irradiation energy) orders of magnitude the cross-sections A_n . This is another confirmation that creation of disorder in our PSi samples is a direct consequence of an electronic slow-down of the projectile.

We note that the difference between the saturation values is very small. Moreover, this saturation value is not 100 %. This can be considered as an indication of the presence of another phenomenon in samples amorphized with high fluences (eventual recrystallization process). This is not discussed in this manuscript.

Crystalline silicon irradiation

As already mentioned, crystalline silicon remains intact when irradiated in the electronic regime with single ion species. Ion-crystalline silicon interactions are not well understood and remain subject to investigations due to lack of information for the electronic system [49]. The melting temperature of cSi is $T_{\text{melting}} = 1683$ K given by an approximation based on the thermal spike model [12]. The energy deposition required for damaging cSi is above 30 KeV.nm^{-1} [50].

The energy required to damage the 56 % PSi samples was found to be less than 3 KeV.nm^{-1} [48], as a threshold. This difference may be due to the low thermal conductivity of PSi compared to that of the cSi, resulting in an increase of the local heating.

The damaged layers will be thermally characterized in the following section.

3.3 Impact of irradiation on porous silicon thermal conductivity

Previous sections of this chapter discussed in details the effect of swift heavy ions irradiation on PSi in the electronic regime. The formation of amorphous tracks is expected to degrade the thermal conductivity of the studied samples. This part is dedicated to the analysis of the experimental results obtained using two thermal characterization techniques: micro Raman thermometry (Section 3.3.1) and scanning thermal microscopy (Section 3.3.2). The results of the two techniques are then compared and discussed, allowing a better understanding of thermal conductivity degradation in porous silicon irradiated with swift heavy ions.

3.3.1 Micro-Raman thermometry

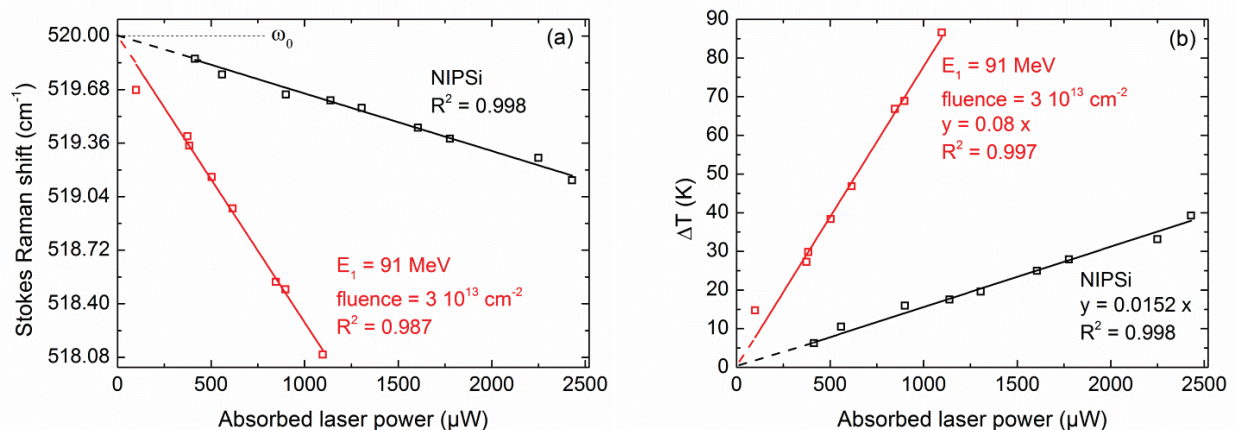


Figure 3.14 Thermal conductivity determination using micro Raman thermometry. **(a)** Stokes Raman shift as a function of the absorbed laser intensity before (black squares) and after (red squares) irradiation. Dashed lines are linear fits intercepting at the room-temperature peak position point (ω_0). The slopes of these curves are the total thermal resistance of the studied samples. **(b)** Corresponding temperature rise (ΔT) as a function of the absorbed laser intensity. Dashed lines are forced linear fits intercepting at (0, 0). The slopes of these curves are related to the sample effective thermal conductivities.

Micro Raman thermometry measurements were carried out on our ten irradiated PSi samples and on the non-irradiated one in an open air environment at temperature $23 \text{ }^\circ\text{C}$. Thermal conductivity values were determined accordingly to the procedure detailed in Chapter 2, using the ‘power variation’ method. Figure 3.14 (a) shows the Stokes Raman shift versus the absorbed laser power using an absorbance $A = 0.9$ for the porous silicon of 56 % porosity. The laser spot radius for the 532 nm laser (objective x50 and NA 0.5), was $1.9 \text{ }\mu\text{m}$. The value

of the absorption coefficient is 8300 cm^{-1} [7]. As seen in Figure 3.14 (a), the fits show linear dependence between Stokes Raman shift and the laser intensity, with a larger slope for the NIPSi. The resulting temperature rise (ΔT) is plotted versus the absorbed laser power in Figure 3.14 (b) and fitted with lines passing by (0, 0) (added to the figure but not measured experimentally). $R^2 = 0.998$ (for the NIPSi) and 0.987 (for the irradiated one) are an indication of the quality of the fit of the Raman data. The slope is directly proportional to the thermal resistance of the sample indicating that the irradiated PSi sample (sample E) has a lower thermal conductivity than the NIPSi one. The resulting effective thermal conductivity values are shown in Figure 3.15. A decrease in PSi effective thermal conductivity in the expected order (i.e. while increasing fluence) is obtained. For a given ion fluence, the effective thermal conductivity is the lowest one for the highest energy. Error bars were plotted considering a 10 % of uncertainty on each measurement (the maximum error in Raman measurements).

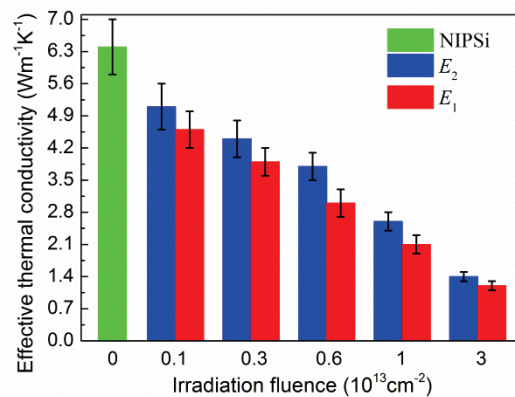


Figure 3.15 Effective thermal conductivity as a function of the irradiation fluence for the PSi of 56 % porosity obtained by Raman thermometry. The results show a decrease in PSi effective thermal conductivity, starting from the NIPSi (green rectangle) to the irradiated samples at the lowest (blue rectangles) and the highest (red rectangles) energies.

3.3.2 Scanning thermal microscopy

SThM measurements were carried out on all the irradiated PSi samples and on the non-irradiated one in an open air environment at temperature 23 °C. Thermal conductivity values were obtained according to the procedure detailed in Chapter 2, using the ‘purely experimental’ method, considering that PSi and calibration bulk samples interact in the same way with the tip. We used a straight Wollaston tip perpendicular to samples surfaces.

We plotted the calibration curve for thermal conductivity determination using five calibration samples of well-known thermal conductivities (see Figure 3.16). The point (0.025, 0) was added to the figure and not measured experimentally, taken as the reference when the tip is out of contact far from the sample in air ($\lambda = 0.025 \text{ W.m}^{-1}.\text{K}^{-1}$). Thermal conductivity values were taken from *Goodfellow* and *Neyco*. Calibration sample surfaces were polished to avoid any topographic influence on the thermal signal. By using well-known thermal conductivity samples and while repeating the same measurement ten times on each sample, the relative

dissipated power can be obtained experimentally. The equation of the forced linear fit of the experimental data of the calibration samples ($R^2 = 0.993$) represented by a red line is then used to calculate our NIPSi and IPSi samples effective thermal conductivities after measuring experimentally the relative dissipated probe power $\Delta P/P$ of each sample. The error bars denote the maximum and the minimum of $\Delta P/P$ among each set of measurements.

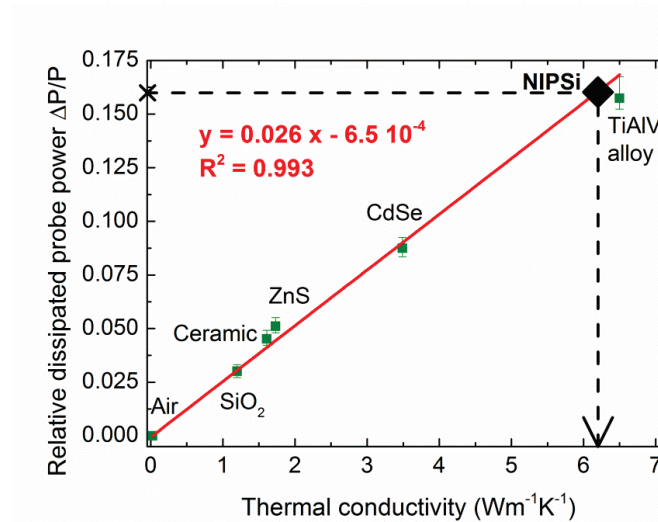


Figure 3.16 $\Delta P/P$ calibration curve as a function of samples thermal conductivities (showing a good linear relation (red straight forced line) with $R^2 = 0.993$). The ‘air’ green square datum was not measured experimentally and added to the graph as the reference point (0.025, 0). The black dashed lines are plotted to guide the eye showing sample thermal conductivity determination of the NIPSi (56 % porosity) (black diamond) based on the displayed equation.

The calculated effective thermal conductivity values are shown in Figure 3.17. A decrease in PSi effective thermal conductivity in the expected order is obtained. For a given ion fluence, the effective thermal conductivity is the lowest one for the highest energy.

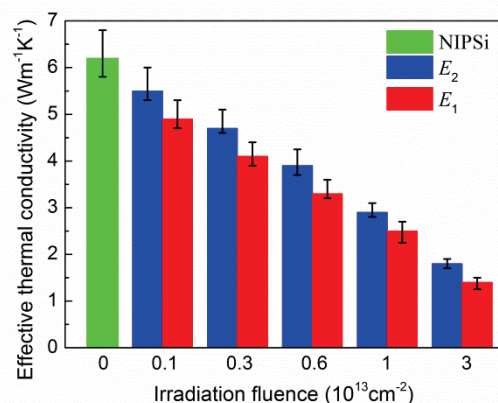


Figure 3.17 Effective thermal conductivity as a function of the irradiation fluence for the PSi of 56 % porosity obtained by SThM. The results show the decrease in PSi effective thermal conductivity, starting from the NIPSi (green rectangle) to the irradiated ones at the lowest (blue rectangles) and the highest (red rectangles) energies. Error bars were plotted considering the maximum and the minimum in $\Delta P/P$.

3.3.3 Comparison of the results

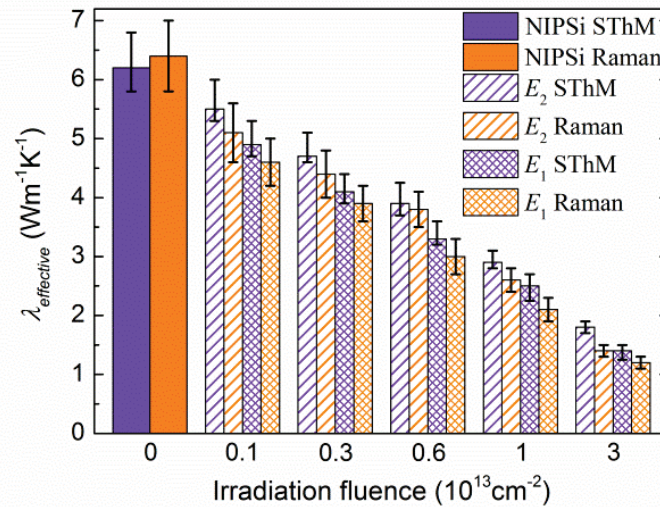


Figure 3.18 Effective thermal conductivity as a function of the irradiation fluence of the PSi of 56 % porosity obtained by SThM and micro-Raman thermometry. Violet color is dedicated to SThM results while orange one is dedicated to micro-Raman thermometry. NIPSi are shown in full orange and violet rectangles, while irradiated ones are shown in hatched (E_2 energy) and crossed (E_1 energy) orange and violet rectangles. Error bars for SThM were plotted considering the maximum and the minimum in $\Delta P/P$ while for micro-Raman thermometry considering $\pm 10\%$ of each obtained value.

The histogram in Figure 3.18 shows the evolution of the effective thermal conductivity of PSi (56 % porosity) irradiated at two different energies (E_1 and E_2) while increasing the irradiation fluence. The results obtained from micro-Raman thermometry and SThM measurements are in very good agreement. The results of the two techniques show a decrease in PSi thermal conductivity while increasing the irradiation fluence. At a given fluence, a lower thermal conductivity is achieved for the highest irradiation energy. Furthermore, a linear relation is established between our IPSi samples and the amorphous fraction (see Figure 3.19). The lowest IPSi thermal conductivity value ($1.2 \text{ W}\cdot\text{m}^{-1}\cdot\text{K}^{-1}$) obtained in this study is more than 5.3 times smaller than that of the NIPSi one ($6.4 \text{ W}\cdot\text{m}^{-1}\cdot\text{K}^{-1}$) and more than two orders of magnitude smaller than that of bulk silicon. It is comparable to that of SiO_2 ($1.2 \text{ W}\cdot\text{m}^{-1}\cdot\text{K}^{-1}$) [51][52][53][54] and is close to $1.1 \text{ W}\cdot\text{m}^{-1}\cdot\text{K}^{-1}$, the effective thermal conductivity of PSi (porosity 75 %) [7]. This means that by irradiating PSi of medium porosity (good mechanical stability) we can obtain thermal conductivities values close to the ones of NIPSi of higher porosity, thus avoiding mechanical strength problems known at high porosity. The found value is in the range of that of SiO_2 , considered as one of the best solid insulators used in microelectronics.

It is difficult to find in literature exactly the same porous silicon sample as the one we manufactured, but our NIPSi thermal conductivity is in good agreement with already published results [4][55][8].

Comparison with existing models

We now compare our results with a model that allows obtaining the thermal conductivity of PSi irradiated with swift heavy ions developed by Newby et al. [7]. In this model the partially amorphous porous silicon structure is considered as parallel wires of amorphous and crystalline phases. The effective thermal conductivity of a partially amorphous PSi layer is then given by [7]:

$$\lambda_{IPSi} = (1 - P)[\lambda_{Si}(1 - \zeta_a) + \lambda_{aSi} \zeta_a], \quad (3.9)$$

where P is the porosity, ζ_a is the amorphous fraction and λ_{Si} , λ_{aSi} are the effective thermal conductivities of, respectively, the crystalline silicon nanowires and the amorphous silicon. Theoretical studies demonstrated that amorphous silicon thermal conductivity can vary between 1 and 5 W.m⁻¹.K⁻¹ [56]. To our best knowledge, no experimental value for λ_{Si} , at room temperature, was obtained for nanowires of 11 nm in diameter (the diameter of our Si crystallites). We applied this model to fit our experimental data, while keeping λ_{Si} as variable and $\lambda_{aSi} \in [1; 5]$ W.m⁻¹.K⁻¹. The resulting best fit gives $\lambda_{Si} = 15.2$ W.m⁻¹.K⁻¹ and $\lambda_{aSi} = 2.3$ W.m⁻¹.K⁻¹ with $R^2 = 0.98$. With this mode, our crystallites of 11 nm in diameter turned out to have λ_{Si} larger than that of single crystalline silicon nanowires of 22 nm in diameter ~ 10 W.m⁻¹.K⁻¹ [58].

As a result, we proceeded in a different way. The effective thermal conductivities of our samples are also fitted linearly versus the amorphous phase for the two irradiation energies and for the two used characterization techniques. The same slopes are obtained with an intercept with a relative variation of 3 %. This variation is related to the very small difference in the NIPSi effective thermal conductivities obtained by each technique. The obtained equation is

$$\lambda_{IPSi} = -\eta (\zeta_a - 1) + \chi, \quad (3.10)$$

where $\eta = g_0 \lambda_{bulk Si} = 5.67$ W.m⁻¹.K⁻¹ and $\chi = \lambda_{IPSi100\%}$. λ_{Si} is the thermal conductivity of the bulk silicon and $\chi = \lambda_{IPSi100\%}$ is the thermal conductivity of the irradiated porous silicon with $\zeta_a = 100\%$. g_0 is the percolation coefficient proposed by Gesele et al [4] which depends on the microtopology of the porous system, especially on the interconnected crystallites, so on $(1 - P)$. The $-$ sign makes the slope negative as an indication of the reduction of λ_{IPSi} when increasing the irradiation fluence. For Raman (χ_R) and SThM (χ_S) linear fits, we find $\chi \in [0.7 - 1]$ W.m⁻¹.K⁻¹. In our study the percolation coefficient after irradiation g_0 was found to be equal to $(1 - P)^4$.

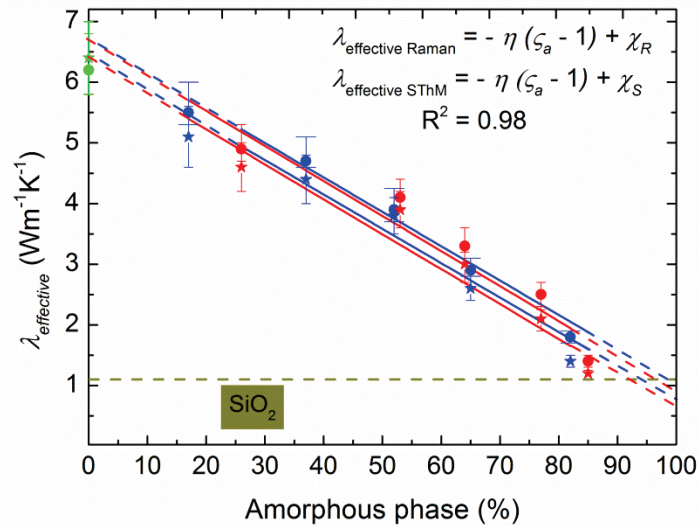


Figure 3.19 Effective thermal conductivity as a function of the amorphous phase based on Raman (full stars) and SThM (full circles) measurements. NIPSi is depicted in green color while the blue (red) color is dedicated to the lowest (highest) irradiation energy.

3.4 Summary and perspectives

Understanding the effect of swift heavy ions irradiation on porous silicon thermal conductivity was crucial to analyze the results of this study. To do so, PSi samples with 56 % porosity were irradiated with ^{129}Xe ions (heavy ions) at two different energies and five different fluences. In order to study the effect of irradiation on the studied samples, both irradiated and non-irradiated samples were analyzed. The studied porous silicon samples have an average crystallite diameter of 11 nm. We performed an experimental analysis at the microscopic scale of the 10 μm thick porous layer, with the following assumptions:

- the characterized medium size 10 μm is considered to be larger than the effective mean free path of the heat carrier (smaller than bulk mean free path), so a diffusion regime is observed at this scale;
- the characterized medium has a homogenous and isotropic thermal conductivity. We do not consider the effect of possible different orientations.

Based on calculations executed using SRIM software, we could plot the stopping power curves and obtain the projected range values for the two irradiation energies and then demonstrate that the irradiation process occurred in the electronic regime. As nuclear collisions occur in the underlying Si substrate, the whole PSi layer is irradiated in the electronic regime. As a consequence the damage created (structure amorphisation) is homogenous along the ion path in the 10 μm thick porous layer. We therefore considered that the thermal conductivity of the porous layer is homogeneous and isotropic.

We demonstrated a very good agreement between micro-Raman thermometry (optical, contactless technique and with volume heat source) and SThM (electrical and contact

technique) measurements done on P_{Si} and I_{PSi} at two different energies. This shows that the rough mechanical contact expected in SThM does not play a significant role. We note that we considered that the thermal conductivity is not temperature dependent. The characterization techniques used in our study are based on thermal excitation of the probed material. We showed a decrease in P_{Si} thermal conductivity by a factor more than 5.3 and a decrease by more than two orders of magnitude in comparison with bulk silicon thermal conductivity. In the end we obtained a lowest effective thermal conductivity of $1.2 \text{ W}\cdot\text{m}^{-1}\cdot\text{K}^{-1}$ close to that of high porous silicon (porosity 75 %), avoiding mechanical fragility due to high porosity in our case. This value is also comparable to the thermal conductivity of SiO₂, one of the usual solid insulators. We found a linear relation between the effective thermal conductivity and the amorphous fraction, which can now be used for thermal conductivity prediction if the amorphous is known.

It would be interesting to use higher ion fluence to check if the 100 % amorphous limit can be reached or if some recrystallization process occurs. Still for a better understanding of the interaction mechanisms of ions with the porous structure, transmission electron microscopy would be helpful. Indeed, this would give a localization of the amorphous phase for which different hypothesis are possible:

- crystalline core and amorphous shell of the dendrites;
- amorphisation of the smallest dendrites with a size threshold.

These observations could be completed with a modelling of the interaction using the thermal spike model for P_{Si}. Finally, as we propose to use this highly insulating material for MEMS applications, it would be helpful to study the mechanical properties of this system by accessing the Young modulus.

To improve our understanding of thermal properties, performing 2D Atomic Force microscopy (AFM) images would be helpful to have an idea on samples roughness, which may be the cause of the small differences between the results obtained from the two characterization techniques. In addition, it would be interesting to study the thermal conductivity as a function of the depth of the material, by etching progressively the surface. This could give an idea about the amorphisation homogeneity in depth and its effect on the effective thermal conductivity.

Bibliography

- [1] G. Benedetto, L. Boarino, and R. Spagnolo, "Evaluation of thermal conductivity of porous silicon layers by a photoacoustic method". *Appl. Phys. A Mater. Sci. Process.*, vol. 64, no. 2, pp. 155–159, 1997.
- [2] V. Lysenko, S. Périchon, B. Remaki, D. Barbier, and B. Champagnon, "Thermal conductivity of thick meso-porous silicon layers by micro-Raman scattering". *J. Appl. Phys.*, vol. 86, no. 12, p. 6841, 1999.
- [3] S. Périchon, V. Lysenko, P. Roussel, B. Remaki, B. Champagnon, D. Barbier, and P. Pinard, "Technology and micro-Raman characterization of thick meso-porous silicon layers for thermal effect microsystems". *Sensors Actuators, A Phys.*, vol. 85, pp. 335–339, 2000.
- [4] G. Gesele, J. Linsmeier, V. Drach, J. Fricke, and R. Arens-Fischer, "Temperature-dependent thermal conductivity of porous silicon". *J. Phys. D. Appl. Phys.*, vol. 30, no. 21, p. 2911, 1997.
- [5] C. Populaire, B. Remaki, V. Lysenko, D. Barbier, H. Artmann, and T. Pannek, "On mechanical properties of nanostructured meso-porous silicon". *Appl. Phys. Lett.*, vol. 83, no. 7, p. 1370, 2003.
- [6] S. P. Duttagupta, X. L. Chen, S. A. Jenekhe, and P. M. Fauchet, "Microhardness of porous silicon films and composites". *Solid State Commun.*, vol. 101, no. 1, pp. 33–37, 1997.
- [7] P. J. Newby, B. Canut, J.-M. Bluet, S. Gomès, M. Isaiev, R. Burbelo, K. Termentzidis, P. Chantrenne, L. G. Fréchette, and V. Lysenko, "Amorphization and reduction of thermal conductivity in porous silicon by irradiation with swift heavy ions". *J. Appl. Phys.*, vol. 114, no. 1, p. 014903, 2013.
- [8] M. Isaiev, P. J. Newby, B. Canut, A. Tytarenko, P. Lishchuk, D. Andrusenko, S. Gomès, J.-M. Bluet, L. G. Fréchette, V. Lysenko, and R. Burbelo, "Thermal conductivity of partially amorphous porous silicon by photoacoustic technique". *Mater. Lett.*, vol. 128, pp. 71–74, 2014.
- [9] A. Meftah, F. Brisard, J. M. Costantini, E. Dooryhee, M. Hage-Ali, M. Hervieu, J. P. Stoquert, F. Studer, and M. Toulemonde, "Track formation in SiO₂ quartz and the thermal-spike mechanism". *Phys. Rev. B*, vol. 49, no. 18, pp. 12457–12463, 1994.
- [10] C. Trautmann, S. Klaumünzer, and H. Trinkaus, "Effect of stress on track formation in amorphous iron boron alloy: ion tracks as elastic inclusions". *Phys. Rev. Lett.*, vol. 85, no. 17, pp. 3648–3651, 2000.
- [11] M. Toulemonde, C. Dufour, Z. Wang, and E. Paumier, "Atomic and cluster ion bombardment in the electronic stopping power regime: A thermal spike description". *Nucl. Instruments Methods Phys. Res. Sect. B Beam Interact. with Mater. Atoms*, vol. 112, no. 1–4, pp. 26–29, 1996.
- [12] M. Toulemonde, C. Dufour, and E. Paumier, "Transient thermal process after a high-energy heavy-ion irradiation of amorphous metals and semiconductors". *Phys. Rev. B*, vol. 46, no. 22, pp. 14362–14369, 1992.
- [13] D. Kanjilal, "Swift heavy ion-induced modification and track formation in materials". *Curr. Sci.*, vol. 80, no. 12, pp. 1560–1566, 2001.
- [14] V. Lehmann and U. Gösele, "Porous silicon formation: A quantum wire effect". *Appl. Phys. Lett.*, vol. 58, no. 8, pp. 856–858, 1991.
- [15] R. Memming and G. Schwandt, "Anodic dissolution of silicon in hydrofluoric acid solutions". *Surf. Sci.*, vol. 4, no. 2, pp. 109–124, 1966.
- [16] M. J. J. Theunissen, "Etch Channel Formation during Anodic Dissolution of n-type silicon in aqueous hydrofluoric acid". *Solid State Sci. Technol.*, no. 111, 1972.
- [17] L. T. Canham, *Properties of Porous Silicon*. UK, 1997.
- [18] C. S. Solanki, R. R. Bilyalov, J. Poortmans, J.-P. Celis, J. Nijs, and R. Mertens, "Self-Standing Porous Silicon Films by One-Step Anodizing". *J. Electrochem. Soc.*, vol. 151, no. 5, p. C307, 2004.
- [19] T. Defforge, M. Diatta, D. Valente, F. Tran-Van, and G. Gautier, "Role of Electrolyte Additives during Electrochemical Etching of Macropore Arrays in Low-Doped Silicon". *J. Electrochem. Soc.*, vol. 160, no. 4, pp. H247–H251, 2013.
- [20] S. Billat, M. Thönissen, R. Arens-Fischer, M. Berger, M. Krüger, and H. Lüth, "Influence of etch stops on the microstructure of porous silicon layers". *Thin Solid Films*, vol. 297, pp. 22–25, 1997.
- [21] M. Thönissen, S. Billat, M. Krüger, H. Lüth, M. G. Berger, U. Frotscher, and U. Rossow, "Depth inhomogeneity of porous silicon layers". *J. Appl. Phys.*, vol. 80, no. 5, p. 2990, 1996.
- [22] V. Lysenko, S. Périchon, B. Remaki, and D. Barbier, "Thermal isolation in microsystems with porous silicon". *Sensors Actuators, A Phys.*, vol. 99, no. 1–2, pp. 13–24, 2002.
- [23] R. Smith and S. Collins, "Porous silicon formation mechanisms". *J. Appl. Phys.*, vol. 71, no. 8, pp. R1–R22, 1992.
- [24] R. Juhasz and J. Linnros, "Three-dimensionally controlled size-reduction of silicon nanopillars by photoelectrochemical etching". *Appl. Phys. Lett.*, vol. 78, no. 20, p. 3118, 2001.
- [25] S. R. Onnebeck, S. Ottow, J. Carstensen, and H. F. Oll, "Crystal Orientation Dependence of Macropore Formation in n-Si With Backside-Illumination in HF-Electrolyte". *J. Porous Mater.*, vol. 356, pp. 353–356, 2000.

- [26] C. Populaire, “Propriétés physiques du silicium poreux : traitements et applications aux microsystèmes”. *PhD Thesis*, 2005.
- [27] I. H. Campbell and P. M. Fauchet, “The effects of microcrystal size and shape on the one phonon Raman spectra of crystalline semiconductors”. *Solid State Commun.*, vol. 58, no. 10, pp. 739–741, 1986.
- [28] M. N. Islam, A. Pradhan, and S. Kumar, “Effects of crystallite size distribution on the Raman-scattering profiles of silicon nanostructures”. *J. Appl. Phys.*, vol. 98, no. 2, p. 024309, 2005.
- [29] J. F. Ziegler, M. D. Ziegler, and J. P. Biersack, “SRIM – The stopping and range of ions in matter (2010)”. *Nucl. Instruments Methods Phys. Res. Sect. B Beam Interact. with Mater. Atoms*, vol. 268, no. 11–12, pp. 1818–1823, 2010.
- [30] H. Liu, “A novel optical bio-chemical sensor based on hybrid nanostructures of Bowtie nanoantennas and Fabry-Perot Interferometer,” *Thesis*, 2013.
- [31] T. Nychyporuk, “Nouvelles Morphologies du Silicium Nanostructuré Issues de l’Anodisation Electrochimiques : Elaboration, Propriétés Physico-Chimiques et Applications”. *PhD Thesis*, 2006.
- [32] J. Lefevre, “Etude des effets d’irradiation dans le polytype cubique du carbure de silicium par les techniques spectroscopiques de photoluminescence et de résonance paramagnétique électronique” *PhD Thesis*, 2008.
- [33] W. Wesch, A. Kamarou, and E. Wendler, “Effect of high electronic energy deposition in semiconductors”. *Nucl. Instruments Methods Phys. Res. Sect. B Beam Interact. with Mater. Atoms*, vol. 225, no. 1–2, pp. 111–128, 2004.
- [34] O. Osmani, I. Alzahr, T. Peters, B. Ban d’Etat, A. Cassimi, H. Lebius, I. Monnet, N. Medvedev, B. Rethfeld, and M. Schleberger, “Damage in crystalline silicon by swift heavy ion irradiation”. *Nucl. Instruments Methods Phys. Res. Sect. B Beam Interact. with Mater. Atoms*, vol. 282, pp. 43–47, 2012.
- [35] B. Canut, N. Bonardi, S. M. M. Ramos, and S. Della-Negra, “Latent tracks formation in silicon single crystals irradiated with fullerenes in the electronic regime”. *Nucl. Instruments Methods Phys. Res. Sect. B Beam Interact. with Mater. Atoms*, vol. 146, no. 1–4, pp. 296–301, 1998.
- [36] A. Simon, F. Paszti, A. Manuaba, and A. Z. Kiss, “Three-dimensional scanning of ion-implanted porous silicon”. *Nucl. Instruments Methods Phys. Res. Sect. B Beam Interact. with Mater. Atoms*, vol. 158, no. 1–4, pp. 658–664, 1999.
- [37] M. Massoud, B. Canut, P. Newby, L. Frechette, P. O. Chapuis, and J. M. Bluet, “Swift heavy ion irradiation reduces porous silicon thermal conductivity”. *Nucl. Instruments Methods Phys. Res. Sect. B Beam Interact. with Mater. Atoms*, vol. 341, pp. 27–31, 2014.
- [38] J. Smith, M. Brodsky, B. Crowder, M. Nathan, and A. Pinczuk, “Raman Spectra of Amorphous Si and Related Tetrahedrally Bonded Semiconductors”. *Phys. Rev. Lett.*, vol. 26, no. 11, pp. 642–646, 1971.
- [39] H. Richter, Z. P. Wang, and L. Ley, “The one phonon Raman spectrum in microcrystalline silicon”. *Solid State Commun.*, vol. 39, no. 5, pp. 625–629, 1981.
- [40] E. Bustarret, M. A. Hachicha, and M. Brunel, “Experimental determination of the nanocrystalline volume fraction in silicon thin films from Raman spectroscopy”. *Appl. Phys. Lett.*, vol. 52, no. 20, p. 1675, 1988.
- [41] R. Tsu, J. Gonzalez-Hernandez, S. S. Chao, S. C. Lee, and K. Tanaka, “Critical volume fraction of crystallinity for conductivity percolation in phosphorus-doped Si:F:H alloys”. *Appl. Phys. Lett.*, vol. 40, no. 6, pp. 534–535, 1982.
- [42] D. Han, J. D. Lorentzen, J. R. Weinberg-Wolf, and L. E. McNeil, “Raman study of thin films from amorphous-to-microcrystalline silicon prepared by hot-wire chemical vapor deposition”. *J. Chem. Inf. Model.*, vol. 53, no. c, p. 160, 1989.
- [43] M. Ledinský, A. Vetushka, J. Stuchlík, T. Mates, A. Fejfar, J. Kočka, and J. Štěpánek, “Crystallinity of the mixed phase silicon thin films by Raman spectroscopy”. *J. Non. Cryst. Solids*, vol. 354, pp. 2253–2257, 2008.
- [44] C. Smit, R. A. C. M. M. van Swaaij, H. Donker, A. M. H. N. Petit, W. M. M. Kessels, and M. C. M. van de Sanden, “Determining the material structure of microcrystalline silicon from Raman spectra”. *J. Appl. Phys.*, vol. 94, no. 5, p. 3582, 2003.
- [45] E. Vallat-Sauvain, C. Droz, F. Meillaud, J. Bailat, A. Shah, and C. Ballif, “Determination of Raman emission cross-section ratio in hydrogenated microcrystalline silicon”. *J. Non. Cryst. Solids*, vol. 352, no. 9–20, pp. 1200–1203, 2006.
- [46] P. Newby, “Fabrication De Semiconducteurs Poreux Pour Améliorer L’Isolation Thermique Des MEMS” *PhD Thesis*, 2014.
- [47] S. Miro, D. Grebille, D. Chateigner, D. Pelloquin, J. P. Stoquert, J. J. Grob, J. M. Costantini, and F. Studer, “X-ray diffraction study of damage induced by swift heavy ion irradiation in fluorapatite”. *Nucl. Instruments Methods Phys. Res. Sect. B Beam Interact. with Mater. Atoms*, vol. 227, no. 3, pp. 306–318, 2005.
- [48] B. Canut, M. Massoud, P. Newby, V. Lysenko, L. Frechette, J. M. Bluet, and I. Monnet, “Damage creation in porous silicon irradiated by swift heavy ions”. *Nucl. Instruments Methods Phys. Res. Sect. B Beam Interact. with Mater. Atoms*, vol. 327, no. 1, pp. 99–102, 2014.
- [49] O. Osmani, “Irradiation effects of swift heavy ions in matter” *PhD Thesis*, 2011.

- [50] A. Kamarou, W. Wesch, E. Wendler, A. Undisz, and M. Rettenmayr, "Radiation damage formation in InP, InSb, GaAs, GaP, Ge, and Si due to fast ions". *Phys. Rev. B - Condens. Matter Mater. Phys.*, vol. 78, no. 5, pp. 1–12, 2008.
- [51] A. Delan, M. Rennau, S. E. Schulz, and T. Gessner, "Thermal conductivity of ultra low-k dielectrics". *Microelectron. Eng.*, vol. 70, no. 2–4, pp. 280–284, 2003.
- [52] M. G. Burzo, P. L. Komarov, and P. E. Raad, "Thermal transport properties of gold-covered thin-film silicon dioxide". *IEEE Trans. Components Packag. Technol.*, vol. 26, no. 1, pp. 80–88, 2003.
- [53] M. B. Kleiner, S. A. Kuhn, and W. Weber, "Thermal conductivity measurements of thin silicon dioxide films in integrated circuits". *IEEE Trans. Electron Devices*, vol. 43, no. 9, pp. 1602–1609, 1996.
- [54] Y. S. Touloukian, R. W. Powell, C. Y. Ho, and P. G. Klemens, *Thermophysical Properties of Matter-The TPRC Data*, Volume 2. 1971.
- [55] S. Gomès, L. David, V. Lysenko, A. Descamps, T. Nychyporuk, and M. Raynaud, "Application of scanning thermal microscopy for thermal conductivity measurements on meso-porous silicon thin films". *J. Phys. D. Appl. Phys.*, vol. 40, no. 21, pp. 6677–6683, 2007.
- [56] Y. He, D. Donadio, and G. Galli, "Heat transport in amorphous silicon: Interplay between morphology and disorder". *Appl. Phys. Lett.*, vol. 98, no. 14, p. 144101, 2011.
- [57] P. Chantrenne, J. L. Barrat, X. Blase, and J. D. Gale, "An analytical model for the thermal conductivity of silicon nanostructures". *J. Appl. Phys.*, vol. 97, no. 10, pp. 1–8, 2005.
- [58] D. Li, Y. Wu, P. Kim, L. Shi, P. Yang, and A. Majumdar, "Thermal conductivity of individual silicon nanowires". *Appl. Phys. Lett.*, vol. 83, no. 14, pp. 2934–2936, 2003.

Chapter 4. Thermal conductivity of suspended silicon phononic membranes

Considering complementary-metal-oxide-semiconductor (CMOS) compatible thermoelectric applications, Si is obviously the material of choice not only for the large scale integration, but also due to its advantageous high Seebeck coefficient. Major efforts have been devoted to reduce the thermal conductivity of silicon by nanostructuring, while maintaining its existing electronic properties for thermoelectric applications. To this end, free-standing silicon films have been used to study experimentally the effect of the change in the characteristic size on phonon transport [1][2][3][4]. Due to the huge progress in the field of nanotechnologies, it has become possible to control and manipulate the phonons by introducing periodicity in the material to form phononic crystals (PhNCs). Up to date, the evidence of coherent phonon heat conduction in nanostructured Si materials obtained by experimental means [1][2][5], at room temperature, remains debatable and generally heat transport in this kind of structure remains not well understood.

This chapter is dedicated to the measurement, at room temperature, of the thermal conductivity of engineered suspended Si membranes. In Section 4.1, we present the manufacturing process of PhNC suspended Si membranes. In Section 4.2, we highlight the method used for performing SThM experiments on suspended membranes. We then show the effect of the tip position during a scan. We also discuss a new method for the determination of the thermal conductivity. In the end of this section we display the results obtained from this original technique. In Section 4.3, we highlight two methods used for performing micro-Raman thermometry. Then we show that 1D analytical models fail to accurately determine the temperature rise in suspended membranes and thus FEM simulations are required. A precise calculation procedure of the absorbance for suspended membranes, which is a critical parameter for the determination of the thermal conductivity by micro-Raman thermometry, is also detailed. In Section 4.4 we compare the results obtained from the two characterization techniques.

4.1 Sample preparation

Our samples were manufactured by V. Lacatena [6][7] and M. Haras [8] at IEMN laboratory in Lille, France. Different suspended membranes were prepared for this study: plain membranes and perforated membranes with three different pitches, 60 nm (P60), 80 nm (P80) and 100 nm (P100). Electron beam lithography was used to draw the patterns, membranes and holes, on a silicon on insulator (SOI) wafer using the ‘dots-on-the fly’ technique. This technique relies on increasing the electron beam step size up to the desired pitch while keeping regular spaced pixels. This step was followed by etching processes for membrane release. Two different suspended membrane configurations were studied: suspended membranes with and without Pt heater and serpentine sensors. When the heater and the sensors are present, a 100 nm thick silicon nitride layer is needed for electrical insulation. The Pt was deposited by thermal evaporation means. Figure 4.1 (a) depicts a top view SEM image

of the suspended Si membranes with a heater in its middle and two sensors at its two ends. Figure 4.1 (b) is a cross-section sketch of the same configuration. The suspended membrane of 30 μm long can be either plain or perforated.

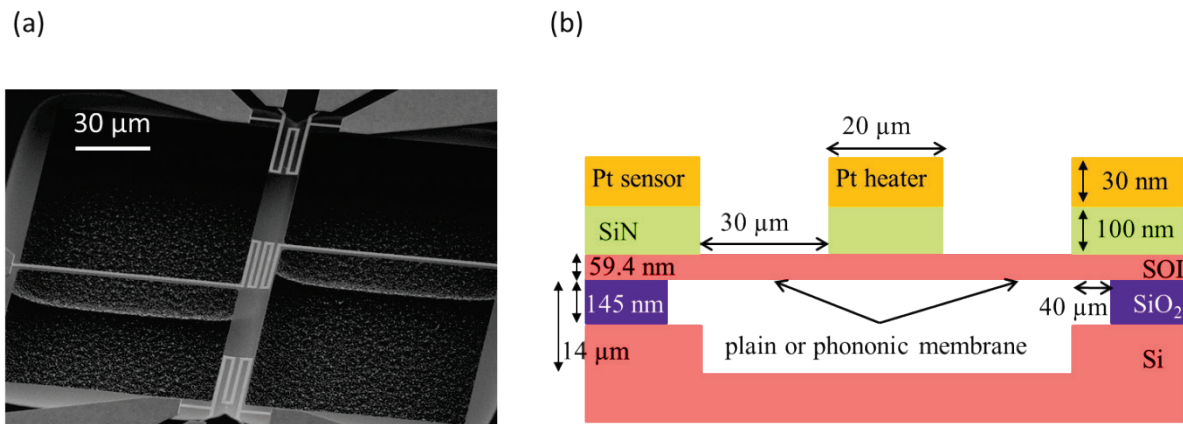


Figure 4.1 (a) Top-view SEM image of the suspended membrane with a Pt heater and two Pt sensors. (b) Cross-section schematic of the same suspended membrane.

Figure 4.2 (a) is a cross-sectional sketch of the second configuration. Figure 4.2 (b) is a top view SEM image of a 200 μm long, 10 μm large and 59.4 ± 0.3 nm thick suspended Si membranes without heater and without sensors. It also shows the 20 μm large ‘underetched’ parts. Figure 4.2 (c) is a zoom on the PhNC membrane showing the periodic holes with P60. White shells are observed around the holes. Their impact on the calculation of the absorbance will be detailed in Section 4.3.4. The thickness of the membranes (e) was obtained by ellipsometry in Lille. The experiments were performed on the SOI part at the end of each manufacturing process. The membranes are suspended at 14 μm from the Si substrate. The height of the air cavity was obtained by means of profilometry. The advantages of the manufacturing process of our perforated membranes are the easy layout, the writing time which is consistently reduced by three orders of magnitude with respect to the conventional lithography strategies and the reproducibility of obtaining a period of 60 nm which is the second smallest pitch, for PhNCs applications, obtained compared to the actual state of the art. The smallest pitch up to date is 34 nm and was obtained by Yu et al. [5]. Their manufacturing process is based on transferring the patterns from a platinum mask into the silicon layer. This may induce deposition of impurities deposition on the suspended membranes that may strongly affect the phonon heat transport. Note that the platinum is known as a non CMOS compatible material.

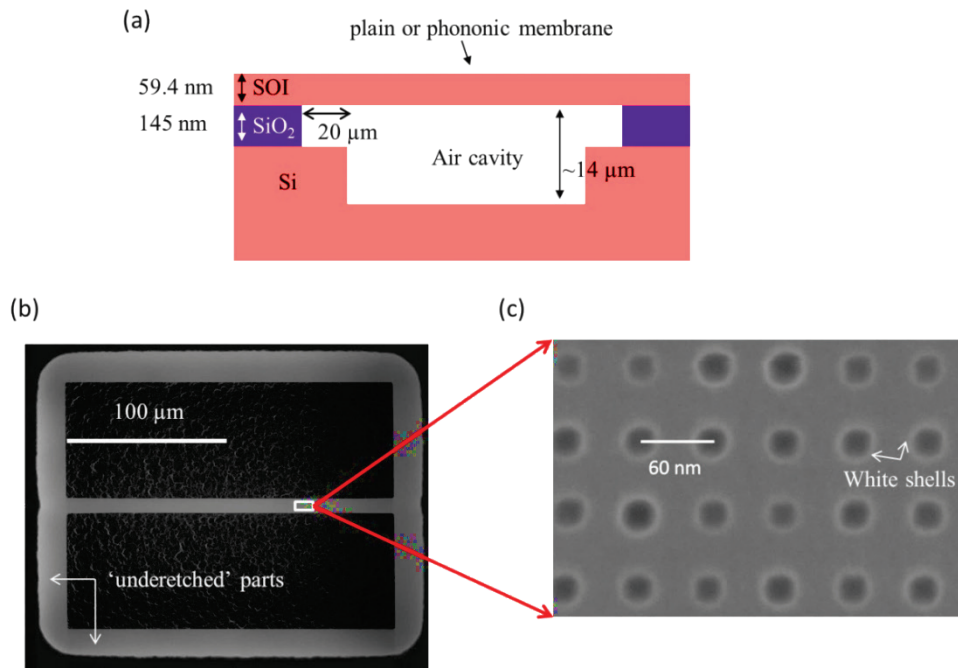


Figure 4.2 (a) Cross-sectional schematic of the suspended membrane. (b) Top SEM image of the same suspended membrane showing the ‘underetched’ parts. (c) Zoom from (b) showing the PhNC membrane with a pitch of 60 nm.

4.2 SThM on suspended membranes

The sample was placed in the SThM microscope in an open air environment at room temperature. The microscope has a CCD camera that allows an approximate manual positioning of the probe close to the sample. A motor connected to a computer is then used to bring the tip into contact with the sample. The tip is placed on the SOI part close to the membrane, and considered as the starting point. The AFM force was chosen in a way to avoid strong membrane buckling during the measurements. The tip linear displacement was done manually via screws. After each measurement at a given point, the tip was retrieved from the contact and placed at 50 μm above the sample before moving it to the next point.

4.2.1 Impact of the scan direction

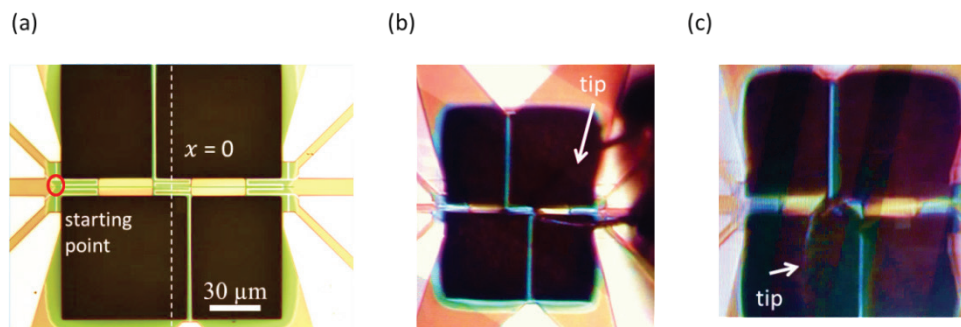


Figure 4.3 (a) Optical image showing the starting point of the scan ($x = -70 \mu\text{m}$). (b) Tip perpendicular to the suspended membrane. (c) Tip parallel to the suspended membrane.

The heat exchange between the tip and the membrane depends on the tip position and on the way the sample is placed under it. In order to study the impact of the scan direction on the measurements we used the membranes with the heater and the sensors. We first placed the tilted tip in the middle of the ‘underetched’ part close to the first extremity of the suspended membrane, defined as the starting point (see Figure 4.3 (a)). We first performed a perpendicular scan (see Chapter 2) as shown in Figure 4.3 (b). We then performed a parallel scan as shown in Figure 4.3 (c).

The results from the two scans are plotted in Figure 4.4. Figure 4.4 (a) depicts the profiles related to the local thermal resistance obtained on the studied membranes using a perpendicular scan. We observe a large difference between the plain (black solid circles) and its corresponding phononic membrane (blue solid circles). This means that the tip exchanges more heat with the plain membrane, which means that the plain membrane is more conductive than the phononic one. We also observe a large difference in ΔV between the starting position and the other side of the membrane close to the bath, $750 \mu\text{V}$ which corresponds to about 6 K. This difference is due to the position of the tip and its shape. While performing a perpendicular scan with a tilted tip and while the tip is approaching the other extremity of the membrane it starts to exchange heat with the SOI and the membrane at the same time. This induces a large decrease in the tip temperature and gives rise to an asymmetric profile. Figure 4.4 (b) depicts the profiles related to the thermal resistance obtained on the same membranes using a parallel scan. As for the perpendicular scan we observe that the plain membrane is more conductive than the same perforated one. In this case the profiles are symmetric but with a slight difference at the heat baths for the phononic membrane. This small difference may be due to a bad positioning of the sample under the tip. In fact the left side of the tip may be closer to the bath than its right part. This problem can be resolved by rotating the sample-holder.

We highlighted the impact of the scan direction on the experimental results. When using a tilted tip, suspended membranes with heater and sensors turned out to be difficult to evaluate and analyze due to the complicated geometry. We add that this geometry may give rise to serious complications when analyzing Raman data. Therefore, the other configuration will be used in the following sections.

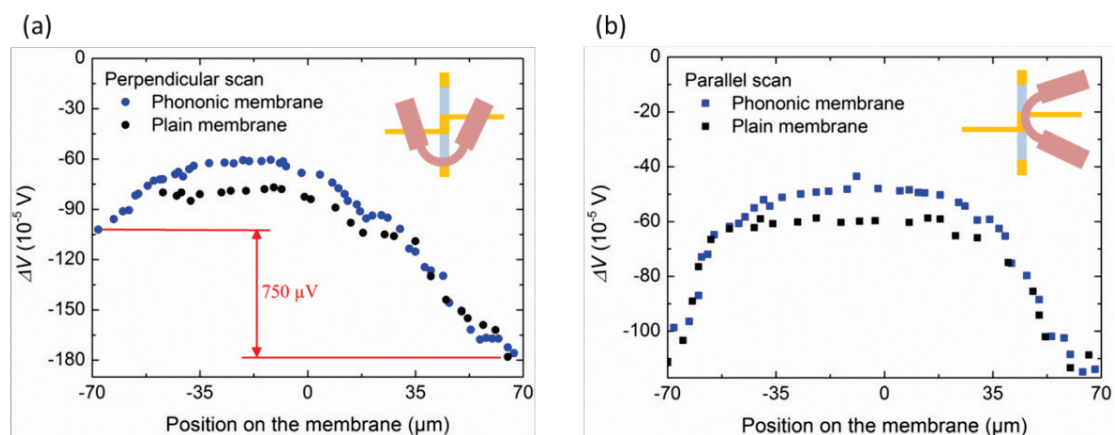


Figure 4.4 (a) Voltage profiles obtained from a perpendicular scan on a plain membrane and on its corresponding phononic membrane. (b) Same as (a) but with a parallel scan.

Cavity effect

In order to evaluate the impact of the air cavity below the suspended membrane on the total thermal profile, we cut the membrane at its two extremities and at the extremities of the two beams holding it. The tip is brought into contact with the SOI close to the cavity and is manually displaced in the x direction. The resulting thermal resistance profile of the cavity is plotted in Figure 4.5 and is compared to the two cases where the plain and its phononic membrane are present. The figure shows the impact of the cavity on the total thermal profile. We observe that with the presence of the membrane the tip exchanges more heat with it inducing a lower value of ΔV . But the cavity cannot be neglected in the analysis of the tip cooling. This profile is not used in the following but it could be subtracted from the obtained one on suspended membranes. The jump in the profile is obtained where the tip is into contact with the SOI. Note that only half of the profile is plotted due to technical issues when performing the scan.

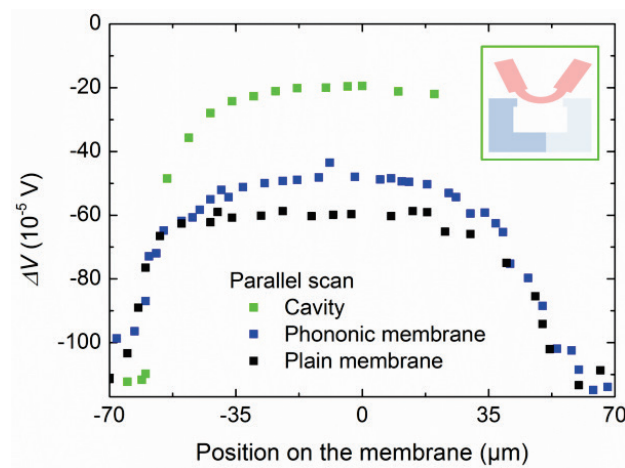


Figure 4.5 Voltage variation obtained from a parallel scan on a plain membrane (black squares), its phononic membrane (blue squares) and with the cavity only (green squares).

4.2.2 Plain and phononic membranes

Four different plain membranes of the same width $10 \mu\text{m}$ and the same thickness 59.4 nm with different lengths $L = 200, 125, 100$ and $75 \mu\text{m}$ in the configuration of Figure 4.2 were first investigated. Figure 4.6 (a) depicts the voltage variation profiles obtained on the plain membranes. Figure 4.6 (b) is obtained from Figure 4.6 (a) using equations 2.10 and 2.12. We expect to obtain the same thermal conductivity for all the plain membranes. The results show that the longer the membrane the higher the tip temperature and the more resistant to heat flow it is. From a macroscopic point of view this may be due to the longer path that heat has to flow along to get to a bath. The plateaus may be associated to the heat losses from the membranes to the environment. Note that this could be also due to a larger air cavity. We also observe a variation in the tip temperature between the contact with the SOI and the extremity of the membranes as an indication of a change in local thermal resistance.

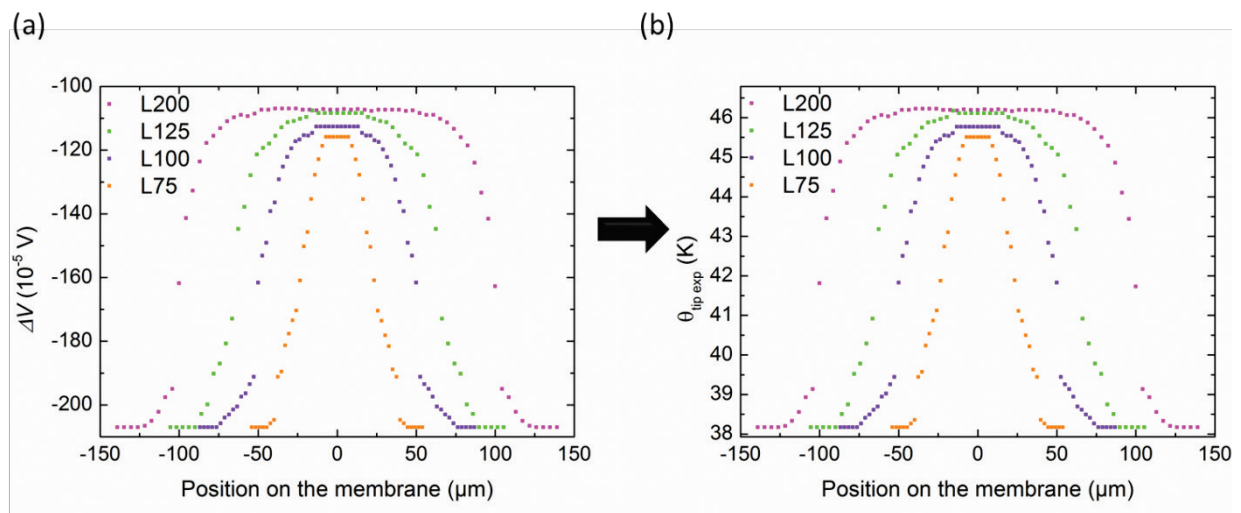


Figure 4.6 (a) Voltage profiles for four plain suspended membranes of the same cross sectional area but with different lengths. (b) Corresponding average tip temperature profiles.

The same 200 μm long plain membrane was compared to three phononic membranes of the same dimensions (Figure 4.7 (a)). Forty seven measurement points were obtained on each membrane. Figure 4.7 (b) is obtained from Figure 4.7 (a) using equations 2.10 and 2.12. The higher the plateau the lower the heat exchange between the tip and the membrane, thus the lower the thermal conductivity. This means that the membrane with P60 has the lowest thermal conductivity and the order of the plateaus follows the expected trend. The values of the thermal conductivity of the membranes will be discussed in the following section.

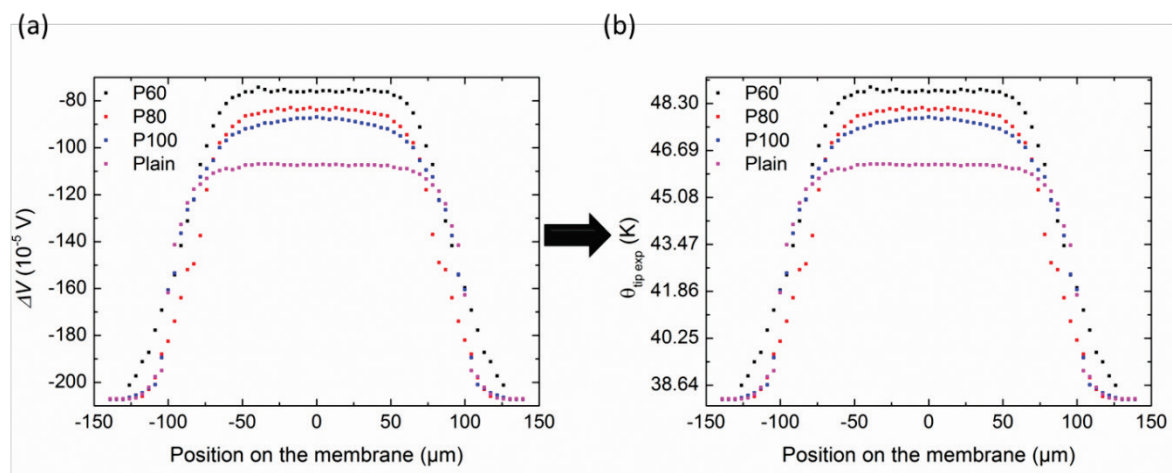


Figure 4.7 (a) Voltage profiles for four suspended membranes of the same dimensions, Plain (pink solid squares), P60 (black solid squares), P80 (red solid squares) and P100 (blue solid squares). (b) Corresponding average tip temperature profiles.

4.2.3 Sensitivity of the technique

Suspended silicon membranes of thicknesses close to the one used in this study (59.4 nm) can have thermal conductivities higher than $20 \text{ W}\cdot\text{m}^{-1}\cdot\text{K}^{-1}$ [4]. Is the SThM technique sensitive to

this kind of structure? In order to answer this question, FEM simulations were performed by accounting for the real configuration (Figure 4.8 (a)). The same tilted tip used in Chapter 2 is placed at 240 nm above the suspended membrane in its middle. Figure 4.8 (b) depicts a 2D temperature distribution in the (xy) plane. It shows that the maximum temperature rise on the membrane surface is smaller than that of the tip obtained in Figure 4.8 (a).

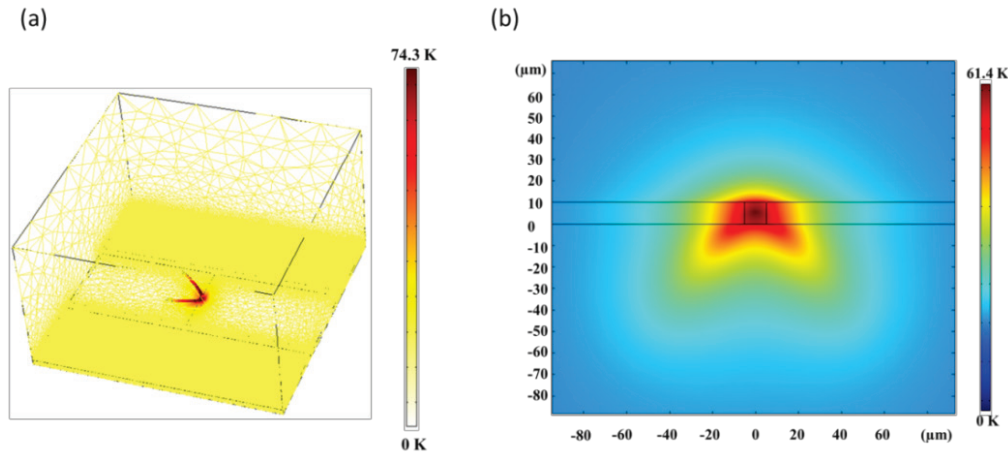


Figure 4.8 Results of simulations done on a 59.4 nm thick, 10 μm large and 200 μm long suspended membrane with $\lambda_{\text{membrane}} = 10 \text{ W}\cdot\text{m}^{-1}\cdot\text{K}^{-1}$ **(a)** Modelled geometry showing the maximum tip temperature rise. **(b)** Temperature rise distribution on the surface of the membrane from (a) and in the air around.

The average tip temperature rise with respect to the room temperature is represented as a function of the membrane (bulk) thermal conductivity by the red (green) curve in Figure 4.9. The same box of air used in Chapter 2 was also used for the configuration of the suspended membranes. Figure 4.9 shows that the SThM technique remains sensitive to membrane thermal conductivities between 20 and 60 $\text{W}\cdot\text{m}^{-1}\cdot\text{K}^{-1}$. It is shown that the sensitivity (slope of the curve) almost vanishes for bulk materials of the same thermal conductivities. Note that in this case we simulate the sensitivity of the technique based on heat conduction through air. The sensitivity of the technique may be even higher if we account for heat transport at the contact.

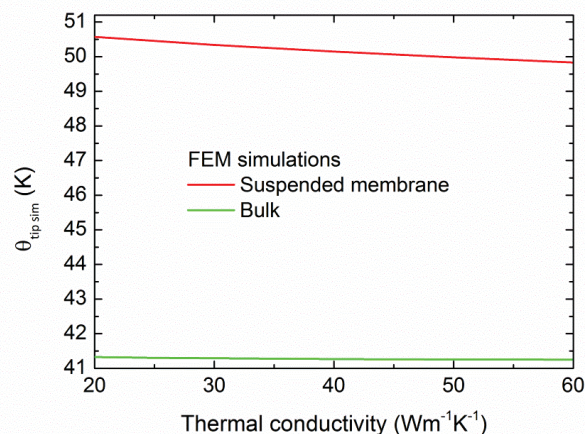


Figure 4.9 Study of the sensitivity of the SThM technique on bulk (green curve) and on suspended membranes (red curve) using FEM simulations: tip temperature rise in these two cases.

4.2.4 Membrane thermal conductivity from SThM

The SThM technique is very sensitive to the environment around the tip. This makes the analysis of the results delicate. In order to find the thermal conductivities of the suspended membranes we suggest decoupling the contributions of air and contact conductions. The former is simulated using the 3D model showed in the previous section, while the latter takes advantage from a 2D axisymmetric model (see Figure 4.10 (a)). This is the ‘Experimental and FEM simulations’ method already mentioned in Chapter 2. The average tip temperature at the contact can be written as $\Delta\theta_{contact} = \theta_{tip\ sim} - \theta_{tip\ exp}$. We first simulate the transfer through the air with FEM to obtain $\theta_{tip\ sim}$. The values of $\Delta\theta_{contact}$ are summarized in Table 4.1.

Sample	$\lambda_{membrane}$ (W.m ⁻¹ .K ⁻¹) Tested	$\theta_{tip\ exp}$ (K)	$\theta_{tip\ sim}$ (K)	$\Delta\theta_{air} = 54.84$ $- \theta_{tip\ sim}$ (K)	$\Delta\theta_{contact}$ (K)	$\frac{\Delta\theta_{contact}}{(\Delta\theta_{contact} + \Delta\theta_{air})}$
Polyimide	See Chapter 2	47.82	48.21	6.63	0.39	0.056
Fused quartz		40.64	42.94	11.9	2.3	0.162
ZnS		39.42	42.47	12.37	3.05	0.198
ZrO ₂		38.12	42.11	12.73	3.99	0.239
CdSe		36.82	41.86	12.98	5.04	0.280
L200		40	46.18	50.15	4.69	3.97
	45	46.18	50.06	4.78	3.88	0.448
	50	46.18	49.98	4.86	3.8	0.439
	60	46.18	49.83	5.01	3.65	0.421
L125	40	46.1	50.04	4.8	3.94	0.451
	45	46.1	49.94	4.9	3.84	0.439
	50	46.1	49.85	4.99	3.75	0.429
	60	46.1	49.68	5.16	3.58	0.410
L100	40	45.76	49.87	4.97	4.11	0.453
	45	45.76	49.76	5.08	4	0.441
	50	45.76	49.66	5.18	3.9	0.429
	60	45.76	49.46	5.38	3.7	0.407
L75	40	45.5	49.44	5.4	3.94	0.422
	45	45.5	49.31	5.53	3.81	0.408
	50	45.5	49.18	5.66	3.68	0.394
	60	45.5	48.95	5.89	3.45	0.369

Table 4.1 Summary of all tip temperature rise from FEM ($\theta_{tip\ sim}$) and from experiments ($\theta_{tip\ exp}$). $\Delta\theta_{air}$ and $\Delta\theta_{contact}$ are, respectively, the contribution of air and contact conductions. The ratio $\frac{\Delta\theta_{contact}}{(\Delta\theta_{contact} + \Delta\theta_{air})}$ is the contribution of the contact to heat transfer. $\theta_{oc} = 54.84$ K (see Chapter 2).

The second step is to evaluate the heat flux within the material. The system {membrane, air cavity, silicon substrate} can be assimilated to a multilayer. We will estimate the thermal conductivity of this multilayer. By defining a temperature boundary condition on a circular surface of radius b , the thermal conductance of an effective bulk can be written as $G = 4b\lambda_{effective}$ [9]. In order to obtain $\lambda_{membrane}$ we need first to find b . To achieve this, we rely on the plain membranes of different lengths. For each membrane and for a given

$\lambda_{membrane}$ we calculate $\theta_{tip\ sim}$ and then $\Delta\theta_{contact}$ (see Table 4.1). For each $\Delta\theta_{contact}$ and by using the calibration curve in Chapter 2 (see Figure 2.29) we can obtain a $\lambda_{effective}$. Then for each $\lambda_{effective}$ we can calculate a contact radius. The results for the four plain membranes are plotted in Figure 4.10 (b). For each membrane the data are fitted linearly. The resulting b is the place where the minimum possible dispersion value of total standard deviation is obtained. We obtain $b = 285$ nm which corresponds to $\lambda_{plain\ membrane} = 39.2$ W.m⁻¹.K⁻¹. This is the procedure that allows obtaining both an effective size for the thermal exchange at contact and the thermal conductivity of the membrane. The same radius b is then applied for determining the thermal conductivity of the membranes with P100, P80 and P60.

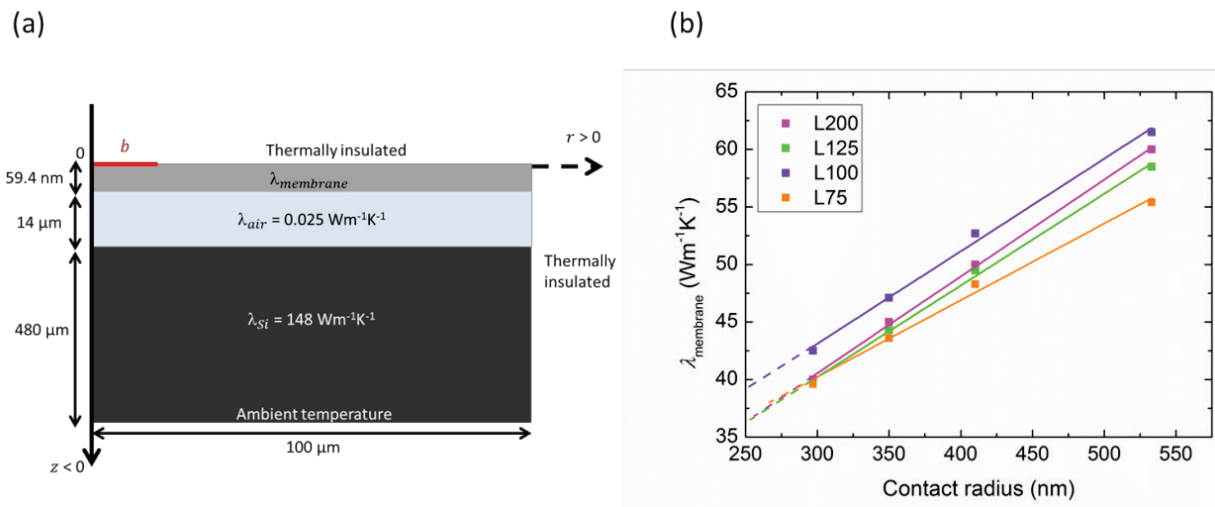


Figure 4.10 (a) 2D axisymmetric schematic of the geometry for modeling heat transfer below the contact, including the boundary conditions. The red line is the contact radius b where $T >$ ambient temperature. (b) $\lambda_{membrane}$ as a function of the contact radius for four different plain membranes. The solid lines are linear fits. The dashed lines are extensions of the linear fits.

The thermal conductivities of the studied suspended membranes are given in Figure 4.11. As expected, P60 has the lowest thermal conductivity: 14.2 W.m⁻¹.K⁻¹. This value is about 2.8 times lower than that of the plain one of the same thickness, and is more than one order of magnitude lower than that of bulk silicon. The uncertainty plotted for the plain membrane is the total standard deviation, while the error bars for P100, P80 and P60 are the uncertainties resulting from the used technique. We note that the contribution of the contact to heat transfer is much lower on bulk materials than on suspended membranes (see last column in Table 4.1). In fact larger part of a tilted tip on bulk materials exchanges heat with the sample. However, for both, bulk and suspended geometries, heat transfer through the air remains larger than that through the contact.

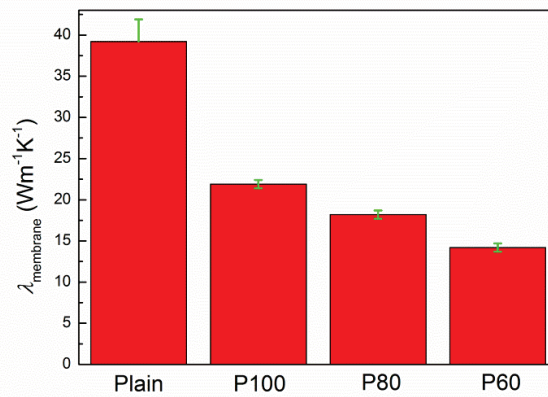


Figure 4.11 Effective thermal conductivities of the 200 μm long, 10 μm large and 59.4 nm thick suspended membranes.

SThM measurements are based on detecting a heat flux across a tip-sample contact. The signal is not only proportional to the sample thermal conductivity, but also influenced by an unknown thermal contact resistance. In order to overcome this problem, we proposed here a new way based on the decoupling of the contributions of air and contact conductions, which takes advantage of a calibration curve including this contact resistance. As a result, it is not needed to determine it directly. This method requires carrying out FEM simulations in addition to the experimental work. We note that the obtained thermal conductivities by SThM may be mainly cross-plane ones.

4.3 Micro-Raman thermometry measurement method

The experimental configuration is illustrated in Figure 4.12 (a). A 473 nm laser was focused by an Olympus 100x objective with NA 0.95 on the sample placed in an open air environment at room temperature. This configuration implies a heat source distribution that is axisymmetric in the radial direction and uniform in the vertical direction, because the membrane thickness (i.e. 59.4 nm) is much smaller than its radial direction and is much smaller than the penetration depth of silicon at this wavelength (590 nm). The excited Raman scattering signal was collected by a Labram ARAMIS (Jobin-Yvon) spectrometer. As shown in Figure 4.12 (a), the back side of the sample is not etched, so the optical transmissivity of the membrane could not be measured. The absorbance is one of the crucial parameters to know for modeling. This parameter will be discussed in details in Section 4.3.4. As discussed in Chapter 2, the laser spot radius is also a critical parameter for the determination of the thermal conductivity. We found $\sigma = 0.6 \mu\text{m}$ by performing knife-edge measurements (see Figure 2.10 (b)). Two different measurement methods were performed: ‘power variation’ and ‘temperature profile’. The former is similar to that one described in Chapter 2 and is used in Chapter 3, while the latter consists in performing a scan on the suspended membranes at a given laser power density on the sample. For the ‘power variation’ method, the laser is focused in the middle of the membrane (see Figure 4.12 (b)) and the input laser power is tuned using neutral density filters to change the membrane heating and subsequently changing the Raman peak shift due to temperature rise. For the ‘temperature profile’ method, the laser

is focused in the middle of the membrane, then it is brought on the SOI close to the ‘underetched’ part, the starting point of the scan (see Figure 4.12 (c)). In this case a temperature profile is obtained using only one laser power. We note that the ‘power variation’ method was performed at INSA de Lyon in Villeurbanne, while the ‘temperature profile’ was performed by our colleagues at IEMN in Lille with the same equipment (laser, objective and spectrometer).

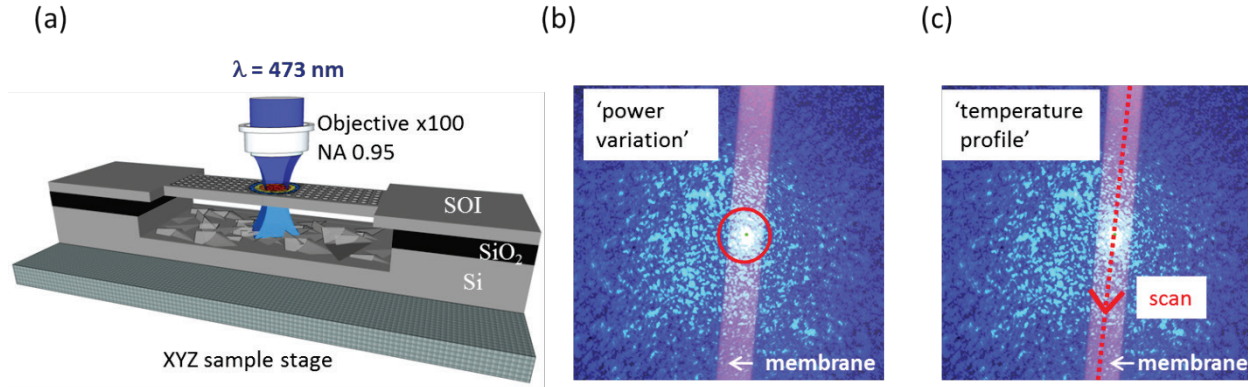


Figure 4.12 (a) Schematic showing the configuration of the studied geometry. (b) The principle of the ‘power variation’ method. (c) The principle of the ‘temperature profile’ method. (b) and (c) are photography of the focused laser spot on the membrane.

4.3.1 FEM simulations and analytical calculations

We will now analyze if heat transfer in illuminated suspended membranes can be represented by an analytical model, by solving the fin equation (see Figure 4.13). In any case, this will provide some clues on the expected temperature profiles.

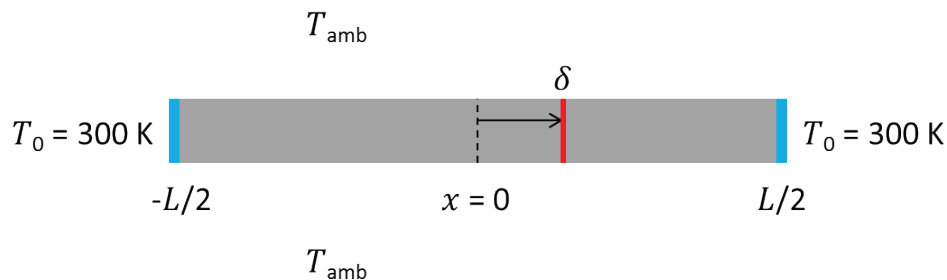


Figure 4.13 Schematic of the suspended membrane. The heat source is applied in δ .

We consider a slab of $200 \mu\text{m}$ long, $10 \mu\text{m}$ large and 60 nm thick. The ends of the slab are set at room temperature. By considering a pointlike power source and by assuming one-dimensional (T is a function of x only, the origin is in the middle of the membrane) steady-state conduction in an extended surface of constant thermal conductivity (λ) and uniform

cross-sectional area (A_c), with no volume heat generation and with negligible thermal radiation compared to solid or gas conduction, the fin equation is of the form:

$$\frac{d^2T}{dx^2}(x) - \frac{hp}{\lambda A_c}(T(x) - T_{am}) = 0, \quad (4.1)$$

where h is the heat transfer coefficient from the membrane to air (some radiation effects can be embedded in h if $h \neq 0$), p is the perimeter of the membrane and T_{am} is the surrounding temperature. Equation 4.1 can be written as

$$\frac{d^2\Delta T}{dx^2}(x) - m^2\Delta T(x) = 0, \quad (4.2)$$

where $\Delta T = T - T_{am}$ and $m^2 = \frac{hp}{\lambda A_c}$. Here h is considered to be temperature independent. A section of the membrane can be considered as isothermal if the Biot number is much less than unity, $Bi = \frac{h(A_c/p)}{\lambda} \ll 1$. In our case $Bi = 2.982 \cdot 10^{-8} \left(\frac{h}{\lambda}\right)$. In the following analysis we chose $h = 3000 \text{ W.m}^{-2}.\text{K}^{-1}$ and $\lambda = 80 \text{ W.m}^{-1}.\text{K}^{-1}$ ($Bi = 1.12 \cdot 10^{-6} \ll 1$). The heat source can have different position along the x axis. Its position from $x = 0$ is denoted by δ . Thus the symmetry of the temperature profile breaks down: the amount of heat flux in the membrane is not anymore the same in both propagation directions. On the left side (l), the solution of equation 4.2 can be written as:

$$\Delta T_l(x) = H \text{ch}(mx) + F \text{sh}(mx), \quad (4.3)$$

where ch and sh are, respectively, the hyperbolic cosine and sine. To solve this equation, two boundary conditions are needed:

$$\left\{ \begin{array}{l} \Delta T_l\left(-\frac{L}{2}\right) = 0, \\ \lambda A_c \frac{d\Delta T_l}{dx}(\delta) = l AP_0, \end{array} \right. \quad (4.4)$$

$$\left\{ \begin{array}{l} \Delta T_l\left(-\frac{L}{2}\right) = 0, \\ \lambda A_c \frac{d\Delta T_l}{dx}(\delta) = l AP_0, \end{array} \right. \quad (4.5)$$

where AP_0 is the absorbed heat source power. On the right side (r) the solution of equation 4.2 can be written similarly as:

$$\Delta T_r(x) = M \text{ch}(mx) + N \text{sh}(mx). \quad (4.6)$$

To solve this equation two boundary conditions are also needed:

$$\left\{ \begin{array}{l} \Delta T_r\left(\frac{L}{2}\right) = 0, \\ -\lambda A_c \frac{d\Delta T_r}{dx}(\delta) = r AP_0, \end{array} \right. \quad (4.7)$$

$$\left\{ \begin{array}{l} \Delta T_r\left(\frac{L}{2}\right) = 0, \\ -\lambda A_c \frac{d\Delta T_r}{dx}(\delta) = r AP_0, \end{array} \right. \quad (4.8)$$

where $r + l = 1$ due to energy conservation. The calculation gives:

$$r = \frac{\text{ch}(m\delta)\text{sh}(m\delta)[1 - \text{th}^2\left(\frac{mL}{2}\right)]}{2\text{th}\left(\frac{mL}{2}\right)} + \frac{1}{2}, \quad (4.9)$$

$$\Delta T_l(x) = \frac{lAP_0}{\lambda A_c m} \left[\frac{\text{th}\left(\frac{mL}{2}\right)\text{ch}(mx) + \text{sh}(mx)}{\text{th}\left(\frac{mL}{2}\right)\text{sh}(m\delta) + \text{ch}(m\delta)} \right], \quad (4.10)$$

$$\Delta T_r(x) = \frac{rAP_0}{\lambda A_c m} \left[\frac{-\text{th}\left(\frac{mL}{2}\right)\text{ch}(mx) + \text{sh}(mx)}{\text{th}\left(\frac{mL}{2}\right)\text{sh}(m\delta) - \text{ch}(m\delta)} \right], \quad (4.11)$$

where th is the hyperbolic tangent. For $AP_0 = 0.3 \times 10^{-3}$ W, the temperature rise at the power source is plotted in Figure 4.14 (a) as a function of the source position. The nonsymmetrical profile is formed of red and black curves with a maximum temperature level at the pointlike heat source. The black parts of the curves are the results obtained from equation 4.10, while the red ones are the results obtained from equation 4.11.

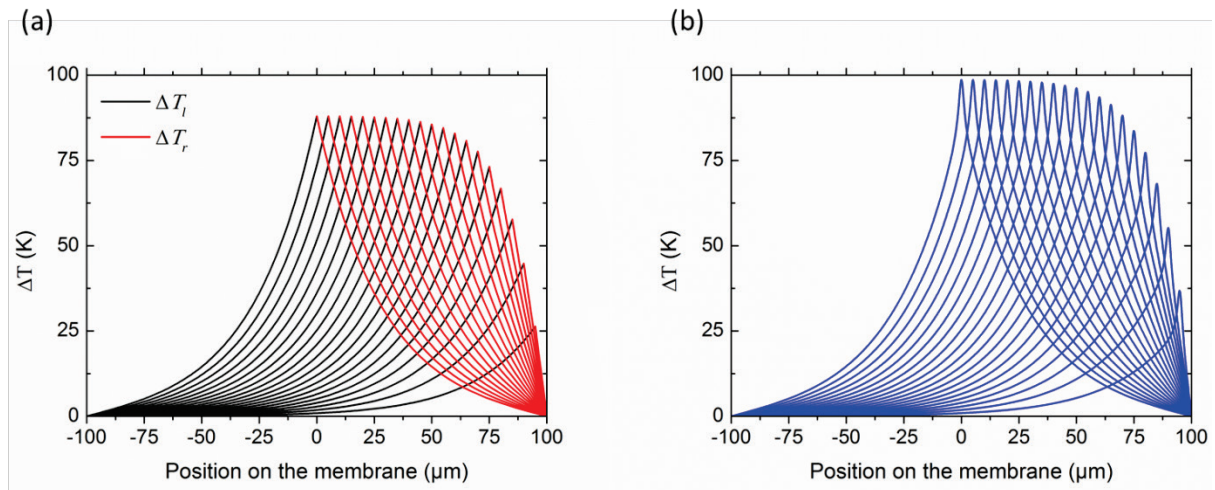


Figure 4.14 Temperature rise along the half of the membrane from (a) the analytical model and (b) the FEM simulations. The other part of the profile is symmetric to the plotted one.

Using FEM simulations, we will now reproduce the temperature profile using a heat source applied in the whole volume of the slab. This time we modeled the real laser heat source. We consider that the absorbed laser power in the slab spreads as Gaussian function along the in-plane direction and distributes uniformly in the cross-plane direction. We can write

$$P(r) = \frac{A \cdot P_0}{e\pi\sigma^2} e^{\left(\frac{-r^2}{\sigma^2}\right)}. \quad (4.12)$$

Figure 4.14 (b) is the result of the FEM simulations showing the temperature profile along half of the membrane using the Gaussian shape of the laser. The obtained nonsymmetrical

temperature rise profile (for $\delta \neq 0$) has a maximum temperature level at the center of the laser heat source and appears to be similar to the 1D results.

Figure 4.15 (a) depicts the difference in the temperature profile for FEM simulations and analytical model. The two profiles match perfectly except close to $x = 0$. This difference in shape shown in the inset of Figure 4.15 (a) is due to the consideration of the Gaussian profile in FEM simulations. We also notice that the maximum temperature level is not the same. A relative increase by 13 % is obtained from FEM simulations. By choosing the maximum temperature level at each heat source position and completing the graph by symmetry with respect to $x = 0$, the temperature profiles are plotted in Figure 4.15 (b). The profiles are not parabolic but rather a plateau is obtained due to the heat losses to the surrounding. Based on Figure 4.15 (c), the 13 % of difference induces a relative error of 20 % in thermal conductivity determination. For low thermal conductivities (i.e. $5 \text{ W.m}^{-1}\text{.K}^{-1}$) this relative error may reach 47 %. This means that in our case, the analytical model used by Murphy et al. [10] for the determination of the thermal conductivity of suspended nanowires cannot be applied. For this reason, FEM simulations are used in the following sections while accounting for the real configuration.

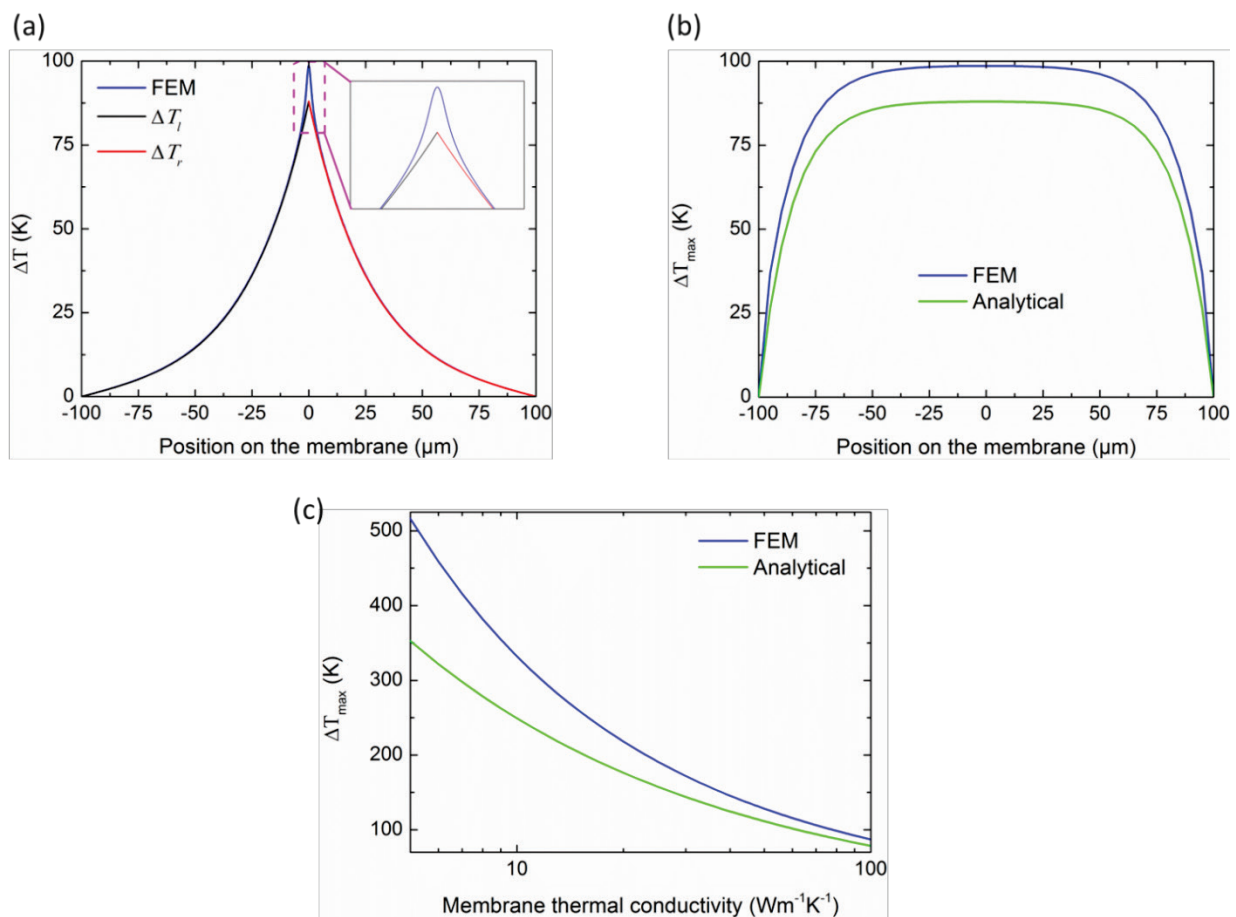


Figure 4.15 (a) Temperature rise showing the difference in maximum temperature level and in shape of the peaks. The heat source is applied in the middle of the membrane at $x = 0$. **(b)** Profiles resulting from the maximum temperature rise at each position of the power source. **(c)** Maximum temperature rise as a function of the membrane thermal conductivity from analytical (green curve) and FEM simulations (blue curve).

We note that for $h = 0$ Figure 4.14 reduces to a parabola, which is also the well-known shape of the fin equation formed for a volume heat generation instead of a pointlike heat source. In this case the obtained temperature profile is similar to the one generated by Joule heating as is the case in electrothermal techniques. However, we show in the Appendix that the temperature profiles are different for $h \neq 0$.

4.3.2 Determination of the membrane heat loss coefficient

For quantitative analysis, it is crucial to determine the coefficient describing the heat losses to the environment (h) of the suspended membranes. At room temperature and at ambient pressure, this coefficient represents the heat losses through conduction/convection mechanisms and can embed radiation under some conditions. In order to find it, we first perform experiments at room temperature in vacuum conditions. This allows us to obtain the temperature profile along the suspended membrane by considering that $h = 0$. This profile is then compared to another one measured in air at ambient pressure where $h \neq 0$. These two steps allow us to obtain the average heat loss coefficient of the membrane h_{membrane} . In fact, in vacuum, the only cause that is responsible for heat losses is radiation, which is considered to be negligible in our study.

The configuration used in FEM simulations is shown in Figure 4.16. The membrane is 200 μm long, 10 μm large and 59.4 nm thick. Note that the choices of h_{SOI} , h_s , λ_{SOI} and λ_s do not affect the maximum temperature in the middle of the membrane. But the choices of h_s and λ_s can affect the temperature profile when the laser spot is focused close to the ‘underetched’ part. As this part has a geometry that is close to the suspended membrane, we set $h_s = h_{\text{membrane}}$ and $\lambda_s = \lambda_{\text{membrane}}$.

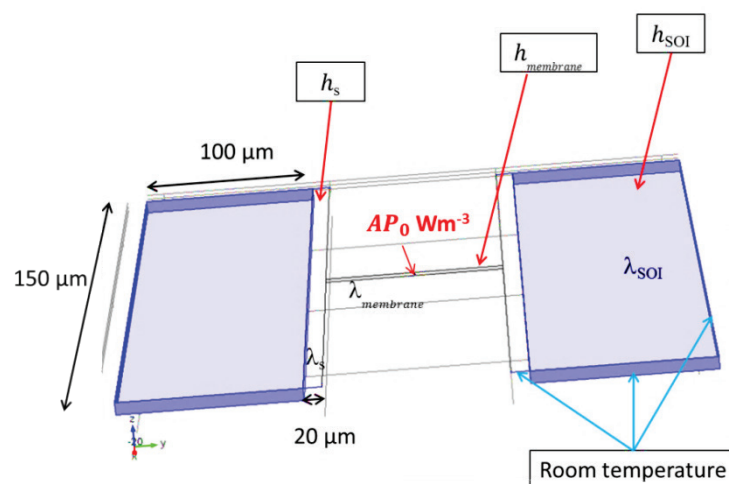


Figure 4.16 Configuration of the modelled geometry.

Two experiments were performed on the 200 μm long plain membrane under vacuum conditions using two different laser powers (185 μW and 394 μW) in Lille. Figure 4.17 depicts the results from the experiments done with a laser power of 185 μW . The absorbed laser power is AP_0 with $A = 10.63\%$. The calculation of the absorbance will be detailed in

Section 4.3.4. In order to simulate the experiments performed under vacuum conditions, the only variable parameter in the model is the thermal conductivity of the membrane. By varying it, the experimental data (orange open squares) are fitted by the solid line (orange curve) obtained from FEM simulations (see Figure 4.17). We find $\lambda_{membrane} = 59.5 \text{ W.m}^{-1}.\text{K}^{-1}$. This value was then used in the model to fit the data obtained experimentally under ambient conditions. This time the only parameter to vary is h_m . By varying it, the fit (green curve) is obtained for $h_{membrane} = 2500 \text{ W.m}^{-2}.\text{K}^{-1}$. This value is the average heat loss coefficient of the suspended membrane. The same values of $\lambda_{membrane}$ and $h_{membrane}$ were found for $P_0 = 394 \mu\text{W}$. We note that in our case the obtained thermal conductivity (in vacuum) by micro-Raman thermometry is an in-plane thermal conductivity.

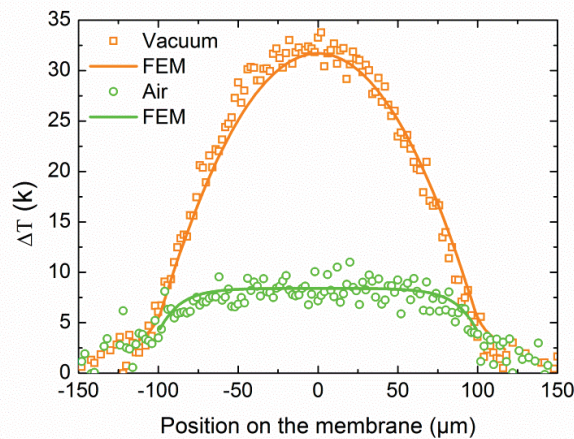


Figure 4.17 Determination of the heat loss coefficient using the ‘temperature profile’ method. Experiments performed under vacuum (green open circles) are fitted using FEM simulations (green curve). The obtained thermal conductivity is used in FEM simulations (orange curve) to fit the experimental data obtained in an open air environment (orange open squares).

4.3.3 Temperature measurements

For the two methods, the temperature reference was taken for the minimum laser power to avoid any sample heating and so any shift from the Si Raman line at room temperature ($\omega_0 = 520 \text{ cm}^{-1}$). The temperature rise is deduced from equation 2.1 and is plotted in Figures 4.18 (a) and (b). Figure 4.18 (a) is a plot of the temperature rise as a function of the input laser power resulting from the ‘power variation’ method. It shows that the slope obtained on the membrane with a pitch of 60 nm is smaller than that obtained on the membranes with P80 and P100. This means that without accounting for the absorbance of the membranes, the membrane with P80 seems to be less conductive than that with P60.

Figure 4.18 (b) is a temperature profile plot for power source $P_0 = 1.08 \text{ mW}$. It shows that the plateaus obtained for the membrane with P80 and with P100 are higher than that obtained for the membrane with P60. This suggests again that based on the experimental work and without performing FEM simulations, the membranes with P80 and with P100 seem to be less conductive than the one with P60. The obtained results from the two methods are in good agreement.

We can also observe that the temperature profiles for the membranes with P80 and P100 do not follow a straight plateau level. Relative variations of 19 % and 23 % near the membrane ends are observed for P80 and P100, respectively (see Figure 4.18 (b)). A possible explanation for this is a sample scan which is not parallel to the membrane. Indeed a higher temperature rise is expected when the laser spot is near the side of the membrane. In order to confirm this hypothesis, we performed FEM simulations at two different locations on the membrane ($x = -95 \mu\text{m}$; $y = 4 \mu\text{m}$) and ($x = 0$; $y = 0$) (see Figure 4.18 (c)). The results show a relative decrease in the maximum temperature rise of 25 % between the two positions which is bigger than the two experimental values 19 % and 23 %. Consequently, the plateau level should be defined as the lowest temperature level.

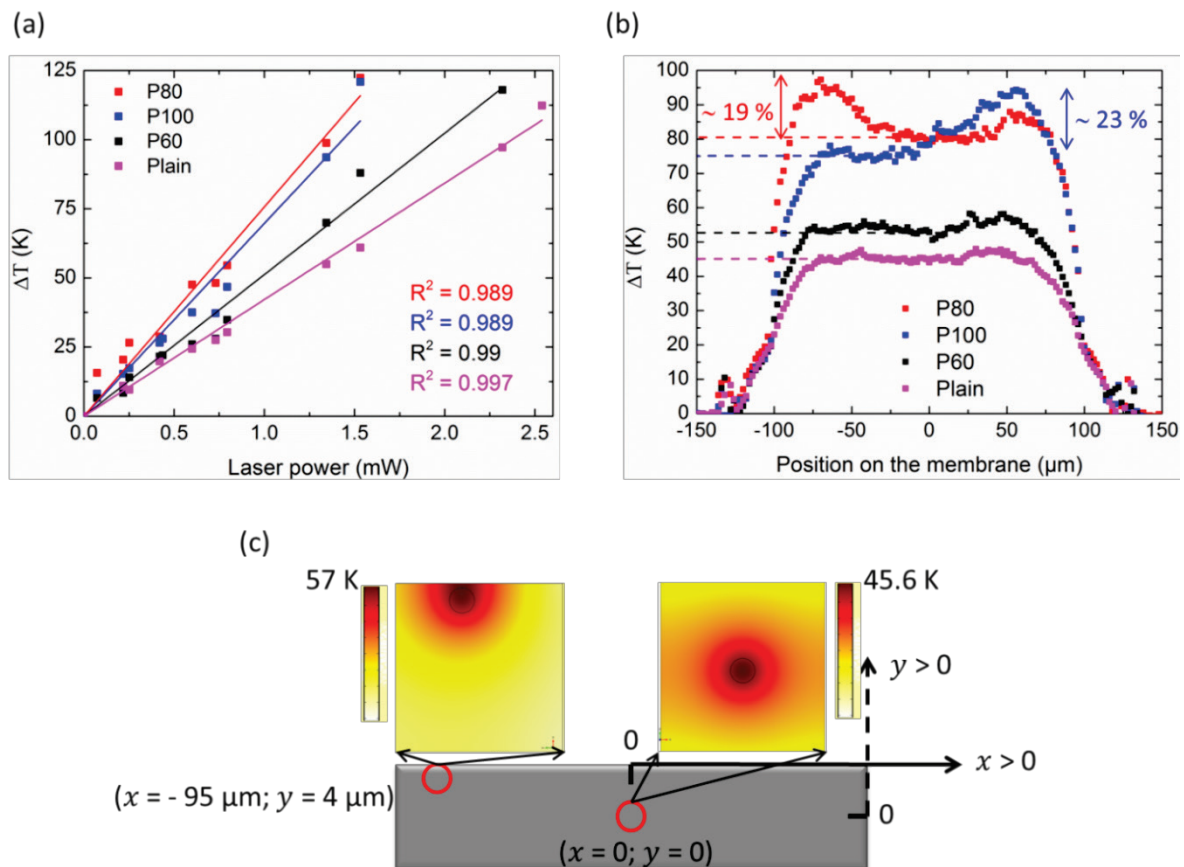


Figure 4.18 (a) Temperature rise as function of the laser power from the ‘power variation’ method. (b) Temperature rise as a function of the laser position on the membrane. (c) Schematic showing the position of the laser at two different points of the membrane with their 2D temperature distribution profiles.

4.3.4 Calculation of the absorbance

The absorbance is one of the most important parameter to know for the determination of the thermal conductivity by micro-Raman thermometry. Our samples are not back-etched, thus it was not possible to measure the transmissivity of the suspended membranes by placing a photometer under the sample. In our case numerical methods are needed to explore the optical properties of the plain and the perforated membranes. We used a numerical algorithm written

by Liu [11] based on the Rigorous Coupled-Wave Analysis (RCWA) method. The RCWA method is most typically applied to solve scattering from periodic structures. The basic idea of RCWA is to expand the electromagnetic field within the studied layer into Fourier-space (reciprocal space), represented by a sum of spatial harmonics [12]. In our model, a plane wave illuminates the photonic crystal slab from the top with arbitrary angles. The coordinate system is oriented such that the z -axis is perpendicular to the studied layer, and the structure is assumed to be periodic in the xy -plane, as shown in Figure 4.19. The source is placed at $z = 0$, where the reflectance of the membrane is calculated. The transmittance is calculated in the transmission layer where the device resides. The absorbance is determined from the conservation of the energy. The complex refractive index of silicon for $\lambda = 473$ nm was taken from Vuye et al. [13] and found to be equal to $4.4655 - 0.0474i$ for temperatures varying between 300 K and 420 K.

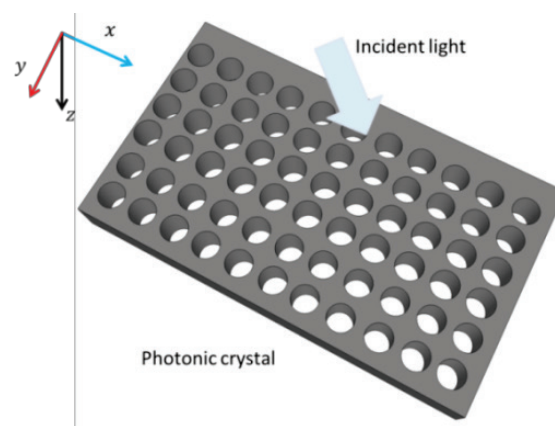


Figure 4.19 Schematic of a two-dimensional periodic structure simulated using RCWA.

4.3.4.1 Study of the membrane thickness

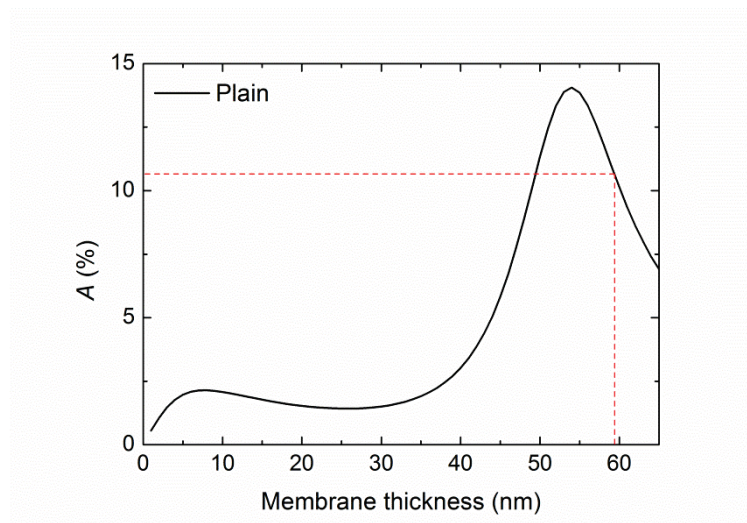


Figure 4.20 Absorbance as a function of the plain membrane thickness.

Figure 4.20 depicts the variation of the absorbance as a function of the plain membrane thickness which presents a maximum for $e = 54$ nm. As the thickness uncertainty from ellipsometry measurements is 0.3 nm, we deduced the absorbance for $e = 59.1$ nm, $e = 59.4$ nm and $e = 59.7$ nm. The obtained values are, respectively, $A = 10.81$ %, $A = 10.63$ %, and $A = 10.38$ %. Note that A surprisingly decreases while increasing the thickness of the plain membrane. We will see in Section 4.3.5 the effect of this variation in A on the thermal conductivity of the plain membranes.

4.3.4.2 Hole size study

The results obtained with the RCWA method are very sensitive to the dimensions of the periodic structures. Membranes with P60, P80 and P100 have circular holes of different diameters. We used the ImageJ software, which is an open source image processing and analysis program for making statistical distribution studies on the hole radii. For each perforated membrane a SEM image with high resolution (see Figure 4.2 (c)) was used. The difference in contrasts allows determining the size of each hole present in the SEM image. For the three pitches the SEM images show white shells around the holes (see Figure 4.2 (c)). Figure 4.21 (a) depicts the radius size distribution of 28 holes while considering the white shells as matter. It gives a mean radius $R_{\text{mean}} = 11.4$ nm and a standard deviation $SD = 0.5$ nm. Note that it was not possible to look at more than 28 holes at the same time using SEM due to the small features we are dealing with, limiting the observed field.

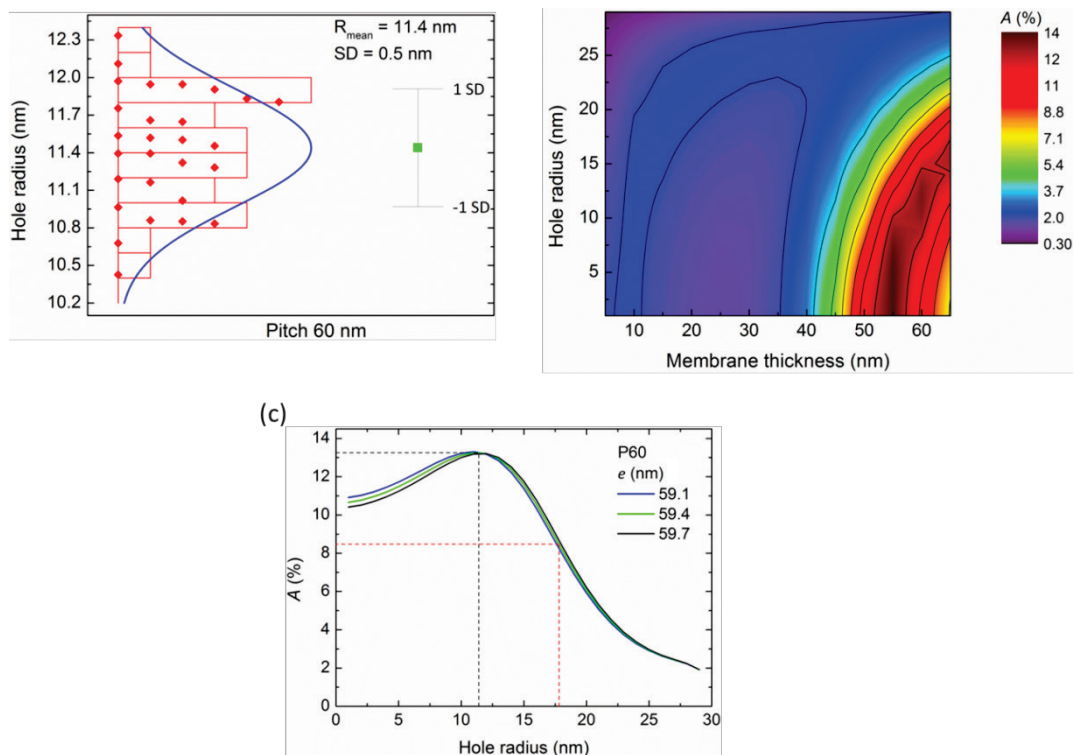


Figure 4.21 (a) Statistical study of the hole size distribution obtained on the membrane with P60. The white shells are considered as Si. (b) 2D plot showing the absorbance for different hole radii and membrane thicknesses, as calculated with the RCWA method. (c) Absorbance calculated for the membrane with P60. The black (red) dashed lines show the absorbance when accounting for the white shells as Si (transparent).

Figure 4.21 (b) is a 2D plot showing the absorbance for different hole radii and membrane thicknesses. Figure 4.21 (b) shows that we are close to a region where the absorbance can vary a lot when the hole radius varies. So by plotting the absorbance as a function of the hole radius for $e = 59.1$ nm, 59.4 nm and 59.7 nm (see Figure 4.21 (c)), we can observe a maximum peak of absorbance in the curves. For the obtained $R_{\text{mean P60}} = 11.4$ nm the absorbance is located at the maximum $A = 13.26$ %, and is represented by the black dashed line in Figure 4.21 (c) for the three curves. In contrast, if we consider that the hole is from its center up to the edge of the white shells, we obtain $R_{\text{mean P60 wp}} = 17.8$ nm, so an absorbance $A = 8.5$ %, represented by the red dashed line in Figure 4.21 (c). We will see in Section 4.3.5 the effect of this important relative decrease by 36 % in the absorbance on the determination of the thermal conductivity. We proceeded in the same way for membranes with P80 and P100. The results are shown in Figures 4.22 (a) and (b). In these cases, the relative variation in the absorbance when the white shells are considered or not as matter, is about 1 % for P80 and about 7.4 % for P100. The relative difference in the absorbance, due to thickness uncertainty, for the three curves of each pitch is always less than 0.5 %.

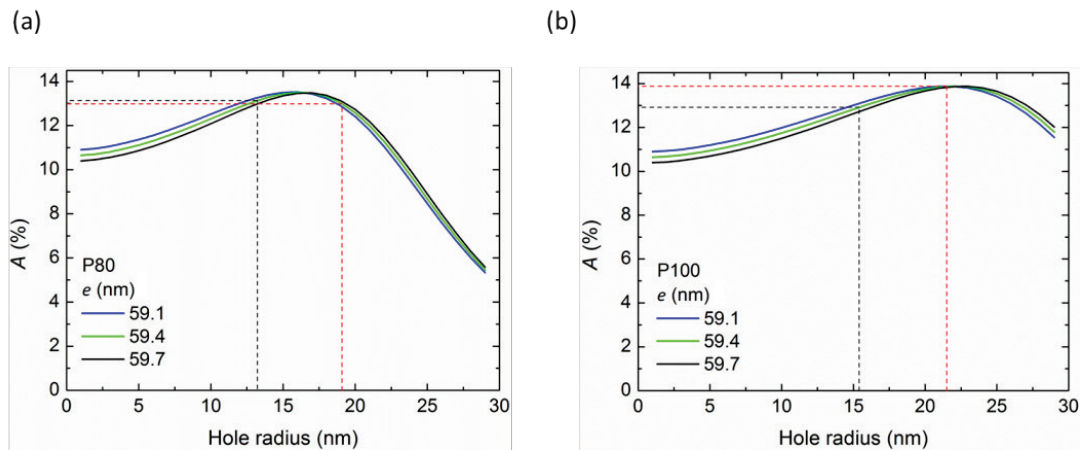


Figure 4.22 (a) Absorbance calculated for the membrane with P80. **(b)** Absorbance calculated for the membrane with P100. For **(a)** and **(b)** the black (red) dashed lines show the absorbance when accounting for the white shells as Si (transparent).

In conclusion, this parametric study of the absorbance shows that, in our case, thickness uncertainty has little influence on absorbance, while hole radius uncertainty due to the presence of white shells has a critical influence, in particular for the membrane with P60. The minimum, mean and maximum values of the calculated absorbance are summarized in Table 4.2 and Table 4.3. The porosities are calculated following $\pi R_{\text{hole}}^2 / \text{pitch}^2$. The resulting thermal conductivities based on these absorbance values will be discussed in the following section.

(a)

P60 (white shells = Si)	A (%)	Porosity (%)
$R_{\text{mean } 60} - \text{SD}; e = 59.1 \text{ nm}$	13.3	11.13
$R_{\text{mean } 60}; e = 59.4 \text{ nm}$	13.26	11.33
$R_{\text{mean } 60} + \text{SD}; e = 59.7 \text{ nm}$	13.18	11.13

(b)

P80 (white shells = Si)	A (%)	Porosity (%)
$R_{\text{mean } 80} - \text{SD}; e = 59.1 \text{ nm}$	13.39	9.61
$R_{\text{mean } 80}; e = 59.4 \text{ nm}$	13.13	8.54
$R_{\text{mean } 80} + \text{SD}; e = 59.7 \text{ nm}$	12.77	7.54

(c)

P100 (white shells = Si)	A (%)	Porosity (%)
$R_{\text{mean } 100} - \text{SD}; e = 59.1 \text{ nm}$	13.23	8.14
$R_{\text{mean } 100}; e = 59.4 \text{ nm}$	12.91	7.44
$R_{\text{mean } 100} + \text{SD}; e = 59.7 \text{ nm}$	12.55	6.78

Table 4.2 The white shells are considered as Si. **(a)** Absorbance and porosity for the membrane with P60. **(b)** Absorbance and porosity calculations for the membrane with P80. **(c)** Absorbance and porosity calculations for the membrane with P100. For **(a)**, **(b)** and **(c)** the minimum, mean and maximum values of A are shown.

(a)

P60 (white shells = transparent)	A (%)	Porosity (%)
$R_{\text{mean } 60 \text{ wp}} - \text{SD}; e = 59.1 \text{ nm}$	7.68	29.21
$R_{\text{mean } 60 \text{ wp}}; e = 59.4 \text{ nm}$	8.46	27.63
$R_{\text{mean } 60 \text{ wp}} + \text{SD}; e = 59.7 \text{ nm}$	9.27	26.1

(b)

P80 (white shells = transparent)	A (%)	Porosity (%)
$R_{\text{mean } 80 \text{ wp}} - \text{SD}; e = 59.1 \text{ nm}$	12.51	19.23
$R_{\text{mean } 80 \text{ wp}}; e = 59.4 \text{ nm}$	13	17.71
$R_{\text{mean } 80 \text{ wp}} + \text{SD}; e = 59.7 \text{ nm}$	13.33	16.25

(c)

P100 (white shells = transparent)	A (%)	Porosity (%)
$R_{\text{mean } 100 \text{ wp}} - \text{SD}; e = 59.1 \text{ nm}$	13.86	15.47
$R_{\text{mean } 100 \text{ wp}}; e = 59.4 \text{ nm}$	13.86	14.51
$R_{\text{mean } 100 \text{ wp}} + \text{SD}; e = 59.7 \text{ nm}$	13.87	13.58

Table 4.3 Same as **Table 4.2** with the white shells considered as transparent.

4.3.5 Membrane thermal conductivity from micro-Raman thermometry

We now study the effect of the absorbance on the determination of the membranes thermal conductivity. We first investigate the case where the white shells are considered as Si. In this case, we consider that, for each membrane, the absorbance is calculated for R_{mean} and $e = 59.4 \text{ nm}$ (second row in Tables 4.2 (a), (b) and (c)). Figure 4.23 (a) depicts the results from the ‘power variation’ method. By comparing them to the ones obtained in Figure 4.18

(a) (ΔT as a function of incident laser power and not the absorbed one), we observe a change in the order of the slopes. The slope for the membrane with P60 becomes the smallest one, which implies that this membrane has the lowest thermal resistance, so the highest thermal conductivity. Using FEM simulations we could determine the thermal conductivities obtained from the ‘power variation’ and the ‘temperature profile’ methods (see Figure 4.23 (b)). We observe that the thermal conductivity of the membrane with P60 is close to that of the plain membrane. If we consider the diffusive regime where phonons are propagating incoherently, they should experience more boundary scattering in the membrane with P60 than in the plain one. This means that the former should have a higher thermal resistance, so a lower thermal conductivity. Therefore the observed behavior is surprising.

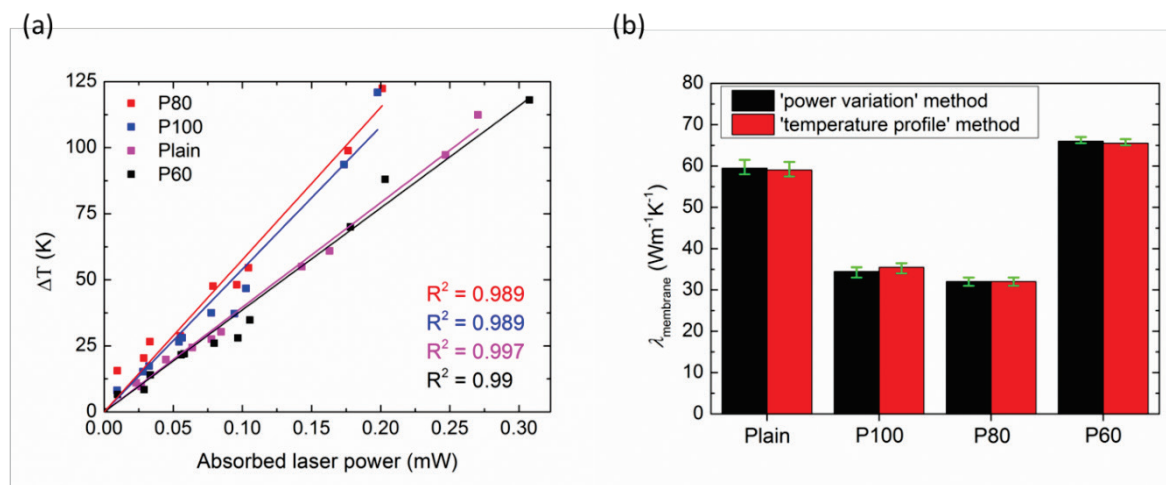


Figure 4.23 Thermal conductivity determination using micro Raman thermometry. The white shells are considered as Si for the absorbance calculations. (a) Temperature rise as a function of the absorbed laser power. The solid lines are linear fits of the experimental data. The slopes of these curves are related to the sample effective thermal conductivities. (b) Thermal conductivity values obtained from the ‘power variation’ (black columns) and the ‘temperature profile’ (red columns) methods.

We now investigate the case where the white shells are considered as transparent. In this case, we consider that, for each membrane, the absorbance is calculated for R_{mean} and $e = 59.4$ nm (second row in Tables 4.3 (a), (b) and (c)). This time the change in the order of the slopes shown in Figure 4.24 (a) points out that the membrane with P60 has the highest slope, so the lowest thermal conductivity. Figure 4.24 (b) depicts the expected behavior of thermal conductivity. The thermal conductivities of the perforated membranes are lower than that of the plain one. Moreover, as expected the thermal conductivity decreases with decreasing the pitch. The lowest thermal conductivity obtained for the membrane with P60 is $30.5 \text{ W}\cdot\text{m}^{-1}\cdot\text{K}^{-1}$ which is more than 4.8 times lower than that of bulk silicon. This value is about two times smaller than the thermal conductivity of the plain membrane of the same thickness. For both cases the error bars for the membranes with P60, P80 and P100 were plotted using the highest and the lowest absorbance values (first and third rows in Tables 4.2 (a), (b) and (c) and Tables 4.3 (a), (b) and (c)). The error bars for the plain membrane were plotted by accounting for the uncertainty in the membrane thickness.

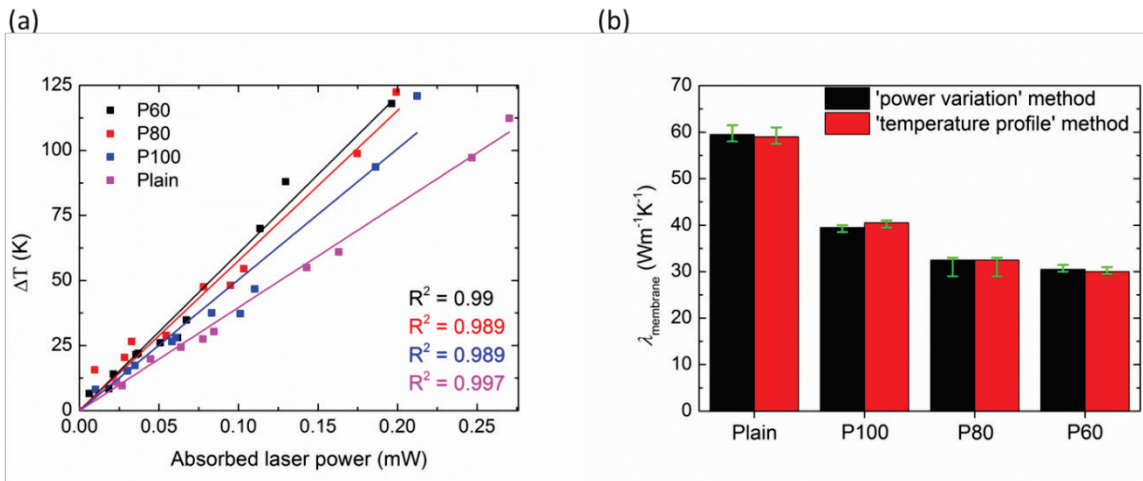


Figure 4.24 Thermal conductivity determination using micro Raman thermometry. The white shells are considered as transparent for the absorbance calculations. **(a)** Temperature rise as a function of the absorbed laser power. The solid lines are linear fits of the experimental data. The slopes of these curves are related to the sample effective thermal conductivities. **(b)** Thermal conductivity values obtained from the ‘power variation’ (black columns) and the ‘temperature profile’ (red columns) methods.

4.4 Comparison of the results

The thermal conductivities of the plain membrane obtained by SThM (39.2 W.m $^{-1}$.K $^{-1}$) and by micro-Raman thermometry (59.5 W.m $^{-1}$.K $^{-1}$) are both lower than that obtained by Nomura et al. [14] for 145 nm thick suspended silicon membranes (75 W.m $^{-1}$.K $^{-1}$). This result can be explained as the thinner the membrane, the lower the thermal conductivity. We note that the value obtained by SThM is closer to the one obtained by Chavez-Angel et al. [4] for membranes of the same thickness (30 W.m $^{-1}$.K $^{-1}$), while the value obtained by micro-Raman thermometry is in good agreement with the measured in-plane thermal conductivity (55 W.m $^{-1}$.K $^{-1}$) of silicon layers of the same thickness, in a SOI configuration, obtained by Ju and Goodson [15].

The well-known model of Fuchs and Sondheimer [16] describes the bulk thermal conductivity ($\lambda_{\text{bulk Si}}$) to membrane thermal conductivity ($\lambda_{\text{membrane}}$) relationship as follows [17]

$$\frac{\lambda_{\text{plain membrane}}}{\lambda_{\text{bulk Si}}} = F(K_n, p), \quad (4.13)$$

where

$$F(K_n, p) = 1 - \frac{3K_n}{2}(1-p) \int_1^\infty \left(\frac{1}{t'^3} - \frac{1}{t'^5} \right) \frac{1 - e^{-t'/K_n}}{1 - p e^{-t'/K_n}} dt', \quad (4.14)$$

$K_n = \Lambda/e$ (see Chapter 1), e refers to the membrane thickness and Λ is the average phonon mean free path, $1/t' = \cos \theta$, where θ is the angle between the direction of propagation of the phonon and the axis perpendicular to the membrane boundaries. p is the specular reflection

coefficient (see Chapter 1). This model considers only in-plane heat conduction. By considering that the walls of the membranes, at room temperature, are completely diffuse (see Chapter 1) and considering a MFP distribution following [4], we plotted the solid red curve in Figure 4.25 (a). Based on this result, our plain membranes are expected to have a thermal conductivity about $30 \text{ W.m}^{-1} \cdot \text{K}^{-1}$, the same obtained by Chavez-Angel et al. [4]. Figure 4.25 (a) shows also the reduction in the thermal conductivity of plain membranes for different fixed MFP values. The obtained result for the plain membrane from SThM (micro-Raman thermometry) (see Figure 4.25 (b)) is close to that obtained from the blue solid line (purple dashed line) with $\Lambda = 400 \text{ nm}$ ($\Lambda = 250 \text{ nm}$) (see Figure 4.25 (a)). Thus phonons in the plain membrane characterized by micro-Raman thermometry (SThM) have an average $\Lambda_{\text{plain Raman}} = \lambda_{\text{Raman plain membrane}} / \lambda_{\text{bulk Si}} \times 250 = 100 \text{ nm}$ ($\Lambda_{\text{plain SThM}} = \lambda_{\text{SThM plain membrane}} / \lambda_{\text{bulk Si}} \times 400 = 104 \text{ nm}$).

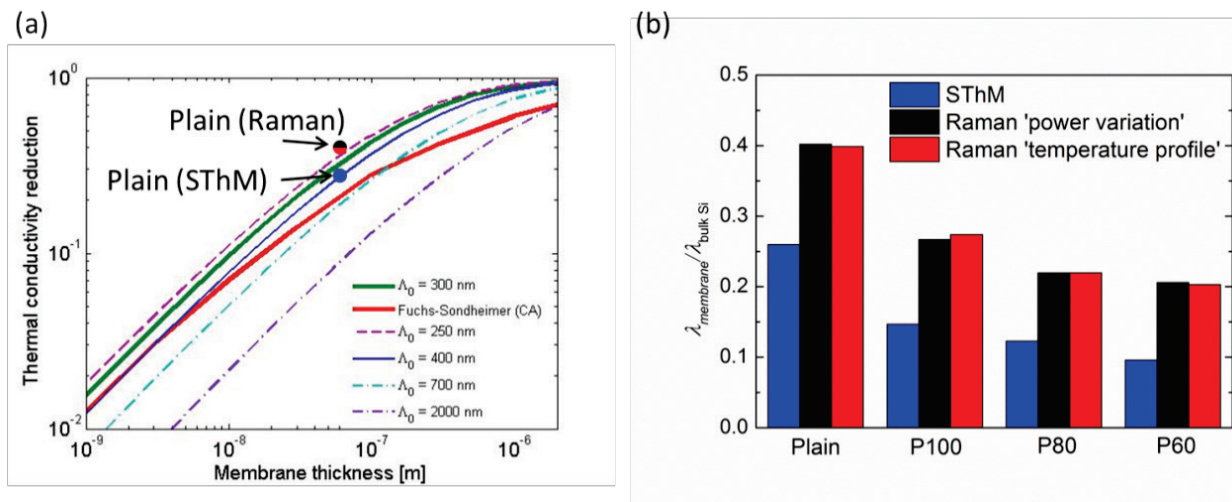


Figure 4.25 (a) Theoretical thermal conductivity reduction as a function of membrane thickness. **(b)** Experimental thermal conductivity reduction $\lambda_{\text{membrane}} / \lambda_{\text{bulk Si}}$ of the suspended membranes. Results are presented by blue, black and red columns from, respectively, the SThM technique, the ‘power variation’ and the ‘temperature profile’ methods.

The histogram in Figure 4.25 (b) depicts the normalized thermal conductivities of the investigated phononic membranes by micro-Raman thermometry (white shells = transparent) and SThM with respect to the bulk. It shows a decrease in the thermal conductivity between the plain and the perforated suspended membrane geometries. Moreover, it points out that for the PhNC membranes the smaller the pitch the lower the thermal conductivity. However, the obtained thermal conductivities by SThM are lower than the ones obtained from micro-Raman thermometry. For instance the thermal conductivity of the plain membrane obtained by SThM is 1.5 times smaller than the value obtained by micro-Raman thermometry. The lower thermal conductivity obtained from SThM can be attributed to

- the non-consideration of a thermal resistance between the air and the membrane;
- the probing of the cross-plane thermal conductivity which may be different from the in-plane one obtained from micro-Raman thermometry;

- the theoretical calculations of the absorbance of the membranes, which do not account for possible additional surface effects or exact hole geometry.

In order to better understand the origin of the reduction in the thermal conductivity of the PhNC membrane, traditional thermal conductivity models were used (see Figure 4.26). First, we used a simple model that accounts for the material removal. The resulting normalized thermal conductivities $\lambda_{\text{phononic membrane}}/\lambda_{\text{plain}} = 1 - P$ are represented by the blue line in Figure 4.26. As expected, this model strongly underestimates the observed reduction in λ , as it only accounts for the volume and neglects the hole shape and surface area. So analytical porosity models that account for the boundaries due to the hole shapes and surface area were also used. The olive curve represents the results of the Russel model $\frac{\lambda_{\text{phononic membrane}}}{\lambda_{\text{plain}}} = (1 - P^{\frac{2}{3}})/(1 - P^{\frac{2}{3}} + P)$ [18][19], while the red and purple curves represent, respectively, the results of the Eucken model $\frac{\lambda_{\text{phononic membrane}}}{\lambda_{\text{plain}}} = (1 - P)/(1 + P/2)$ [18][19] and the results of the Maxwell-Garnett model $\frac{\lambda_{\text{phononic membrane}}}{\lambda_{\text{plain}}} = (1 - P)/(1 + P)$ [2]. All these models still underestimate the experimental reduction in λ . This implies that the reduction is not only due to an increase in the porosity. Therefore, in addition to the material removal, boundary scattering may be the reason for the reduction in the thermal conductivity of the membranes. This reduction is more important for the smallest pitch where phonons experience more scattering at the hole boundaries. Our experimental results from the two characterization techniques confirm the reduction in the thermal conductivity while decreasing the pitch. Experimental values obtained, at room temperature, in [20][2][1], show the same trend, while a further reduction in λ is shown by the Maxwell-Garnett and the Eucken models compared to the one obtained in [14].

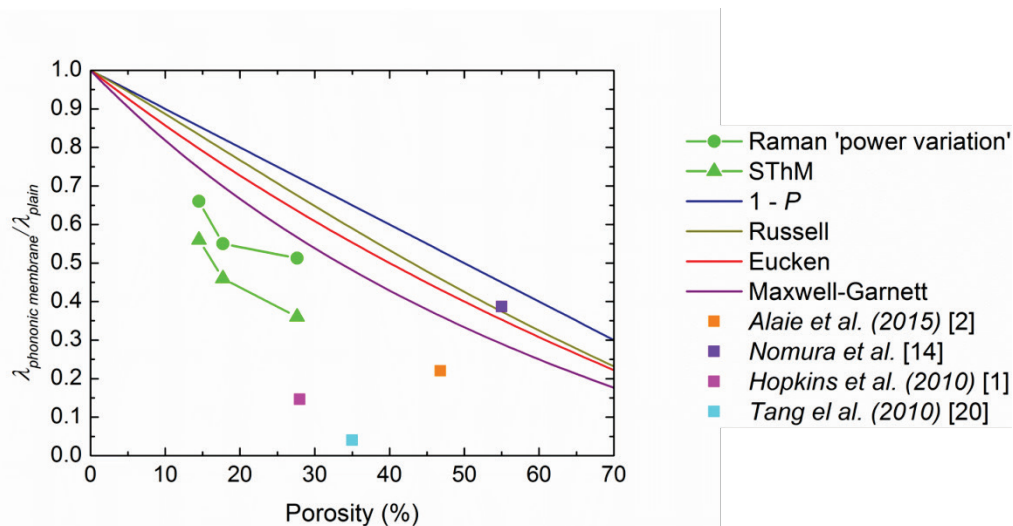


Figure 4.26 Normalized thermal conductivities of PhNC samples vs porosity. The experimental results are compared to various models and values obtained in the literature. Due to the very good agreement between the two Raman methods, only results from the ‘power variation’ method were plotted.

The effect of the boundaries on heat transport in the perforated suspended membranes can be represented by plotting the thermal conductivity of the latter as a function of the surface to

volume ratio S/V (see Figure 4.27), where $S = 2 L w - 2 (N_w N_L 2 \pi R_{hole}^2) + N_w N_L 2 \pi R_{hole} e + 2 w e + 2 L e$ (N_w and N_L are, respectively, the number of holes along the width w and the length of the membrane) and $V = e L w - N_w N_L \pi R_{hole}^2 e$ (see Figure 4.28). Our experimental results confirm the reduction in the thermal conductivity while increasing S/V , this is due to the increasing scattering that phonons can experience. The upper abscissa in Figure 4.27 shows V/S which provides an idea about the characteristic length for a given configuration. Comparing our results to the ones obtained in literature, it turned out to be difficult to make a firm conclusion as the values are too much dispersed.

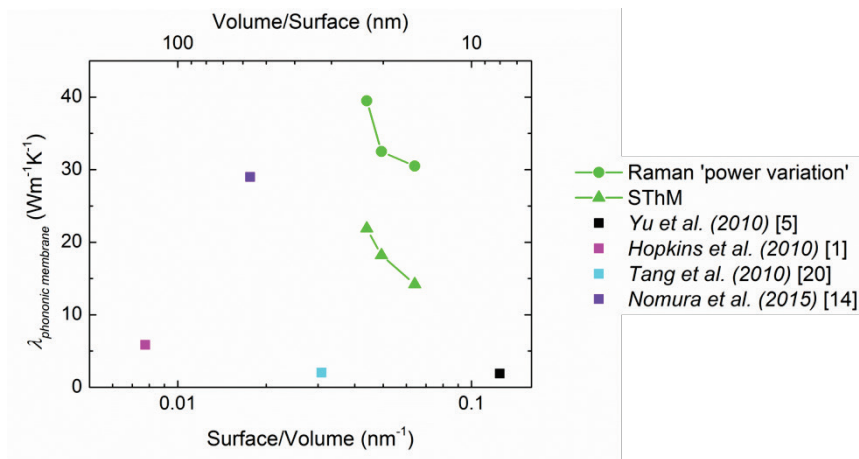


Figure 4.27 Thermal conductivities of the PhNC samples as a function of Surface/Volume ratio. The experimental results are compared to values obtained in the literature. Due to the very good agreement between the two Raman methods, only results from the ‘power variation’ method were plotted.

Hopkins et al. [1], Alaie et al. [2] and Yu et al. [5] suggested, at room temperature, that not only phonon boundary scattering and porosity are responsible for the reduction in the thermal conductivity of their PhNC membranes. They attributed the additional reduction in thermal conductivity to phonon coherence effects. But the characteristic lengths in [1] and [2] are larger than 100 nm. Theoretically speaking, based on Figure 1.10, it is not possible to see coherence effects at room temperature for these membranes. In our case, phonon coherence is expected to appear at 4 K for the membrane with P60 where the characteristic length is the neck size (~ 24 nm) (see Chapter 1).

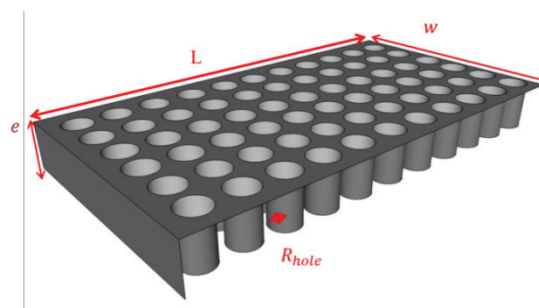


Figure 4.28 Schematic of a PhNC membrane showing its dimensions. $N_w = 6$ and $N_L = 11$.

4.5 Summary and perspectives

In this chapter, a SThM technique and two micro-Raman thermometry methods able to measure, respectively, cross-plane and in-plane thermal conductivities are introduced and applied to plain and PhNC suspended silicon membranes. For the SThM part, we showed the effect of the tip position while scanning the membranes. We also succeeded in obtaining the thermal conductivity of the suspended membranes by suggesting a new data analysis method. We note that the obtained contact radius 285 nm in our case may be smaller if dealing with a straight tip (90° with respect to the sample surface). The results show a decrease in the thermal conductivity of the PhNC membranes while decreasing the pitch compared to the plain membrane of the same thickness. Compared to the plain membranes (bulk silicon), a maximum decrease in thermal conductivity of about 2.8 times (more than one order of magnitude) is obtained for P60. For the micro-Raman thermometry part, we succeeded in obtaining the thermal conductivity of the suspended membranes, with a single scan laser technique, after finding experimentally the heat loss coefficient. The results from the two micro-Raman thermometry methods are in very good agreement. Compared to the plain membrane (bulk silicon), a maximum decrease in thermal conductivity of about 2 (more than 4.8) times is obtained for P60. The RCWA method was used for the exact calculation of the absorbance of the membranes. Rigorous studies of the hole sizes were performed showing the effect of the mean hole size on the absorbance, and so on the determination of the thermal conductivity. The SThM and the micro-Raman thermometry results show the same trend in the decrease of the thermal conductivity, when considering for the latter the white shells observed around the holes as transparent. As a result, we believe that the white shells should indeed be considered as transparent. The uncertainty could come from the fact that the holes, during the etching process, are not etched in a straight direction. The reduction in the in-plane thermal conductivity reveals that in addition to the porosity, phonon boundary scattering, both at the hole surfaces and at the interfaces, is sufficient to describe this reduction.

All the present results were obtained at room temperature. Since the implementation of SThM at low temperature is complicated and the Raman signal essentially disappears at such temperature, alternatives have to be found. The photothermal method used by the group of Nomura is a possibility. However, a method allowing reaching optimally the lowest temperatures is the electro-thermal technique. It is likely that such measurements will be performed soon on the samples. We note that theoretical studies and phonon dispersion relation computation would be helpful for a better understanding of the origin of the reduction in the thermal conductivity for the PhNC membranes. At the sub-100 nm scale, it is key to perfectly characterize the samples. Performing transmission electron microscopy (TEM) experiments would help to understand the nature of the white shells around the holes. The nature of the walls is to be known with the best possible resolution and we remind that oxidizing the PhNC membranes would be advantageous towards a higher decrease in thermal conductivity. Finally, exploring thicker membranes would be helpful to accentuate the effect of the period. Indeed, the characteristic period size is currently too close to be completely disentangled from the decrease due to the thickness. Finally, investigating PhNC membranes with arbitrarily distributed holes, while keeping the same characteristic lengths, would highlight the effect of the periodicity on phonon transport. To observe such effect at room

temperature, it would be needed to find a material with contributing wavelengths larger than a few nanometers. This stays currently a challenge.

Bibliography

- [1] P. E. Hopkins, C. M. Reinke, M. F. Su, R. H. Olsson, E. A. Shaner, Z. C. Leseman, J. R. Serrano, L. M. Phinney, and I. El-Kady, "Reduction in the thermal conductivity of single crystalline silicon by phononic crystal patterning". *Nano Lett.*, vol. 11, no. 1, pp. 107–112, 2011.
- [2] S. Alaie, D. F. Goettler, M. Su, Z. C. Leseman, C. M. Reinke, and I. El-Kady, "Thermal transport in phononic crystals and the observation of coherent phonon scattering at room temperature". *Nat. Commun.*, vol. 6, p. 7228, 2015.
- [3] M. Nomura, J. Nakagawa, Y. Kage, J. Maire, D. Moser, and O. Paul, "Thermal phonon transport in silicon nanowires and two-dimensional phononic crystal nanostructures". *Appl. Phys. Lett.*, vol. 106, no. 14, 2015.
- [4] E. Chavez-Angel, J. S. Reparaz, J. Gomis-Bresco, M. R. Wagner, J. Cuffe, B. Graczykowski, A. Shchepetov, H. Jiang, M. Prunnila, J. Ahopelto, F. Alzina, and C. M. Sotomayor Torres, "Reduction of the thermal conductivity in free-standing silicon nano-membranes investigated by non-invasive Raman thermometry". *APL Mater.*, vol. 2, no. 1, 2014.
- [5] J.-K. Yu, S. Mitrovic, D. Tham, J. Varghese, and J. R. Heath, "Reduction of thermal conductivity in phononic nanomesh structures". *Nat. Nanotechnol.*, vol. 5, no. 10, pp. 718–21, 2010.
- [6] V. Lacatena, M. Haras, J. F. Robillard, S. Monfray, T. Skotnicki, and E. Dubois, "Phononic engineering of silicon using 'dots on the fly' e-beam lithography and plasma etching". *Microelectron. Eng.*, vol. 121, pp. 131–134, 2014.
- [7] V. Lacatena, "Fabrication and thermal characterization of phononic engineered silicon membranes for thermoelectric applications". *PhD thesis*, 2016.
- [8] M. Haras, "Thermoélectricité non-conventionnelle basée sur les technologies silicium en film minces". *PhD thesis*, 2016.
- [9] S. Lefevre, "Modélisation et élaboration des métrologies de microscopie thermique à sonde locale résistive. Thesis". 1994.
- [10] K. F. Murphy, B. Piccione, M. B. Zanjani, J. R. Lukes, and D. S. Gianola, "Strain- and defect-mediated thermal conductivity in silicon nanowires," *Nano Lett.*, vol. 14, no. 7, pp. 3785–3792, 2014.
- [11] J. Liu, "Fabrication and Optical Simulation of Periodic Nanostructures and their Applications". *PhD thesis*, 2016.
- [12] F. G. Kaspar, "Diffraction by thick, periodically stratified gratings with complex dielectric constant" *J. Opt. Soc. Am.*, vol. 63, no. 1, pp. 37–45, 1973.
- [13] G. Vuys, S. Fisson, V. Nguyen Van, Y. Wang, J. Rivory, and F. Abelès, "Temperature dependence of the dielectric function of silicon using in situ spectroscopic ellipsometry". *Thin Solid Films*, vol. 233, no. 1–2, pp. 166–170, 1993.
- [14] M. Nomura, Y. Kage, J. Nakagawa, T. Hori, J. Maire, J. Shiomi, R. Anufriev, D. Moser, and O. Paul, "Impeded thermal transport in Si multiscale hierarchical architectures with phononic crystal nanostructures". *Phys. Rev. B - Condens. Matter Mater. Phys.*, vol. 91, no. 20, pp. 1–6, 2015.
- [15] Y. S. Ju and K. E. Goodson, "Phonon scattering in silicon films with thickness of order 100 nm". *Appl. Phys. Lett.*, vol. 74, no. 20, p. 3005, 1999.
- [16] K. Fuchs, "The conductivity of thin metallic films according to the electron theory of metals". vol. 157, no. 1936, pp. 100–108, 1937.
- [17] F. Warkusz, "Size effects in metallic materials," *Electrocompon. Sci. Technol.*, vol. 5, pp. 99–105, 1978.
- [18] L. Yang, N. Yang, and B. Li, "Extreme low thermal conductivity in nanoscale 3D Si phononic crystal with spherical pores". *Nano Lett.*, vol. 14, no. 4, pp. 1734–1738, 2014.
- [19] D. Song and G. Chen, "Thermal conductivity of periodic microporous silicon films". *Appl. Phys. Lett.*, vol. 84, no. 5, pp. 687–689, 2004.
- [20] J. Tang, H. T. Wang, D. H. Lee, M. Fardy, Z. Huo, T. P. Russell, and P. Yang, "Holey silicon as an efficient thermoelectric material". *Nano Lett.*, vol. 10, no. 10, pp. 4279–4283, 2010.

Chapter 5. Towards phonon coherence in porous silicon superlattices

2D phononic structures require developed and complicated manufacturing steps in the nanotechnology domain. In order to propose an easier way to analyze phonon coherence effects, this chapter introduces a one-dimensional Si-based phononic structure. Before exposing the final configuration, a calibration method is detailed. To end the chapter, a characterization method is proposed for the measurement of the thermal properties of the samples.

5.1 Introduction

Superlattices provide interfaces between the two different materials constituting them (see Figure 5.1 (a)). These interfaces can be considered as Kapitza resistances, inducing phonon diffuse scattering, thus destroying coherence. This phenomenon also reduces the thermal conductivity of the structure. Therefore, the separation and the analysis of contributions of periodicity and interfaces to the reduction in the thermal conductivity become complicated. Porous silicon superlattices (PSi-SLs) are made of alternating layers of different porosities starting from the same Si wafer. This may reduce the effect of the interfacial thermal resistances, which are supposed to be responsible for the suppression of the presence of coherent phonons in many experiments. Therefore, PSi-SLs can be seen as novel interesting coherent structures where the periodicity cannot be associated to sharp interfaces, but rather the layers of different porosities are interconnected (see Figure 5.1 (b)). Previous studies showed phonon coherence in III-V and oxide superlattices manufactured, respectively, using MOCVD [1] and MBE [2]. Despite the good control of these deposition and growth processes, strain, dislocation due to lattice mismatch may occur. Interface mixing may also occur. All these phenomena affect heat transport in superlattices. Note that interface mixing may be the cause of the absence of the minimum in thermal conductivity in [1]. On the other hand, the growth techniques are expensive and not compatible with CMOS technology.

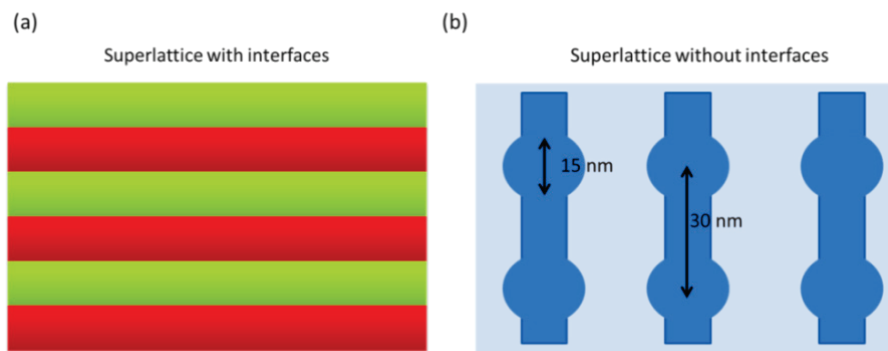


Figure 5.1 (a) Superlattice with interfaces made of two different materials. (b) Superlattice without interfaces made of porous silicon.

The possibility of modulating the refractive index by controlling the porosity (P) made of porous silicon (PSi) an interesting material for many photonic applications. It is in particular due to the possibility to manufacture Bragg mirrors. Vincent [3] was the first, in 1993, to obtain Bragg mirrors using mesoporous silicon structured in a multilayer configuration. Parsons et al. [4][5], Bruyant et al. [6], Aliev et al. [7] and Thomas et al. [8] showed that the modulation of the elastic properties through the porosity of the periods constituting the porous silicon superlattices (PSi-SLs) may result in Brillouin zone-folding effects. Such folding is often accompanied by the appearance of bandgaps in the phonon frequency spectrum. Their results, for micrometric porous layers, revealed that PSi-SLs can show stop bands for wavelengths in the GHz frequency range. Thus, PSi-SLs can constitute one-dimensional hypersonic phononic-photonic crystals. As we are interested in thermal phonons located in the THz frequency range, we propose the manufacturing of PSi-SLs with nanometric porous layers with periods shorter than 30 nm. These structures may lead to phonon band folding for THz frequencies. Using this configuration, we aim at evidencing the phonon coherence effect in Si-based materials at 4 K (see Figure 1.10). We note that in PSi-SLs prepared by electrochemical means, dislocations and lattice mismatch problems are avoided due to the use of the same material (here Si). In addition the process is cheap and CMOS compatible in comparison to the ones used in [1] and [2].

5.2 Formation of porous silicon superlattices

PSi-SLs can be formed by alternating the current density (J) between two different values. Etching times have then to be adjusted for thickness control due to important etching kinetic variation with J . PSi layers were formed by electrochemical etching of <100> monocrystalline boron-doped p^+ silicon wafers 500 μm thick. The electrolyte consists of 48 wt% HF and pure ethanol in a volume ratio of 1:1. Boron doping level is about 10^{19} cm^{-3} , which corresponds to a resistivity of 0.01-0.02 $\Omega\cdot\text{cm}^{-1}$. The choice of p^+ Si wafer was due to the very good controllability of the anodization process and the possibility of reducing the layer thickness down to the pore dimension. The electrochemical anodization was done in a fridge where the temperature can be monitored. Experiments were performed at $-35 \text{ }^\circ\text{C}$. Working at low temperature allows slowing down the anodization process as we aim at obtaining very thin PSi layers using short etching time (t), and especially to reduce the interface fluctuations [9].

5.2.1 Calibration of the anodization cell

5.2.1.1 Micrometric porous silicon mono- and bilayers

The best characterization technique for PSi-SLs with nanometric periods is transmission electron microscopy (TEM). However, this technique cannot be used as a regular characterization method, since it is costly and requires long preparation times. For this reason microreflectivity was used to guaranty the quality of our periodic PSi layers, while TEM was performed on selected samples. The aim was to obtain high modulation in the porosities (refractive index) of the nanometric porous layers constituting the period of the PSi-SL. Hence, two current densities and two etching times are needed. In that event, a calibration of the anodization cell is needed as a first step towards the PSi-SLs configuration. Due to time

constraints, we used a calibration curve (see Figure 5.2) obtained by Guillermain et al. [10], on $e = 8.8 \mu\text{m}$ thick porous layers, using the same anodization cell at INL laboratory. We worked towards obtaining $P_1 = 75 \%$ ($P_2 = 30 \%$) as porosity of the first (second) porous layer. To that end, based on Figure 5.2 and using equation 3.6, P_1 corresponds to the refractive index 1.5 ($J_1 = 6.5 \text{ mA.cm}^{-2}$) and P_2 corresponds to a refractive index 2.55 ($J_2 = 0.3 \text{ mA.cm}^{-2}$). Therefore we used the same current densities but with different etching times. The anodization parameters are summarized in Table 5.1.

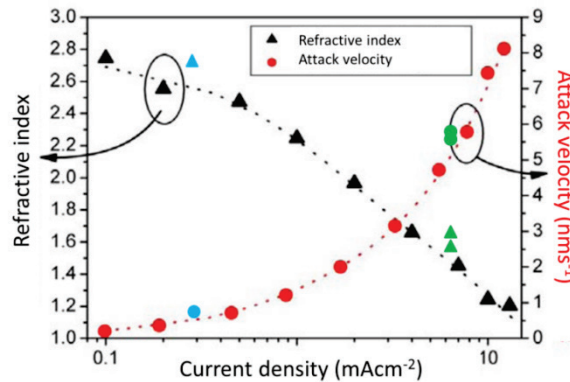


Figure 5.2 Calibration curve for the formation of porous silicon at $-40 \text{ }^\circ\text{C}$ with an electrolyte that consists of 48 wt% HF and pure ethanol in a volume ratio of 1:1 [10]. The blue and green data are our experimental data obtained at $-35 \text{ }^\circ\text{C}$ and added to the original figure.

Each experimental spectrum obtained from microreflectivity was fitted with a theoretical curve, by varying the thickness and the refractive index of the porous layers, with respect to the amplitude and the position of the peaks. The obtained porosities and attack velocities are added to the original figure from [10] (see Figure 5.2). We observe that our experimental data do not match well the calibration curve. In fact, the temperature of our anodization cell was $-35 \text{ }^\circ\text{C}$, larger than the one used in [10] ($-40 \text{ }^\circ\text{C}$). In our case, the electrochemical etching of Si is faster so the attack velocity should be greater, which is in good agreement with the obtained results (see Figure 5.2). We also observe a difference in the porosity mainly for the low porosity. Here again, the temperature may have an impact. The obtained porosities in our case are $P_1 = 70 \%$ and $P_2 = 24 \%$. P_1 is the average porosity obtained from the two experimental data using J_1 .

Sample	w1b2	w1f1	w1c2
$J \text{ (mAcm}^{-2}\text{)}$	0.3	6.5	6.5
$t \text{ (s)}$	7200	1440	1440
n	2.74	1.67	1.58
$e \text{ (}\mu\text{m)}$	4.32	8	8.17
$P \text{ (}\%\text{)}$	24	68	72
Attack velocity (nm.s ⁻¹)	0.6	5.55	5.67

Table 5.1 Summary of the anodization parameters.

Mazzoleni et al. [11] showed that the refractive indices and etching rates are modified in presence of a multilayer structure. As a consequence, the second step is the optimization of PSi-bilayers using the same anodization parameters mentioned before. Guillermain et al. [10] highlighted the origin of this problem and suggested to start the formation of PSi multilayers with the layer of the highest porosity. Indeed, starting with the layer of the lowest porosity disrupt the penetration of the electrolyte, and does not allow the regeneration of fluoride ions (F^-). Rather, having the layer of the highest porosity on top of a bilayer and applying etch-stop times (t_{stop}) while $J = 0$ favors the ion enrichment. In this test experiment, we aimed at obtaining a bilayer of two porous silicon layers of $d_1 = 3.6 \mu\text{m}$ and $d_2 = 4 \mu\text{m}$, using the same current densities J_1 and J_2 with $t_1 = 642 \text{ s}$ and $t_2 = 6667 \text{ s}$. The etch-stop time was $t_{stop} = 10t_1$ as recommended by Billat et al. [12]. The resulting reflectivity spectrum from our bilayer PSi formed of two porous layers of P_1 and P_2 is displayed by the blue curve in Figure 5.3. Figure 5.3 (a) shows that the simulated theoretical profile (red curve) for the expected porosities and layer thicknesses does not match the experimental curve (blue curve). Therefore, an adjustment of the layer thicknesses was performed while keeping the same P_1 and P_2 . The best fit was obtained for $d_1 = 3.56 \mu\text{m}$ and $d_2 = 3.92 \mu\text{m}$ (see Figure 5.3 (b)). These values are close to the expected ones. Note that the theoretical fit does not consider the interface roughness. Therefore, we conclude that it becomes difficult to follow the same procedure for the characterization of more than two thick porous silicon layers.

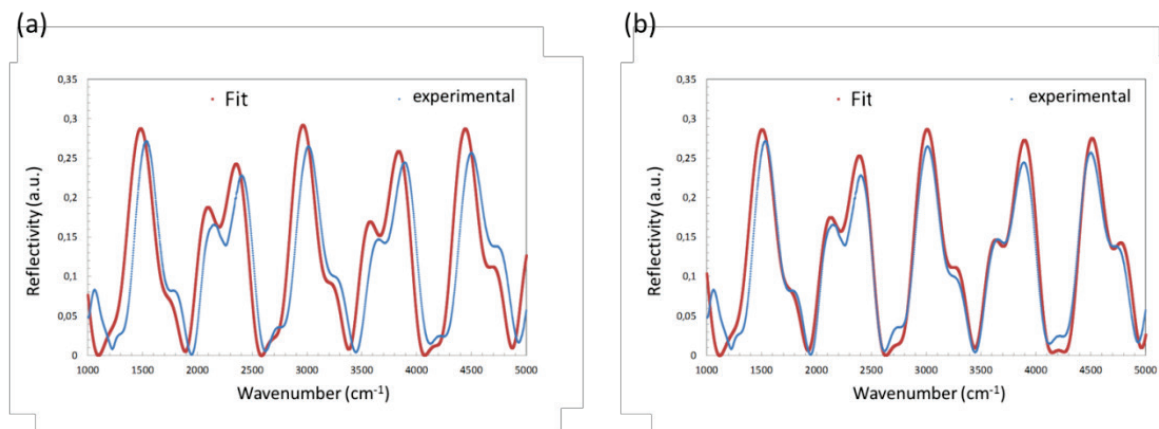


Figure 5.3 Reflectivity spectra for a PSi bilayer at $-35 \text{ }^\circ\text{C}$ (a) Simulated profile (red curve) with the expected thicknesses. (b) Fit of the experimental curve. The electrolyte consists of 48 wt% HF and pure ethanol in a volume ratio of 1:1.

5.2.1.2 Nanometric porous silicon monolayer

As microreflectivity requires layers thicker than the reflected wavelengths for making the obtained spectrum exploitable, X-ray reflectivity was considered for the characterization of a 30 nm thick mono porous silicon layer with a porosity of 24 % formed on a 500 μm thick bulk Si. The X-ray reflectivity (XRR) method is nondestructive and can be used for evaluating the layer structure, thickness, density, and surface or interface roughness of thin or multilayer films. To this aim, a PSi layer was prepared using a current density of $0.3 \text{ mA}\cdot\text{cm}^{-2}$

and with an etching time of 50 s. XRR experiments were performed with Dr Romain Bachelet at INL (Ecole Centrale de Lyon). The experimental reflectivity spectrum is represented by the black curves in Figure 5.4. There is only an intensity decay with a reflection angle while the expected Kiessig fringes [13] are vanished. The red curves in Figure 5.4 illustrate the simulated reflectivity profiles. The adjustable parameters are the layer thickness, the relative density (ρ_{PSi}/ρ_{Si}) and the surface and interface roughness. For both simulated profiles we set $d = 30$ nm, $\rho_{PSi}/\rho_{Si} = 0.76$ (see equation 3.4). For the simulated profile in Figure 5.4 (a) we set the interface (rms) roughness and the surface (rms) roughness to be equal to 0.2 nm, while for the one in Figure 5.4 (b) they are considered as free parameters. The resulting simulated profile in Figure 5.4 (a) does not fit the experimental one and depicts many Kiessig fringes. Rather, a very good fit of the experimental spectrum is observed in Figure 5.4 (b). In this case, the resulting surface and interface (PSi/Si) roughness are, respectively, 0.8 nm and 8.9 nm. The larger roughness of the PSi/Si interface compared to that of the surface may result from the pores propagation front [14]. Our PSi/Si interface roughness value is in agreement with that obtained by Chamard et al. [15] (7.5 nm) for 37.2 nm thick p-type porous layers. Another possible explanation for this high value is that a change in the porosity at the interface between the porous layer and the bulk Si has occurred resulting in a transition layer [15]. We believe that this effect will be reduced by manufacturing PSi-SLs, where the interfaces between two porous layers are interconnected and no abrupt transition should occur.

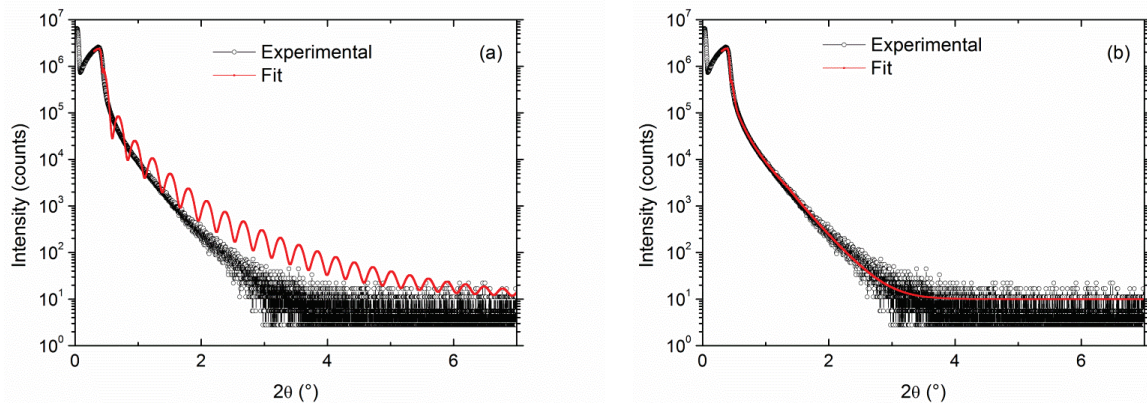


Figure 5.4 X-ray reflectivity profile of mono porous silicon layer of 30 nm thickness. $P = 24$ % **(a)** Simulated profile (red curve) with low interface roughness 0.2 nm. **(b)** Simulated profile (red curve) with interface roughness 8.9 nm.

5.2.1.3 Porous silicon superlattice: nanometric periods

Following the characterization of mono and bi PSi layers, we aim now at manufacturing PSi-SLs with nanometric layers. Figure 5.5 depicts the reflectivity spectrum obtained on a PSi-SL of 23 periods with 3.105 μm as total thickness. Each period is made of two porous layers, the first (second) layer has $d_1 = 105$ nm ($d_2 = 30$ nm), $P_1 = 70$ % ($P_2 = 24$ %) and $t_1 = 19$ s ($t_2 = 50$ s) with $t_{1stop} = 190$ s ($t_{2stop} = 500$ s). This structure should provide an asymmetrical Bragg reflector with its gap center at a wavelength [16]

$$\lambda = 2(n_1d_1 + n_2d_2), \quad (5.1)$$

where n_1 and n_2 are, respectively, the refractive indices of the first and the second layer. We obtain $\lambda = 507$ nm. Our experimental spectrum shows a Bragg plateau centered at 500 nm (see Figure 5.5). This implies a good agreement between the theoretical expected and experimental results. Note that a variation of 1 nm in the thickness of the layer with the lowest porosity may induce a shift of 6 nm in the position of the center of the Bragg plateau.

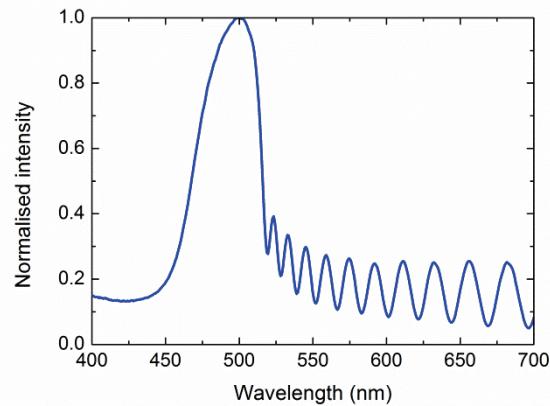


Figure 5.5 Reflectivity spectrum from a PSi-SL with 135 nm periodicity.

This result was encouraging for attempting to manufacture PSi-SLs with shorter periods. Our PSi-SL is formed of ten periods with a total thickness of 580 nm (see Figure 5.6). The anodization parameters used are as follows: $J_1 = 6.5 \text{ mA.cm}^{-2}$, $t_1 = 5 \text{ s}$, $t_{1stop} = 50 \text{ s}$, $J_2 = 0.3 \text{ mA.cm}^{-2}$, $t_2 = 50 \text{ s}$, $t_{2stop} = 500 \text{ s}$. Each period is made of two porous layers of thicknesses $d_1 = 28 \text{ nm}$ and $d_2 = 30 \text{ nm}$, with $P_1 = 70 \%$ and $P_2 = 24 \%$. Using equation 5.1, this superlattice is expected to provide a Bragg plateau centered at $\lambda = 255 \text{ nm}$. In order to probe this superlattice using microreflectivity an excitation source and a detector in the ultraviolet wavelengths range are required. Due to equipment limitations and as we plan to manufacture even shorter periods for future work, we decided to use TEM to look at our 580 nm thick PSi-SL.

Cross-sectional TEM lamella was prepared by David Troadec at IEMN laboratory in Lille by means of focused ion beam (FIB). TEM experiments were performed with Dr. Lucian Roiban at MATEIS laboratory (INSA de Lyon) in Villeurbanne. Figure 5.6 (a) depicts the PSi-SL formed on bulk silicon. The total thickness is 600 nm, close to the expected one 580 nm. Moreover, the presence of a periodic crystal is indicated by the change in the color densities in the SL (see Figure 5.6 (a)).

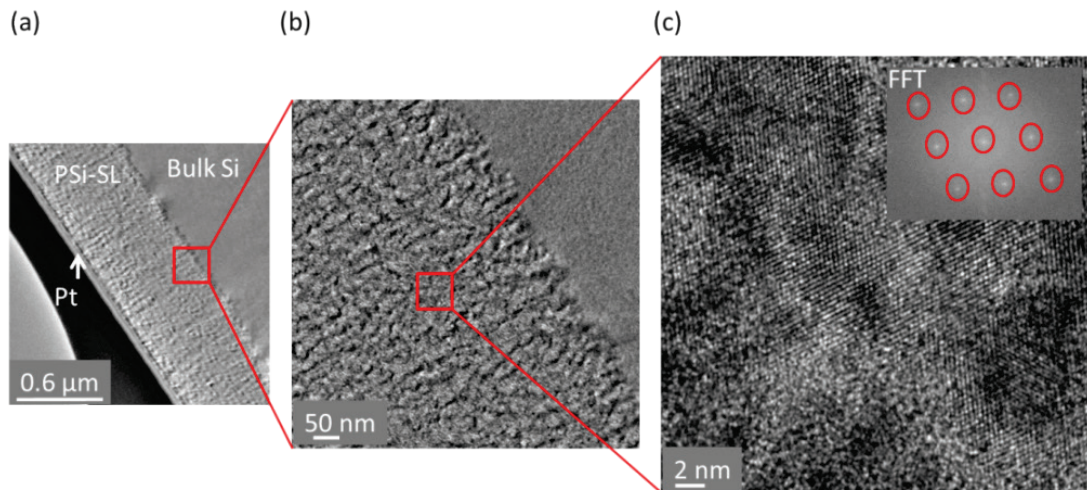


Figure 5.6 PSi-SL. **(a)** 600 nm thick PSi-SL with 10 periods of 58 nm each on bulk silicon with a 10 nm Pt layer on top. **(b)** Zoom from **(a)** showing the porous structures. **(c)** Zoom from **(b)** showing the atomic resolution with the FFT as inset. Red circles are drawn to guide the eyes.

If we compare this Figure with Figure 5.7 (a) with a micrometric period, it is hard to distinguish between them due to the very short period in our case. Figure 5.6 (b) is a zoom obtained from Figure 5.6 (a). We do not observe the formation of an intermediate layer, seen by Amato et al. [16], obtained due to abrupt change in the current (see Figure 5.7 (b)). Moreover, the interfaces do not seem to be sharp but rather the layers are interconnected. If the periodicity is present, this result can be in favor of rendering the proof of phonon coherence more evident in such crystal. Figure 5.6 (c) is an atomic resolution TEM imaging obtained from a zoom from Figure 5.6 (b). The inset in this image is its fast Fourier transform (FFT). The measured distance between two bright spots (3.13 \AA) indicates that the walls of porous silicon have (111) orientation [17], which is different from the bulk one, (100). This result is in good agreement with that obtained by Tsu et al. [18].

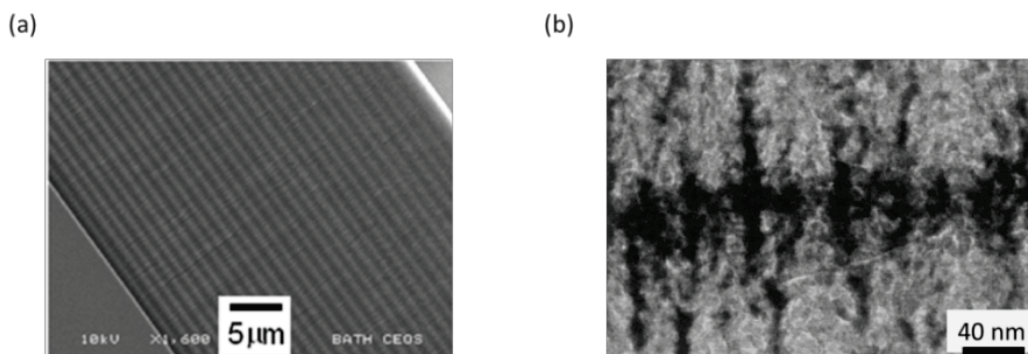


Figure 5.7 **(a)** SEM image of PSi-SL with a period of $2.42 \mu\text{m}$ ($d_1 = 1.21 \mu\text{m}$ and $d_2 = 1.21 \mu\text{m}$) [8]. **(b)** TEM image, at high magnification, of a PSi-SL [16].

5.3 Towards thermal characterization of porous silicon superlattices

PSi-SLs thermal properties will be studied using the 3ω method [19], an electrical method that consists in depositing a transducer which plays, at the same time, the role of a heater and a thermometer. The transducer needs to be electrically conductive and with a temperature-dependent resistance to measure the thermal response from the sample. We chose gold (Au) as a candidate to perform the measurements. The transducers were manufactured at UCB laboratory (INSA de Lyon), Villeurbanne, using laser lithography with the help of Dr Céline Chevalier. This is a direct writing method that does not require the use of a photomask as in the case of photolithography. The manufacturing process is displayed in Figure 5.8 and is detailed as follows:

- Sample's top covering with AZ 5214E photoresist at 3000 rpm (revolutions per minute) for 30 s.
- Bake at 120 °C for 90 s.
- Sample exposure to laser beam. We note that the time writing changes depending on the area of the pattern.
- AZ developer for 10 s.
- Deposition of 5 nm of Cr and 100 nm of Au by thermal evaporation means.
- Liftoff in acetone solution placed in ultrasonic cleaner.

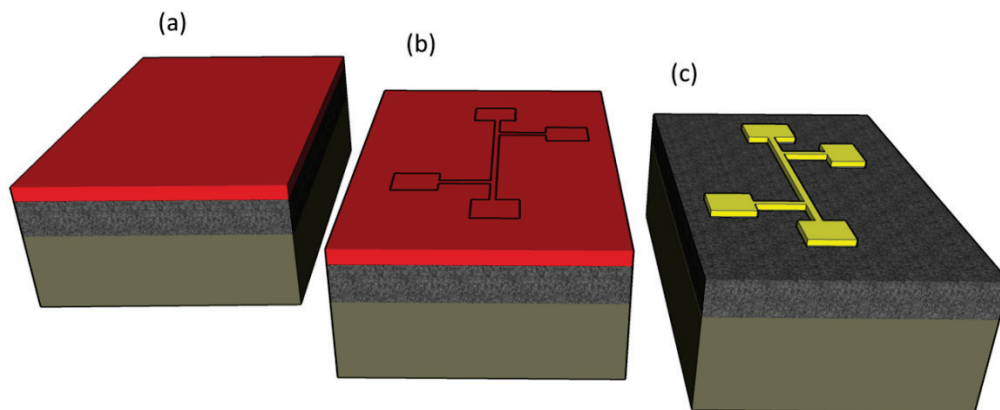


Figure 5.8 Manufacturing process of Au transducers using laser lithography. **(a)** PSi-SL is covered with AZ 5214E photoresist. **(b)** The laser draws the patterns on the photoresist; following to this step the sample is put in AZ developer to take out the exposed part. **(c)** 5 nm Cr layer deposition followed by 100 nm Au deposition; this step is followed by a liftoff in acetone.

Figure 5.9 shows the principle of the 3ω measurements where an ac current is injected in two of the four pads while the response of the transducer is obtained by measuring the output voltage from the two other pads. 5 nm thick Cr layer was deposited beneath the 200 μm long, 10 μm large and 100 nm thick Au wire for adhesion enhancement reasons.

The measurements of the thermal conductivity of PSi-SLs are planned at cryogenic temperatures at CETHIL laboratory.

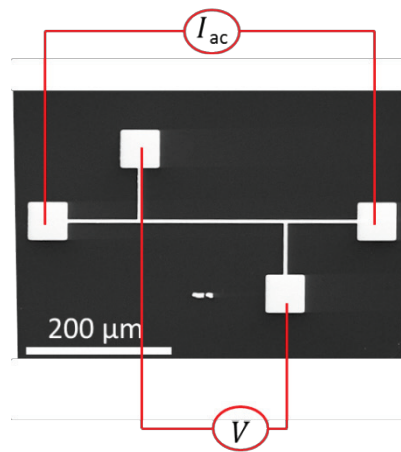


Figure 5.9 SEM image showing the principle of the 3ω measurements. $200 \mu\text{m}$ long, $10 \mu\text{m}$ large and 100 nm thick Au central wire deposited on 5 nm thick Cr layer on top of PSi.

5.4 Summary and perspectives

The goal of this chapter was to introduce PSi-SL as new configuration for the evidence of thermal phonon coherence in Si. We showed three different characterization techniques that could be applied to porous silicon layers. Microreflectivity requires the preparation of thick layers, limiting its application to PSi-SLs of very thin porous layers. X-Ray reflectivity can be applied to thin porous silicon layers but the simulated profiles for data analysis require the knowledge of multiple parameters. TEM remains the best technique for looking at the structure of PSi-SLs with short periods. The limitation of this technique is that it requires complicated sample preparations. We showed that PSi-SL does not have well defined interfaces, but rather the porous layers are interconnected. In the end of this chapter, we pointed out that the roughness of porous silicon does not disturb the deposition of gold wires on top of a PSi-SL opening the way for electrothermal characterization- like 3ω measurements. Now that the samples are ready, their thermal properties will be studied by performing 3ω measurements at cryogenic temperatures.

The formation of PSi-SLs starting from a silicon wafer requires the use of two different current densities and time attacks. Unfortunately, these parameters may not be well controlled, thus inducing errors in layer porosities and thicknesses. Another possible way for the manufacturing of PSi-SLs is epitaxially growing silicon layers with different doping level. In this case, only one current density and time attack are needed. The thickness of the layer is defined by epitaxial means and the porosity depends on the doping level of the layer. This interesting alternative can allow obtaining PSi-SLs with well-defined nanometric porous layers that can be used for the demonstration of coherent heat conduction. Finally, towards this end, aperiodic multilayer structures with the same number of layers and the same total thickness of P_1 and P_2 materials could be prepared for undoubtable evidence of periodicity effect on the thermal conductivity (if any).

Bibliography

- [1] M. N. Luckyanova, J. Garg, K. Esfarjani, A. Jandl, M. T. Bulsara, A. J. Schmidt, A. J. Minnich, S. Chen, M. S. Dresselhaus, Z. Ren, E. A. Fitzgerald, and G. Chen, “Coherent Phonon Heat Conduction in Superlattices”. *Science*, vol. 338, no. 6109, pp. 936–939, 2012.
- [2] J. Ravichandran, A. K. Yadav, R. Cheaito, P. B. Rossen, A. Soukiassian, S. J. Suresha, J. C. Duda, B. M. Foley, C.-H. Lee, Y. Zhu, A. W. Lichtenberger, J. E. Moore, D. A. Muller, D. G. Schlom, P. E. Hopkins, A. Majumdar, R. Ramesh, and M. A. Zurbuchen, “Crossover from incoherent to coherent phonon scattering in epitaxial oxide superlattices”. *Nat. Mater.*, vol. 13, no. 1, p. 168, 2013.
- [3] G. Vincent, “Optical properties of porous silicon superlattices”. *Appl. Phys. Lett.*, vol. 64, no. 18, pp. 2367–2369, 1994.
- [4] L. C. Parsons and G. T. Andrews, “Observation of hypersonic phononic crystal effects in porous silicon superlattices”. *Appl. Phys. Lett.*, vol. 95, no. 24, 2009.
- [5] L. C. Parsons and G. T. Andrews, “Brillouin scattering from porous silicon-based optical Bragg mirrors”. *J. Appl. Phys.*, vol. 111, no. 12, 2012.
- [6] A. Bruyant, G. Lerondel, P. J. Reece, and M. Gal, “All-silicon omnidirectional mirrors based on one-dimensional photonic crystals”. *Appl. Phys. Lett.*, vol. 82, no. 19, pp. 3227–3229, 2003.
- [7] G. N. Aliev, B. Goller, D. Kovalev, and P. A. Snow, “Hypersonic acoustic mirrors and microcavities in porous silicon”. *Appl. Phys. Lett.*, vol. 96, no. 12, pp. 2010–2013, 2010.
- [8] L. Thomas, G. N. Aliev, and P. A. Snow, “Hypersonic rugate filters based on porous silicon”. *Appl. Phys. Lett.*, vol. 97, no. 17, pp. 2010–2013, 2010.
- [9] P. J. Reece, G. Lerondel, J. Mulders, W. H. Zheng, and M. Gal, “Fabrication and tuning of high quality porous silicon microcavities”. *Phys. Status Solidi Appl. Res.*, vol. 197, no. 2, pp. 321–325, 2003.
- [10] E. Guillermain, “Dispositifs nanophotoniques à ondes de surface en silicium poreux: technologie et application à la bio-détection”. *PhD thesis*, 2007.
- [11] C. Mazzoleni and L. Pavesi, “Application to optical components of dielectric porous silicon multilayers,” *Appl. Phys. Lett.*, vol. 67, no. 1995, p. 2983, 1995.
- [12] S. Billat, M. Thönissen, R. Arens-Fischer, M. G. Berger, M. Krüger, and H. Lüth, “Influence of etch stops on the microstructure of porous silicon layers”. *Thin Solid Films*, vol. 297, pp. 22–25, 1997.
- [13] H. Kiessig, *Ann Phys*, vol. 10, pp. 715–768, 1931.
- [14] D. Buttard, G. Dolino, D. Bellet, T. Baumbach, and F. Rieutord, “X-ray reflectivity investigation of thin p-type porous silicon layers”. *Solid State Commun.*, vol. 109, no. 1, pp. 1–5, 1998.
- [15] V. Chamard, P. Bastie, D. Le Bolloch, G. Dolino, E. Elkaïm, C. Ferrero, J.-P. Lauriat, F. Rieutord, and D. Thiaudière, “Evidence of pore correlation in porous silicon: An x-ray grazing-incidence study”. *Phys. Rev. B*, vol. 64, no. 24, p. 245416, 2001.
- [16] G. Amato, L. Boarino, A. M. Rossi, G. Lerondel, and A. Parasini, “Low dimensional porous silicon superlattices”. *Mater. Sci. Eng.*, vol. 69–70, no. 1999, pp. 48–52, 1999.
- [17] H. E. Swanson, M. C. Morris, and E. H. Evans, *Standard X-ray Diffraction Powder Patterns*. Washington, D.C.: National Bureau of Standards, 1956.
- [18] R. Tsu, H. Shen, and M. Dutta, “Correlation of Raman and photoluminescence spectra of porous silicon”. *Appl. Phys. Lett.*, vol. 60, no. 1, pp. 112–114, 1992.
- [19] D. G. Cahill, “Thermal conductivity measurement from 30 to 750 K: The 3ω method”. *Rev. Sci. Instrum.*, vol. 61, no. 2, pp. 802–808, 1990.

General conclusions

This report was dedicated to the structural and thermal characterization of Si-based thermally-insulating materials compatible with CMOS technology and to the manufacturing of some of them. Two ways for thermal conductivity reduction are possible and were envisaged: phonon boundary scattering in the particle (incoherent) regime and phonon coherence. Two characterization techniques to determine the thermal conductivity of nanoobjects were used: micro-Raman thermometry and scanning thermal microscopy (SThM).

We first presented amorphous materials made of porous silicon (PSi) irradiated by swift heavy ions. Materials of porosity of 56 % and ^{129}Xe ions were used in our study. The low thermal conductivity of amorphous materials is attributed to incoherent phonons with extremely short mean free path. The study included the manufacturing process of PSi samples irradiated at two different energies and five different fluences, followed by the characterization of their thermal properties. We demonstrated that crystalline silicon is amorphized in the electronic regime with single ion species. The determination of the amorphous fractions due to sample irradiation was realized by micro-Raman spectroscopy. Micro-Raman thermometry and SThM, both, showed a linear decrease of thermal conductivity while increasing the amorphization phase, to achieve a reduction in thermal conductivity by more than two orders of magnitude compared to bulk Si. We observed that PSi retains its initial porosity as the amorphization did not induce structural changes. The great benefits of irradiation are the obtaining of better thermal insulating materials, with thermal conductivities close or even lower than those of high porous materials without suffering from mechanical stability. Our 56 % porous silicon with an amorphous fraction of 81 % turned out to have a thermal conductivity very close to that of silicon dioxide, known as one of the best solid insulators. In complex geometries analytical models fail in the determination of the thermal conductivity and FEM simulations were required. For SThM, calibration samples of well-known thermal conductivities were used.

We then investigated suspended membranes in plain and periodically perforated configurations. The goal so far was to study heat conduction in these membranes using micro-Raman thermometry and SThM at room temperature. The former technique probes mostly the in-plane thermal conductivity (in vacuum), while the latter may probe the cross-plane one. Results from the two techniques show a decrease in the thermal conductivity from the plain configuration to the perforated ones while decreasing the period. SThM measurements showed a decrease in the plain membranes by a factor larger than 3.7 compared to bulk silicon. It also exhibited a maximum decrease in thermal conductivity by more than one order of magnitude for the smallest period of 60 nm compared to the bulk. This corresponds to a reduction factor of 2.8 in comparison to the plain membrane. Micro-Raman thermometry performed on the suspended membranes showed a reduction in the thermal conductivity of the plain membrane by a factor 2.5 compared to bulk Si. When applied to the phononic

membranes, a maximum decrease in the thermal conductivity by a factor 5 (2) compared to the bulk (plain membrane) was obtained.

In addition to the two previous types of materials, an innovative Si-based configuration was proposed for evidencing thermal phonon coherence at cryogenic temperatures. It consists of PSi superlattices. Structural characterization dealing with nanometric PSi layers of thicknesses about 28 nm was initiated. Au wires were deposited on the PSi superlattice for 3ω measurements at cryogenic temperatures. The thermal characterization step will be performed soon.

The quantitative determination of the thermal conductivity of suspended membranes by SThM required a deep understanding of heat transfer between the tip and the studied sample. When dealing with suspended membranes, calibration samples, alone, are not anymore sufficient for thermal conductivity determination. To this end an innovative method was proposed based on decoupling the contribution of air and contact to heat transfer between the tip and the sample. FEM simulations were required to model the real configuration for studying the heat transfer between the tip and the sample. The tilted tip exchanges more heat with the sample and so the technique is more sensitive to the thermal conductivity of the studied samples. By fitting the experimental data from SThM measurements, a new promising out-of-contact measurement technique was proposed and can be applied for the determination of the thermal conductivity of materials with configurations different than that of bulk ones.

The quantitative determination of the thermal conductivity of suspended membranes by micro-Raman thermometry required also the use of FEM simulations when analytical models failed again to offer precise deduction of the thermal conductivity of suspended membranes. Results from this technique are based on different parameters, but the absorbance is the main critical parameter that should be carefully determined in the case of suspended membranes and especially for the perforated ones. The results showed that if not accounting for the good radius of the holes, the determination of the thermal conductivity, especially for the smallest pitch cannot be performed.

We believe that the present results confirm theoretical predictions and provide a firm basis for future experimental determination of incoherent and coherent thermal transport in nanostructures at room temperature or below, in amorphous and crystalline materials of interest for electronics and energy-harvesting devices.

Appendix. Comparison between volume heat generation and pointlike heat source

By solving the fin equation for a volume heat generation and by using the same configuration and parameters as in Section 4.3.1 we find that

$$\Delta T(x) = \frac{AP_0}{\lambda S L m^2 \operatorname{ch}(mL/2)} \left[\operatorname{ch}\left(\frac{mL}{2}\right) - \operatorname{ch}(mx) \right]. \quad (\text{A.1})$$

Using equation A.1 and by normalizing to the maximum temperature level at $x = 0$, we plotted the black curve in Figure A.1. The red curve was obtained following the same procedure with the case of a pointlike heat source using equation 4.11. It is interesting to note that the two normalized profiles are not similar when the heat loss coefficient $h \neq 0$, in contrast to the case for $h = 0$ where parabola are found.

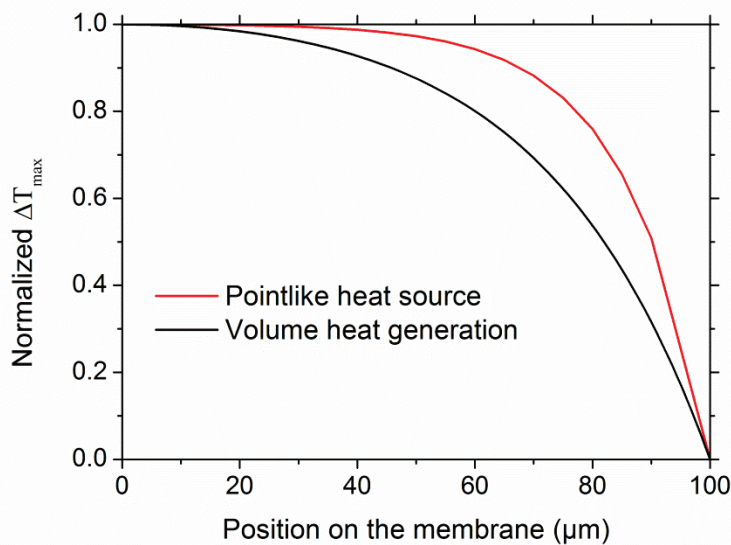


Figure A.1 Normalized maximum temperature rise at each position on the membrane.



FOLIO ADMINISTRATIF

THESE DE L'UNIVERSITE DE LYON OPEREE AU SEIN DE L'INSA LYON

NOM : MASSOUD
2016

DATE de SOUTENANCE : 20 juin

(avec précision du nom de jeune fille, le cas échéant)

Prénoms : MOUHANNAD

TITRE : Experimental characterization of heat transfer in nanostructured silicon-based materials

NATURE : Doctorat

Numéro d'ordre : 2016LYSEI063

Ecole doctorale : Matériaux

Spécialité : Matériaux

RESUME : Ce mémoire de thèse aborde la caractérisation expérimentale du transfert thermique à l'échelle nanométrique dans des matériaux compatibles avec les procédés de la micro-électronique. Pour cela deux techniques de caractérisation sont appliquées chacune à deux différents systèmes, le silicium mésoporeux irradié et les membranes de silicium suspendues.

La première technique de caractérisation est la thermométrie micro-Raman. La puissance du laser chauffe l'échantillon exposé. La détermination de la conductivité thermique nécessite la modélisation de la source de chaleur par la méthode des éléments finis. Dans les cas considérés la modélisation de la source de chaleur repose sur différents paramètres qui doivent être soigneusement déterminés.

La seconde technique de caractérisation est la microscopie à sonde locale (d'acronyme anglais SThM), basée sur le principe de la microscopie à force atomique (d'acronyme anglais AFM). Utilisée en mode actif, la sonde AFM est remplacée par une sonde résistive de type Wollaston qui est chauffée par effet Joule. Utilisée en mode AFM contact, cette technique permet une excitation thermique locale du matériau étudié. La détermination de la conductivité thermique nécessite l'analyse de la réponse thermique de la sonde au moyen d'échantillons d'étalonnage et également via la modélisation dans le cas des géométries complexes. L'effet de la position de la pointe sur le transfert de chaleur entre la pointe et l'échantillon est étudié. Une nouvelle méthode de découplage entre le transfert de chaleur entre la pointe et l'échantillon, respectivement à travers l'air et au contact, est proposée pour la détermination de la conductivité thermique des géométries complexes.

Les résultats obtenus avec les deux techniques pour les échantillons de silicium mésoporeux irradiés à l'aide d'ions lourds dans le régime électronique sont en bon accord. Ils montrent la dégradation de la conductivité thermique du silicium mésoporeux suite à une augmentation dans la phase d'amorphe lorsque la dose d'irradiation croît.

Les résultats obtenus sur les membranes de silicium suspendues montrent une réduction de la conductivité thermique de plus de 50 % par rapport au silicium massif. Lorsque la membrane est perforée périodiquement afin de réaliser une structure phononique de période inférieure à 100 nm, cette réduction est approximativement d'un ordre de grandeur.

Un chapitre introduisant un matériau prometteur à base de silicium pour observer des effets de cohérence phononique conclut le manuscrit.

MOTS-CLÉS : Nanothermométrie; microscopie à sonde locale; thermométrie micro-Raman; conductivité thermique; phonons; transfert conductif; silicium mésoporeux; irradiation ions lourds; régime électronique; silicium amorphe, membranes suspendues, membrane phononique; super-réseaux; cohérence phononique

Laboratoire (s) de recherche : Institut des Nanotechnologies de Lyon (INL) et Centre d'Energétique et de Thermique de Lyon (CETHIL)

Directeur de thèse: Jean-Marie BLUET

Président de jury : FRANCESC Alzina

Composition du jury :

ALZINA	Francesc	Directeur de recherche (ICN2)	Président
VOLZ	Sébastien	Directeur de recherche (ECP)	Rapporteur
LERONDEL	Gilles	Professeur (UTT)	Rapporteur
ROBILLARD	Jean-François	Maître de conférences (IEMN)	Examineur
BEZENCENET	Odile	Ingénieur-docteur (Thales)	Examinatrice
BLUET	Jean-Marie	Professeur (INSA)	Directeur de thèse
CHAPUIS	Pierre-Olivier	Chargé de recherche (INSA)	Co-directeur de thèse

